Moldavian Journal
of the Physical Sciences

GUIDELINES FOR AUTHORS

The "Moldavian Journal of Physical Sciences" appears quarterly and publishes in English papers referring to original scientific research in physics and related fields, including applications in electronics and technology, material engineering and device physics. A review paper for every issue is planned and short communications with hot news are encouraged.

Papers must be prefaced by a brief abstract in English up to 100 words. Single space of the rows in the manuscript is required.

Authors are invited to send two printed copies of their papers, as well as an electronic record on a $3^{1/4}$ inches diskette, or by e-mail, in English. The articles will be edited by using WORD for Windows. Chapters must be numbered by using Arabic figures, as follows:

3. Experimental results.
3.1. Results analysis.
3.2. Methods of calculus.

Formulae must be written very clearly and easy-to-read. Do not use non-explained abbreviations. Illustrations and diagrams must be realized on computer drafts (on images). All graphic and text objects must be of very good quality and easy to read. Figures included in the text are preferable.

Reference citations will be presented as follows: author's forename initial and last name, journal name, volume, page number, year (in parentheses), for example: F.A. Moldovan, S.P. Russu, Phys. Rev. Let. 85, 357, (2000). Complete title, publisher, city and year will be written for book's author's name and forename initial, for example: M. Teodorescu, Cooperation in science and technology with Eastern and European countries, Editura Tehnica, Bucuresti, vol. 1, 1992. References into the text will be made within square brackets, for example [7]; reference citation numbers must be made successively, as they appear into the text.

Manuscripts of regular papers should be limited up to 10 pages and will be signed by authors; they also must be marked "Ready to print". Reviews are limited up to 20 pages. Maximum 4 pages are admitted for short communications. One full page of the journal (size A4) contains 54 rows with 95 characters/row; font size - 12. Page set up: top, left, right – 2,5; bottom – 3,5 cm. The very manuscript which is marked "Ready to print" will be published within 6 months from sending.

The submitted papers must be reviewed, if possible, by two independent reviewers. The papers must contain original work and have not submitted for publication to any other journal. The papers which have been published previously, as well those accepted to be published in other reviews, will be not be admitted by Editorial Board; the authors have to mention this situation.

Proofs will be sent to authors for checking. Corrections must be restricted to errors since modifications to the text may be charged to the author. The publishers reserve the right to adapt the presentation of an article to conform to our style. After their publishing in our journal, the manuscripts and corresponding illustrations become the property of Editorial Board and will not be returned to the authors. The same for the papers, which have not been admitted for publication. The publishing in our journal is made free of charge.

All rights are reserved by "Journal". Any reproduction or dissemination of the information herein, even as excerpts of any extent, is permitted only by written consent of the Editorial Board.

The papers sent for publishing are considered not secret. The authors only are responsible for this in front of their own institutes or employers. Authors have to mention their complete address and telephone, fax number and e-mail.

Papers from around the world can be sent to be published to the following address:
Department of Mathematical, Physical and Technical Sciences, 5 Academy St., MD 2028 Kishinev, the Republic of Moldova, tel. (+37322) 72-71-57, 73-81-66; E-mail: vcantser@phys.asm.md, E-mail of responsible secretary: sofiadonu@yahoo.com

ON POSSIBLE SCALING OF THE NORMAL-STATE IN-PLANE RESISTIVITY AND ASPECTS OF THE PSEUDO-GAP PROBLEM IN Ba(Fe$_{1-x}$Co$_x$)As$_2$

E. Arushanov [2], G. Fuchs [1], S. Levcenko [2], and S. -L. Drechsler [1]

[1] *Leibniz-Institut für Festkörper- und Werkstoffforschung Dresden - IFW Dresden, Helmholtzstr. 20, Dresden, D-01069 Germany*

[2] *Institute of Applied Physics, Academy of Sciences of Moldova, Chisinau, MD2028 Republic of Moldova*
E-mails: arushanov@hotmail.com, g.fuchs@ifw-dresden.de

Abstract

The zero field in-plane normal-state resistivity of the Ba(Fe$_{1-x}$Co$_x$)As$_2$ ($x = 0.0$–0.3) single crystal above T_c can be reproduced among other possibilities by a very simple expression $\rho(T) = \rho_0 + aT \exp\left(-\dfrac{2\Delta}{T}\right)$ and scaled thereby using the temperature independent energy scale Δ, resistivity ρ_Δ, and residual resistivity ρ_0 as scaling parameters (E. Arushanov, *et. al.* Supercond. Sci. Technol., 24, 105004 (2011)). We show that this Δ is related to the inflection point T_{ip} of $d\rho/dT$, $\Delta/T_{ip} = 1.5$.

1. Introduction

Recently, transition-metal oxypnictides composed by an alternate stacking of Ln$_2$O$_2$ layers and T$_2$Pn$_2$ layers (Ln:La, Pr, Ce, Sm, Nd; T: Fe, Co, Ni, Ru; Pn: P or As) have been identified as novel high-T_c materials [1–5]. The discovery of superconducting transition temperatures up to $T_c = 26$ K in LaFeAsO$_{1-x}$F$_x$ with $x = 0.11$ [1] with a primitive tetragonal ZrCuSiAs-type (1111-type) structure has captured the imaginations of physicists and chemists worldwide. It has been found that the replacement of the nonmagnetic La by magnetic rare earth elements substantially increases T_c to its current record of 56.3 K [6] for this structure class. Subsequent works have led to the identification of superconductors with similar FeAs layers in the body-centered-tetragonal ThCr2Si$_2$-type (122-type) structure. To date, the maximum T_c value achieved for this structure class is 38 K for Ba$_{0.6}$K$_{0.4}$Fe$_2$As$_2$ [7].

Attention has largely shifted from the 1111 to the 122- and 11-type compounds, even though they have lower T$_c$, mainly because of the possibility of growing large single crystals of the latter compounds providing more definitive characterizations of the properties, especially by neutron scattering [5].

The electronic phase diagrams of Ba(Fe$_{1-x}$Co$_x$)As$_2$ ($x = 0.0$–0.3) pnictide superconductors in the normal state based on the analysis of electrical resistivity have been reported for a wide range of doping [8–10]. Despite the similarity of the phase diagrams of cuprates and iron based pnictides, it has been well established that the underlying physics of these compounds is different. Cuprates are doped charge transfer insulators with properties tightly related to strong

electron correlations, while iron pnictides are less correlated metallic systems with a spin density wave (SDW) state at low doping [9] for most of the so-called parent compounds under certain circumstances (ignoring special pressure or strain effects as well as the special case of the so-called codoping of electrons and holes). All $Ba(Fe_{1-x}Co_x)As_2$ phase diagrams [8-10] show an asymmetric shape of the superconducting dome with, however, some difference in compositions corresponding to maximum T_c and to the phase boundary (T_c vanishes at $x \leq 0.16$ [9] or at $x \leq 0.18-0.2$ [8, 10]). Thus, the shape of the superconducting dome is really different from that of the cuprates.

It has been shown that the temperature-dependent resistivity $\rho(T)$ of several members of the iron-pnictide superconductor family including $Ba(Fe_{1-x}Co_x)As_2$ can be scaled using energy scale $\varDelta$, resistivity $\rho_\varDelta$, and residual resistivity ρ_0 as scaling parameters [11−16]. In this study, based on our previous $Ba(Fe_{1-x}Co_x)As_2$ scaling data [13, 14], we show that Δ is related to inflection point T_{ip} of $d\rho/dT$, namely, $\Delta/T_{ip} = 1.5$ and $T_{sdw} \sim T_{ip}$ in the underdoped regime.

2. Results and discussion

The scaling behavior of the normal state resistivity for $Ba(Fe_{1-x}Co_x)As_2$ ($x = 0.00-0.30$) was analyzed using the scaling methods reported in [17−19] and experimental data presented in [9, 10]. Using the following astonishing simple expression for the scaling function of ρ

$$\rho(T) \ = \ \rho_0 \ + \ aT \ \exp \ \left(- \frac{2\Delta}{T} \right) \ , \tag{1}$$

(where ρ_0 is the residual resistivity and 2Δ defines the energy scale controlling the linear and superlinear behavior) proposed by Moshchalkov [17] we have obtained a good fit for $\rho(T)$ of $Ba(Fe_{1-x}Co_x)As_2$ samples with x ranging from 0.0 to 0.3 in a broad temperature region (see Fig. 1) and the obtained nearly "universal" scaling-law for

$$r(t) = (\rho - \rho_o)/(\rho_\varDelta - \rho_o) \quad \text{with} \quad t = T/2\Delta \ , \tag{2}$$

for all Co concentrations (see Fig. 2, note that $\rho_\varDelta$ is the resistivity at $t = 1$, i.e. at $T = 2\Delta$).

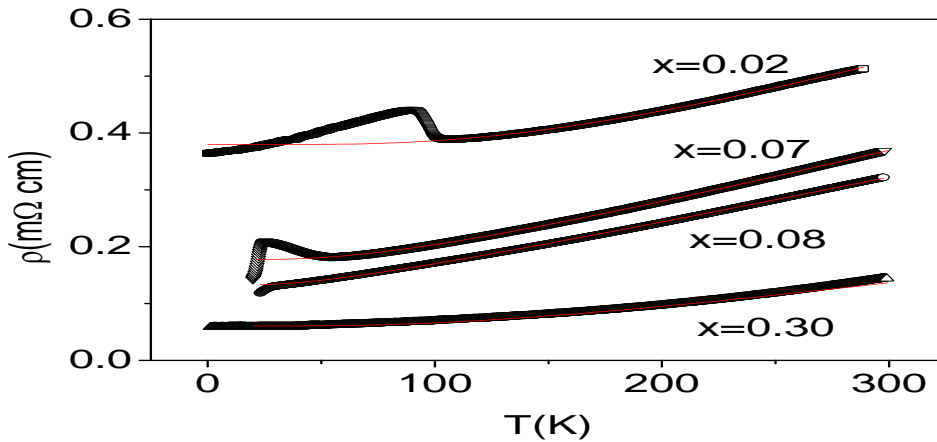**Fig. 1.** Temperature dependence of resistivity for $Ba(Fe_{1-x}Co_x)_2As_2$ ($x = 0.02, 0.075,$ and 0.30). The solid lines represent a fit using Eq. (1) (the figure is taken from [13]).

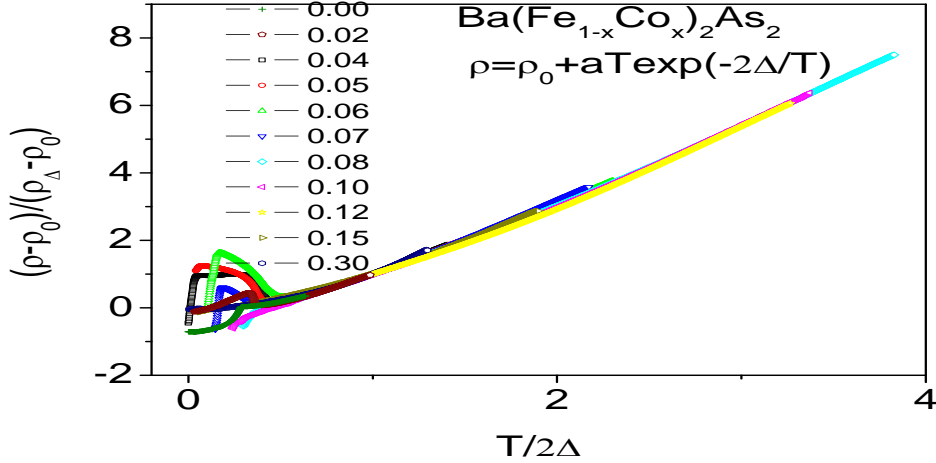**Fig. 2.** Scaling analysis on the temperature dependence of the resistivity of various Ba(Fe$_{1-x}$Co$_x$)$_2$As$_2$ samples ($0 \le x \le 0.3$). The temperature is rescaled with Δ (an energy scale) and the resistivity is given by $\dfrac{\rho - \rho_0}{\rho_\Delta - \rho_0}$ in which the extrapolated residual resistivity ρ_0 has been subtracted and ρ_Δ is the resistivity at $T = 2\Delta$. (the figure is taken from [13]).

Thereby adopting the validity of Eq. (1), one arrives approximately at a "universal" quasi-linear "scaling" function for a wide temperature region of $1.5 < t < 7$, if the off-set --1.8 is ignored:

$$r(t) = t \exp(1-1/t) \approx -1.8 + 2.6\,t\ , \tag{3}$$

(see also Fig. 2). Empirically, we obtained a slightly different expression:

$$r(t) \approx -1.8 + 2.426\,t\ . \tag{4}$$

Thus, the two material and sample dependent parameters ρ_0 and a that still appear in Eq. (1) are almost eliminated in Eqs. (3) and (4).

It should be noted that, in many cases, an alternative power-law fit

$$\rho(T) = \rho_o + AT + BT^2\ , \tag{5}$$

including both a non-Fermi liquid linear term and a standard Fermi-liquid quadratic temperature term due to electron–electron interaction applied in [26] yields although a slightly worse but, in principle, quite similar accuracy compared to Eq. (1). In [26], this behavior was dubbed as an argument for a "lacking" pseudo-gap. Anyhow, the weak point of both approaches ((1) and (5)) is the broad temperature region up to $T = 300$ K and above included in the fit because this way the improper inclusion of a region above T^* into the fit might strongly affect/falsify the analysis. This is especially dangerous in the overdoped region where the pseudo-gap phase is believed to vanish. Therefore, rigorously speaking, both approaches should be considered simply as a more or less convenient formal description of available resistivity data including only a few parameters.

Within a consequent microscopic description of a pseudo-gap scenario, one would expect a dominant contribution to the total conductivity by the non-gapped fraction of "normal" quasi-particles and a strongly temperature dependent one from the pseudo-gapped subsystem. Then, for a monotonously increasing or constant pseudo-gap at low-temperatures, the observed (fitted) residual and low-temperature resistivity should be determined, at first glance, only by the

"normal" quasi-particles. (In case of a non-Fermi liquid for the "normal" subsystem, the situation becomes even more unclear with respect to the origin of ρ_0 !). In this context, the success of both expressions is very surprising. Alternatively, the total conductivity should be determined by a small number of highly mobile quasi-particles in the pseudo-gap phase. To the best of our knowledge, a similar situation can take place only in an anisotropic nodal gapped phase.

The obtained 2Δ values presented in Table 1 show a minimum at about $x = 0.07–0.08$ which corresponds to the highest T_c value, a strong enhancement with x decreasing down to 0, and a weaker one with increasing x in the optimal doped–overdoped regimes ($x = 0.08–0.3$). It should be noted that, in the underdoped regime, the characteristic energy Δ almost linearly drops with increasing doping [13]. A similar variation of Δ and/or the characteristic temperature is observed in $YBa_2Cu_3O_x$ [17] and $La_{2-x}Sr_xCuO_4$ [20] as well as in other members of the cuprate family (see, e.g., Fig. 11 in [19]); this is qualitatively consistent with the doping dependence of their pseudo-gap-values reported in the interpretations of ARPES, tunnelling, and other measurements [19]. In general, pseudogap related features have attracted considerable attention for several unconventional superconductors and correlated compounds including also reports for several iron pnictide superconductors studied by various experimental techniques, such as Knight-shift, anisotropic transport, NMR, and ARPES. Qualitatively, the pseudo-gap is generally understood as a partial gapping of the Fermi surface, while other parts remain metallic.

Table 1. Scaling parameter Δ and deflection temperature T_{ip} for $Ba(Fe_{1-x}Co_x)_2As_2$ derived from the resistance and superconducting transition temperatures T_c data reported by Rollier-Albenque et al. [9] and Fang et al. [10] . Superconducting transition temperatures T_c are also taken from [9, 10]

$Ba(Fe_{1-x}Co_x)_2As_2$ [10]	2Δ (K)	T_c (K)	T_{ip} (K)	$Ba(Fe_{1-x}Co_x)_2As_2$ [9]	2Δ (K)	T_c (K)	T_{ip} (K)
$x = 0.00$	469	-	156.3	$x = 0$	450		128.3
$x = 0.02$	303	-	101	$x = 0.014$	326		108.7
$x = 0.04$	212	8	70.7	$x = 0.02$	289		96.3
$x = 0.05$	195	11	65	$x = 0.03$	223	2	74.3
$x = 0.06$	130	19	43.3	$x = 0.04$	173	8	57.7
$x = 0.07$	137	22.5	45,7	$x = 0.045$	157	12	52.2
$x = 0.08$	78	25	26	$x = 0.055$	134	19	44.7
$x = 0.10$	89	24	29.7	$x = 0.06$	106	21	35.3
$x = 0.12$	92	20	30.7	$x = 0.07$	72	25	23.9
$x = 0.15$	156	11	52	$x = 0.08$	70	23	23.3
$x = 0.30$	231		77	$x = 0.12$	101	16	33.6
				$x = 0.14$	125	11	
				$x = 0.20$	208		69.3

Thus, the electronic density of states at the Fermi level decreases at low temperatures. However, on a quantitative level, there is a considerable scattering for various methods; in particular, this concerns energy scale Δ or 2Δ introduced above for the scaling of the resistivity

(see also some remarks given below). However, in spite of a still missing proper microscopic understanding, there are several serious physical problems related to the pseudo-gap even on a phenomenological level. If the pseudo-gap characterizes the order parameter of a special thermodynamic phase competing or sometimes coexisting with superconductivity, there should be a sizable temperature dependence at least in the vicinity of the corresponding phase boundary, in particular, at least close to its onset temperature usually denoted as T^*. In cases of anisotropic pseudo-gaps, phases with nodes, such a temperature dependence, cannot be ignored at all! Only in isotropic nodeless cases at $T << T^*$, this scenario might be meaningful for the interpretation of experimental data. For a first estimate, ignoring strong coupling effects, the evaluation of T^* by adopting the well-known BCS-relation $2\Delta = 3.52 \, k_B T^*$ might be useful. Thus, for a derived pseudo-gap as small as 100 K, only a low-temperature fit of any quantity below 50 K makes sense. In the following, we will adopt this isotropic and temperature independent scenario for the sake of simplicity. A detailed comparison with other approaches and analysis of other physical properties will be given elsewhere. Thereby, it should be borne in mind that, starting from a semi-microscopic model for the pseudo-gapped and remaining unaffected electrons at the complex Fermi surfaces, one will come up with different pseudo-gap values because the weight of each point at the Fermi surface is certainly different for different physical properties affected, for instance, in the case of transport properties by the local Fermi velocities and the impurity dependent intra- and interband scattering rates. All these subtle points are ignored in a formal comparison of different measurements without adopting a certain microscopic model for the underlying multiband electronic structure.

It should be noted that, in cuprates, both Δ and scaling parameter T^* show a strong decrease with increasing x in the underdoped regime [18, 20] and almost constant values in overdoped regime ($La_{2-x}Sr_x CuO_4$, $x = 0.22$–0.34) [20]. The observed compositional dependence of Δ in $Ba(Fe_{1-x}Co_x)As_2$ ($x = 0.0$–0.3) in the overdoped regime is different from that reported for cuprates.

The first and second derivatives of the temperature dependence of resistivity for the $Ba(Fe_{1-x}Co_x)As_2$ system reported by Rullier-Albenque et al. [9] and Fang et al. [10] were analyzed, and the value of inflection point T_{ip} for $d\rho/dT$ was determined (see Fig. 3 and Table 1).

It is shown in Fig. 3 for a representative $\rho(T)$ curve that inflection point T_{ip} for $d\rho/dT$ is closely related to Δ, namely, $\Delta/T_{ip} = 1.5$ for that scaling function $\rho(T)$ (Eq. 1). It is noteworthy that, in a formal sense, this is close to the well-known prediction of the BCS theory: $\Delta/T^* = 1.76$, where the superconducting gap and the transition temperature have been replaced by their pseudo-gap related counter parts. To avoid possible misunderstandings, we emphasize that, in the present context, there is no direct and obvious relation of the former to the corresponding "real" superconducting gap and/or the superconducting transition temperature T_c for the compounds under examination. The $Ba(Fe_{1-x}Co_x)As_2$ phase diagram is presented in Fig. 4.

We can see a reasonable correlation between the T_{SDW} values reported in [10] and our T_{ip} data with $T_{sdw} \sim T_{ip}$ in the underdoped regime. According to [21], the Ba-, Sr-, and Ca-122 magnetic parent compounds with $2\Delta_{SDW}/T_N \approx 5.3, 8.7$, and even 12 exhibit large deviations from the BCS relation as observed in recent optical measurements. In our opinion, this observation indicates the importance of strong coupling and retardation effects well beyond the validity of a weak coupling BCS-type description. The above suggests that, within our approach, a connection between the magnetic SDW-gap and the pseudo-gap is unlikely and/or the inflection point temperature T_{ip} mentioned above might be of some other origin.
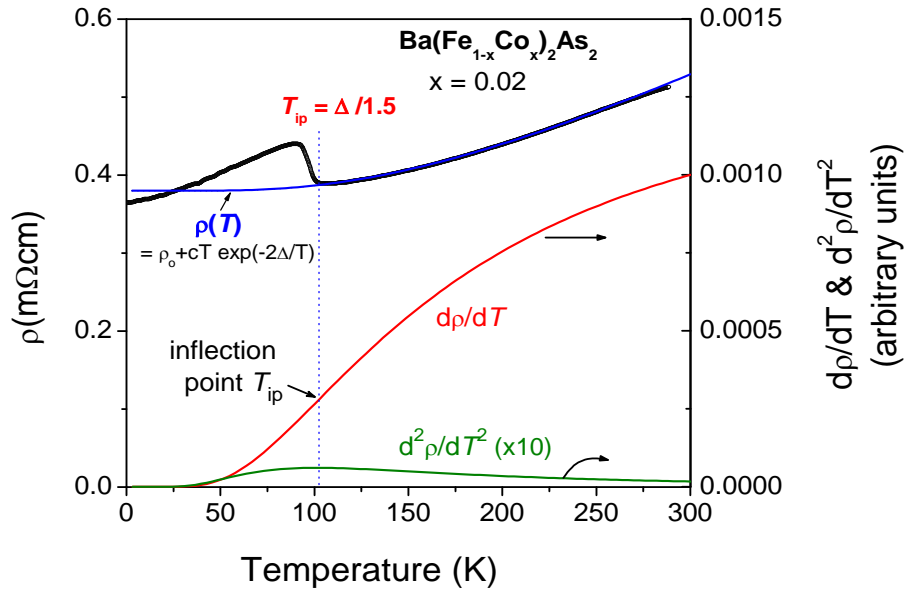
Fig. 3. Temperature dependence of the resistivity of $Ba(Fe_{1-x}Co_x)_2As_2$ for x = 0.02 (black solid line). The data were fitted by $\rho(T)$ according to Eq. (1) (blue line). The first derivative $d\rho/dT$ (red line) with the inflection point at $T = T_{ip}$ and $d^2\rho/dT^2$ (green line) which is 10 times magnified are shown.
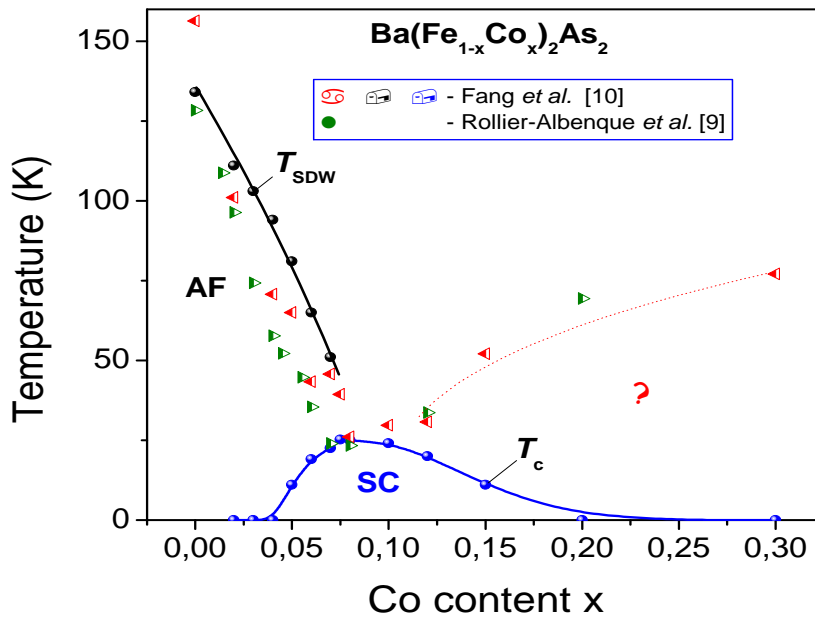
Fig. 4. Phase diagram of $Ba(Fe_{1-x}Co_x)_2As_2$ systems $(0 \leq x \leq 0.3)$. The T_{ip} values were calculated using the resistivity data reported by Rullier-Albenque et al. [9] and Fang et al. [10]. The T_{sdw} and T_c values were taken from [10].

Following [22], we could say that our observation of a doping independent scaling law in the normal state of pnictide superconductors could be probably used as an indication that a pseudogap-like behavior is the reason for a predominant energy scale which controls the low energy excitations. The possible existence of a pseudo-gap in $LaO_{1-x}F_xFeAs$ and $SmFeAsO_{1-x}F_x$ compounds has been reported by Liu et al. [23], Jia et al. [24], and Ou et al. [25] on the base of high resolution photoemission measurements as well as for isomorphic $Ca(Fe_{1-x}Co_x)As_2$ [27] on the basis of NQR measurements with the electric field gradient along the *c*-axis. The reported pseudogap for $x = 0.063$ of (88 ± 6) K is comparable with that for $x = 0.08$ and 0.1 for the Ba counter part (see Table 1) with the data of [10] and $x = 0.07$ of [9]. However, the temperature dependent spin-latice relaxation rate $1/T_1T$ cannot be attributed to an isotropic pseudo-gap. For the isovalently doped $BaFe_2(As_{0.45}P_{0.55})_2$ system [28], a similar value has been reported. However, at variance with our analysis, nothing could be observed in the overdoped regions. A pseudo-gap like behavior has been also derived from NMR spin relaxation rates and Co Knight-shift as well as for interlayer resistivity measurements for $Ba(Fe_{1-x}Co_x)As_2$ [26] but not for the intralayer one. For completeness, note that no pseudo-gap behavior could be derived from STM-measurements for the title compounds [29]. This lacking observation might be ascribed to specific surface properties, whereas bulk sensitive specific heat data for $Ba(Fe_{1-x}Co_x)As_2$ for the linear electronic specific heat (Sommerfeld coefficient) [30] are in conflict by a factor of two with the presence of both usual high-energy and low-energy mass renormalizations and compatible with a reduced electronic density of states which might be caused by a pseudo-gap for a subgroup of electrons. Similar problems for the empirical mass enhancement arise also for overdoped $BaFe_2(As_{0.45}P_{0.55})_2$ samples if the pure band mass scaling shown in Fig. 5 of [31] is adopted. In the context of the transport data reported here, one might suppose that only a subgroup of fast electrons is mainly affected by the pseudo-gap. Comparison of the Δ values for the two samples shown in Table 1 reveals some scattering for the latter. This might be ascribed to different amounts of disorder. Therefore, a systematic study of possible correlations and the amount of disorder as measured by the residual resistivity is of considerable general interest for the elucidation of the microscopic mechanism behind the pseudo-gap.

The microscopic interpretation of the observed gap-like feature Δ is rather unclear at present. One option in connection with the pseudo-gap-like feature more pronounced in the interlayer direction at a significantly larger energy scale would be given by an extremely anisotropic pseudogap observed by our sensitive scaling method for the first time also in the planar direction. Alternatively, it might be related to a slight misorientation in the studied resistivity data taken from the literature and our scaling method could be used as an additional technique to detect it by measuring an angular-dependent admixed *c*-axis contribution. The presence of an inflection point might be also related to a starting saturation phenomena pointing to a lower limit of the mean free path like in the well-known Joffe-Regel scenario given by the interatomic distance.

Among other possibilities for a pseudo-gap like scenario in general, at least three scenarios are worth studying theoretically in more detail: (i) a long-range Coulomb interaction disorder related feature; (ii) a pairing mechanism related pseudo-gap as discussed for the cuprates, and (iii) a band structure related feature from a band slightly below the Fermi energy whose excitations provide additional charge carriers at higher temperatures. A thermal delocalization of localized electrons would also add charge carriers In general, a corresponding systematic study of other FeAs-based pnictides is of considerable interest and might be useful in discriminating between the proposed scenarios and elucidating the unclear nature of the pseudo-gap.

3. Conclusions

The zero-field normal-state resistivity for various levels of doping for $Ba(Fe_{1-x}Co_x)As_2$ (x = 0.05−0.30) can be scaled onto a single universal curve. Energy scale Δ, resistivity ρ_Δ, and residual resistivity ρ_0 are suitable scaling parameters for $Ba(Fe_{1-x}Co_x)As_2$ (x = 0.05−0.30). The existence of a universal metallic $\rho(T)$ curve is interpreted as an indication of a single mechanism which dominates the scattering of the charge carriers in $Ba(Fe_{1-x}Co_x)As_2$ (x = 0.05−0.30) and/or changes in the number of available charge carriers due to a specific electronic structure. We have shown that Δ is related to inflection point T_{ip} of $d\rho/dT$, Δ/T_{ip}=1.5 with $T_{SDW} \sim T_{ip}$ in the underdoped regime. Further comprehensive studies are required to clarify the microscopic nature of the observed Δ and its possible relation to the pseudo-gap reported in numerous recent studies based on other experimental techniques. Regardless of the final applicability of certain pseudo-gap scenarios to iron pnictides and related compounds, the empirical findings presented in this study are expected to be useful for any sophisticated microscopic description hopefully achieved in the near future.

References

[1] Y. Kamihara, T. Watanabe, M. Hirano, and H. Hosono, J. Am. Chem. Soc. 108, 3296, (2008).

[2] Y. Kamihara, H. Hiramatsu, M. Hirano, R. Kawamura, H. Yanagi, T. Kamiya, and H. Hosono, J. Am. Chem. Soc. 128, 10012, (2006).

[3] T. Y. Chen, Z. Tesanovic, R. H. Liu, X. H. Chen, and C. L. Chien, Nature 453, 761, (2008)

[4] G. F. Chen et al., Phys. Rev. Lett. 100, 247002, (2008).

[5] Z. A. Ren et al., Mater. Res. Innovation. 12, 105, (2008).

[6] C. Wang et al., Europhys. Lett. 83, 67006, (2008).

[7] M. Rotter, M. Tegel, and D. Johrendt, Phys. Rev. Lett. 101, 107006, (2008).

[8] J. H. Chu, J. G. Analytis, C. Kucharczyk, and I. R. Fisher, Phys. Rev. B 79, 014506, (2009).

[9] J. F. Rullier-Albenque, D. Colson, A. Forget, and H. Alloul, Phys. Rev. Lett. 103, 057001, (2009).

[10] L. Fang et al., Phys. Rev. B 80, 140508, (2009).

[11] E. Arushanov, S. Levcenko, G. Fuchs, and S. -L. Drechsler, J. Supercond. Nov. Magn. 26, 2727, (2013).

[12] E. Arushanov, S. Levcenko, G. Fuchs, and S. -L. Drechsler, J. Supercond. Nov. Magn. 25, 1753, (2012) .

[13] E. Arushanov, S. Levcenko, G. Fuchs, B. Holzapfel, S. -L. Drechsler, and L. Schultz, J. Supercond. Nov. Magn. 24, 2285, (2011).

[14] E. Arushanov, G. Fuchs, S. Levcenko, S. L. Drechsler, B. Holzapfel, and L. Schultz, Supercond. Sci. Technol. 24, 105004, (2011).

[15] E. Arushanov, S. Levcenko, G. Fuchs, and S. -L. Drechsler, Physica C 471, 509, (2011).

[16] E. Arushanov, S. Levcenko, G. Fuchs, B. Holzapfel, S. -L. Drechsler, and L. Schultz, Physica C 471, 237, (2011).

[17] V. V. Moshchalkov, J. Vanacken, and L. Trappeniers, Phys. Rev. B 64, 214504, (2001).

[18] J. Vanacken, L. Trappeniers, P. Wagner, L. Weckhuysen, V. V. Moshchalkov, and Y. Bruynseraede, Phys. Rev. B 64, 184425, (2001).

[19] H. G. Luo, Y. H. Su, and T. Xiang, Phys. Rev. B 77, 014529, (2008).

[20] H. Y. Hwang, B. Batlogg, H. Takagi, H. L. Kao, J. Kwo, R. J. Cava, J. J. Krajewski, and W. F. Peck, Phys. Rev. Lett. 72, 2636, (1994).

[21] A. Charnukha, D. Pröpper, T. I. Larkin, D. L. Sun, Z. W. Li, C. T. Lin, T. Wulf, B. Keimer, A. V. Boris, et al., Phys. Rev. B 88, 184511, (2013).

[22] B. Wuyts, V. V. Moshchalkov, and Y. Bruynseraede, Phys. Rev. B 53, 9418, (1996).

[23] H. Y. Liu et al., Chin. Phys. Lett. 25, 3761, (2008).

[24] X. W. Jia et al., Chin. Phys. Lett. 25, 3765, (2008).

[25] H. W. Ou et al., Sol. St. Commun. 148, 504, (2008).

[26] M. A. Tanatar, N. Ni, A. A. Thaler, S. L. Bud'ko, P. C. Canfield, and R. Prozorov, Phys. Rev. B 82, 134528 (2010); Phys. Rev. B 89, 1445514, (2014).

[27] S. H. Baek, H. -J. Grafe, L. Harnagea, S. Singh, S. Wurmehl, and B. Büchner, Phys. Rev. B 84, 094510, (2011).

[28] T. Shimojima, T. Sonobe, W. Malaeb, et al., Phys. Rev. B 89, 045101, (2014).

[29] F. Massee, J. Kaas, E. van Heumen, S. de Jong, R. Husman, H. Luigies, J. B. Goedkoop, and M. S. Golden, Euro. Phys. Lett. 92, 57012, (2010).

[30] C. Meingast, F. Hardy, R. Heid, P. Adelmann, A. Böhmer, P. Burger, D. Ernst, R. Fromknecht, P. Schweiss, and T. Wolf, Phys. Rev. Lett. 108, 177004, (2012).

[31] P. Walmsley, C. Putzke, L. Malone, et al., Phys. Rev. Lett. 110, 257002, (2013).

Co(II) COORDINATION NETWORKS BASED ON TWO RIGID DICARBOXYLIC ACIDS: SYNTHESIS, STRUCTURES, AND APPLICATIONS: A LITERATURE OVERVIEW (2005-2015)

Diana Chisca

Institute of Applied Physics, Academy of Science of Moldova, Academiei str. 5, Chisinau, Republic of Moldova
E-mail: chisca.diana.ich@gmail.com

Abstract

Co(II) coordination networks as an integral part of metal-organic materials have been in focus of materials scientists and crystal engineers for the last two decades. This interest stems not only from their reported fascinating architectures and remarkable adsorption properties being the inherent properties of the majority of the so far known metal-organic frameworks, but also from the unique place that Co(II) atom occupies among the transition metals due to its pronounced magnetic properties and colorimetric features. This review highlights the Co(II) mixed-ligand polymeric dicarboxylates built on two rigid dicarboxylic acids, the widely used 1,4-benzenedicarboxylic acid (H_2bdc) and its closest analogue, 4,4'-biphenyldicarboxylic acid (H_2bpdc) that have been reported in the past 10 years. It is focused on: (1) the nature and coordination abilities of Co(II); (2) the synthetic pathways; (3) the impact of size and rigidity of the spacer ligands in the generated coordination networks; (4) examples of one-, two- and three-dimensional coordination polymers; and (5) potential applications of Co(II) coordination polymers.

1. Introduction

Crystal engineering of transition metal complexes, especially coordination polymers (CPs), has been greatly developed in the past decade. Synthesis, characterization, and reactivity of CPs formulated as a coordination compound with repeating coordination entities extending in 1, 2, or 3 dimensions [1], including metal-organic frameworks (MOFs) formulated as a coordination network with organic ligands containing potential voids [1], have been an active research field in recent years. Of great interest are not only the design and synthesis of CPs, but also their enormous variety of intriguing structural topologies, as well as their potential applications in gas sorption, catalysis, luminescence, magnetism, nonlinear optics, and medicine [2, 3]. The most powerful strategy for the architecture of diverse structural topologies in MOFs is the selection of an appropriate multidentate ligand as a linker in connecting metal ions to achieve one-, two-, or three-dimensional network structures [4, 5].

Since 2005, when Co(II)-based MOF-71, Co(bdc)(dmf) and MOF-78, Co(Hpdc)(H_2O)(dmf) (Hpdc=2,7-tetrahydropyrenedicarboxylate) were reported by Yaghi et al. [6], great attention has been paid to coordination chemistry of cobalt complexes with carboxylate

ligands, due to the fact that polynuclear cobalt carboxylates are suitable candidates for structural assembly of new coordination solids with diverse network architectures and useful properties [7]. Thus, in 2009, Zhou and et al. demonstrated that MOF-74-M (M=Mg, Mn, Co, Ni, Zn; MOF-74 = M_2(dhbdc)$(H_2O)_2(H_2O)_{0.6}$(EtOH)$_{1.6}$, dhbdc=2,5-dihydroxybenzenedicarboxylate), which possess a high concentration of metal open sites, yielded excess storage capacities [8], while among the five isostructural analogues, CoMOF-74 stands ahead for methane and acetylene uptake [9] and exhibits the highest thermodynamic propylene-propane selectivity [10]. Among the indisputable advantages of cobalt ion against other transition metals, stands its diverse coordination capacity with the range of geometries, including the octahedral, tetrahedral, square-pyramidal, trigonal bipyramid, and square-planar ones [11], and its vapochromism [12] since the cobalt-containing MOFs can have a wide range of colors, which makes it easy, in many cases, to identify different phases [13].

The most common intrinsic Co(II) colors are very light pink for octahedral coordination and intense blue for tetrahedral coordination [14]. For distorted octahedral coordination, the pink color can intensify to orange, dark-red, purple, and violet depending on the ligand and the type of distortions. For compounds having both tetrahedral and octahedral coordinated ions, the colors are usually from green to blue depending on the distortions and the ratio of cobalt atoms in the two coordination geometries [15]. This property makes Co(II) coordination networks attractive as chemical sensors [16].

Similar to other MOFs based on transition metals, nowadays the Co(II) coordination networks contain a great many of ligands and expand from the carboxylic networks, including the above-mentioned MOF-71, MOF-78, and CoMOF-74, to the mixed-ligand systems based on the combination of at least two ligands, for example, anionic dicarboxylate and neutral pyridine/bipyridine type ligands [17, 38, 59, 71] or combining both of these functions in one molecule [18]. Based on the information provided by the Cambridge Structural Database (CSD) that now contains data on nearly 700 000 crystal structures [19] it might be stated that carboxylic acids occupy a special place in the Co(II) MOF's crystal engineering, and since it is hard to cover all of them, this overview will be restricted to the reported examples of Co(II) mixed-ligand CPs with two rigid aromatic dicarboxylic acids, 1,4-benzenedicarboxylic acid (H_2bdc) and 4,4'-biphenyl-dicarboxylic acid (H_2bpdc) (Scheme 1), in combination with the neutral ligands summarized in Table 1.

These two ligands, 1,4-benzenedicarboxylic acid (H_2bdc) and 4,4'-biphenyl-dicarboxylic acid (H_2bpdc) (Scheme 1) have been used in the synthetic schemes because they can exhibit a short bridge via one carboxylic group or a long one via the phenyl (biphenyl) moiety which leads to varieties of multi-dimensional MOFs with different kinds of topologies [20].

As bridging ligands, dicarboxylates are of immense interest in the construction of polymeric coordination architectures not only because these polymers have a wide range of structural diversities and potential applications as porous and magnetic materials, but also because dicarboxylates are capable of functioning as hydrogen bond donors and/or acceptors [21].

Table 1. List of ligands with abbreviations

Abbreviations	Ligand	Abbreviations	Ligand
L1	4,4'-dipyridyl-N,N'-dioxide	L30	4,4'-bis(imidazol-1-yl)diphenylether
L2	1,2-bis(4-pyridyl)hydrazine	L31	1,4-bis(imidazol-1-yl)-butane
L3	2-(4-thiazolyl)benzimidazole	L32	2,2'-dipyridyl-N-oxide
L4	1,4-bis-(3-pyridyl)-2,3-diaza-1,3-butadiene	L33	N,N'-bis(3-pyridinyl)-1,4-benzenedicarboxamide
L5	N,N'-bis-pyridin-4-ylmethylene-hydrazine	L34	3,5-bis(4-pyridyl)-1H-1,2,4-triazole
L6	2-(pyridin-3-yl)benzimidazole	L35	4,4-bis(imidazole-yl)biphenyl
L7	2,8-di(1H-imidazol-1-yl)dibenzothiophene	L36	3,5-bis(5-(pyridin-4-yl)-4H-1,2,4-triazol-3-yl)pyridine
L8	2-(4-carboxyphenyl)imidazo(4,5-f)(1,10)phenanthroline	L37	N,N'-bis(2-pyridyl)-2,6-diaminopyridine
L9	2,5-bis-(3-pyridyl)-3,4-diaza-2,4-hexadiene	L38	2-(2-pyridyl)-benzimidazole
L10	3-pyridylisonicotinamide	L39	2,2'-bipyridine
L11	1,2-bis-[2-(1H-1,3-imidazol-1-ylmethyl)phenoxy]ethane	L40	1,4-bis(imidazol-1-yl-methyl)-benzene
L12	1-benzylimidazole	L41	4-[bis(3,5-dimethyl-3H-pyrazol-3-yl)methyl]benzoic acid
L13	2,7-bis(ethoxybenzimidazole)-naphthalene	L42	1,6-bis(imidazol-1-yl)-hexane
L14	1,5-bis(ethoxybenzimidazole)-naphthalene	L43	1,3-bis(5,6-dimethylbenzimidazol-1-ylmethyl)benzene
L15	1,3-bis(5,6-dimethylbenzimidazol-1-yl)-2-propanol	L44	N,N'-bis-pyridin-4-ylmethylene-naphthalene-1,5-diamine
L16	4-(Hydrazinomethyl)pyridine	L45	dimethylamide
L17	1,4-diazabicyclo[2.2.2]octane	L46	N,N'-bis-4-pyridyl-isophthalamide
L18	1,10-phenanthroline	L47	1,3-bis(imidazol-1-yl)benzene
L19	2,7-bis(ethoxyimidazole)-naphthalene	L48	3,3',5,5'-tetramethyl-4,4'-bipyrazole
L20	1,3-bis(2-methylbenzimidazol-1-ylmethyl)benzene	L49	1,2-bis[2-(2-pyridinyl)ethylidene]hydrazine
L21	2,6-bis(imidazole-1-yl)pyridine	L50	3-amino-1,2,4-triazole
L22	4-(4-carboxyphenyl)-2,2',4,4-terpyridine	L51	4,4'-di(1H-imidazol-4-yl)biphenyl
L23	4,4'-bipyridinium-N-methyl-4-benzonitrile	L52	1,3-bis(2-methylimidazolyl)propane
L24	4,4'-bipyridinium-N-methyl-3-benzonitrile	L53	4,4'-(2,5-diethoxy-1,4-phenylene) dipyridine
L25	pyridyl-N-oxide	L54	1,4-bis(5,6-dimethylbenzimidazol-1-ylmethyl)benzene
L26	4-methylpyridine N-oxide	L55	1,1'-bis(5,6-dimethylbenzimidazole)methane
L27	3,5-di(pyridine-4-yl)benzoic acid	L56	N,N,N',N'-tetrakis(4-(4-pyridine)-phenyl) biphenyl-4,4'-diamine
L28	1,3-bis(4-pyridyl)propane	dma	N,N-dimethylacetamide
L29	1,3,5-tris(pimidazol-ylphenyl)benzene	dmf	N,N-dimethylformamide
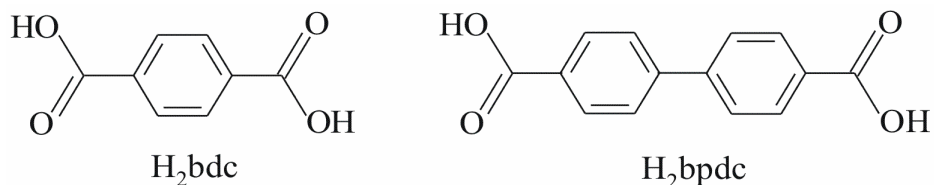
Scheme 1. Structural formulae for dicarboxylic acids with acronyms used in this study.

In this overview, the attempt has been undertaken to summarize the recent progress in design, syntheses, and single crystal structural investigations of Co(II) coordination supramolecular networks based on dicarboxylate aromatic ligands with one and two aromatic rings. The overview covers the works published in the last decade, 2005−2015.

2. Mixed-ligand Co(II) CPs with rigid dicarboxylic acids

Rigid ligands, such as benzene polycarboxylic acids and heterocyclic aromatic compounds, are known as good candidates for assembly in the form of CPs. Among them, historically first was H_2bdc as one of the best spacers for design and construction of MOFs, due to the equally spaced carboxylate groups, rigidity of the phenyl skeleton and especially its various bridging abilities [22].

The statistical analysis of Co(II) CPs with aromatic dicarboxylic acids, such as phenyl and biphenyl dicarboxylic acids, has been undertaken based on the data extracted from the Cambridge Structural Database (CSD, version 1.17, 2015) and from the current scientific sources (Fig. 1). It has been revealed that Co(II) coordination networks only with H_2bdc and H_2bpdc have been reported so far.
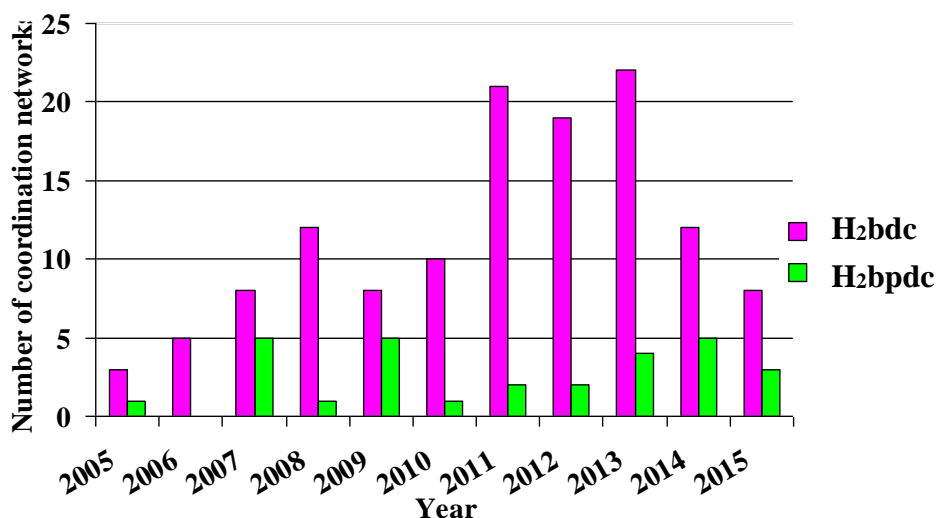
Fig. 1. Histogram with distribution of Co(II) CPs with aromatic dicarboxylic ligands.

2.1 Synthesis

Four main synthetic strategies (saturation, diffusion, hydro(solvo)thermal, microwave and ultrasonic methods) for obtaining CPs are extracted from the literature [23] and summarized in Tables 2 and 3 for H_2bdc and H_2bpdc, respectively. Improvement of synthetic procedure is essential in order to obtain high-quality single crystals suitable for X-ray measurements. It is widely documented that the structure and topology of CPs generated from transition metals and organic ligands can be controlled by the selection of ligands, pH of the

reaction medium, solvents, metal ions, metal-to-ligand ratios, reaction temperature, counterions, and so forth [3, 5]. In particular, solvent nature is an important factor since its structure, as well as chemical properties, can influence the rate of crystal growth and the final structure. A large number of new MOFs have been constructed in the presence of the templating molecules showing unprecedented structural characteristics and, in some cases, solvent-induced properties, such as enhancement of porosity [24], electrochemical property [25], catalytic activity [26], and so forth. The CPs are generally synthesized in the liquid phase by using a solvent as a medium to induce the self-assembly of a regular framework. The reaction can be carried out by mixing a solution of metal ions with a solution of ligands at room temperature or under hydrothermal/solvothermal conditions (where one or all components are poor soluble compounds) [27]. For example, compounds $[Co(bdc)(pyz)]_n$ and $\{[Co(bpdc)(2,2'\text{-bpy})(H_2O)]_n \cdot nH_2O\}_n$ (where pyz = pyrazine, 2,2'-bpy=2,2'-bipyridine) were prepared under hydrothermal conditions at high temperatures of 120–200ºC in a neutral or slightly acid medium [28]. The $\{[Co_2(bdc)_2(ted)] \cdot 2dmf \cdot 3H_2O\}_n$ compound (where ted=triethylenediamine) was prepared by the layered-solution method using $CoCl_2$, triethylenediamine, and H_2bdc in DMF and methanol solvents as starting materials [29]. The $\{[Zn_2Co(bpdc)_3(dmf)_2] \cdot 4dmf\}_n$ complex was prepared via solvothermal synthesis from mixtures of the respective transition metal salts and H_2bpdc [30].

2.2. Mode of coordination

Dicarboxylates are widely used in the supramolecular assembly as mono-, bi- or multi-dentate ligands because they can adopt a variety of coordination modes to the metal centers. The generalizations reported herein are made on the CSD statistics for the cobalt(II) ion coordination modes in the polymeric dicarboxylates and based on the Harris notation [31] (Scheme 2).
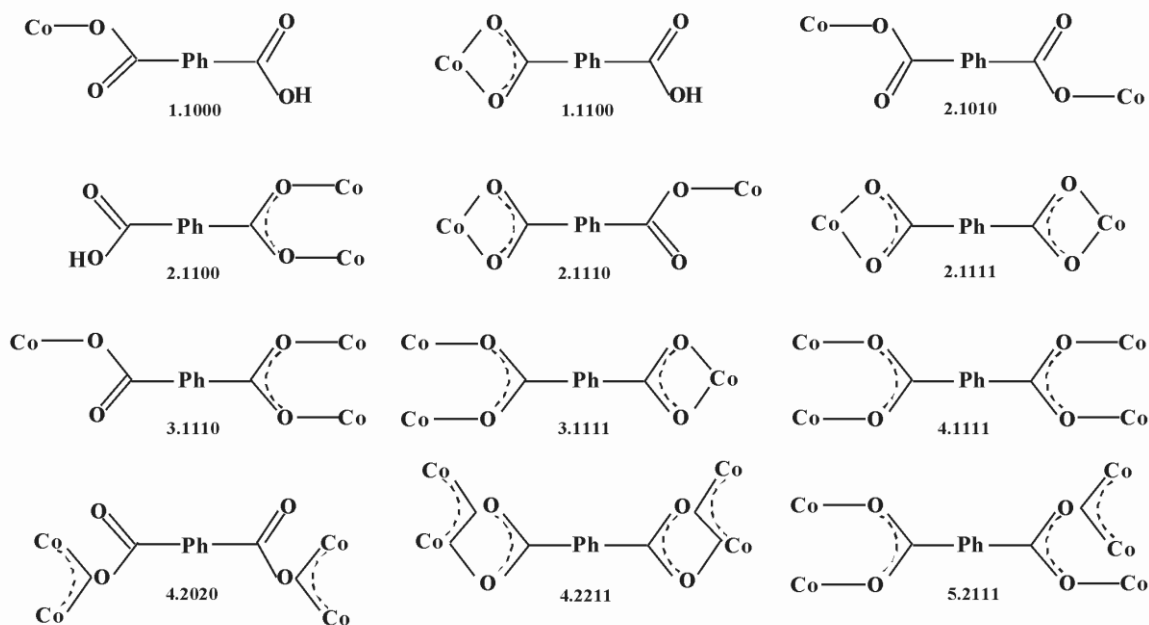
Scheme 2. Crystallographically established modes of carboxylate coordination to the Co(II) metal atoms.

2.3. Dimensionality of polymeric Co(II) dicarboxylates

The organization of the building blocks together can lead to CPs of different dimensionalities, such as one-, two-, or three-dimensional architectures. In order to illustrate the wide diversity of Co(II) CPs with dicarboxylic acids, some examples are given. They are classified along with their dimensionalities, and our retrieval of the CSD revealed 171 hits of H_2bdc ligand with Co(II) metal, 17 of which are one-dimensional (1D), 32 are two-dimensional (2D), and 65 are three-dimensional (3D) networks, while of 35 hits with H_2bpdc ligand 3 are 1D, 7 are 2D, and 25 are 3D CPs (Fig. 2). The CPs will be further discussed in the hierarchy of increase in their dimensionality (Tables 2, 3). The Figures were reproduced by Mercury facilities [32] using cif files extracted from CSD.
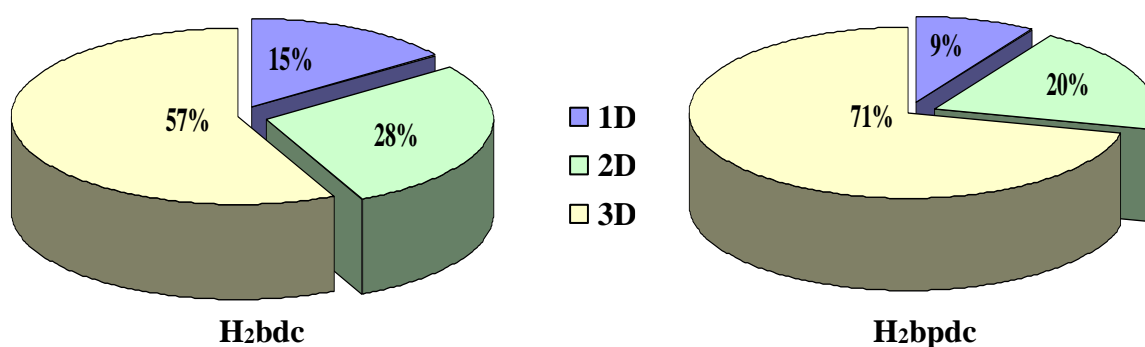

Fig. 2. Histograms with distribution of Co(II) CPs with aromatic dicarboxylic ligands against dimensionalities.

2.3.1. CPs of Co(II) with 1,4-benzenedicarboxylate

2.3.1.1. One-dimensional motifs

The selected 1D arrays are shown in Fig. 3. The crystals of $[Co(bdc)(L_6)_2(H_2O)_2]_n$, were obtained by the hydrothermal synthesis. The compound crystallizes as the linear chain shown in Fig. 3a where the Co(II) atoms are bridged by the monodentate-coordinated bdc anions to form 1D benzenedicarboxylate-bridged polymeric chain structure. The Co(II) atoms are in N_2O_4 octahedral environment [33].

The formation of the zig-zag chains can be induced by the chelate mode of coordination of N-ligand molecules. The zig-zag structure of the $[Co(bdc)(L_3)]_n$ compound, which is shown in Fig. 3b, is provided by the bulky $[Co(II)(L_3)]^{2+}$ corner fragment; each cobalt atom adjusts the distorted N_2O_4-octahedral environment; both carboxylic groups of the bdc ligands act in a bidentate bridging mode [34].

From slow diffusion techniques in a water-methanol medium, crystals of $\{[Co(L_1)(bdc)(H_2O)_2]\cdot[Co(H_2O)_6]\cdot(bdc)\cdot(H_2O)\}_n$ were obtained [35]. The polymeric chain is formed by almost collinear hexacoordinated Co(II) ions in the O_6-octahedral environment doubly bridged by a bdc carboxylate group and a L_1 oxygen. The crystal packing shows bdc dianions and water molecules inserted in between the ribbons (Fig. 3c).

Ladder-like 1D motifs can also be formed. An example is shown in Fig. 3d. In the $\{[Co_2Br_2(bdc)(L_2)_2]\cdot4dma\cdot2H_2O\}_n$ compound [36], the tetrahedral Co(II) ions are coordinated with three different ligand molecules. These Co^{2+} ions are connected by bidentate L_2 ligands to form a 1D wavy chain. Two chains are bridged together by ditopic bdc^{2-} ligands as rungs into a molecular ladder.

Table 2. Selected examples for Co(II)-1,4-benzenedicarboxylate CPs

Composition [a]	Method of synthesis	Color	Coordination number of Co(II)	Dimensionality	Reported properties	Reference, refcode in CSD
{[Co(bdc)(L$_1$)(H$_2$O)$_2$]·[Co(H$_2$O)$_6$]·bdc·H$_2$O}$_n$	slow diffusion	red	6	1D	magnetism	[35] QEYZOK
{[Co$_2$(bdc)Br$_2$(L$_2$)$_2$]·4dma·2H$_2$O}$_n$	hydrothermal	red	4	1D	adsorption	[36] FEFFED
[Co(bdc)(L$_3$)]$_n$	hydrothermal	red	6	1D	–	[34] NIFSUS
{[Co(bdc)$_2$(H$_2$O)$_2$(L$_4$)$_2$Co(H$_2$O)$_4$]·6H$_2$O}$_n$	room temperature	red	6	1D	–	[78] QOMTOD
{[Co(bdc)$_2$(L$_5$)$_3$(H$_2$O)$_4$]·2CH$_3$OH·3H$_2$O}$_n$	room temperature	red	6	1D	–	[79] ZOHQEU
[Co(bdc)(L$_6$)$_2$(H$_2$O)$_2$]$_n$	hydrothermal	red	6	1D	–	[33] CODZOM
{[Co(bdc)(L$_7$)]}$_n$	hydrothermal	colorless	4	2D	–	[80] TONPUJ
{[Co$_2$(bdc)(L$_8$)$_2$]·4nH$_2$O}$_n$	hydrothermal	yellow	6	2D	catalysis	[67] DIMXAA
[Co(bdc)(L$_9$)(H$_2$O)$_2$]$_n$	room temperature	red	6	2D	–	[78] QOMTUJ
[Co(bdc)(L$_{10}$)$_2$]$_n$	hydrothermal	purple	6	2D	–	[81] EGATEN
{[Co(bdc)(L$_{11}$)]·2H$_2$O}$_n$	hydrothermal	red	6	2D	–	[39] APOKEW
[Co$_2$(bdc)$_2$(L$_{12}$)$_4$]$_n$	room temperature	red	6	2D	luminescence	[38] BOFGOT
{[Co(bdc)(L$_{13}$)]·H$_2$O}$_n$	hydrothermal	red	6	2D	luminescence	[69] GOPCEV
{[Co(bdc)(L$_{14}$)(H$_2$O)]·2dmf}$_n$	hydrothermal	red	6	2D	luminescence	[69] NOHBOD
[Co(bdc)(L$_{15}$)]$_n$	hydrothermal	red	4	2D	catalysis	[82] HINTEF
Co{[bdc]$_{0.5}$[Hbdc] [L$_{16}$]}$_n$	hydrothermal	dark red	6	2D	gas storage	[42] CIDDEA
[Co(bdc)(L$_4$)(H$_2$O)$_2$]$_n$	hydrothermal	red	6	2D	–	[37] SODXIU
[Co$_2$(bdc)$_2$(L$_{17}$)]$_n$	desorption	purple	5	2D	gas storage	[60] TONXIE
[Co$_3$(bdc)$_2$(N$_3$)$_2$ (L$_{18}$)$_2$]$_n$	hydrotermal	purple	5	2D	magnetism	[83] IBISAP
{[Co(bdc)(L$_{19}$) (H$_2$O)$_2$]·H$_2$O}$_n$	hydrothermal	yellow	6	2D	luminescence	[84] GOPCAR
[Co(bdc)(L$_{20}$)]$_n$	hydrothermal	pink	4	2D	fluorescence and catalytic	[95] XUBRAP
[Co(bdc)(L$_{21}$)]$_n$	solvothermal	pink	4	2D	–	[96] XUDVEZ
[Co$_3$(bdc)$_3$(dmf)$_2$(H$_2$O)$_2$]$_n$	heating and stirring	purple	6	2D	catalytic activity	[97] DUCQUP
[Co$_2$(bdc)$_2$(L$_{22}$)$_2$(H$_2$O)]$_n$	solvothermal	pink	6	3D	catalysis	[85] DOIXEH
{[Co$_4$(bdc)$_3$(N$_3$)$_4$(L$_{23}$)$_2$]·2nH$_2$O}$_n$	hydrothermal	darkpurple	6	3D	magnetism	[69] KIYCEC

Table 2. (continued)

Composition [a]	Method of synthesis	Color	Coordination number of Co(II)	Dimensionality	Reported properties	Reference, refcode in CSD
{[Co4(bdc)3(N3)4(L24)2]·nH2O}n	hydrothermal	black	6	3D	magnetism	[69] KIYCEC
[Co(bdc)(L25)]n	hydrothermal	pink	6	3D	magnetism	[72] NIKFEU
[Co(bdc)(L26)]n	hydrothermal	pink	6	3D	magnetism	[72] YITMEV
{[Co2(bdc)(L27)2(H2O)]·2H2O·6dmf}n	hydrothermal	red	6	3D	magnetism	[73] TIXKUI
{[Co2(bdc)2(L1)]·H2bdc·2MeOH}n	solvothermal	red	6	3D	magnetism, gas storage	[74] ADAXEK
{[Co2(bdc)2(L1)]·2dmf}n	solvothermal	red	6	3D	magnetism, gas storage	[74] ADAXIO
{[Co(bdc)(L28)]4·6H2O}n	hydrothermal	purple	4	3D	–	[75] BIYFAR
{[Co6(bdc)2(L29)(SO4)]·7dmf}n	hydrothermal	blue	4	3D	reversible SC-SC transformation	[61] GINPAW
{[Co3(L29)(SO4)-(H2O)7.2(bdc)]·(solvent)}n	exposed to air	red	6	3D	reversible SC-SC transformation	[61] GINPAW
{[Co2(bdc)2(L17)]·2dmf·3H2O}n	layered-solution	blue	5	3D	desorption	[29] DIZVAK
{[Co(bdc)·(L30)]·2H2O·dmf}n	hydrothermal	coloress	5	3D	photochemistry	[76] OKIPOO
[Co(bdc)(L18)(H2O)]n	hydrothermal	brown	5	3D	luminescence	[77] RAMHES 02
[Co(bdc)(L31)0.5]n	hydrotermal	dark purple	6	3D	magnetism	[98] GOZTEW
[Co2(bdc)2(L32)]n	solvothermal	pink	6	3D	gas adsorption	[99] LOVVAV
[Co3(bdc)3(L32)2]n	solvothermal	pink	6	3D	gas adsorption	[99] LOVVEZ
[Co3(bdc)3(L33)]n	hydrotermal	pink	5,6	3D	magnetism	[100] DOYMUB
{[Co2(bdc)2(L34)2]·2H2O}n	hydrotermal	red	6	3D	magnetism	[101] ROWVOQ
{[Co2(bdc)2(L34)2]·H2O·MeOH}n	hydrotermal	purple	5,6	3D	magnetism	[101] ROWVUW
[Co(bdc)(L35)]n	solvothermal	purple	4	3D	–	[102] UHOFEE
[Co(bdc)L36·2dmf]n	solvothermal	red	6	3D	electrochemical, sorption, galvanostatic charge-discharge	[103] YUBTIA

[a] For L1-L36 ligands' names, see Table 1.

(a)

(b)

(c)

(d)
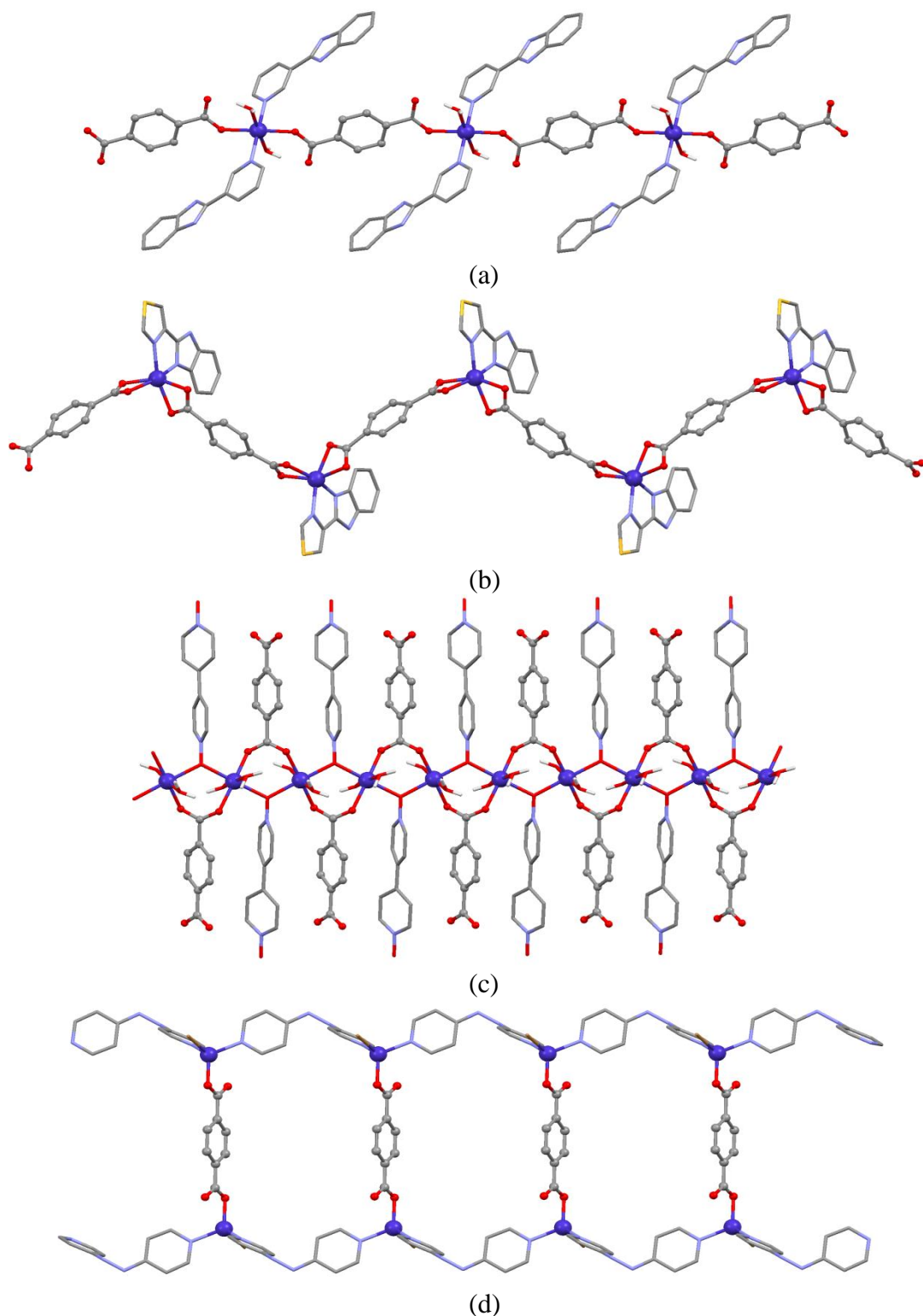
Fig. 3. 1D coordination arrays: linear chain in
catena-[(μ$_2$-terephthalato)-*bis*(2-(pyridin-3-yl)-1*H*-benzimidazole)-diaqua-cobalt(II)] (a) [33], zig-zag
chain in *catena*-((μ$_2$-terephthalato)-(2-(1,3-thiazol-4-yl)-1*H*-benzimidazole)-cobalt(II)) (b) [34],
ribbon in *catena*-((μ$_2$-terephthalato-*O,O'*)-(μ$_2$-4,4'-bipyridine-*N,N'*-dioxide-*O,O'*)-diaqua-cobalt(II)
hexa-aqua-cobalt(II) terephthalate monohydrate) (c) [35],
and ladder in *catena*-((μ$_2$-terephthalato)-*bis*(μ$_2$-4,4'-hydrazine-1, 2-diyldipyridine)-dibromo-di-
cobalt(II)) (d) [36].

2.3.1.2. Two-dimensional motifs

Square grid networks are the simplest examples of the 2D motifs. In these CPs, the metal to ligand proportion is usually 1 : 2. The metal centers are coordinated with four different ligand molecules, and the repetition of this unit allows the propagation of the structure in two dimensions.

Thus, in compound $[Co(bdc)(L_{17})(H_2O)_2]_n$, the metal ions have an octahedral environment: the equatorial positions are occupied by two bdc^{2-} anions and two water oxygen atoms, and the axial positions are occupied by two nitrogen atoms from two L_{17} molecules [37]. Further expansion of the structure through the monodentate bridging bdc^{2-} anions and L_{17} ligands creates a (4,4) rhomboidal layer grid (Fig. 4a).

(a)   (b)

(c)

(d)
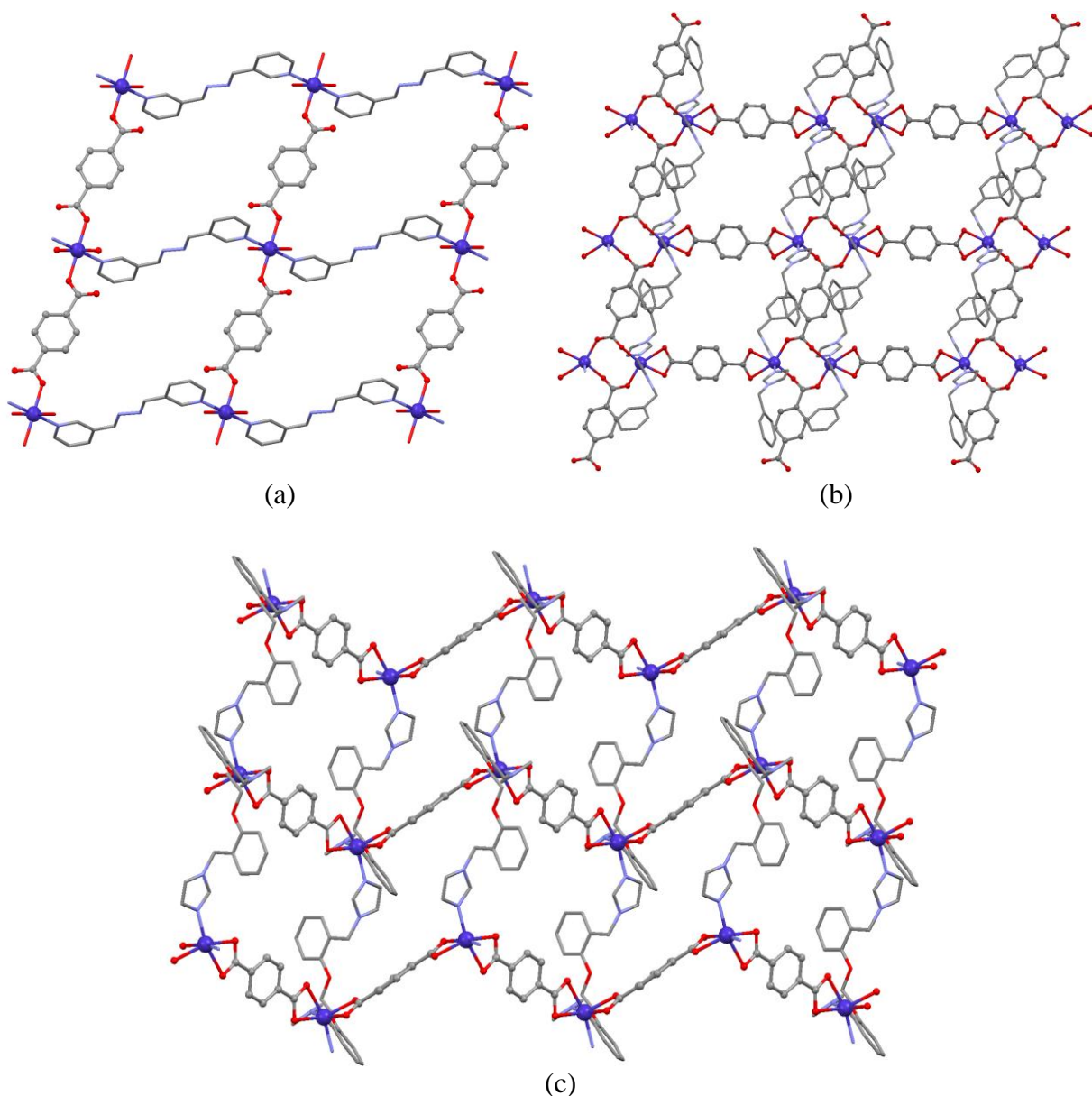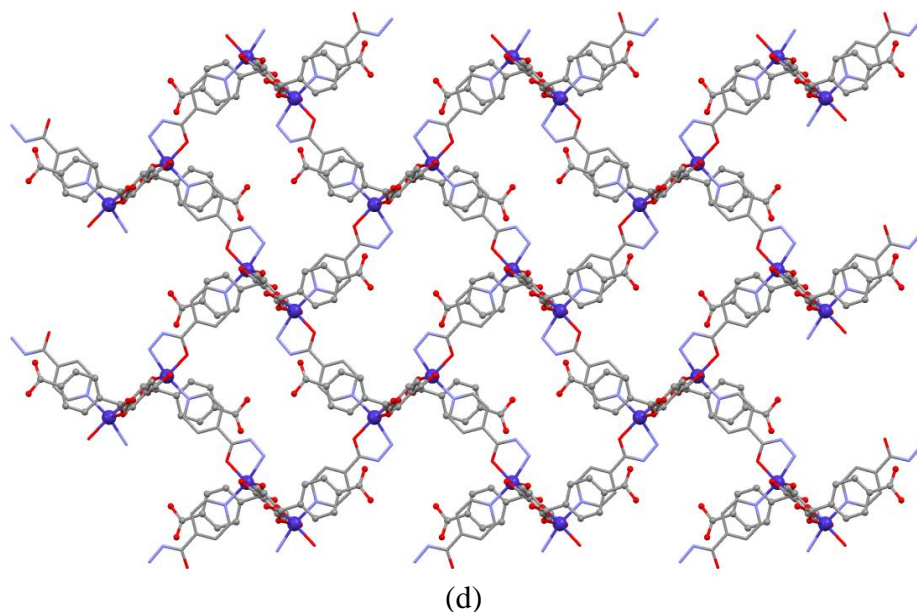
Fig. 4. 2D CPs topology: square grid in *catena*-[(μ_2-terephthalato)-(μ_2-3,3'-(hydrazine-1,2-diylidenedimethylylidene)dipyridine)-diaqua-cobalt(II)] (a) [37], rectangular grid in *catena*-((μ_4-benzene-1,4-dicarboxylato)-(μ_2-benzene-1,4-dicarboxylato)-*bis*(1-benzyl-1*H*-imidazole)-di-cobalt(II)) (b) [38], wave-like layer in *catena*-[(μ_2-benzene-1,4-dicarboxylato)-(μ_2-1,2-*bis*[2-(1*H*-1,3-imidazol-1-ylmethyl)phenoxy]ethane)-cobalt(II) dihydrate] (c) [39], and brick wall in *catena*-((μ_2-terephthalato)-*bis*(terephthalic acid)-*bis*(μ_2-isonicotinohyrazide)-di-cobalt(II)) (d) [41].

The $[Co_2(bdc)_2(L_{12})_4]_n$ crystals result from the reaction of L_{12}, $CoCl_2$, and H_2bdc acid in the presence of Et_3N in a dmf/CH_3OH solution [38]. Analysis of the crystal structure reveals a 2D network with rectangular cavities, as shown in Fig. 4b. The opposite sides of the rectangular cavity are formed by two crystallographically different bdc anions acting in different coordination modes; the metal secondary building unit (SBU) represents the binuclear cluster, $\{Co_2(COO)_4\}$.

In the extended structure of compound $\{[Co(bdc)(L_{11})]\cdot 2H_2O\}_n$ obtained under hydrothermal reaction of L_{11} with Co(II), in the presence of H_2bdc [39], the Co(II) cations are six-coordinated: each bdc^{2-} dianion acts in a bis-bidentate chelating mode to bridge the adjacent Co(II) cations to form zig-zag one-dimensional chains. These chains are linked by L_{11} ligands into a two-dimensional wave-like sheet (Fig. 4c).

If the metal ions are only coordinated with three ligand molecules giving a "T-shape" around the node, layers are formed and the motifs are referred to as honeycomb [40], brick wall [41], herringbone [42] (Fig. 4d), etc.

2.3.1.3. Three-dimensional motifs

The extension of the coordination complexes can occur in three dimensions from the nodes through the ligand connectors. The H_2bdc acid is an example of a 2-connecting ligand. For example, it has been used in the 3D motifs such as a diamondoid network, where each node is connected to four bridging ligands in a tetrahedral way, reproducing a diamond-like network. This motif has been found in the structure obtained from Co(II) ions as nodes and the H_2bdc acid, and 1,4-*bis*(2-methylbenzimidazol-1-ylmethyl)benzene (bmb) as connectors [43]. The Co(II) ion is in a distorted tetrahedral geometry defined by two nitrogen atoms of two bmb ligands and two oxygen atoms from two separated bdc^{2-} anions and the resulting structure is a threefold diamondoid framework (Fig. 5).

(a)   (b)
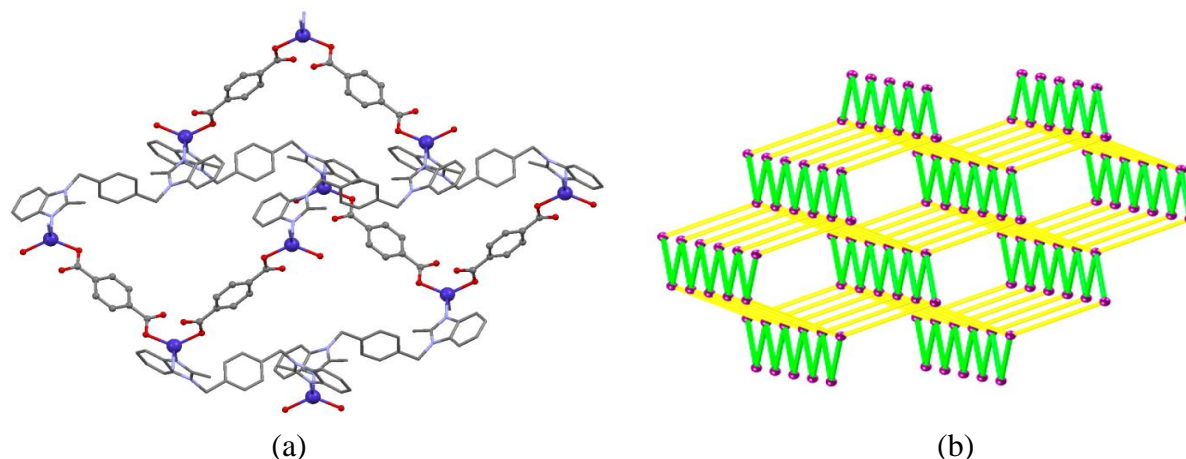
Fig. 5. Perspective view of the single diamondoid net in
catena-(*bis*(μ$_2$-terephthalato)-(μ$_2$-1,1'-(1,4-phenylenebis(methylene))-*bis*(2-methyl-1*H*-benzimidazole))-di-cobaltmonohydrate): (a) Schematic illustration of the 3D **dia** topology [43] (b).

At higher temperatures or using a longer reaction time, it is possible to obtain 3D complexes with octahedral Co(II) nodes, such as [Co(bdc)(pyz)]$_n$ (where pyz=pyrazine), where one (4,4) layer with the **sql** topology is formed with bdc dianions capping the cobalt binuclear unit, as shown in Fig. 6a (the carboxylate groups are coordinated to the cobalt ions in the equatorial sites). The pyrazine molecules are linked to the cobalt ions through the apical positions for the expansion of the structure in the third direction [44] (Fig. 6b).

A number of other three-dimensional motifs with dicarboxylic acid have been observed with different net topologies: **fcu** [45], **pcu** [46], **fsc** [47], **sra** [48], and other motifs. All of these CPs show a high stability; they present more or less large cavities filled with non-coordinating solvent molecules and/or similar networks by interpenetration.

(a)   (b)
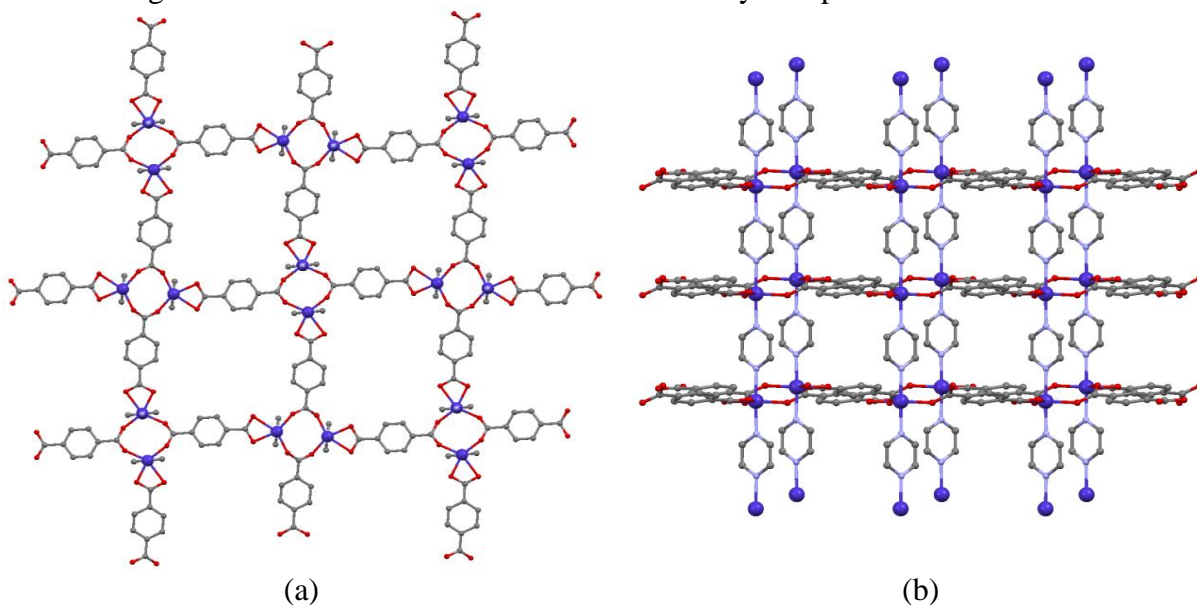
Fig. 6. 3D CP [Co(bdc)(pyz)]$_n$: {Co(bdc)}$_n$ sheet (a) and perspective view of the three-dimensional motif [44] (b).

2.3.2. CPs of Co(II) with 4,4'-biphenyldicarboxylate

2.3.2.1. One-dimensional motifs

From the CSD search, there are three 1D CPs with an H_2bpdc ligand synthesized by the solvothermal [49] and hydrothermal [28] methods; all these compounds form a 1D zigzag chain (Table 3).

The crystal structure of $\{[Co(bpdc)(L_{37})]\cdot1.5H_2O\}_n$ is formed by a neutral 1D zig-zag chain composed of $[Co(bpdc)(L_{37})]$ entities and free solvent disordered water molecules. The cobalt atoms are six-coordinated in a distorted $[CoN_3O_3]$ octahedral coordination environment with three carboxyl oxygen atoms from two bpdc ligands and a nitrogen atom of one L_{37} located in the basal sites and the other two nitrogen atoms from the L_{37} taken on the apical positions, as depicted in Fig. 7 [49].
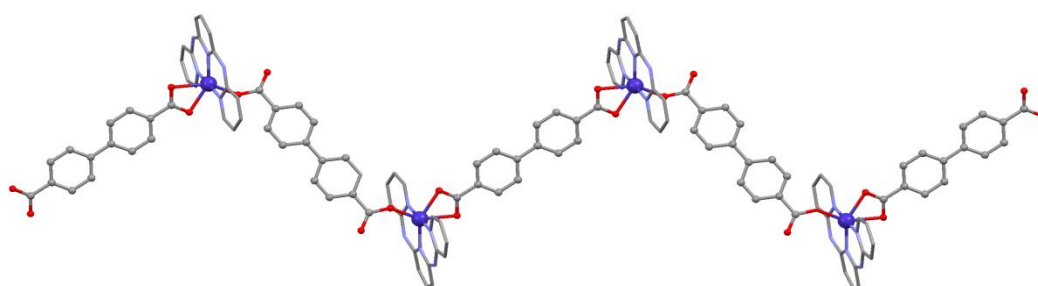
Fig. 7. 1D zig-zag polymeric chain of complex $\{[Co(bpdc)(L_{37})]\cdot1.5H_2O\}_n$ [49].

2.3.2.2. Two-dimensional motifs

Figure 8 illustrates some of the 2D network motifs that have thus far been observed in Co(II) CPs with H_2bpdc ligand. A polyrotaxane-like network is observed in compound $[Co(bpdc)(L_{41})]_n$. This CP contains two functionally different ligands, one ligand, usually a conformationally N-donor flexible ligand, serves to assemble a molecular unit with loops, whereas the other ligand, typically a long rigid polycarboxylate, forms metal-polycarboxylate substructures (e.g., chains or sheets) and, more importantly, provides a linear rod to insert those loops [50]. The asymmetric unit of this compound consists of one Co(II) ion, one L_{41} molecule, and one bpdc^{2-} anion. Each Co(II) ion is four-coordinated with distorted tetrahedral geometry composed of two carboxylic O atoms from two bpdc^{2-} anions and two N atoms from two L_{41} ligands. The extension of the structure into a 2D sheet is accomplished by linear bpdc^{2-} anions (Fig. 8a).

In the extended structure of compound $\{[Co(bpdc)(L_{43})_{1.5}(H_2O)](L_{43})\}_n$ obtained under hydrothermal reaction of $CoCl_2\cdot6H_2O$, H_2bpdc, and L_{43} in distilled water and DMF, each Co(II) ion exhibits a distorted octahedral environment composed of two carboxylic O atoms from three bpdc^{2-} anions and three N atoms from three L_{43} ligands and one water molecule. Each octahedral Co atom coordinates to three L_{43} ligands to form a 2D brick wall network with a (6, 3) topology (Fig. 8b) [50].

Three other 2D motifs with H_2bpdc have been observed with grid like [86, 55] and triangular grid [30] networks (Table 3).

Table 3. Selected examples for Co(II)- 4,4'-biphenyldicarboxylate CPs

Composition [a]	Method of synthesis	Color	Coordination number of Co(II)	Dimensionality	Reported properties	Reference, refcode in CSD
{[Co(bpdc)(L37)]·1.5H2O}n	solvothermal	purple	6	1D	magnetic	[70] JEXNIK
[Co(bpdc)(HL38)(H2O)]n	hydrothermal	red rod-like	4	1D	magnetic	[70] JEXNOQ
{[Co(bpdc)(L39)(H2O)]·nH2O}n	hydrothermal		6	1D	-	[28] OMEYAH
{[CoZn2(bpdc)3(dmf)2]·4dmf}n	solvothermal	purple	6	2D	-	[30] JETXAI
[Co2(bpdc)(L40)2]n	stirred 5 min	blue	4	2D	-	[86] DOGMES
[Co(bpdc)(L41)]n	hydrothermal	purple	4	2D	-	[50] MUNPIV
{[Co(bpdc)(L43)1.5(H2O)]·(L43)}n	hydrothermal	green	6	2D	-	[50] MUNPOB
[Co(bpdc)(L43)]n	hydrothermal	blue	4	2D	-	[50] MUNPUH
[Co(bpdc)(L42)]n	hydrothermal	blue	6	2D	fluorescence and catalytic	[87] ZORBUF
{[Co(bpdc)(L43)](dmf)3}n	solvothermal	pink	4	2D	-	[88] YARFAA
{[Co(bpdc)L44]·(EtOH)}n	solvothermal	brown	6	3D	-	[89] XIHRIQ
{Co3(bpdc)3(dma)2]·(dma)·(EtOH)}n	solvothermal	violet	4, 6	3D	-	[89] XIHRUC
{[Co3(bpdc)4][L45]2·(CH3OH)2(dmf)1.5}n	solvothermal	purple	4, 6	3D	magnetic	[90] MOXDOT
{Co3(bpdc)4}n	solvothermal	purple	6	3D	-	[91] HURGOR
{[Co(bpdc)(L46)]·2dmf}n	temperature	red purple	6	3D	-	[92] IXUWII
{Co3(bpdc)3(L47)}n	solvothermal	violet	4, 6	3D	gas-adsorption	[63] LAYGAV
{[Co2(bpdc)1.5(HL48)]·dmf·CH3CN·H2O}n		purple	4	3D	gas-sorption	[62] BEQFEK
{Co3(bpdc)3(dma)2]·4dma}n	heated, 100 °C	red	6	3D	-	[56] CIFCUR
[Co2(bpdc)4(L49)·3dmf]n	solvothermal	red	6	3D	-	[51] NESSOV
{[Co2(bpdc)(L50)]·dmf}n	solvothermal	red	5	3D	gas-adsorption	[52] FODHUD
{[Co2(bpdc)2(H2L48)]·2dmf}n	solvothermal	purple	5	3D	gas-adsorption, magnetic	[53] GIYJAB
{[Co2(bpdc)(HL51)2]}n	hydrothermal	purple	4	3D	-	[59] NOJSIQ
{[Co(bpdc)(L27)]·(dmf)(H2O)}n	hydrothermal	red	6	3D	-	[93] YOVPAC
{Co3(bpdc)3(L52)(dmf)4}n	solvothermal	pink	4, 6	3D	gas adsorption	[64] LIZSOE
{[Co(bpdc)(L53)]·0.5H2O}n		red	4	3D	optical absorption	[54] WITMET
[Co(bpdc)(L54)]n	hydrothermal	red	4	3D	fluorescence and catalytic	[55] ZORBIT
[Co(bpdc)(L55)(H2O)]n	hydrothermal	red	6	3D	fluorescence and catalytic	[55] ZORCAM
{[Co(bpdc)(HPO4)][H2L17]}n	solvothermal	blue	4	3D	-	[94] SUHMAL
{[Co2(bpdc)2(L56)(H2O)]·2dma}n	hydrothermal	pink	6	3D	gas sorption, magnetic	[71] VOSVAC

(a)

(b)
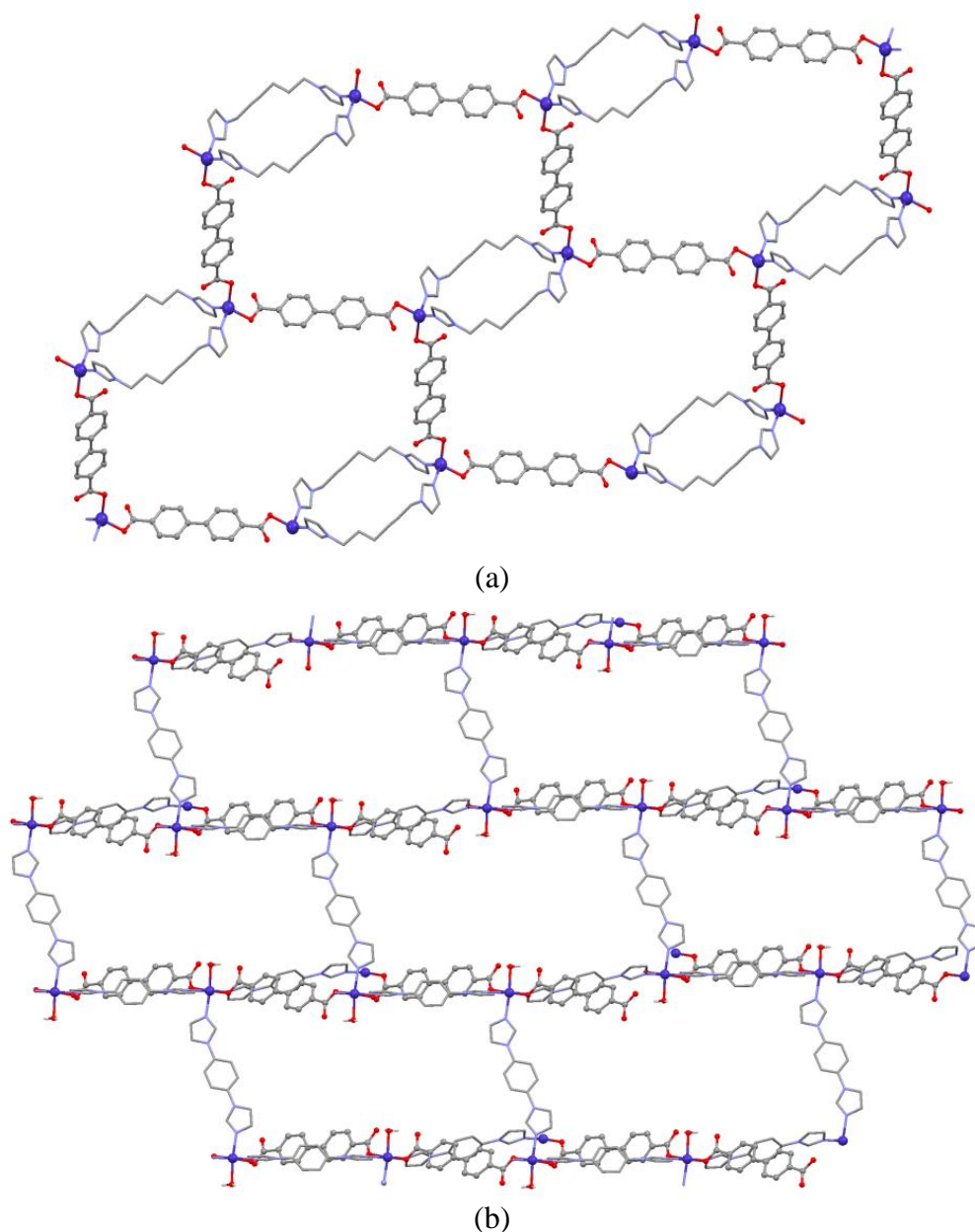
Fig. 8. 2D polyrotaxane-like network in $[Co(bpdc)(L_{41})]_n$ [50] (a); 2D brick wall net constructed from Co(II) centers and L_{43} ligands in $\{[Co(bpdc)(L_{43})_{1.5}(H_2O)](L_{43})\}_n$ (b) [50].

2.3.2.3. Three-dimensional motifs

A number of 3D motifs with H_2bpdc ligand have been observed with different net topologies, **pcu** [51-53], **rob** [54], **dia** [55], **seh** [55], **hxl** [56], **mok** [57], **hms** [58] and other motifs.

The ligands H_2bpdc and L_{51} react with the Co(II) salt to form the $\{[Co_2(bpdc)(HL_{51})_2]\}_n$ compound [59]. The asymmetric unit of this compound contains one Co(II), one partially deprotonated HL^-_{51}, and half the $bpdc^{2-}$ residue. The Co(II) ion is in a distorted tetrahedral coordination environment with three nitrogen atoms from three HL^-_{51} and one oxygen from one carboxylate group of $bpdc^{2-}$ ligand. Each HL^-_{51} coordinates with three Co(II) atoms to form a 2D network, which repeats in an ···ABAB··· stacking sequence and is further connected by $bpdc^{2-}$ ligands to form a 3D InS framework via Co(II)–O coordination interactions (Fig. 9a).

The {[Co(bpdc)(L$_{53}$)]·0.5H$_2$O}$_n$ compound shows a **rob** organisation [54]. Its asymmetric unit consists of one crystallographically independent Co(II) ion, one L$_{53}$ ligand, one deprotonated bpdc ligand, and half the solvent water molecule. Two crystallographically equivalent Co(II) cations are bridged by two carboxylate groups adopting a *bis*-bidentate coordination mode to generate a dinuclear Co(II) secondary building unit. The ladder chains extend in the cross direction to form a 2D network, then combine the L$_{53}$ ligands from vertical direction to construct a 3D **rob** framework (Fig. 9b).

(a)

(b)

(c)
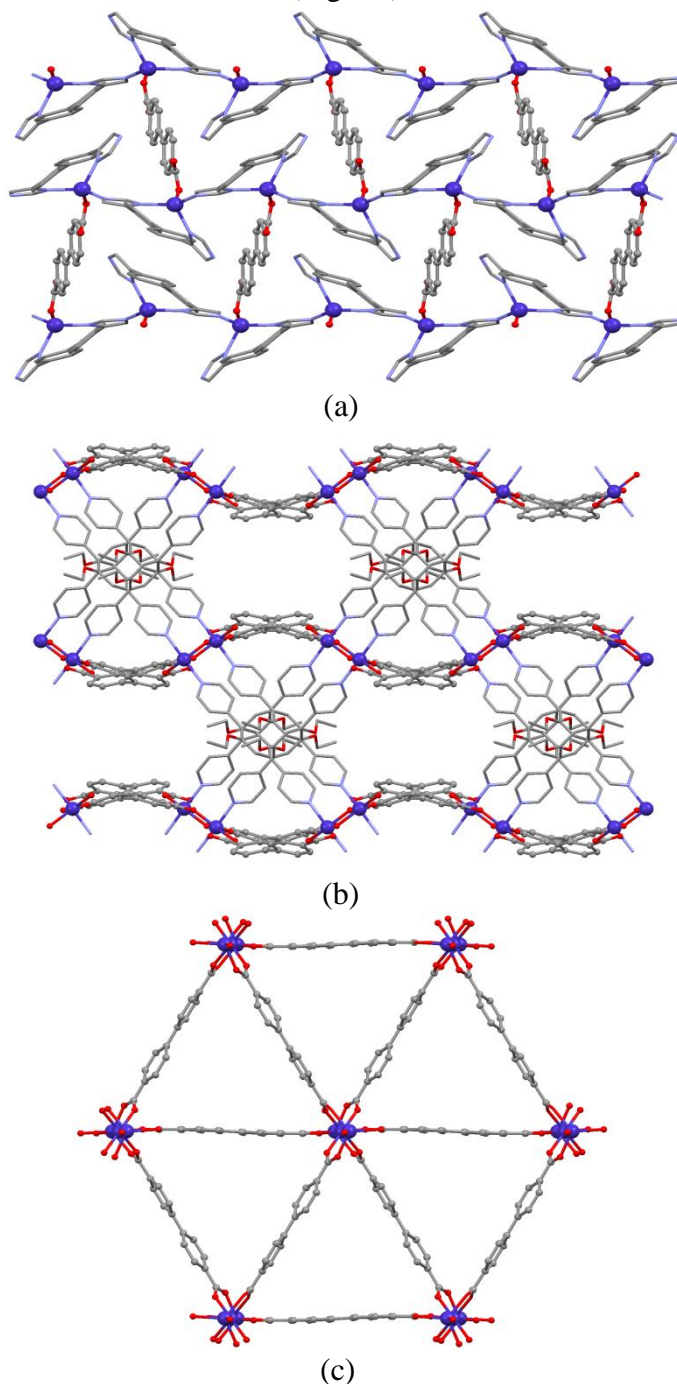
Fig. 9. 3D InS framework in {[Co$_2$(bpdc)(HL$_{51}$)$_2$]}$_n$ (a) [59]; perspectives of 3D framework along the *c* axis in {[Co(bpdc)(L$_{53}$)]·0.5H$_2$O}$_n$ (b) [54]; the **hxl** net in {[Co$_3$(bpdc)$_3$(dma)$_2$]·4dma}$_n$ (c) [56].

The {[Co$_3$(bpdc)$_3$(dma)$_2$]·4dma}$_n$ compound contains trinuclear metal centers with six coordination points; the structure adopted an **hxl** net (Fig. 9c) being assembled via the long ligand H$_2$bpdc [56].

3. Potential applications

The rapidly growing field of design and synthesis of CPs is attributed to their undisputable advantages as new multifunctional materials. Several examples in this part of the review reveal Co(II) MOFs with dicarboxylic ligands as promising materials for applications in gas storage, anion exchange (due to the porosity), luminescence, magnetism, and catalysis.

Gas storage is one of the possible applications for these materials. The $[Co_2(bdc)_2(L_{18})]_n$ compound has a high specific micropore volume of 0.82 cm^3g^{-1}, a hydrogen storage capacity of 2.27 wt % at $-196°C$ and 1 bar, and an excess methane adsorption of 14.0 wt % at 30°C and 75 bar, and is a promising material for hydrogen and methane storage. The host framework shrinks upon inclusion of guest molecules and expands upon guest removal, a fascinating phenomenon in this class of materials [60]. Another example is $\{[Co_6(L_{28})(SO_4)(bdc)_2]\cdot(dmf)_7\}_n$ [61], which has ultramicropores in its structure. The dmf molecules can be removed and substituted with H_2O, methanol, and ethanol. The sorption behavior was studied for CO_2, CH_4, and N_2. The $\{[Co_2(bpdc)(L_{50})]\cdot dmf\}_n$, [52], $\{[Co_2(bpdc)_2(H_2L_{48})]\cdot 2dmf\}_n$, [53], $\{[Co_2(bpdc)_{1.5}(HL_{48})]\cdot dmf\cdot CH_3CN\cdot H_2O\}_n$ [62], and other compounds [63-65] based on positional isomeric 4,4′-biphenyldicarboxylate ligand exhibit a distinct temperature-dependent gas (CH_4, N_2, CH_4) sorption behavior.

Nowadays, MOFs have already been used for new photocatalytic materials in view of their potential applications in the green degradation of organic pollutants [66]. For example, the $\{[Co_2(bdc)(L_8)_2]\cdot 4nH_2O\}_n$ compound is an active catalyst for the degradation of orange G, rhodamine B, methylene blue, and methyl violet [67].

From a magnetic perspective, Co(II) carboxylates have shown to be potential candidates to construct molecular magnets exhibiting various bulk magnetic behavior, such as antiferromagnetism, ferromagnetism, spin canting, ferrimagnetism, and so on [68, 14]. An example of the mixed-ligand CP that well illustrates the magnetic behavior of MOFs is the $\{[Co_4(N_3)_4(bdc)_3(L_{23})_2]\cdot nH_2O\}_n$ complex [69], which reveals weak antiferromagnetic interactions between Co(II) centers. The $[Co(bpdc)(HL_{38})(H_2O)]_n$ [70] and $\{[Co(bpdc)(L_{37})]\cdot 1.5H_2O\}_n$ [70] complexes indicate weak antiferromagnetic interactions between the adjacent Co(II) (S =3/2) ions.

The widely studied Co-based MIL-53 [104] analogues, $[Co(bdc)(L_{25})]_n$ and $[Co(bdc)(L_{26})]_n$ [72, 104] show the spin canting behavior, which is attributed to the existence of a highly symmetric *trans*-$CoO_4bdcO_2L_{26}$ coordination core. There are other CPs of the Co(II) metal and an H_2bpdc ligand with magnetic properties [70, 53, 71].

4. Conclusions

Based on the data stored in the Cambridge Structural Database (CSD) and available literature sources, an attempt has been undertaken to generalize the Co(II) CPs based on two rigid dicarboxylic acid, 1,4-benzenedicarboxylic acid, and 4,4'-biphenyldicarboxylic acid. The overview covers the last-decade period of time-from 2005 to 2015-and shows how the Co(II) CP networks with dicarboxylic ligands can be built to have different dimensionalities using the rich variety of conditions and co-ligands with N-donor atoms. The extended species based on dicarboxylic aromatic acids show particularly intriguing structures for many reasons: they exhibit a large variety of distinct topologies and may serve as potentionally beneficial functional materials. The properties of these polymers range from optical to magnetic and reveal perspectives in many other fields.

References

[1] S. R. Batten, N. R. Champness, X. M. Chen, J. Garcia-Martinez, S. Kitagawa, L. Öhrström, M. O'Keeffe, M. P. Suh, and J. Reedijk, Pure Appl. Chem., 85, 1715, (2013).

[2] (a) B. Moulton, M. J. Zaworotko, Chem. Rev., 101, 1629 (2001); (b) D. Braga, and F. Grepioni, Coord. Chem. Rev., 183,19 (1999); (c) S. Leninger, B. Olenyuk, and P. J. Stang, Chem. Rev., 100, 853, (2000); (d) L. Carlucci, G. Ciani, and D. M. Proserpio, Coord. Chem. Rev., 246, 247, (2003); (e) L. G. Beauvais and J. R. Long, Inorg. Chem., 45, 236, (2006); (f) M. Dinca, A. F. Yu, and J. R. Long, JACS, 128, 8904, (2006); (g) M. Eddaoudi, D. B. Moler, H. Li, B. Chen, T. Reineke, M. O'Keeffe, and O. M. Yaghi, Acc. Chem. Res., 34, 319, (2001); (h) O. Evans and W. Lin, Acc. Chem. Res., 35, 511, (2002); (i) M. E. Davis, Nature, 417, 813, (2002); (j) S. R. Batten and K. S. Murray, Coord. Chem. Rev., 246, 103, (2003); (k) N. L. Rosi, J. Eckert, M. Eddaoudi, D. T. Vodak, J. Kim, M. O'Keeffe, and O. M. Yaghi, Science, 300, 1127, (2003); (l) D. N. Dybtsev, H. Chun, S. H. Yoon, and K. J. Kim, Am. Chem. Soc., 126, 32, (2004); (m) O. M. Yaghi, M. O'Keeffe, N. W. Ockwig, H. K. Chae, M. Eddaoudi, and J. Kim, Nature, 423, 705, (2003).

[3] G. Q. Zhang and J. S. Ma, Cryst. Growth Des., 6, 375, (2006).

[4] (a) O. M. Yaghi and H. Li, JACS, 118, 295, (1996).

[5] (b) T. Shiga, H. Okawa, S. Kitagawa, and M. Ohba, JACS, 128, 16426, (2006).

[6] N. L. Rosi, J. Kim, M. Eddaoudi, B. Chen, M. O'Keeffe, and O. M. Yaghi, JACS, 127, 1504, (2005).

[7] (a) X. F. Wang and Y. Liu, Inorg. Chem. Commun. 27, 76 (2013); (b) A. L. Pochodylo and R. L. LaDuca, Inorg. Chem. Commun. 14, 722, (2011); (c) L. Guan, Y. H. Zhou, and H.Zhang, Inorg. Chem. Commun. 13, 737, (2010).

[8] H. Wu, W. Zhou, and Yildirim T., JACS, 131, 4995, (2009).

[9] Y. He, W. Zhou, R. Krishna, and B. Chen, ChemComm, 48, 11813, (2012).

[10] Y. S. Bae, C. Y. Lee, K. C. Kim, O. K. Farha, P. Nickias, J. T. Hupp, S. T. Nguyen, and R. Q. Snurr, Angew. Chem. Int Ed., 51, 1857, (2012).

[11] J. S. Griffith, Cambridge University Press, 1964.

[12] O. S. Wenger, Chem. Rev., 113, 3686, (2013).

[13] P. B. Lever, Elsevier, Amsterdam, (1986).

[14] M. Kurmoo, Chem. Soc. Rev., 38, 1353, (2009).

[14] (a) D. Cave, J. M. Gascon, A. D. Bond, S. J. Teat, and P. T. Wood, Chem. Commun., 10, 1050 (2002); (b) A. Distler, D. L. Lohse, and S. C. Sevov, J. Chem. Soc. DaltonTrans., 11, 1805 (1999); (c) L. Pan, N. Ching, X. Huang, and J. Li, Inorg. Chem., 39, 5333, (2000).

[16] L. E. Kreno, K. Leong, O. K. Farha, M. Allendorf, Van R. P. Duyne, and J. T. Hupp, Chem. Rev., 112, 1105, (2012).

[17] F. S. Delgado, C. A. Jimenez, P. Lorenzo-Luis, J. Pasan, O. Fabelo, L. Canadillas-Delgado, F. Lloret, M. Julve, and C. Ruiz-Perez, Cryst.Growth Des. 12, 599, (2012).

[18] (a) G. Teng, C. P. Walczak, P. J. Squattrito, D. K. Mohanty, W. Schare, M. R. Giolando, and K. Kirschbaum, Acta Crystallogr., Sect.C: Cryst. Struct. Commun. 65, 76, (2009); (b) J. Wang, X. Jing, Y. Cao, G. Li, Q. Huo, and Y. Liu, CrystEngComm 17, 604, (2015), (c) X. Hua, W. Li, Y. Xu, J. Wu, and W. H. Xuebao (Chin.) (Acta Phys.-Chim.Sin) 28, 1815, (2012); (d) K. Shankar, B. Das, and J. B. Baruah, Eur. J. Inorg. Chem. 2013, 6147, (2013).

[19] C. R. Groom and F. H. Allen, Angew.Chem.Int.Ed., 53 , 662, (2014).

[20] (a) J. He, C. Yang, Z. Xu, M. Zeller, A. D. Hunter, and J. Lin, J. Solid State Chem. 182, 1821, (2009); (b) J. Zhang, L. Wojtas, R. W. Larsen, M. Eddaoudi, and M. J. Zaworotko, JACS 131, 17040, (2009).

[21] S. Q. Wei, X. H. Yin, C. W. Lin, C. J. He, and H. B. Ou, University of Edinburgh, (2013).

[22] (a) H. B. Xu, Z. M. Su, K. Z. Shao, Y. H. Zhao, Y. Liang, and Y. C. Zhang, Inorg. Chem. Commun. 7, 260 (2004); (b) J. Cano, G. De Munno, J. L. Sanz, R. Ruiz, J. Faus, F. Lloret, M. Julve, and A. Caneschi, J. Chem. Soc. Dalton Trans, 67., 1915, (1997).

[23] (a) S. Kitagawa and S. Noro, Compreh. Coord. Chem. 7, 231 (2004); (b) W. Clegg, Compreh. Coord. Chem. 1, 579, (2004).

[24] (a) T. Panda, P. Pachfule, and R. Banerjee, Chem. Commun., 47, 7674 (2011); (b) G. T. Vuong, M. H. Pham, and T. O. Do, Dalton Trans., 42, 550, (2013).

[25] (a) Q. Liu, L. L. Yu, Y. Wang, Y. Z. Ji, J. Horvat, M. L. Cheng, X. Y. Jia, and G. X. Wang, Inorg. Chem., 52, 2817, (2013); (b) J. J. Gassensmith, J. Y. Kim, J. M. Holcroft, O. K. Farha, J. F. Stoddart, J. T. Hupp, and N. C. Jeong, J. Am. Chem. Soc., 136, 8277, (2014).

[26] (a) Z. J. Zhang, L. P. Zhang, L. Wojtas, P. Nugent, M. Eddaoudi, and M. J. Zaworotko, JACS, 134, 924 ,(2012); (b) M. Saito, T. Toyao, K. Ueda, T. Kamegawa, Y. Horiuchi, and M. Matsuoka, Dalton Trans., 42, 9444, (2013).

[27] X. M. Chen and M. L. Tong, Acc. Chem. Res., 40, 162, (2007).

[28] C. Y. Sun, B. Dong, Q. Lv, and X.-J. Zheng, Z. Anorg. Allg. Chem. 637, 276, (2011).

[29] L. G. Zhu and H. P. Xiao, Z. Anorg. Allg. Chem., 634, 845, (2008).

[30] Y. Wang, B. Bredenkotter, B. Riegera, and D. Volkmer, Dalton Trans., 689, (2007).

[31] R. A. Coxall, S. G. Harris, D. K. Henderson, S. Parsons, P. A. Tasker, and R. E. P. Winpenny, Dalton Trans., Harris notation describes the binding mode as [X.Y1Y2Y3 ...Yn], where X is the overall number of metals bound by the whole ligand, and each value of Y refers to the number of metal atoms attached to the different donor atoms. 2349, (2000).

[32] C. F. Macrae, P. R. Edgington, P. McCabe, E. Pidcock, G. P. Shields, R. Taylor, M. Towler, and J. Van de Streek, J. Appl. Cryst., 39, 453, (2006).

[33] X. H. Chen, H. Huang, M. X. Yang, L. J. Chen, and S. Lin, ActaCrystallogr., Sect. C: Cryst. Struct. Chem., 70, 488, (2014).

[34] S. Q. Wei, X. -H. Yin, C. W. Lin, C. J. He, and H. -B. Ou, Synth. React. Inorg., Met.Org., Nano-Met. Chem., 43, 580, (2013).

[35] S. C. Manna, E. Zangrando, J. Ribas, and N. R. Chaudjuri, Dalton Trans., 1383, (2007).

[36] X. M. Liu, R. B. Lin, J. P. Zhang, and X. M. Chen, Inorg. Chem., 51, 5686, (2012).

[37] J. Zhou, L. Du, Y. F. Qiao, Y. Hu, B. Li, L. Li, X. Y. Wang, J. Yang, M. J. Xie, and Q. H. Zhao, Cryst. Growth Des., 14, 1175, (2014).

[38] Q. X. Liu, X. J. Zhao, X. M. Wu, S. W. Liu, Y. Zang, S. S. Ge, Wang X.G., and J. H. Guo, Inorg. Chem. Commun., 11, 809, (2008).

[39] N. N. Yuan, Q. K. Liu, J. P. Ma, R. Q. Huang, and Y. B. Dong, ActaCrystallogr., Sect. C: Cryst.Struct. Commun., 67, 119, (2011).

[40] Y. Sun, S. Liu, Y. Xu, L. Wu, D. Gao, G. Zhang, and D. Z. Liao, Polyhedron, 74, 39, (2014).

[41] G. P. Yong, Y. Z. Li, C. F. Li, Y. M. Zhang, and W. L. She, Dalton Trans., 40, 4131, (2011).

[42] F. B. De Almeida, F. H. Silva, M. I. Yoshida, H. A. De Abreu, and R. Diniz, Inorg. Chim. Acta, 402, 60, (2013).

[43] Q. Guo, C. Xu, B. Zhao, Y. Jia, H. Hou, and Y. Fan, Cryst. Growth Des., 12, 5439, (2012).

[44] A. Abbasi, S. Tarighi, and A. Badiei, Transition Met. Chem., 37, 679, (2012).

[45] S. A. Kumalah, M. V. L. Mempin, A. J. Cairns, and K. T. Holman, J. Am. Chem. Soc. 133, 1634, (2011).

[46] H. J. Lee, P. Y. Cheng, C. Y. Chen, J. S. Shen, D. Nandi, and H. M. Lee, CrystEngComm 13, 4814, (2011).

[47] J. Xu, X. Q. Yao, L. F. Huang, Y. Z. Li, and H. G. Zheng, CrystEngComm 13, 857, (2011).

[48] A. S. Munn, G. J. Clarkson, F. Millange, Y. Dumont, and R. I. Walton, CrystEngComm, 15, 9679, (2013)

[49] L. J. Zhou, Y. Y. Wang, C. H. Zhou, C. J. Wang, Q. Z. Shi, and S. M. Peng, Cryst.Growth Des. 7, 300, (2007).

[50] Y. Liu, Y. Qi, Y. Y. Lv, Y. X. Che, and J. M. Zheng, Cryst.Growth Des. 9, 4797, (2009).

[51] X. R. Hao, G. -S. Yang, K. -Z. Shao, Z. M. Su, G. Yuan, and X. L. Wang, J. Solid State Chem. 198, 143, (2013).

[52] B. Liu, J. Shi, K. -F. Yue, D. S. Li, and Y. Y. Wang, Cryst. Growth Des. 14, 2003, (2014).

[53] L. N. Jia, Y. Zhao, L. Hou, L. Cui, H. H. Wang, and Y. Y. Wang, J. Solid State Chem. 210, 251, (2014).

[54] C. Zhang, M. Zhang, L. Qin, and H. Zheng, Cryst. Growth Des. 14, 491, (2014)

[55] X. X. Wang, B.Yu, K. V. Hecke, and G. H. Cui, RSC Advances 4, 61281, (2014).

[56] S. Y. Yang, H. B. Yuan, X. B. Xu, and R. B. Huang, Inorg.Chim.Acta 403, 53, (2013)

[57] Y. Gong, Y. C. Zhou, T. F. Liu, J. Lu, Proserpio D.M., and Cao R., ChemCommun. 47, 5982, (2011).

[58] Q. Chen, Y. Y. Jia, Z. Chang, T. T. Wang, B. Y. Zhou, R. Feng, and X. H. Bu, Cryst.Growth Des. 14, 5189, (2014).

[59] K. Chen, Y. -S. Kang, L. Luo, Y. Zhao, P. Wang, L. Qing, Y. Lu, and W. -Y. Sun, Polyhedron 79, 239, (2014).

[60] H. Wang, J. Getzschmann, I. Senkovska, and S. Kaskel, Microporous and Mesoporous Mater. 116, 653, (2008)

[61] Q. Chen, Z. Chang, W. C. Song, H. Song, H. B. Song, T. L. Hu, and X. H. Bu, Angew. Chem., Int. Ed., 52, 11550, (2013).

[62] L. Hou, L. N. Jia, W. J. Shi, L. Y. Du, J. Li, Y. Y. Wang, and Q. Z. Shi, Dalton Trans. 42, 6306, (2013).

[63] L. Schlechte, V. Bon, N. Klein, R. Grunker, N. Klein, I. Senkovska, and S. Kaskel, Polyhedron 44, 179, (2012)/

[64] J. T. Shi, K. F. Yue, B. Liu, C. S. Zhou, Y. L. Liu, Z. G. Fang, and Y. Y. Wang, CrystEngComm 16, 3097, (2014).

[65] S. T. Zheng, X. Zhao, S. Lau, A. Fuhr, P. Feng, and X. Bu, JACS 135, 10270, (2013

[66] (a) H. Qu, L. Qiu, X. K. Leng, M. M. Wabg, S. M. Lan, L. L. Wen, and D. F. Li, Inorg. Chem. Commun., 14 1347-1351, (2011); (b) Lin H.S. and Maggard P.A., Inorg. Chem., 47 8044, (2008); (c) Liao Z.L., Li G.D., Bi M.H., and hen J.S., Inorg. Chem., 47, 4844, (2008).

[67] H. Y. Sun, C. B. Liu, Y. Cong, M. H. Yu, H. Y. Bai, and G. B. Che, Inorg. Chem. Commun., 35, 130, (2013).

[68] F. P. Huang, J. L. Tian, W. Gu, X. Liu, S. P. Yan, D. Z. Liao, and P. Cheng, Cryst. Growth Des., 10, 1146, (2010).

[69] S. H. Wang, F. K. Zheng, M. F. Wu, Z. F. Liu, J. Chen, Y. Xiao, R. Li, and G. C. Guo, Cryst. Eng. Comm., 16, 2009, (2014).

[70] L. J. Zhou, Y. Y. Wang, C. H. Zhou, C. J. Wang, Q. Z. Shi, and S. M. Peng, Cryst.Growth Des. 7, 300, (2007).

[71] M. X. Zheng, X. -J. Gao, C. L. Zhang, L. Qin, and H. G. Zheng, Dalton Trans. 44, 4751, (2015)

[72] A. S. Munn, G. J. Clarkson, F. Millange, Y. Dumont, and R. I. Walton, CrystEngComm, 15, 9679, (2013).

[73] C. Hou, Y. Zhao, and W. Y. Sun, Inorg. Chem. Commun., 39, 126, (2014).

[74] D. Liu, Y. Liu, G. Xu, G. Li, Y. Yu, and C. Wang, Eur. J. Inorg. Chem., 2012, 4413, (2012).

[75] Y. H. Wang, Y. W. Li, W. L. Chen, Y. G. Li, and E. B. Wang, J. Mol. Struct., 877, 56, (2008).

[76] J. S. Hu, Y. J. Shang, X. Q. Yao, L. Qin, Y. Z. Li, Z. J. Guo, H. G. Zheng, and Z. L. Xue, Cryst. Growth. Des., 10, 4135, (2010).

[77] P. Z. Li, X. M. Lu, and X. Z. Yang, Inorg. Chim. Acta, 361, 293, (2008).

[78] D. K. Maity, B. Bhattacharya, R. Mondal, and D. Ghoshal, Cryst. Eng. Comm., 16, 8896, (2014).

[79] B. Bhattacharya, D. Maity, P. Pachfule, and D. Ghoshal, Inorg. Chem. Front., 1, 414, (2014).

[80] Z. Q. Shi, Z. J. Guo, and H. G. Zheng, Dalton Trans., 43, 13250, (2014).

[81] J. S. Goldsworthy, A. L. Pochodyl, and R.L. LaDuca, Inorg. Chim. Acta, 419, 26, (2014).

[82] L. Qin, X. H. Zheng, S. L. Xiao, and G. H. Cui, Transition Met. Chem., 38, 891, (2013).

[83] Y. T. Yang, F. H. Zhao, Y. X. Che, and J. M. Zheng, Inorg. Chem. Commun., 14, 1802, (2011).

[84] W. G. Yuan, F. Xiong, H. L. Zhang, W. Tang, S. F. Zhang, Z. He, L. H. Jing, and Qin D.B., CrystEngComm, 16, 7701, (2014).

[85] Y. Gong, M. M. Zhang, P. Zhang, H. F. Shi, P. G. Jiang, and J. H. Lin, CrystEngComm, 16, 9882, (2014).

[86] G. A. Santillan and C. J. Carrano, Inorg.Chem. 47, 930, (2008).

[87] X. X. Wang, B. Yu, K. V. Hecke, and G. H. Cui, RSC Advances 4, 61281, (2014).

[88] X. Z. Song, S. -Y. Song, C. Qin, S. Q. Su, S. N. Zhao, M. Zhu, Z. M. Hao, and H. J. Zhang, Cryst. Growth Des. 12, 253, (2012).

[89] S. H. Kim, H. S. Huh, and S. W. Lee, J. Mol. Struct. 841, 78, (2007).

[90] F. Luo, Y. X. Che, and J. M. Zheng, Cryst. Growth Des. 9, 1066, (2009).

[91] Y. Du, A. L. Thompson, and D. O'Hare, Dalton Trans. 39, 3384, (2010).

[92] Y. Gong, Y. C. Zhou, T. F. Liu, J. Lu, D. M. Proserpio, and R. Cao, ChemCommun. 47, 5982, (2011).

[93] Q. Chen, Y. Y. Jia, Z. Chang, T. T. Wang, B. Y. Zhou, R. Feng, and X. H. Bu, Cryst.Growth Des. 14, 5189, (2014).

[94] Q. -R. Ding, L. M. Li, L. Zhang, and J. Zhang, Inorg.Chem. 54, 1209, (2015).

[95] X. X. Wang, Y. J. Ma, H. H. Li, and G. H. Cui, Transition Met.Chem. 40, 99, (2015).

[96] J. Y. Lee, J. Y. Lee, and H. M. Lee, Inorg.Chem.Commun. 52, 16, (2015).

[97] M. Bagherzadeha, F. Ashouri, and M. Dakovic, J. Solid State Chem. 223, 32, (2015).

[98] Y. Wang, Y. Qi, Q. Li, Z. Lv, and Y. Wang, Polyhedron, 85, 389, (2015).

[99] A. S. Munn, S. Amabilino, T. W. Stevens, L. M. Daniels, G. J. Clarkson, F. Millange, M. J. Lennox, T. Duren, S. Bourelly, P. L. Llewellyn, and R. I. Walton, Cryst. Growth Des., 15 (2), 891, (2015).

[100] W. J. Huang, C. J. Hsu, S. K. Tsai, H. Y. He, J. J. Ding, T. W. Hsu, C. C. Yang, and J. D. Chen, RSC Advances 5, 23374, (2015).

[101] F. P. Huang, C. Yang, H. Y. Li, P. F. Yao, X. H. Qin, S. P. Yan, and M. Kurmoo, Dalton Trans. 44, 6593, (2015).

[102] Z. X. Li, G. Ye, J. Han, Y. Yang, K. Y. Zou, X. Wang, X. L. Wang, and X. F. Gou, Dalton Trans. 44, 9209 ,(2015).

[103] J. P. Meng, Y. Gong, Q. Lin, M. M. Zhang, P. Zhang, H. F. Shi, and J. H. Lin, Dalton Trans. 44, 5407, (2015).

[104] C. Serre, F. Millange, C. Thouvenot, M. Noguès, G. Marsolier, D. Louër, and G. Férey, JACS, 124 (45), 13519, (2002).

EFFECT OF ANISOTROPIC ELASTIC DEFORMATION ON THE FERMI SURFACE CROSS SECTION OF DOPED BISMUTH WIRES EXHIBITING p-TYPE CONDUCTIVITY

A. A. Nikolaeva[1,2*], L. A. Konopko[1,2], A. K. Kobylianskaya[1], and D. Burduja[1]

[1]*Gitsu Institute of Electronic Engineering and Nanotechnologies, Academiei str. 3/3, Chisinau, Republic of Moldova*
[2]*International Laboratory of High Magnetic Fields and Low Temperatures, Wroclaw, Poland*
*E-mail: A.Nikolaeva@nano.asm.md

Abstract

The results of a study of the effect of the anisotropic elastic deformation up to 2% relative elongation on the change in the Fermi surface cross section of Sn-doped Bi wires in a glass envelope with the (10$\underline{1}$1) crystallographic orientation along the axis of elongation have been described. Changes in the Fermi surface cross section are recorded using Shubnikov-de Haas (ShdH) oscillations. It has been shown that the elastic deformation of Bi−0.07at%Sn wires is accompanied by an electronic topological transition at which the carriers of two hole ellipsoids $L_{2,3}$ that are equivalent with respect to the axis of elongation and exhibit high charge carrier mobilities flow into hole ellipsoid L_1 with low carrier mobilities up to a topological transition at which the conductivity occurs only through the holes of hole ellipsoids L_1 and T located at the L and T points of the Brillouin zone. The temperature and deformation dependences of resistance R and thermoelectric power α have been studied. It has been found that the size effect in the Bi−0.07at%Sn wires is evident from the formation of a maximum in $R(T)$ and the sign inversion in $\alpha(T)$ that linearly depend on the reciprocal of diameter $1/d$. It has been shown that the deformation dependence of resistance and thermoelectric power represent the electronic topological transition that occurs during tensile deformation.

1. Introduction

The introduction of Sn impurities into Bi shifts the Fermi level of holes ε_F^T at the T point down the energy scale and leads to a change in the number and nature of energy extremes. In studying the energy spectrum of metals and alloys, deformation effects play a decisive role, which is attributed to the fact that, unlike the doping method, elastic deformation is multiply implemented using the same sample. Doping is conducted using samples of different compositions; thus, there is some uncertainty associated with the replacement of the object of study. The action of deformation on the energy spectrum is more definite. The most spectacular phenomena for the observation of the qualitative restructuring of energy spectra are strong anisotropic elastic deformations [1, 2] which involve a continuous variation in the factor of action on the sample and provide a complete reproducibility of the results. It is significant that the method makes it possible to simultaneously observe the changes in the Fermi surface (FS) topology.

It is known that the deformation of bismuth along different crystallographic directions

leads to changes in the FS of different signs [3, 4]. Any deformation, except for that along the (111) trigonal axis, leads to a decrease in the Bi lattice symmetry and different changes in the three equivalent FS "ellipsoids" differently arranged relative to the load application axis; that is, for each direction, there are at least two groups that differently change under deformation [2–4]. Quantum oscillation effects, such as Shubnikov-de Haas (ShdH) oscillations, are the most informative for studying the energy spectrum of charge carriers and the band structure in semimetals.

Promising objects for the study of changes in the FS under uniaxial deformations are semimetal-based single-crystal wires in a glass envelope because the range of elastic deformation of these materials is about 2–2.5% relative elongation [5–7], which is an order of magnitude higher than the values in bulk samples. An advantage over whiskers lies in the fact that the studied wires are single crystals of a strictly cylindrical shape with the same orientation along the axis [7]. In addition, a glass envelope protects the wires against mechanical impacts during installation, contributes to the achievement of strong elastic deformations up to 2-3%, and blocks the occurrence of shear strains that decrease the limit of elasticity.

This study is focused on the examination of ShdH oscillations in Bi−0.07at%Sb wires in which the Fermi level lies in the zone of light L holes and heavy T holes of the Brillouin zone under the action of an elastic tensile deformation of up to 2% (Fig. 1).
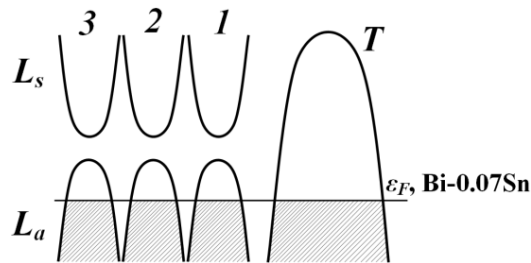
Fig. 1. Schematic representation of the band structure and the Fermi level position in Sn-doped Bi.

Cyclotron masses, charge carrier concentration, Fermi level position, and Dingle temperature were estimated from ShdH oscillations. Deformation dependences of resistance $R(\xi)$ and thermoelectric power $\alpha(\xi)$ at different temperatures were also studied.

2. Materials and Methods

Single-crystal wires in a glass envelope were prepared by liquid-phase casting by the Ulitovsky method [6, 7]. The starting material was a single-crystal ingot of the Bi−0.07at%Sb alloy synthesized by zone recrystallization. Thin Bi−0.07at%Sb wires in a glass envelope had diameters ranging from 200 nm to 1 μm, a strictly cylindrical shape, and the same crystallographic orientation (10$\underline{1}$1) along the wire axis.
The orientation of the samples was determined using angular rotation diagrams of transverse magnetoresistance ($B\perp I$) in magnetic fields of 0−14 T at temperatures of 300−4.2 K (Fig. 2) and ShdH oscillations. Control measurements of the crystallographic orientation and analysis of the single-crystal pattern of the wires in a glass envelope were conducted by the X-ray diffraction method using individual samples. The use of angular rotation diagrams of transverse

magnetoresistance made it possible to orient the magnetic field in certain crystallographic directions ($B \parallel C_2$, $B \parallel C_3$) with respect to the wire axis.
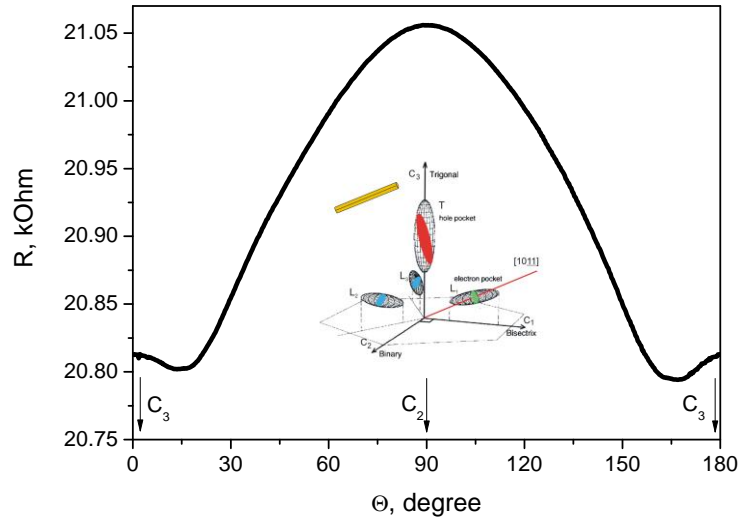
Fig. 2. Angular rotation diagrams of transverse magnetoresistance $R(\Theta)$ of the Bi−0.07at%Sn wire with $d = 600$ nm at $T = 4.2$ K and $B = 0.5$ T. The inset shows a schematic representation of the FS of bismuth in the (10$\underline{1}$1) direction along the wire axis.

To study the wires under the action of elastic tensile deformation, the wire was fixed on a beryllium bronze ring with a diameter of about 5 mm (Fig. 3).
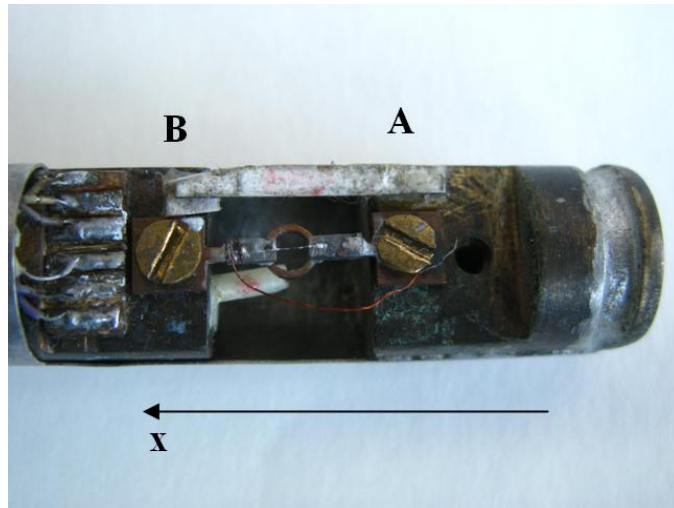
Fig. 3. Image of the sample fixed on a beryllium bronze ring for the determination of the kinetic properties of wires in a glass envelope subjected to the action of elastic tensile deformation.

The wire was fixed on two contact pads of copper-foil coated fiberglass with a size of $2 \times 1 \times 0.5$ mm that were fixed on the ring at a distance of 2–3 mm from each other. All the data—sample signal, temperature, and magnetic field—were transmitted on a computer and

displayed on a monitor during the measurements. The beryllium bronze ring with the sample was placed into a holder, and the entire system was immersed in a Dewar vessel filled with helium (Fig. 3).

The ring extending under the action of an applied force was preliminarily calibrated at $T = 300$ K using a microscope. The above design provided a smooth stretching of the sample up to 2−3% relative elongation; $\xi = \dfrac{\Delta l}{l} = \dfrac{l - l_0}{l} \cdot 100$ % where l is the sample length before stretching in a temperature range of 2−300 K.

Particular attention was paid to compliance with the elastic stretching conditions. To this end, multiple stretching cycles were run and the reproducibility of the results was estimated. The temperature dependences of resistivity, magnetoresistance, and ShdH oscillations in the absence and presence of elastic tensile deformation were measured in an automatic mode on a computer-aided installation in a temperature range of 4.2−300 K at magnetic fields of up to 14 T at the International Laboratory of High Magnetic Fields and Low Temperatures (Wroclaw, Poland).

3. Results and Discussion

Temperature dependences of resistance $R(T)$ and thermoelectric power $\alpha(T)$ of the Bi−0.07at%Sn wires of different diameters in a temperature range of 4.2−300 K (Fig. 4) and the field dependences of longitudinal ($B \parallel I$) and transverse magnetoresistance $R(B)$ ($B \perp I$, $B \parallel C_2$, $B \perp I$, $B \parallel C_3$) in the magnetic field of a solenoid of up to 14 T in the absence of tensile deformation were studied (Fig. 5). Temperature dependences of resistance $R(T)$ of the wires of different diameters exhibit a "metallic" behavior and are linear upon a shift of the size peak in $R(T)$ to a high-temperature range and a decrease in the R_T/R_{300} ratio at 4.2 K with decreasing wire diameter d (inset in Fig. 4a). The "size" dependence of thermoelectric power is evident as a linear dependence of the sign inversion temperature in $\alpha(T)$ on the reciprocal of wire diameter (inset in Fig. 4b).
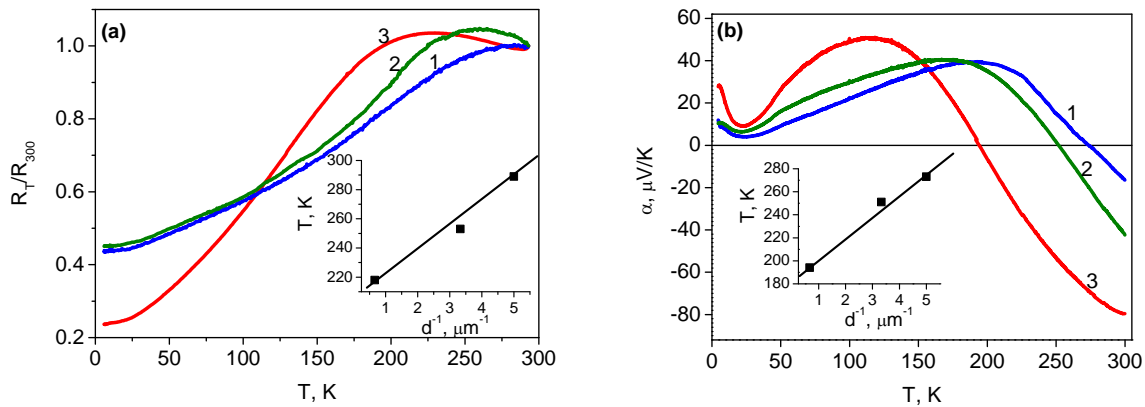
Fig. 4. Temperature dependences of (a) relative resistance $R_T/R_{300}(T)$ and (b) thermoelectric power $\alpha(T)$ of the Bi−0.07at%Sn wires of different diameters: d = (*1*) 0.2, (*2*) 0.3, and (*3*) 1.5 μm. The insets show the dependence of (a) the peak temperature in $R(T)$ and (b) the sign inversion temperature in $\alpha(T)$ on the reciprocal of wire diameter 1/d.

Figure 5 shows field dependences $R(B)$ of the Bi−0.07at%Sn wire in all the main crystallographic directions at 4.2 K. ShdH oscillations are particularly pronounced in derivatives

dR/dB(*B*) (Fig. 5b).
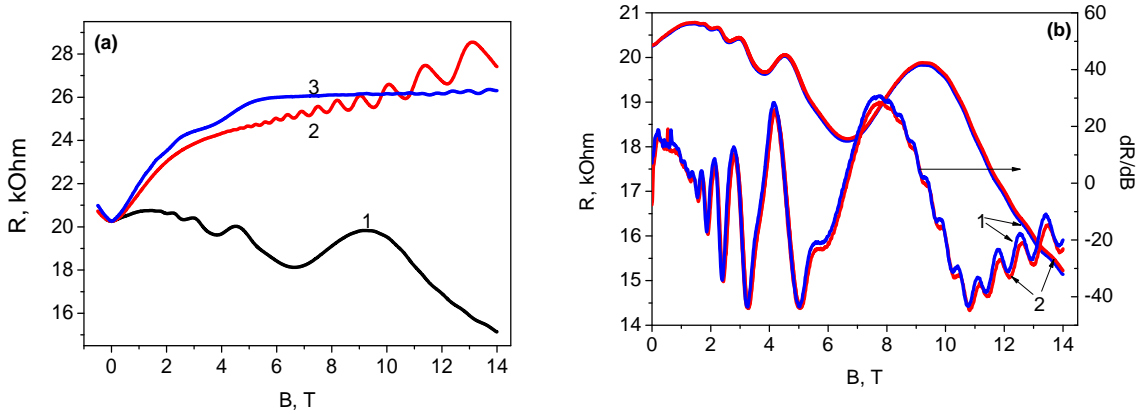
Fig. 5. (a) Field dependences of (*1*) longitudinal (*B* ∥ *I*) and transverse magnetoresistance (*2*) (*B* ⊥ *I*, *B* ∥ C$_3$) and (*3*) (*B* ⊥ *I*, *B* ∥ C$_2$) of the Bi−0.07at%Sn wire with orientation (10$\underline{1}$1) along the wire axis at *d* = 600 nm and *T* = 2.1 K and (b) field dependences of longitudinal magnetoresistance *R*(*B*) (left scale) and derivatives *dR/dB*(*B*) (right scale) of the Bi−0.07at%Sn wire with *d* = 0.6 m at *T* = (*1*) 2.1 and (*2*) 4.2 K.

The periods of the observed ShdH oscillations and the cyclotron masses calculated from the temperature dependences of the oscillation amplitude made it possible to determine the position of the Fermi level of holes at T according to the known relationships of charge carrier concentration and Dingle temperature T_D [8].

It has been found that the Fermi level of T holes ε_F^T is 104 meV as measured from the valence band top at T; that is, it is located in the region of light L holes (Fig. 1) [9], which is in good agreement with the data obtained in [8].

In the second set of measurements, deformation dependences of resistance *R*(ξ) at 4.2 K were recorded. After that, at fixed *Δl/l* values, field dependences of longitudinal magnetoresistance were measured. A successive increase in *Δl/l* made it possible to observe changes in the periods of quantum oscillations of the extreme sections of the L- and T-hole FSs during deformation.

Figure 6 shows the field dependences of longitudinal magnetoresistance *R*(*B*) of the Bi−0.07at%Sn wire with *d* = 600 nm and orientation (10$\underline{1}$1) at varying relative elongation ξ at a temperature of 4.2 K.

It is evident from Fig. 5b that, in the absence of deformation (ξ = 0) at 4.2 K in initial magnetic fields up to 9 T, longitudinal magnetoresistance *R*(*B*) clearly exhibits oscillations of the FS cross sections of two hole ellipsoids L$_{2,3}$ symmetrically arranged relative to the wire axis with a period of *Δ*(*B^{-1}*) = 1.2 · 10^{-5} Oe^{-1}. In the range of strong magnetic fields, oscillations of T holes with a period of *Δ*(*B^{-1}*) = 0.048 · 10^{-5} Oe^{-1} are observed. The region of existence of oscillations of L and T holes at ξ = 0 is clearly bounded by a magnetic field of 8 T (Fig. 5b).

With an increase in the load, field dependences *R*(*B*) exhibit a pronounced effect of negative magnetoresistance; the magnitude of it increases, while the region of existence expands and is shifted to weaker magnetic fields (Fig. 6).

In the magnetic-field dependences of longitudinal magnetoresistance, ShdH oscillations are clearly observed against the background of the monotonic behavior of *R*(*B*) at all elastic deformations.
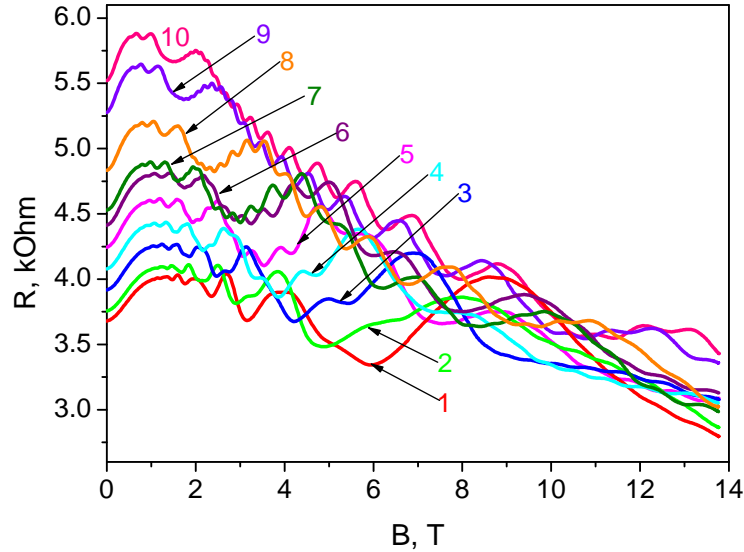
Fig. 6. ShdH oscillations in longitudinal magnetoresistance *R(B)* (*B* ∥ *I*) of the Bi−0.07at%Sn wire with orientation (10$\underline{1}$1) along the axis of the wire with *d* = 600 nm at fixed elastic stretching from ξ = 0 to ξ = 1.9% at *T* = 4.2 K.

Figure 7 shows the dependences of quantum number *n* of ShdH oscillations under different elastic tensile deformations.
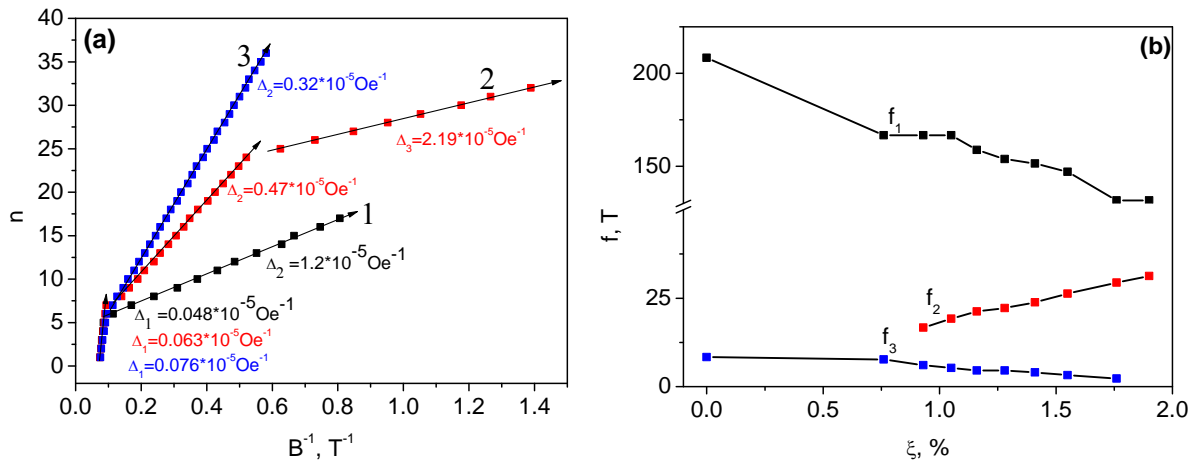
Fig. 7. (a). Dependences of conventional quantum number *n* of ShdH oscillations on reverse field B^{-1} of the Bi−0.07at%Sn wire with orientation (10$\underline{1}$1) along the wire axis and *d* = 600 nm at fixed elastic stretching values ξ of (*1*) 0, (*2*) 1.16, and (*3*) 1.9% and *T* = 4.2 K and (b) deformation dependences of ShdH oscillations of FS cross sections of (*f₁*) T holes and (*f₂*) L_1 and (*f₃*) $L_{2,3}$ hole ellipsoids at *T* = 4.2 K.

The respective periods of ShdH oscillations for the different (L and T) FS cross sections calculated from linear dependences $n(B^{-1})$ in Fig. 7 show the dependences of the ShdH oscillation frequency on the extreme sections of the FS at 4.2 K:

$$f = \left[\Delta \left(1 / B \right) \right]^{-1} = \frac{S_{ex} c}{e h} \qquad (1)$$

It is evident that, as in the case of $\xi = 1\%$, in the intermediate magnetic field range, a new ShdH oscillation frequency of $f = 19.2$ T ($\Delta(B^{-1}) = 0.52 \cdot 10^{-5}$ Oe^{-1}) appears in dependences $R(B)$ in a range of 0.2–5 T (Fig. 7); it increases with increasing load (stretching) and becomes dominant; that is, the region of existence of this frequency expands and is shifted to strong magnetic fields; this fact represents an increase in the minimum extreme cross section of the FS of L_1 holes [10]. In this case, the period of ShdH oscillations of two hole ellipsoids $L_{2,3}$ sharply increases to $4.4 \cdot 10^{-5}$ Oe^{-1} at $\xi = 1.8\%$, and the region of existence of ShdH oscillations of $L_{2,3}$ quasi-ellipsoids is shifted to weak magnetic fields; this fact indicates a sharp decrease in the volume thereof. At $\xi = 1.8\%$, oscillations of the $L_{2,3}$ hole ellipsoids vanish.

Thus, unlike pure Bi wires, the elastic stretching of Bi−0.07at%Sn wires with the same orientation is accompanied by the flow of carriers from two hole quasi-ellipsoids $L_{2,3}$ characterized by more mobile carriers into quasi-ellipsoid L_1 that is extended along the wire axis and has less mobile carriers in the direction of the wire axis. At the same time, the period of oscillations of T holes at a strain of up to 1% varies only slightly; as the load increases to 2% relative elongation, the period increases by a factor of 1.4; this fact indicates a decrease in the volume of the hole ellipsoid at the T point of the Brillouin zone during elastic tensile deformation along the (10$\underline{1}$1) axis (Fig. 7). These changes in the FS topology are accompanied by an increase in the resistance of the wire by a factor of 1.4 at $T = 4.2$ K.

For clarity, Fig. 7a shows the dependences of the ShdH oscillation periods at $\xi = 0$, 1.1, and 1.9%, while Fig. 7b shows the dependences of ShdH oscillation frequencies $f = 1/\Delta(B^{-1})$ for the different FS cross sections (L and T holes).

Stretching of the Bi−0.07at%Sn wires along the (10$\underline{1}$1) axis leads to a change in the symmetry of the lattice and violates the equivalence of L ellipsoids. Thus, the elastic tensile deformation of the Bi−0.07at%Sn wires is accompanied by an electronic topological transition during which the FS composed of three L hole ellipsoids and one T hole ellipsoid changes and, under maximum tensile deformations, consists of one L hole ellipsoid extended along the (10$\underline{1}$1) axis and one T hole ellipsoid: $3_h^L + 1_h^T \rightarrow 1_h^L + 1_h^T$.
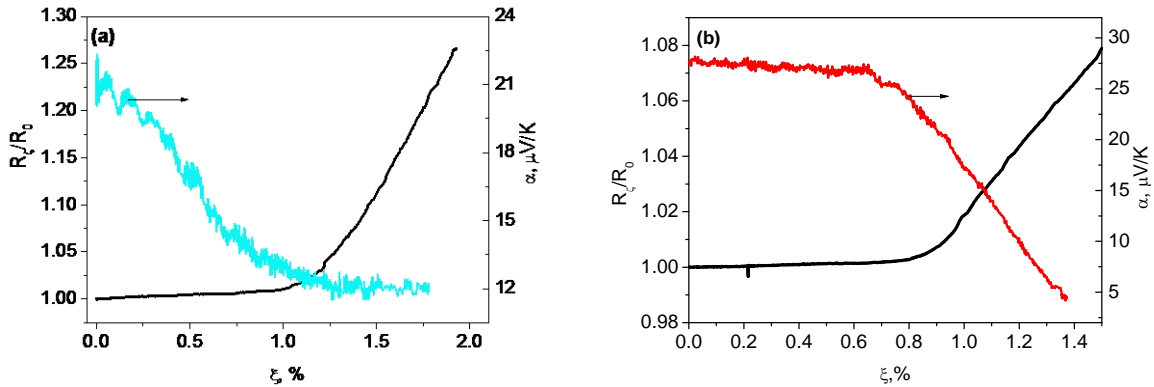
Fig. 8. Deformation dependences of reduced resistance $R_\xi/R_0(\xi)$ and thermoelectric power $\alpha(\xi)$ of the Bi−0.07at%Sn wire at the different temperatures of $T =$ (a) 4.2 and (b) 205 K.

Figure 8a shows deformation dependences of resistance $R_\xi/R_0(\xi)$ and thermoelectric power $\alpha(\xi)$ at a temperature of about 4.2 K. The increase in resistance $R_\xi/R_0(\xi)$ by a factor of 1.3 represents a decrease in the contribution of more mobile carriers of $L_{2,3}$ holes during elastic

deformation. In this case, the thermoelectric power decreases with stretching; however, unlike pure Bi wires, the α value does not become negative; instead, it undergoes saturation; this fact indicates the disappearance of $L_{2,3}$ hole ellipsoids at the transition $3_h^L + 1_h^T \rightarrow 1_h^L + 1_h^T$ at $\xi = 1.3\%$.

(**a**)   (**b**)
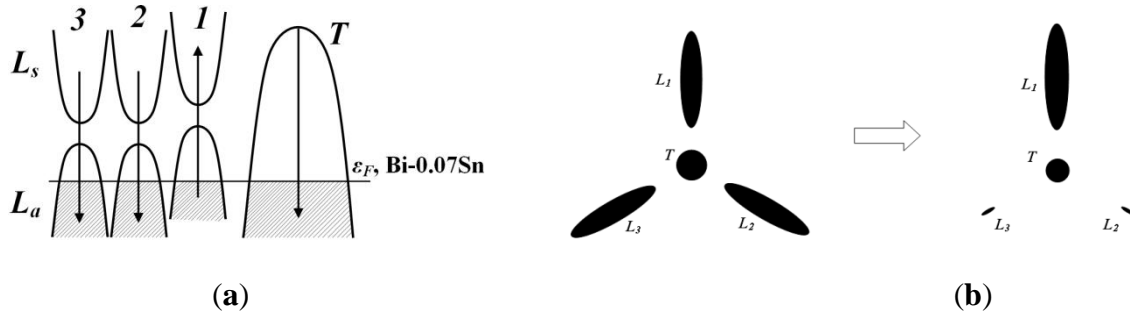
Fig. 9. (**a**) Schematic representation of the band structure and the displacement of the ellipsoids and the Fermi level in the Bi−0.07at%Sn wire with the standard (10$\underline{1}$1) orientation during stretching along the wire axis and (**b**) variation in the FS shape in the Bi−0.07at%Sn wire with the standard (10$\underline{1}$1) orientation during stretching along the wire axis.

At a temperature of 205 K, the thermoelectric power undergoes a sharp linear decrease and exhibits a tendency to change the sign at higher ξ values; this feature is attributed to the fact that, in this temperature range, the smearing of κT leads to the partial involvement of the electrons from ellipsoids $L_{2,3}$ that are shifted down the energy scale during tensile deformation (Fig. 9a).

4. Conclusions

The study of Bi wires doped with 0.07 at % Sn has shown that, in the wires with a thickness of up to 200 nm, the size effects are significantly weaker than in pure Bi with respect to both the resistance and the thermoelectric power. Cyclotron masses of L and T holes, concentrations, and the energy position of the Fermi level of T holes ε_F^T have been calculated from ShdH oscillations.

In studying ShdH oscillations, it has been shown that the uniaxial elastic deformation of the wires is accompanied by an electronic topological transition of $3_h^L + 1_h^T \rightarrow 1_h^L + 1_h^T$, which leads to an increases in resistance $R(\xi)$ and a decrease in the positive thermoelectric power value in the deformation curves in the entire temperature range.

References

[1] E. V. Zarochentsev, S. M. Orel, and S. V. Teplov, Fiz. Tverd. Tela 22(1), 24, (1930).
[2] N. B. Brandt, Yu. P. Gaidukov, E. S. Itskevich, and N. D. Minina, Zh. Eksp. Teor. Fiz. 47(8), 455, (1964).
[3] N. B. Brandt and Ya. G. Ponomarev, Zh. Eksp. Teor. Fiz. 55(10), 1215 (1968).
[4] N. B. Brandt, V. S. Egorov, M. Yu. Lavrenyuk, N. Ya. Minina, and A. M. Savin, Sov. Phys. JETP 62(6), 1303, (1985).

[5] Yu. P. Gaidukov, N. P. Danilova, and M. B. Shcherbina-Samoilova, Zh. Eksp. Teor. Fiz. 77(5), 2125, (1979).

[6] N. B. Brandt, D. V. Gitsu, A. A. Nikolaeva, and Ya. G. Ponomarev, Zh. Eksp. Teor. Fiz. 72, 2332 (1977) [(Sov. Phys. JETP, 45 (6), 1977)].

[7] D. Gitsu, L. Konopko, and A. Nikolaeva, Appl. Phys. Lett. 86, 10210, (2005).

[8] N. B. Brandt and S. M. Chudinov, Elektronnaya struktura metallov, Mosk. Gos. Univ., Moscow, 1973, 331 p.

[9] A. A. Nikolaeva, L. A. Konopko, P. P. Bodiul, and A. K. Tsurkan, J. Thermoelectr. 3, 28, (2014).

[10] A. Nikolaeva, T. Huber, L. Konopko, and A. Tsurkan, J. Low. Temp. Phys. 159, 258, (2010).

STRUCTURE AND ELECTROPHYSICAL PROPERTIES
OF A GaSb−CrSb EUTECTIC COMPOSITE

R. N. Rahimov, I. Kh. Mammadov[*], M. V. Kazimov, D. H. Arasly, and A. A. Khalilova

Institute of Physics of the Azerbaijan National Academy of Sciences;
*Azerbaijan National Academy of Aviation
E-mail: rashadrahim48@gmail.com

Abstract

XRD analysis and microstructure and DSC studies of GaSb-CrSb eutectic composite synthesized by the Bridgman method have been conducted. It has been shown that needle-shaped CrSb inclusions oriented to the solidification direction take part in the GaSb matrix. The initial and final temperature and enthalpy of melting for this composite have been determined. The anisotropy observed in the temperature dependences of Hall coefficient, electrical conductivity, and thermoelectric power of the composite has been attributed to the sort-circuiting effect of metallic inclusions.

1. Introduction

Semimagnetic or diluted magnetic semiconductors are promising materials for the production of high-speed memory systems. It is well known that dilute magnetic semiconductors based on binary semiconductors doped with $3d$-transition metals do not have stable characteristics. From this point of view, eutectic composites based on III−V compounds and 3d-transition metals (Fe, Mn, Co) have reproducible and stable characteristics and do not depend on external factors [1−4]. These composites are promising targets for researchers because of semiconductor and metal properties. These materials consist of a III−V group semiconductor matrix and metal inclusions parallel oriented in the matrix. In these systems, the charge carriers are redistributed at semiconductor−metal boundaries and structural and electronic energy states arise, the fact that is not characteristic of each phase individually. These semiconductor−metal eutectic composites exhibit a behavior similar to that of nonuniform semiconductors. The physical properties of these materials strongly depend on the electronic configuration of $3d$-elements, geometry of inclusions, and the formation of interphase zones between the inclusions and the matrix [5−6].

Previously, we investigated the features of the electron−phonon processes of the eutectic composites based on GaSb and InSb compounds with Fe, Co, and Mn [3−6]. The present work is focused on the synthesis, differential scanning calorimeter (DSC) analysis, and studies of the microstructure and electrophysical parameters of a GaSb−CrSb composite in a temperature range of 80−750 K as a continuation of a cycle of works of the preparation and investigation of eutectic composites.

2. Experimental

The synthesis of GaSb−CrSb eutectic composite was conducted in two stages. Semiconductor GaSb was prepared by alloying the related components in stoichiometric quantities and refining the alloy by horizontal recrystallization method. The eutectic alloys of GaSb−CrSb have been prepared by alloying GaSb and 13.5 wt% CrSb using the vertical Bridgman method. The rate of the crystallization front was set at about 0.3 mm∕min. The resulting crystals exhibited *p*-type conductivity.

XRD intensity data were collected on an Advance-D8 diffractometer using CuK_α radiation. The microstructure and elemental composition of the samples were studied using a FEI Quanta FEG electron microscope and an Oxford Inca X-act EDS system.

The heat flow (DSC) and mass change (TG) were recorded on a PerkinElmer STA 6000 instrument (United States) in a nitrogen atmosphere with a gas flow rate of 20 mL/min and at a heating rate of 10°C/min. The sample with a weight of 123.547 mg was placed in a corundum crucible. The DTA curve was derived from DSC curve differentiation.

The electrical properties of the composite were investigated by means of compensation in a temperature range of 80−750 K and at a magnetic field of 1.3 T in the mutual directions of the electric current, crystallization, heat flow, and magnetic field.

3. Results and discussion

Diffraction patterns of eutectic composite GaSb−CrSb are shown in Fig. 1. This figure also shows data on the diffraction patterns for GaSb and CrSb compounds. Analysis of XRD spectra using TOPAZ and EVA applications has confirmed that this system is diphasic: the most intense peaks corresponding to the (111), (200), (220), (311), (222), (400), (331), (420), and (422) Muller index are identical to the GaSb matrix, while the weak peaks found at $2\theta = 30°$, 44.08°, 52.12°, and 54.13° coincide with the CrSb lines having a hexogonal structure with lattice parameters of $a = 4.121$, $c = 5.467$, $c/a = 1.327$, and the *P63/mmc* space group.
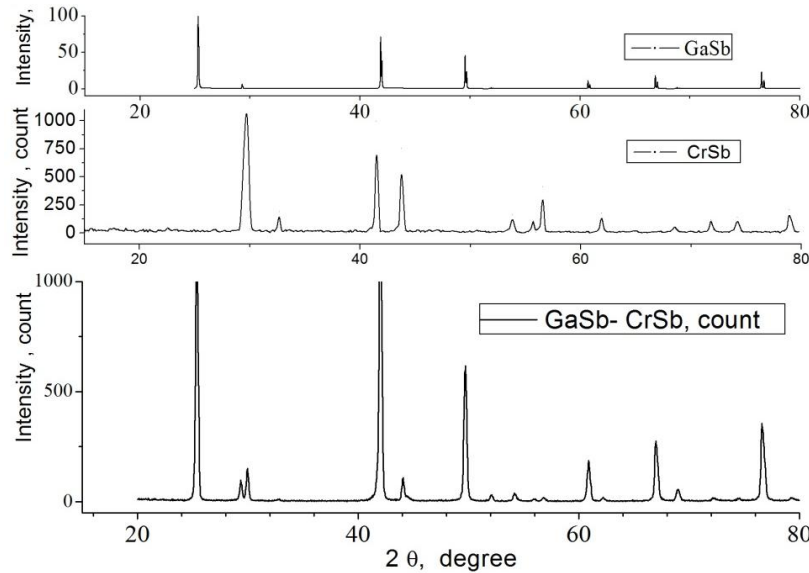
Fig. 1. Comparative diffraction patterns of the GaSb and CrSb compounds and the GaSb−CrSb eutectic composite.
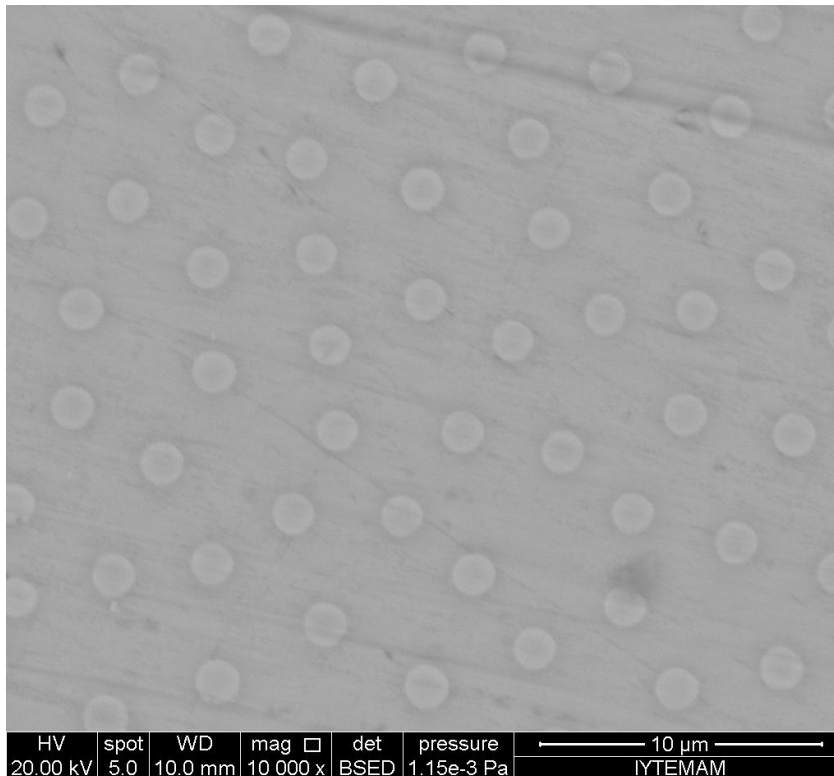
Fig. 2. SEM image of the GaSb−CrSb eutectic composite (magnification of 10000 times).

The data on the microstructure and elemental composition are shown in Figs. 2 and 3. The needle-shaped metallic inclusions are uniformly and parallel distributed in the GaSb matrix. Based on SEM examinations, the oriented needles have a diameter of about 1.4 μm, a length of 20−50 μm, and a density of ∼8 x 10^4 mm^{-2}. The elemental composition data correspond to the GaSb matrix and the CrSb inclusions.

DSC, TG, and DTA curves of the composite in a temperature range of 25−1000°C are presented in Fig. 3. It is evident from the TG curve that the change in weight is 0.154%. The temperature range of 670−700°C, in which the endothermic process occurs and the weight remains unchanged, corresponds to the melting of the composite. It has been found that the initial and final melting temperatures are 670 and 692°C, respectively, and the enthalpy of melting is 56.45808 J/g. The temperature range of 645−670°C, in which the endothermic process occurs and the weight increases, corresponds probably to the oxide process with an enthalpy of 6.3335 J/g.

The results of studies of the temperature dependences of the Hall coefficient $R(T)$, electrical conductivity $\sigma(T)$ and thermoelectric power $\alpha(T)$ measured at the different mutual directions of current (I), magnetic field (B), and crystallization direction are shown in Figs. 5−7. In the temperature dependence of the kinetic coefficients, anisotropy due to the presence of regular metal crystalline inclusions in the semiconductor matrix is observed. Due to shorting action by needle-shaped metallic inclusions, the electrical conductivity increases in the $I \parallel x$ direction and it is significantly different from $\sigma(T)$ in the $I \perp x$ direction. The coefficient of conductivity anisotropy at 80 K is $\sigma_{\parallel}/\sigma_{\perp} = 3.2$ and decreases with increasing temperature: $\sigma_{\parallel}/\sigma_{\perp} = 3$ at 300 K. The electrical conductivity decreases in a temperature range of 400−560 K; however,

above 560 K, it greatly increases and anisotropy completely disappears. The decrease in the electrical conductivity is associated with the occurrence of a new flow of conduction electrons compensating for the hole conductivity. The electron contribution to conduction and to the total mobility increases above 560 K. The deviation on the $\sigma(T)$ dependence observed in a temperature range of 600−650K is possible due to the magnetic phase transition of the CrSb inclusions [7, 8].

a)

b)
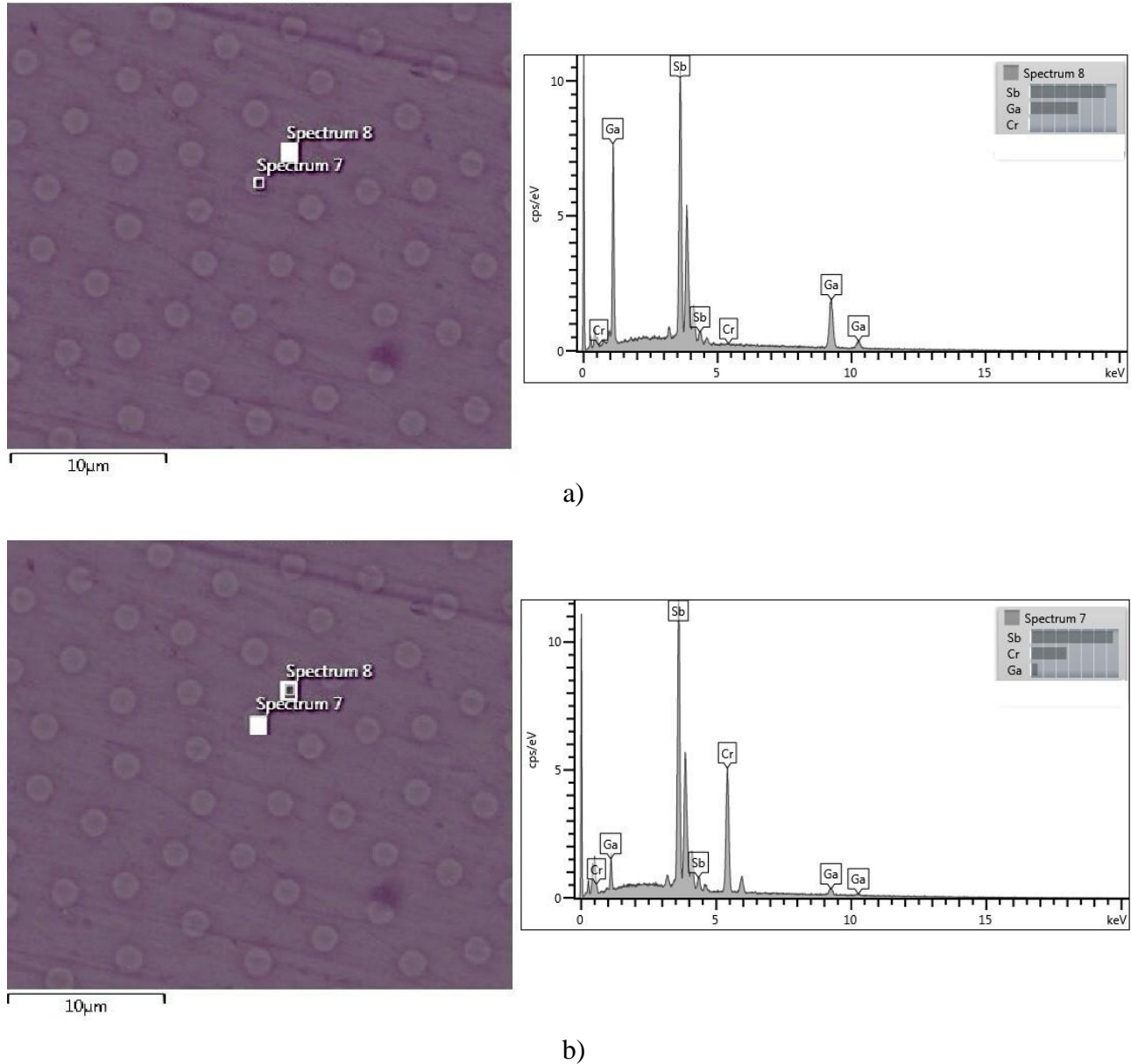
Fig. 3. Elemental compositions of the GaSb–CrSb composite obtained with SEM–EDX from (a) the matrix and (b) inclusion phases.
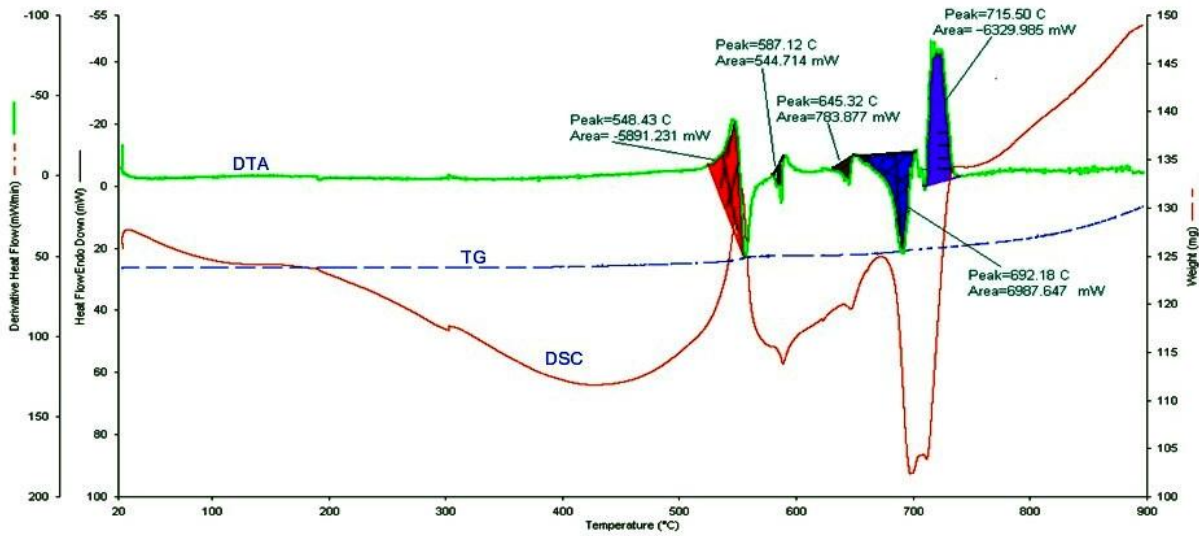
Fig. 4. DSC, TG, and DTA curves of the GaSb–CrSb composite.
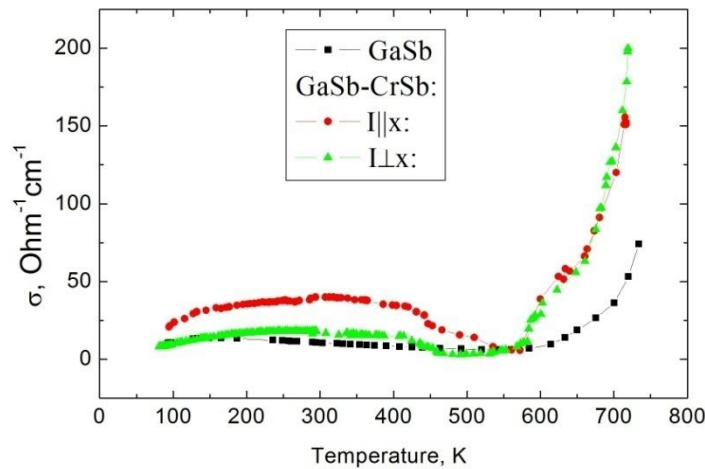
Fig. 5. Temperature dependence of electric conductivity for GaSb and the GaSb–CrSb composite.

As shown in our previous studies [3], the *R* value is maximum if the metallic needles in the matrix are oriented perpendicular to the current direction and parallel to the magnetic field ($I \perp x \parallel$ B) and the behavior of the *R(T)* dependence is approximately the same as that for the matrix. The Hall coefficient drop along the sample in the case of $I \parallel x \perp B$ due to the short-circuiting of the voltage and the Hall voltage in the case of $I \perp x \perp B$ has a minimum value. The temperature dependence of the Hall coefficient *R(T)* measured in the case of $I \perp x \parallel B$ where there is no shorting of any current or potential Hall are plotted in Fig. 6. It is evident from the figure that the Hall coefficient remains unchanged in a temperature range of 80–475 K. The sign of the Hall coefficient changes at temperatures between 490 and 515 K (the inversion point for GaSb is ~560 K).

Strong anisotropy is also observed in the temperature dependence of the thermoelectric power (Fig. 7). The short-circuiting of V_α potential by metallic inclusions at $\Delta T \parallel x$ directions

results from a decrease in the thermopower.
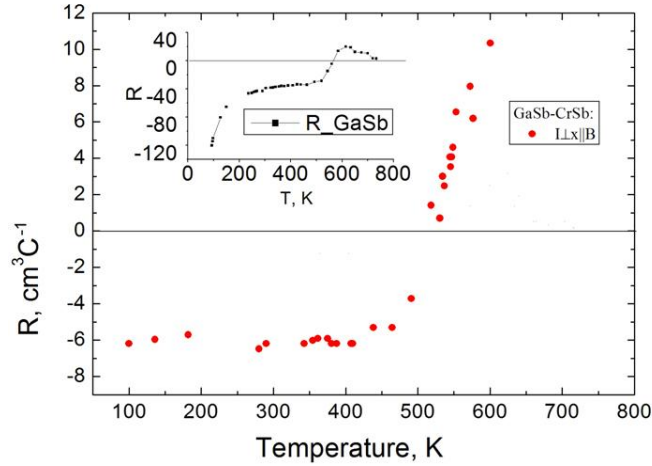
Fig. 6. Temperature dependence of Hall coefficient for GaSb−CrSb composite.
The inset shows the (*R(T)*) dependence for GaSb.
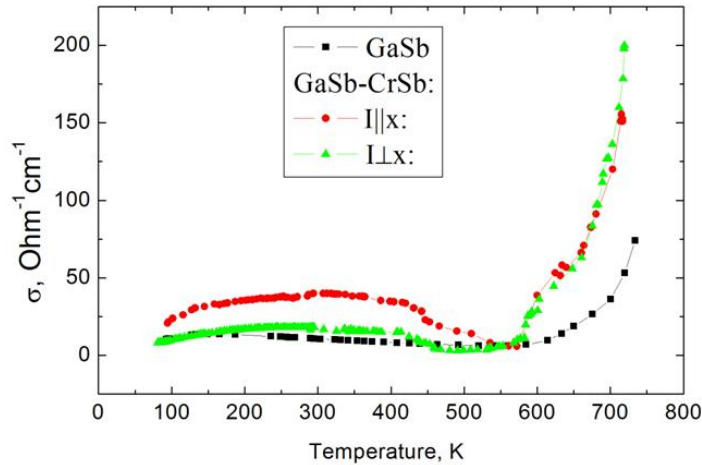
Fig. 7. Temperature dependence of thermoelectric power for the GaSb−CrSb composite.

4. Conclusions

The electron microscopy and XRD studies of GaSb−CrSb have confirmed that the systems consist of a semiconductor matrix and oriented needle-shaped metal inclusions. The initial and final melting temperatures for this composite are 670 and 692°C, respectively; the enthalpy of melting is 56.45808 J/g. The anisotropy observed in the temperature dependence of the kinetic parameters at different mutual directions of current, solidification, magnetic field, and heat flow are attributed to the short-circuiting effect of metallic inclusions. The sign of Hall coefficient of GaSb−CrSb changes in a temperature range between of 490 and 515 K. The deviation in electrical conductivity in a temperature range of 600−650 K is associated with the magnetic phase transition of the CrSb inclusions.

References

[1] A. Müller and M. Wilhem, J. Phys. Chem. Solids, 26, 12, 2029, (1965).

[2] Y. Umehara and S. Koda, J. Jpn. Inst. Met. 50, 7, 666, (1986).

[3] M. I. Aliyev, A. A. Khalilova, D. H. Arasly, R. N. Rahimov, M. Tanoglu, and L. Ozyuzer, J. Phys. D: Appl. Phys. 36, 2627, (2003).

[4] R. N. Rahimov, I. Kh. Mammadov, M. V. Kazimov, D. H. Arasly, and A. A. Xəlilova, J. Qafqaz Univ., Phys. 1, 2, 166, (2013).

[5] M. I. Aliyev, D. H. Arasly, R. N. Rahimov, A. A. Khalilova, I. Kh. Mammadov, and R. M. Jabbarov, Trans. Azerbaijan Nat. Acad. Sci.: Phys. Astron. 27, No. 2, 72, (2007).

[6] M. I. Aliyev, I. Kh. Mammadov, A. A. Khalilova, R. N. Rahimov, and D. H. Arasly, Mold. J. Phys. Sci. 11, No.3, 157, (2012).

[7] T. S. Dijkstra, C. F. Bruggeni, C. Haasi, and R. A. Grooti, J. Phys.: Condens. Matter 1, 9163, (1989).

[8] Yong Liu, S. K. Bose, and J. Kudrnovsky, World J. Eng. **9,** 2, 125, (2012).

STRUCTURE AND OPTICAL PROPERTIES OF GaSe-CdSe COMPOSITES DRIVEN BY Cd INTERCALATION IN GaSe LAMELLAR CRYSTALS

Iuliana Caraman[1], Valeriu Kantser[2], Igor Evtodiev[3], Liviu Leontie[4], Grigory Arzumanyan[5], Dumitru Untila[3], and Liliana Dmitroglo[3]

[1] *Vasile Alecsandri University of Bacau, 157 Calea Marasesti, Bacau, RO 600115 Romania*
[2] *Institute of the Electronic Engineering and Nanotechnologies, Academy of Sciences of Moldova, Chisinau, Republic of Moldova*
[3] *Scientific Research Laboratory for Photonics and Physical Metrology, Moldova State University, Chisinau, Republic of Moldova*
[4] *Faculty of Physics, Alexandru Ioan Cuza University of Iasi, Bul. Carol I, no. 11, Iasi, 700506 Romania*
[5] *Joint Institute for Nuclear Research, Joliot-Curie 6, Dubna, Moscow region, 141980 Russia*

Abstract

A new composite material composed of GaSe and CdSe has been obtained by treatment of GaSe single-crystal lamellas in Cd vapors at temperatures of 773−853 K and intercalation of Cd interlayers. The structure and optical properties of the GaSe-CdSe composite material have been studied. The content of CdSe crystallites was found to grow with increasing treatment temperature or with increasing duration of treatment at a constant temperature. Analysis of XRD, PL, XPS, AFM, and Raman patterns has shown that the heterogeneous composite composed of micro and nanocrystallites of CdSe in GaSe can be obtained by Cd intercalation in a temperature range of 753−853 K. On the basis of Raman spectrum, the vibrational modes of the composite have been identified. The PL of these materials contains emission bands of free and bound excitons, donor-acceptor bands, and bands of recombination via impurity levels. The PL emission spectra measured at a temperature of 78 and 300 K for the composites result from the overlapping of the emission bands of the components of GaSe doped with Cd and the CdSe crystallites.

1. Introduction

Binary $A^{III}B^{VI}$ compounds, a typical representative of which is the GaSe lamellar semiconductor, exhibit a pronounced anisotropy of chemical bonds and optical properties [1]. An elementary lamella is composed of atomic planes arranged in the following sequence: Se−Ga−Ga−Se. The bonds between the elementary lamellas in GaSe crystals are provided by Van der Waals polarization forces, while strong ionic-covalent forces act between the atomic planes within the packets [2−3]. Weak bonds between the packets, along with saturated valence bonds on the surface, lead to the formation of plane-parallel cracks between Se atomic planes with a width of ~0.3 nm [4]. Ions, atoms, and molecules can easily penetrate these cracks; this fact expands the range of applicability of layered semiconductors. By intercalation of GaSe

crystals with Li$^+$ ions [5], it has been shown that this semiconductor can be applied as a solid electrolyte exhibiting characteristics superior to those of metal oxides [6]. By intercalation of GaSe single crystals with Ni, Fe, and Co, it is possible to prepare composite materials and structures with ferromagnetic properties that are promising for use in spintronics [7-9].

In this study, the structure and luminescent properties of GaSe crystals intercalated with Cd from the vapor phase have been examined. Analysis of XRD, PL, XPS, and Raman patterns has shown that a composite composed of micro and nanocrystallites of CdSe in GaSe can be prepared by intercalation with Cd in a temperature range of 753−823 K.

2. Experimental and Crystalline Structure Properties

The original material was p-GaSe single crystals grown by the Bridgman−Stockbarger method [10]. The GASe compound was synthesized from original elements Ga (5N) and Se (5N). Plane-parallel plates with smooth surfaces at an atomic level and a thickness of 20 μm to 5 mm were prepared by splitting the grown single crystals with the crystallographic C_6 axis oriented perpendicular to the axis of the ingot. These plates were cut into rectangular samples with a surface area of 10−20 mm^2. The samples were selected with respect to thickness and placed into quartz tubes with an internal diameter of 15−17 mm together with granules of Cd (5N) taken in an amount of 2 mg/cm^3. After repeated evacuation (2−3 times) to a residual pressure of ~5 · 10^5 Torr and sealing, the containers were subjected to heat treatment at temperatures of 75 to 823 K in an oven with a stable temperature for 6−24 h. In this temperature range, the Cd vapor pressure was in a range of 20−560 mmHg.

XRD patterns of the prepared composites were recorded on a DRON-4 diffractometer using CuK$_α$ radiation (λ = 1.5406 Å) in the range of diffraction angles 2Θ of 10°−80° with a resolution of 0.050 at a rate of 10° min^{-1}. Photoluminescence (PL) spectra of the composites prepared by heat treatment of GaSe single crystals in Cd vapors were excited with laser radiation with Nd^{+3} (λ = 532 nm) with an average power of 100 mW. The PL in a temperature range of 78−300 K was analyzed using a monochromator with a diffraction grating of 600 and 1200 mm^{-1} (an area of 180 × 130 mm^2) and recorded using an electronic photomultiplier with a multialkali photocathode. The spectral resolution of measurements of PL and PC did not exceed 1 meV in the entire studied spectral range. Raman scattering spectra at T = 300 K were analyzed using a Raman microsystem.

The crystal lattice of the GaSe compound is composed of layered packets, which in turn are formed by four atomic planes of Se and Ga (Fig. 1a).

The Cd atoms of the intercalation occupy positions between the Se planes of two elementary packets neighboring to four selenium atoms from the first configuration sphere in both packets. At fairly high temperatures of $T \geq 653$ K, at which the Se−Ga bonds are fairly weak, the bonds between Ga and Se are broken and form new compounds of the Cd−Se type, which are much more energetically stable than GaSe. Thus, during a high-temperature heat treatment at 750−830 K, CdSe clusters and condensation centers of Ga atoms are formed in the GaSe plates. Since the saturated valence bonds on the surface of the elementary packets (Se−Ga−Ga−Se) (Fig. 1b), a long-term exposure (24−30 days) to normal atmosphere leads to the formation of a nanostructured layer of oxides of the constituting elements on the outer surface of the GaSe plates [2].

Surface nanostructuring of the GaSe plates by treatment in Cd vapors at high temperatures is much more pronounced compared to a normal temperature. The surface of GaSe plates freshly

cleaved from perfect single crystals is smooth at an atomic level. The treatment in an atmosphere of Cd vapors at a temperature of $T \geq 593$ K (at 593 K, the Cd vapor pressure is 0.1 mmHg), micrometer-sized regions of different shapes are formed on the surface of the plates.
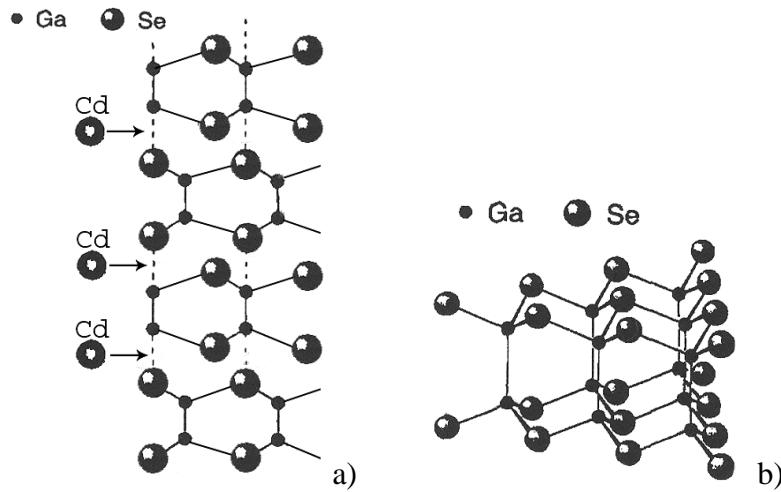
Fig. 1. Arrangement of atomic planes in ε-GaSe crystals.

Atomic spectrum analysis of the points, which can be easily conducted at the surface of the GaSe plates, has shown that they represent clusters of metallic Ga, which are in a liquid state at a temperature of 303 K. As noted above, GaSe single-crystal lamellas are composed of planar packets of atoms so that the plane of Se atoms is located on the surface. They can easily be combined with Cd to form layers of CdSe on the surface. This transformation results in a loss of valence bonds between the Ga atoms in the two atomic planes in the packet ...Se−Ga−Ga−Se...
Figure 4 shows an AFM image of the surface of the GaSe plate subjected to heat treatment at a temperature of 833 K for 24 h. Under these conditions of formation of the composite, pyramidal and conical structures with base dimensions on the order of a few hundreds of nanometers are formed on the (001) face of the GaSe plates. The height of these structures is up to 15−20 nm, which corresponds to more than ten layered packets of the Se−Ga−Ga−Se type.
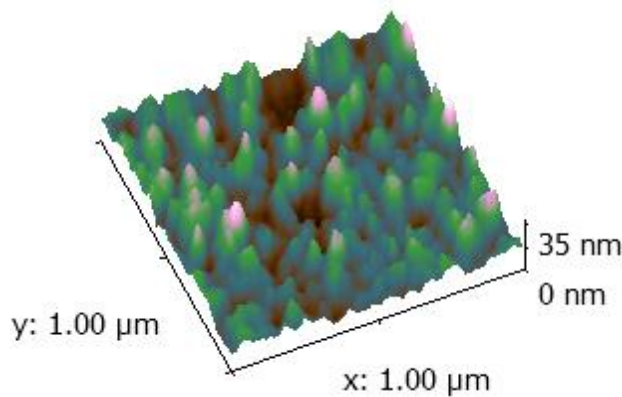
Fig. 2. AFM image of the surface of the GaSe lamella subjected to heat treatment in Cd vapors at a temperature of 833 K for 24 h.

The crystalline structure of the new components of the composite prepared by heat treatment of GaSe single-crystal plates in Cd vapors was studied by X-ray diffraction and Raman scattering. Figure 3 shows XRD patterns of two samples prepared by treatment of GaSe plates with a thickness of 0.3 and 1.2 mm in Cd vapors at a temperature of 753 (Fig. 5a) and 833 K (Fig. 5b) for 24 h.
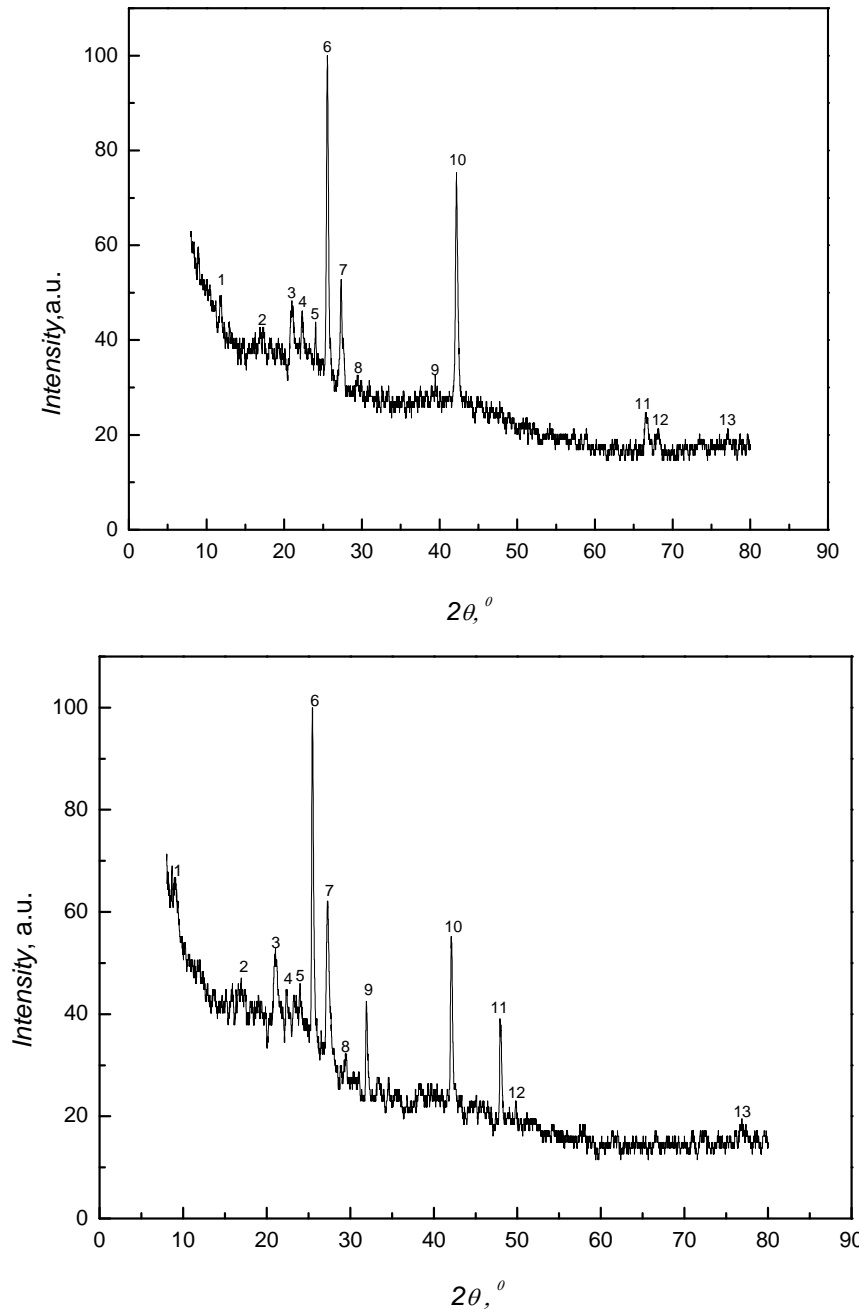
Fig. 3. XRD pattern of the GaSe lamella treated in Cd vapors at a temperature of
(a) 753 and (b) 833 K for 24 h.

Table 1 lists the 2θ diffraction angles corresponding to the diffraction lines, the intensity of the lines, the identification of a lot of the planes in which X-ray diffraction occurs, and the respective

compound.

Table 1. Identification of the GaSe-CdSe composite according to XRD patterns

No.	753 K		Identification	833 K		Identification
	2θ	I (a.u.)		2θ	I (a.u.)	
1	22.35	46.1	[002] *GaSe*	20.96	51.7	[002] *GaSe*
2	25.56	100	[101] *CdGa₂Se₄*	25.49	100	[002] *CdGa₂Se₄*
3	27.33	52.8		27.27	62.1	
4	42.17	75.3	[004] *GaSe*	31.93	42.5	[004] *GaSe*
5	66.5	24.7		42.08	55.2	
6	8.93	59.65	[002] *CdSe*	47.93	39.1	[002] *CdSe*
7	11.85	49.05	[001] *CdSe*	9.05	66.48	[101] *CdSe*
8	17.34	42.25		16.97	46.24	
9	20.99	47.44	[103] *CdSe*	22.46	44.23	[103] *GaSe*
10	22.32	45.43		57.91	17.80	[110] *CdSe*
11	29.53	32.24		76.93	19.19	[222] *CdGa₂Se₄*
12	39.39	31.22	[210] *GaSe*			[310] *CdGa₂Se₄*
13	68.14	20.40				[210] *GaSe*
14	73.5	20.00				
15	76.93	20.00				

It is evident from Fig. 3 and Table 1 that the diffraction lines of the ensembles of planes of both the GaSe-based composite and the crystallites composed of CdSe are clearly detected. Along with XRD reflections of crystalline clusters of CdSe in GaSe, both at 753 and 833 K, reflections from the ensemble of the [101] plane of the $CdGa_2Se_4$ compound are clearly recorded. A change in the intensity ratio of the XRD reflections with an increase in the treatment temperature from 753 to 833 K (with a respective increase in the Cd vapor pressure) is indicative of an increase in the concentration of CdSe crystallites in the composite. Narrow contours of reflections of the ensembles of the [002], [101], and [110] planes can be used as a criterion of high perfection of CdSe crystallites, while a considerable broadening of the contour of the diffraction lines from the [004] and [210] atomic planes of the hexagonal network of gallium monoselenide is indicative of the degradation of the base material (GaSe single crystal). Comparison of Figs. 5a and 5b shows that an increase in the concentration of Cd atoms in the composite upon switching from 753 to 833 K leads to a significant increase in the content of both CdSe and $CdGa_2Se_4$.

3. Optical Properties

The presence of micrometer-sized regions of different shapes on the surface of the plates in the form of circular dots with unordered areas is clearly evident in reflected light and much more pronounced in a polar field of monochrome light in reflection and luminescence (Fig. 4).
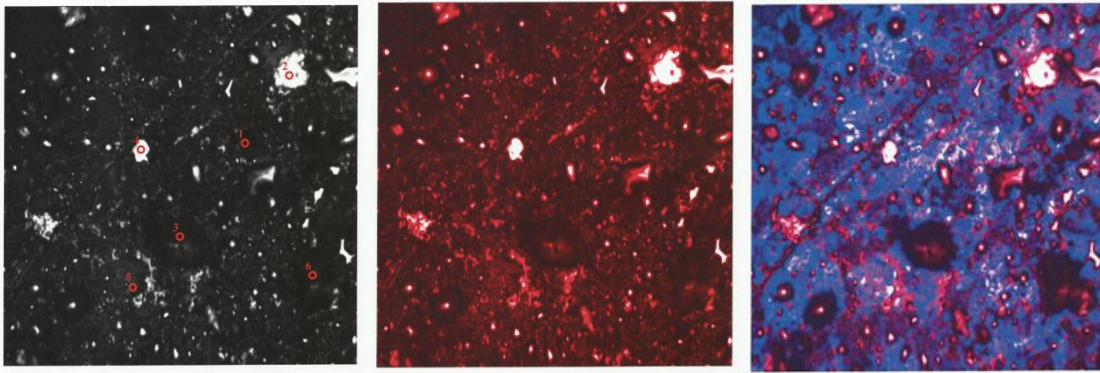
Fig. 4. Microscopic image in reflected light and luminescence on the surface of the GaSe lamella
subjected to treatment in Cd vapors at a temperature of 823 K for 24 h.
The recorded area is $193.3 \times 193.3 \ \mu m^2$.

Additional information about the nature of the structures formed on the surface of GaSe
plates is provided by luminescent emission spectra measured at room temperature. Figure 5
shows PL spectra recorded at $T = 300$ K in bright (point *1*) and dark regions (point *3*). It is
evident from the comparison of these curves that the PL intensity at the bright points (*1, 5*) is
about 5−6 times higher than at the dark points. However, at points *1* and *5*, the PL band peak is
shifted by ~20 meV to higher energies and is indicative of splitting into two subbands peaking at
1.818 and 1.797 eV.

It can be assumed that the PL bands of the GaSe−CdSe composites prepared by heat
treatment of GaSe crystals in Cd vapors are formed by overlapping of the respective bands of the
constituting compounds GaSe and CdSe.
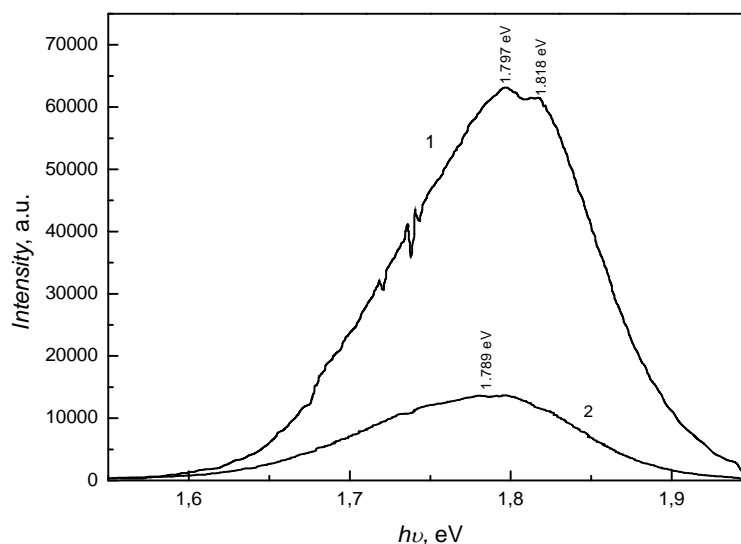
Fig. 5. PL spectra of the composite prepared by a heat treatment of GaSe crystals in Cd vapors at a
temperature of 773 K for 24 h: (curve *1*) bright points on the surface (*1, 5*) and (curve *2*) dark points (*3, 4*).

Figure 6 shows the Raman scattering spectrum of the GaSe–CdSe composite prepared by heat treatment of GaSe single-crystal plates in Cd vapors at a temperature of 773 K for 6 h. The spectra exhibit vibration bands of the crystal lattice of the original material (GaSe) and the newly formed compound (CdSe). The wave numbers and intensities of the bands of Raman scattering in the GaSe–CdSe compound are shown in Table 2.
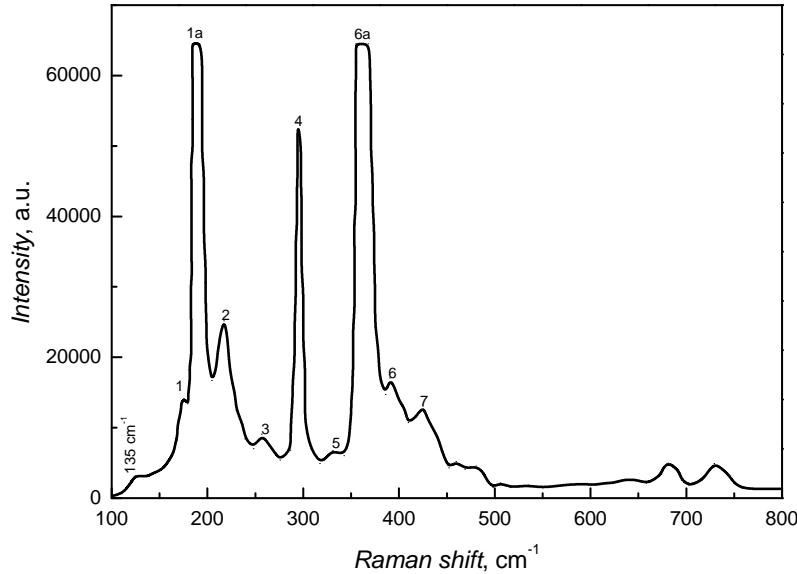
Fig. 6. Raman spectrum of the GaSe lamella subjected to treatment in
Cd vapors at a temperature of 773 K for 6 h.

Table 2. Vibration modes of the crystal lattice of the GaSe–CdSe composite obtained from the Raman spectrum

No.	$\widetilde{\nu}$, cm^{-1}	Intensity (a.u.)	Compound	Vibration symmetry
	135.0	3000	*GaSe*	A$_1$
1	174.4	14000	*CdSe*	E(TO)
1a	188.9	>60000	*GaSe*	
2	217.5	25000	*GaSe*	E(TO)
3	256.8	8000	*GaSe*	E'(LO)
4	295.4	52000	*GaSe*	
5	329.9	6000	*GaSe*	
6	361.6	>60000		
6a	393.9	16000	*CdSe*	
7	426.8	12000	*CdSe*	

It is evident from Table 2 that, along with the monophononic vibration modes in the GaSe crystals, the vibration bands of the crystal lattice of the CdSe compound are also clearly pronounced. The lower intensity of the diffusion bands in the CdSe crystallites compared to GaSe corresponds to the percentage composition of the composite prepared at a temperature of 733 K.

These results are consistent with the data on the intensity of the XRD reflections from the planar systems in the GaSe and CdSe crystals shown in Table 1.

Both the classification of vibration modes by the type of symmetry and the energy shifts of the Raman bands associated with combination of different vibration modes are well known for GaSe single crystals [12–13]. The reduced intensity of resonance vibration modes E(TO) (267.5 cm^{-1}) and E'(LO) (256.8 cm^{-1}) compared to the bands (188.9 and 361.6 cm^{-1}) can be attributed to the fact that the formation of the composite is accompanied by the degradation of the crystal lattice of the original GaSe compound.

The PL spectra of GaSe and CdSe crystals are also well known at low temperatures of $T \leq 78$ K. The PL of these materials contains emission bands of free and bound excitons, donor−acceptor bands, and bands of recombination via impurity levels [14]. Figure 7 shows the PL spectra of the GaSe and CdSe crystals measured at temperatures of 300 and 78 K and the spectra of the compounds prepared by heat treatment at temperatures of 753 and 833 K for 20 and 24 h. The PL spectrum of the GaSe crystals at a temperature of 300 K exhibits a donor−acceptor band peaking at 2.00 eV and an impurity band at 1.94 eV. At a temperature of 78 K, the PL spectrum exhibits an emission line of localized excitons (hν = 2.092 eV), a donor−acceptor emission band (hν = 2.072 eV), and an intrinsic impurity band peaking at 1.920 eV. Figure 7 (curves *5, 6*) shows that the PL spectrum of the CdSe single-crystal compound at temperatures of 300 and 78 K exhibits an emission band with a symmetrical contour peaking at 1.720 and 1.790 eV, respectively. The PL spectra measured at $T = 300$ K for the GaSe−CdSe composite prepared by treatment in Cd vapors at temperatures of 823 and 853 K exhibit a broad band without pronounced characteristic features with two low-intensity peaks at 1.78 and 1.72 eV, respectively.

Fig. 7. PL emission spectra of the ε-GaSe and CdSe crystals and the GaSe−CdSe composite at temperatures of 78 and 300 K: (*1, 2*) the GaSe single crystal at temperatures of 300 and 78 K; (*3, 4*) GaSe annealed in Cd vapors at a temperature of 823 K for 20 h; (*5, 6*) the CdSe single crystal at temperatures of 300 and 78 K; and (*7, 8*) GaSe annealed in Cd vapors at a temperature of 853 K for 24 h.

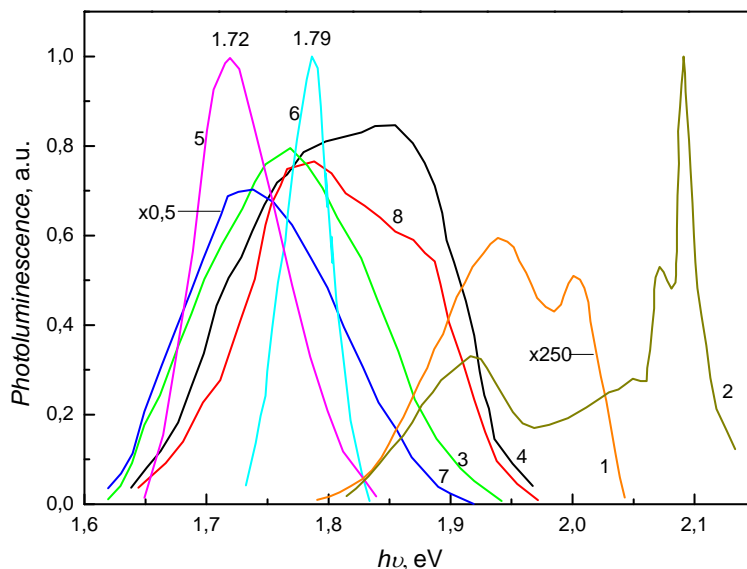An increase in the duration of intercalation from 20 to 24 h, along with an increase in temperature from 823 to 853 K, results in a shift of the emission peak to lower energies by ~60 meV and, simultaneously, to an increase in the PL band intensity by about 2 times. Comparison of the PL spectra of GaSe subjected to intercalation with Cd (curve *1*) and CdSe (curve *5*) clearly shows close agreement between the peaks of the respective bands. The extension of the PL band contour to high energies results from the overlapping of the impurity PL bands of the GaSe lamellas and CdSe crystalline clusters of the composite. Note that a decrease in the temperature of the sample from 300 to 78 K results in a more than 200 times increase in the intensity of the PL spectrum of the GaSe lamellas, which leads to an increase in the fraction of GaSe crystals in the intensity distribution of the emission band of the GaSe−CdSe composite. Figure 7 shows the PL emission spectra measured at a temperature of 78 (curves 4, 8) and 300 K (curves 3, 7) for the GaSe lamellas treated in Cd vapors at a temperature of 823 and 853 K, respectively. It is evident that the PL band contour has a complex structure, which probably results from the overlapping of the impurity emission band of GaSe with an absolute maximum at 1.920 eV and the emission band of the CdSe compound peaking at 1.79 eV. Treatment of the GaSe single-crystal plates in Cd vapors at high temperatures, along with the intercalation of Cd atoms between the elementary packets and the formation of CdSe crystallites, leads to doping of the residue of GaSe with Cd, while the newly formed CdSe crystals are doped with Ga. The PL spectra of GaSe crystals doped with Cd in a concentration of 0.01−0.1 at % that were measured at a temperature of 78 K have been thoroughly studied in [15]. The Cd concentrations in GaSe higher than 0.01 at % lead to the formation of defects and screening in the exciton binding and, simultaneously, to the formation of a dominant emission band with a weak peak shifted to lower energies: 1.95 eV at $C = 0.01$ at % and 1.75 eV at $C = 0.05$ at %. Therefore, we can assume that the PL spectra shown in Fig. 6 by curves *4* and *6* at $T = 78$ K and by curves *3* and *7* at $T = 300$ K are the result of the overlapping of the PL bands of the GaSe compound doped with Cd in concentrations of less than 0.05 at % and the CdSe crystallites formed during intercalation at temperatures of $T \geq 753$ K.

4. Conclusions

(i) A new composite material composed of GaSe and CdSe microcrystals has been prepared by treatment of GaSe single-crystal lamellas in Cd vapors at temperatures of 773−853 K. The content of the CdSe crystallites increases with increasing treatment temperature or with increasing duration of treatment at a constant temperature.

(ii) XRD patterns and Raman spectra have shown that the CdSe crystallites of the composite are fairly perfect, while the remaining GaSe is composed of strongly deformed and structurally imperfect crystals.

(iii) New micro- and nanostructures composed of GaSe and CdSe crystallites are formed on the surface of the GaSe lamellas subjected to treatment at 833 K for 24 h.

(iv) The PL emission spectra measured at a temperature of 78 and 300 K for the composite prepared by the intercalation of Cd atoms in GaSe at a temperature of 773−823 K result from the overlapping of the emission bands of the components of GaSe doped with Cd and the CdSe crystallites.

References

[1] K. R. Allakhverdiev, T. Baykara, S. Joosten, E. Günay, A.A. Kaya, A. Kulibekov (Gulubayov), A. Seilmeier, and E.Yu. Salaev, Opt. Commun. 261, 60, (2006).

[2] Z. S. Basinski, D. B. Dove, and E. Mooser, Helv. Phys. Acta 34, 373, (1961).

[3] R. H. Friend and A. D. Yoffe, Adv. Phys. 36 1, (1987).

[4] M. Jouanne, C. Julien, and M. Balkanski, Phys.Status Solidi, B 144, K147, (1987).

[5] C. M. Julien and M. Balkanski, Mater. Sci. Eng. B 100, 263, (2003).

[6] C. M. Julien, Mater. Sci. Eng. R 40, 47, (2003).

[7] Z. D. Kovalyuk, V. B. Boledzyuk, V. V. Shevchuk, V. M. Kaminskii, and A. D. Shevchenko, Fiz. Tekh. Poluprovodn. 46, 8, (2012).

[8] M. Zerrouki, J. P. Lacharme, M. Ghamnia, C. A. Sebenne, and B. Abidri, Appl. Surf. Sci. 181 (1−2), 160, (2001).

[9] I. I. Grigorchak, V. V. Netyaga, and Z. D. Kovalyuk, J. Phys.: Cond. Matter 9, L191, (1997).

[10] N. B. Singh, R. Narayanan, A. X Zhao, V. Balakrishna, R.H. Hopkins, D. R. Suhre, N. C. Fernelius, F. K Hopkins, and D. E. Zelmon, Mater. Sci. Eng. B 49, 243, (1997).

[11] S. Shigetomi, T. Ikari, and H. Nishimura, J. Appl. Phys. 69 (11), 7936, (1991).

[12] N. M. Gasanly, N. N. Melnik, V. I. Tagirov, and A. A. Yushin, Phys. Status Solidi (b) 135, K107, (1986).

[13] R. M. Hoff and J.C. Irwin, Phys. Rev. B 10, 3464, (1974).

[14] V. Capozzi and M. Montagna, Phys. Rev. B 40, 3182, (1989).

[15] O. A. Balitskii, Mater. Lett. 60, 594, (2006).

PREPARATION AND OPTICAL PROPERTIES OF LAMELLAR GaSe–ZnSe NANOCOMPOSITES

M. Caraman[1], D. Untila[1], V. Canţer[2], Ig. Evtodiev[1], Iu. Caraman[3], O. Susu[4], and L. Leontie[4]

[1]*Laboratory for Photonics and Physical Metrology, Faculty of Physics and Engineering, Moldova State University, A. Mateevici str. 60, Chisinau, MD-2009 Republic of Moldova*
[2]*Institute of Electronic Engineering and Nanotechnologies, Academy of Sciences of Moldova, Academiei str. 3/3, Chisinau, MD-2028 Republic of Moldova*
[3]*Vasile Alecsandri University of Bacau, Calea Marasesti 157, Bacau, 600115 Romania*
[4]*Faculty of Physics, Alexandru Ioan Cuza University of Iasi, bul. Carol I 11, Iasi 700506 Romania*

Abstract

ZnSe–GaSe nanocomposite plates photoluminescent in a photon energy range of 1.80−2.64 eV were obtained via exposing GaSe single-crystal plates to a Zn-vapor heat treatment at temperatures of 673−873 K. The photoluminescence spectrum is dominated by the self-activated emission band of ZnSe with a maximum at 2.04 eV. The average size of the ZnSe crystallites is ~45 nm. The absorption spectrum of the composite consists of two regions characteristic of direct optical transitions in GaSe crystals with a band gap of 1.99 eV and ZnSe crystallites with a band gap of 2.56 eV at room temperature.

1. Introduction

Layered III−VI group semiconductors, in particular of GaSe, have been intensively studied in recent years because of promising application in optoelectronics (visible region), nonlinear optical devices, and radiation generation/detection in THz domain [1−4].
GaSe single crystals are composed of flat Se−Ga−Ga−Se elementary packages perpendicular to its C_6 crystallographic axis [5].
The links between the packages are of Van der Waals type, much weaker than those between four monoatomic sheets inside a package, accomplished by ionic-covalent (predominant) forces. This feature results in a marked anisotropy of mechanical properties (facilitating intercalation) and electric, optical, and photoelectric characteristics.
At the same time, the valence bonds of chalcogen atoms at the interface between stratified packages are almost closed; the relative arrangement of elementary packages provides the formation of a subnanometric (0.3 nm) gap between the neighboring packages favoring the intercalation of diverse atomic (molecular) ions between chalcogen planes [6−8].
GaSe intercalation may lead to new physical properties of the material, such as ferromagnetism and magnetoresistivity.
Owing to compensated valence bonds at the surface of stratified packages, gallium monoselenide intercalated with Li and H also displays marked solid electrolyte properties [9, 10].
The presence of Se atomic planes at the surface of GaSe plates enables obtaining

heterojunctions exhibiting visible photosensitivity by heat treatment under normal atmosphere or metal vapor atmosphere [11].

By metal vapor-heat treatment of layered GaSe single crystals, a metal-chalcogen compound layer is formed at the GaSe surface, together with intercalation of metal atoms between stratified packages to form lamellar nanocomposites.

In this work, the composition and optical properties of the composite obtained by Zn vapor-phase intercalation of GaSe single-crystal plates are studied.

2. Experimental

p-GaSe single crystals, which were used as starting materials, were grown by the Bridgman technique from their component elements (Ga and Se, both of 5N purity) taken in stoichiometric portions.

Hole concentration and mobility at room temperature were about 4×10^{14} cm^{-3} and 35 cm^2/(V·s), respectively.

GaSe plates with a thickness of 100−300 μm obtained by splitting single crystalline ingots along the (0001) atomic planes were used for the preparation of the composite. They exhibited mirror-like surfaces showing no defects visible at 600× magnification.

Selected GaSe single-crystal plates were placed, together with 5% Zn, in quartz ampoules with an internal diameter of 10–12 mm; the ampoules were evacuated to 5×10^{-5} Torr, tightly closed, and placed in an electric oven with stabilized temperature for heat treatment at 833 K for 3−24 h. As a result of the heat treatment, the surface of the GaSe plate was covered by an orange granular layer with a micrometer size. The surfaces of the freshly split plates also exhibited a granular microstructure.

The crystal structure and composition of the as obtained material were analyzed by X-ray diffraction (XRD) technique using a DRON-4 diffractometer (CuK$_\alpha$ radiation, $\lambda = 0.154182$ nm). Measurements were conducted in an angular range of $10° < 2\theta < 80°$ with a peak resolution of 0.05° and 10° min^{-1} scan speed.

Diffuse reflectance spectra were registered using an M-40 spectrophotometer equipped with an integrating sphere. A pressed BaSO$_4$ powder was used as a white reference standard.

Low-temperature photoluminescence (PL) measurements were conducted using a cryostat with quartz windows in a temperature range of 78−300 K. The PL of the GaSe-based samples was excited using a N$_2$ laser ($\lambda = 337.4$ nm) with an average power of 100 mW. The PL spectral characteristics of as obtained samples at 78 K were recorded on a spectrophotometric setup including a monochromator with a diffraction grating (600 and 1200 mm^{-1}) and a photomultiplier with a multi-alkaline Na$_2$KSb:Cs photocathode. The energy resolution was up to 2 meV over the entire measuring range.

3. Experimental results and interpretation

Fig. 1 shows the X-ray diffraction pattern of the primary GaSe single crystal.
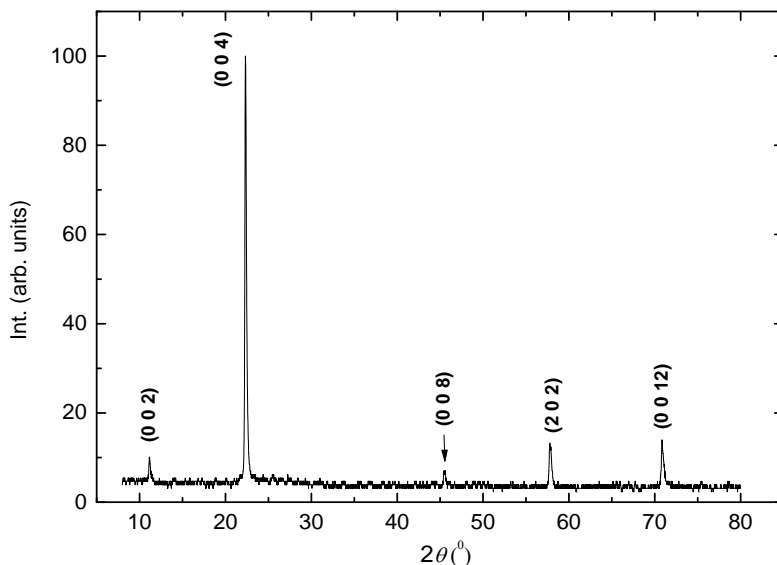
Fig. 1. XRD patterns of the primary GaSe single crystals.

2θ angular positions of diffraction lines and their relative intensities, along with respective Miller indices, are listed in Table 1.

Table 1 Structural parameters of primary GaSe single crystals

Experimental Values		ICDD-JCPDS cards			
2θ (°)	I (a. u.)	PDF	2θ (°)	I	$h\,k\,l$
11.24	10.1	GaSe/37-0931(hex)	11.10	62	0 0 2
22.43	100	GaSe/37-0931(hex)	22.27	100	0 0 4
45.58	7	GaSe/37-0931(hex)	45.66	10	0 0 8
57.89	12.4	GaSe/37-0931(hex)	57.97	27	2 0 2
70.85	14	GaSe/37-0931(hex)	71.08	17	0 0 12

X-ray diffraction patterns of GaSe exhibit the intense characteristic (004) diffraction line and four low-intensity peaks labeled as (0 0 2), (0 0 8), (2 0 2), and (0 0 12). From the XRD patterns, hexagonal lattice parameters were found to be a=3.75 Å and c=15.85 Å and correspond to ε-GaSe modification.

Fig. 2 shows the XRD patterns of the composite obtained by a 24-h heat treatment of GaSe plates at 833 K in a Zn vapor atmosphere.
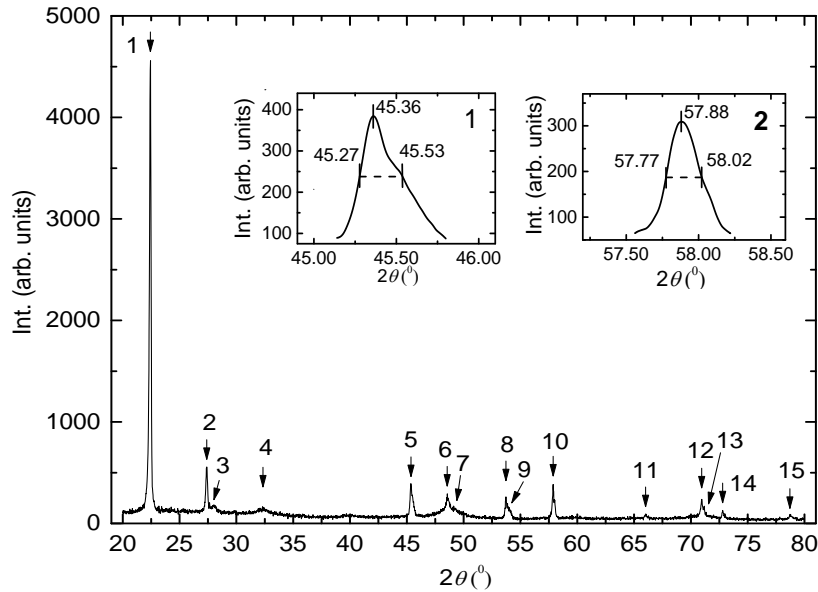
Fig. 2. X-ray diffraction pattern of the composite obtained by Zn-vapor heat treatment of the GaSe plates at 833 K for 24 h. Inset 1 shows the XRD line contour with $2\theta = 45.36°$ from the planes with Miller indexes (2 2 0) of the ZnSe lattice. Inset 2 shows the XRD line contour with $2\theta = 57.88°$ from the planes with Miller indexes (2 0 2) of the GaSe lattice.

It is evident from Fig. 2 that the XRD patterns of the composite (24-h heat treatment of GaSe plates in Zn vapors at 833 K) contains, in addition to characteristic lines of GaSe, a series of supplementary reflections, which are listed in Table 2.

Fig. 2 and Table 2 suggest that the supplementary XRD lines can be attributed to the (1 1 1), (2 2 0), (3 1 1), and (3 3 1) lattice planes of ZnSe formed by reaction of Zn atoms with Se atoms from the outer atomic planes of Se–Ga–Ga–Se packages. The (3 1 1) and (3 3 1) lines display a relatively wide contour (Fig. 2, insets 1 and 2), which indicates small sizes of the diffracting crystallites.

Crystallite mean size (*D*) was estimated by means of the Debye–Scherrer formula [12]

$$d = \frac{0.94\,\lambda}{\beta\,\cos\theta} \tag{1}$$

where λ is X-ray wavelength, θ represents the Bragg diffraction angle, and β denotes the angular full width at half maximum (FWHM) intensity. For $\beta = 4.55 \times 10^{-3}$ and $2\theta = 45.36°$, from the above formula, an average ZnSe crystallite size of ~45 nm was found. By using the same relation for the line located at $2\theta = 57.88°$, a value of ~63 nm is obtained for the crystallite size of GaSe from the composite.

Microcrystallites on the outer surface of the ZnSe–GaSe composite act as light diffusion centers, which do not allow direct measurement of linear reflectance and optical transmittance of the composite plates.

The spectral dependence of absorption coefficient for the ZnSe–GaSe composite plates was determined from diffuse reflection measurements using the Kubelka –Munk function [13]:

$$F(R_\infty) = \frac{\alpha}{S} = \frac{(1 - R_\infty)^2}{2R_\infty} \tag{2}$$

where α is the absorption coefficient, S is the light diffusion coefficient (depends on wavelength and size of diffusing particles), and R_∞ is the diffuse reflection coefficient.

The optical transition type and associated band gap of the semiconductor material can be determined via analyzing the following function [14]:

$$(F(R_\infty) \cdot \mathrm{hv})^2 = \left(\mathrm{hv} - E_g\right)^n \tag{3}$$

where $n = 2$ and $1/2$ for indirect and direct allowed optical transitions, respectively.

Table 2 Structural parameters of GaSe plate, heat treated for 24 h in Zn vapors, at 833 K.

	Experimental Values		ICDD-JCPDS cards				
No.	2θ (°)	I (a. u.)	PDF	2θ (°)	I	$h\,k\,l$	Compound
1	22.44	4558	PDF 811971	22.338	99.9	0 0 6	GaSe
2	27.38	556	PCPDFWINv.2.3	27.223	100	1 1 1	ZnSe
3	28.02	182	PDF 781927	28.013	6.5	1 0 1	GaSe
4	32.34	160	PDF 370931	32.328	5	1 0 3	GaSe
5	45.36	392	PCPDFWINv.2.3	45.231	7.0	2 2 0	ZnSe
6	48.56	292	PDF 370931	48.583	17	1 1 0	GaSe
7	49.12	172					
8	53.72	262	PCPDFWINv.2.3	53.645	44	3 1 1	ZnSe
9	53.86	194	PDF 781927	53.969	28.0	1 1 4	GaSe
10	57.88	384	PDF 811971	57.725	4.8	2 0 2	GaSe
11	66.02	94					
12	70.96	238	PDF 781927	70.961	7.4	1 0 11	GaSe
13	71.18	170	PDF 370931	71.088	17	0 0 12	GaSe
14	72.80	128	PCPDFWINv.2.3	72.731	13	3 3 1	ZnSe
15	78.72	90	PDF 811971	78.722	3.2	1 2 2	GaSe

Fig. 3 shows the $(F(R_\infty) \cdot \mathrm{hv})^2$ dependence on the photon energy for the as prepared composite.

It is evident from this figure that two linear portions are clearly pronounced: one is located in the region of 1.9−2.2 eV, while the other lies in a range of 2.5−3.0 eV.

By extrapolating these linear parts to $(F(R_\infty) \cdot \mathrm{hv}) = 0$, the optical band gap of semiconductor material for respective spectral domains can be determined according to Eq. (3); in this way, a value of 1.99 eV, which corresponds to GaSe single crystals, and 2.56 eV, which is in good agreement with the band gap of ZnSe in thin films [15, 16], have been found.
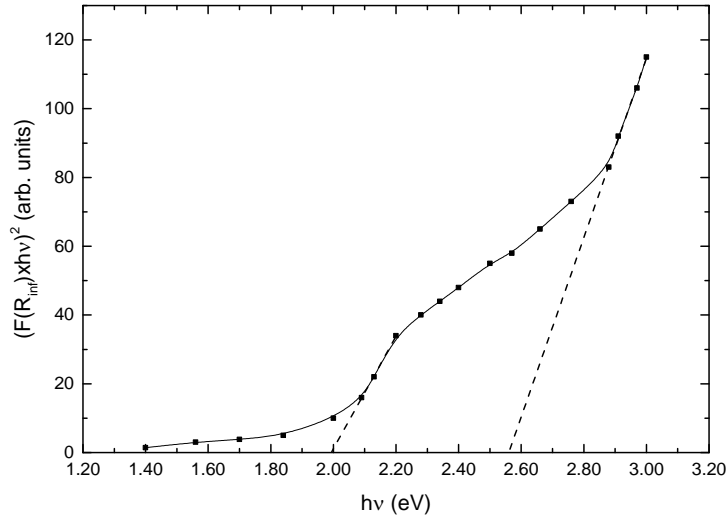
Fig. 3. $(F(R_\infty) \cdot \mathbf{hv})^2$ dependence on photon energy for the as prepared composite material.

Fig. 4 shows the PL spectrum recorded at $T = 80$ K from the (0001) surface of the heat-treated GaSe single-crystal plate.
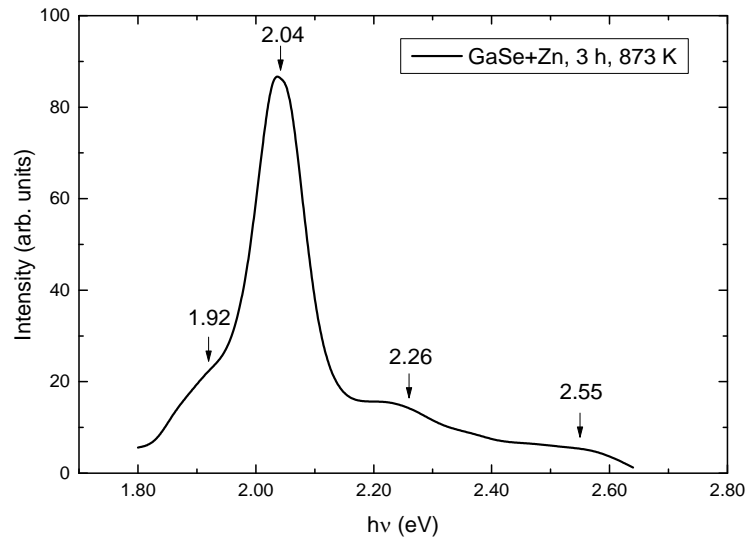
Fig. 4. PL spectrum recorded at 80 K from the (0 0 0 1) GaSe surface heat-treated in Zn vapors at 873 K for 3 h.

It is known that the PL spectrum recorded at 80 K corresponding to the (0 0 0 1) natural surface of GaSe single crystals contains the emission line of bound direct excitons, with a maximum at 2.098 eV, and two low intensity emission bands of indirect excitons, at 2.04 eV, as well as phononic repetitions of the bound exciton lines [17, 18].

At the same time, (Zn, Cd) doping concentrations up to 0.5 at % are known to produce PL quenching and create PL impurity bands in a photon energy region of 1.25−1.80 eV [19−21].

It is evident from Fig. 4 that the PL spectrum from the (0 0 0 1) surface of the GaSe plates covers a wide range of photon energies, from 1.80 eV to 2.64 eV, with a predominant maximum at 2.04 eV and three low intensity bands localized at 1.92, 2.26, and 2.55 eV. This structure can

be explained if we assume that a polycrystalline ZnSe layer is formed at the surface of the heat-treated GaSe plate in Zn vapors, which is capable of producing a PL emission. Taking into account that the energy gap of ZnSe at 78 K is $E_g = 2.812$ eV, from the PL spectrum (Fig. 4), it can be assumed that the PL emission of the ZnSe layer formed on the GaSe surface is determined by deep recombination levels. The PL bands with a maximum at 2.26 eV (green) and 2.042 eV (orange) are well known as characteristic emission bands of ZnSe single crystals at 78 K.

Fig. 4 shows that the PL spectrum is dominated by the emission band with a maximum at 2.042 eV, which is considered [22, 23] as a self-activated band. In this spectral region, a low intensity emission band of GaSe indirect excitons is also present [17], which is preceded by an intense PL band of direct localized excitons, with a maximum at 2.098 eV. The absence of a direct exciton emission line in the composite material (Fig. 4) indicates the presence of structural defects in GaSe crystals from the composite, which effectively shield the electron−hole bonds. It is evident from Fig. 4 that FWHM of the PL band with a maximum at 2.042 eV is ~0.12 eV; therefore, it *cannot* be associated with the excitonic emission in GaSe crystals from the composite.

It is also known that low Cu and Cd impurity concentrations (≤0.01at %) in GaSe lead to the formation of a PL band at 1.90 eV, which allows us to state that the impurity PL band with a maximum at 1.92 eV can be attributed to the luminescent emission of the ZnSe−GaSe composite.

4. Conclusions

Heat treatment of single crystalline GaSe plates in Zn vapors leads to the formation of a ZnSe layer on the outer surface of GaSe, while Zn intercalated atoms between the Se atomic planes of layered Se−Ga−Ga−Se packages give rise to nanocrystalline ZnSe layers inside the GaSe plates.

GaSe and ZnSe micro- and nanocrystallites act as light diffusion centers for the spectral region from the vicinity of the fundamental absorption threshold of these materials. The absorption spectrum from this spectral range was calculated using the empiric Kubelka-Munk formula. Analysis of the absorption spectrum of the composite reveals two major contributions— of the ZnSe ($E_g = 2.56$ eV) and GaSe ($E_g = 1.99$ eV) crystallites—at room temperature.

The PL spectrum of the ZnSe−GaSe composite surface is determined by the luminescent emission of the ZnSe layer from the outer surface of plates, in which, together with characteristic ZnSe bands (2.26 and 2.042 eV), an impurity band of the GaSe crystals with a maximum at 1.92 eV is observed.

References

[1] A. Castellano, Appl. Phys. Lett. 48 (4), 298 (1986).
[2] E. Bringuier, A. Bourdon, N. Piccioli, and A. Chevy, Phys. Rev. B 49, 16971, (1994).
[3] Ch. Ferrer-Roca, J. Bouvier, A. Segura, M. V. Andrés, and V. Muñoz, J. Appl. Phys. 85 (7), 3780, (1999).
[4] L. Yan-Zhao, W. Xin-Bing, M. Liang, Z. Du-Luo, and C. Zu-Hai, Chin. Phys. Lett. 28 (3), 034201 (2011).
[5] Y. Depeursinge, Il NuovoCimentoB 64 (1), 111, (1981).
[6] F. O. Ivashchishin and I. I. Grygorchak, Phys. Solid State 52 (10), 2026, (2010).
[7] Z. D. Kovalyuk, V. B. Boledzyuk, V. V. Shevchyk, V. M. Kaminskii, and A. D. Shevchenko,

Semiconductors 46 (8), 971, (2012).

[8] C. M. Julien and M. Balkanski, Mater. Sci. Eng. B 100 (3), 263, (2003).

[9] C. M. Julien, Mater. Sci. Eng. R 40 (2), 47, (2003).

[10 Z. D. Kovalyuk, M. M. Pyrlya, and V. B. Boledzyuk, J. Optoelectron. Adv. Mater. 5(4), 869, (2003).

[11] V. P. Savchyn and V. B. Kytsai, Thin Solid Films, 361–362, 123, (2000).

[12] W.-.F. Wu and B.-S. Chiou, Thin Solid Films, 298, 221, (1997).

[13] S. I. Boldish and W. B. White, Am. Mineral. 83, 865, (1998).

[14] J. Tauc, Amorphous and Liquid Semiconductors, Plenum, New Zork, 1974 (Chapter 4).

[15] R. Le Toullec, N. Piccioli, M. Mejatty, and M. Balkanski, Nuovo Cimento 38B, 159, (1977).

[16] R.K. Swank, Phys. Rev. 153, 844, (1967).

[17] V. Capozzi, Phys. Rev. B 28(8), 4620, (1983).

[18] V. Capozzi and A. Minafra, J. Phys. C: Solid State Phys. 14, 4335, (1981).

[19] S. Shigetomi, T. Ikari, and H. Nakashima, J. Appl. Phys. 74, 4125, (1993).

[20] S. Shigetomi, T. Ikari, and H. Nakashima, Phys. Stat. Sol. (a), 160, 159, (1997).

[21] S. Shigetomi, T. Ikari, and H. Nishimura, J. Appl. Phys. 69, 7936, (1991).

[22] G. B. Stringfellow and R.H. Bube, Phys. Rev. 171, 903, (1968).

[23] S. Iida, J. Phys. Soc. Jpn. 25 (1), 177, (1968).

NANOWIRE-BASED ELECTRONIC AND OPTOELECTRONIC DEVICES

Iu. Dubcovetchi

Free International University of Moldova, Vlaicu Parcalab str. 52, Chisinau, MD-2012
Republic of Moldova

Abstract

A brief review of nanowires used in electronic and optoelectronic devices that could enable diverse applications is given. Nanowire field-effect transistors, nanowire lasers, as well as crossed nanowire structures and nanowire heterostructures, are discussed. Due to the possibility of controlling the key parameters (chemical composition, structure, size, doping, etc.) on a nanoscale, these devices exhibit new or enhanced functions crucial to many areas of technology.

1. Semiconductor nanowires

There is growing interest in the development of nanoscale devices that could enable new functions and/or greatly enhanced performance. Semiconductor nanowires are a powerful class of materials that, through controlled growth and organization, are opening up substantial opportunities for nanoscale electronic and optoelectronic devices [1].

Semiconductor nanowires [2], nanocrystals [3], and carbon nanotubes [4] offer many opportunities for the assembly of nanoscale devices. The rational control of key nanomaterial parameters, such as chemical composition, structure, size, and doping is central to implement applications on a nanoscale. These parameters determine the electronic and optoelectronic properties of device function. Moreover, semiconductor nanowires represent a nanomaterial system where these key parameters have been best controlled to date.

Another critical point in the development of nanowire building blocks is the recently demonstrated controlled growth of axial and radial heterostructures [5], where the composition and/or doping is modulated down to the atomic level along or perpendicular to the axes of nanowires, respectively. The ability to prepare controlled and diverse axial and radial heterostructures sets nanowires apart from other nanomaterials, such as carbon nanotubes, and, as discussed below, represents a substantial advantage for the development of increasingly powerful and unique nanoscale electronic and optoelectronic devices crucial to future applications.

2. Nanowire field-effect transistors

Investigations of nanowire field-effect transistors show that theirs performance level can be compared with respective planar devices [1]. Studies have also demonstrated the high electron mobility of epitaxial InAs nanowire field-effect transistors with a wrap-around gate structure. This conclusion is significant since the nanowire field-effect transistors are fabricated using unconventional methods, which opens up opportunities that are not possible in areas with conventional single-crystal wafer-based electronics and optoelectronics.

In addition, nanowire field-effect transistors can be used as extremely powerful sensors for ultrasensitive detection of biological and chemical species [6]. Binding to the surface of an

nanowire field-effect transistor is analogous to applying a gate voltage, which leads to the depletion or accumulation of carriers which led to a change in the nanowire conductance.

3. Crossed nanowire structures

Nanowire building blocks and device architectures can open up new opportunities in electronics and optoelectronics. For example, crossed nanowire field-effect transistors can be configured from one nanowire as the active channel and another crossed nanowire as the gate electrode separated by a thin SiO_2 dielectric shell on the Si nanowire surface [1]. This concept has been first demonstrated using Si nanowires as the channel and GaN nanowires as the gate electrodes for NOR logic-gate structures (Fig. 1a) [7].   The idea of crossed nanowires demonstrates a general approach for uniquely addressing a large array of nanowire devices. Selective chemical modification is used to differentiate specific cross points in a four-by-four crossed Si nanowire field-effect transistor array (Fig. 1b), which allow selecting the necessary address of the four individual outputs (Fig. 1c). Thus, crossed nanowire arrays can serve as the basis for addressable integrated nanosystems.
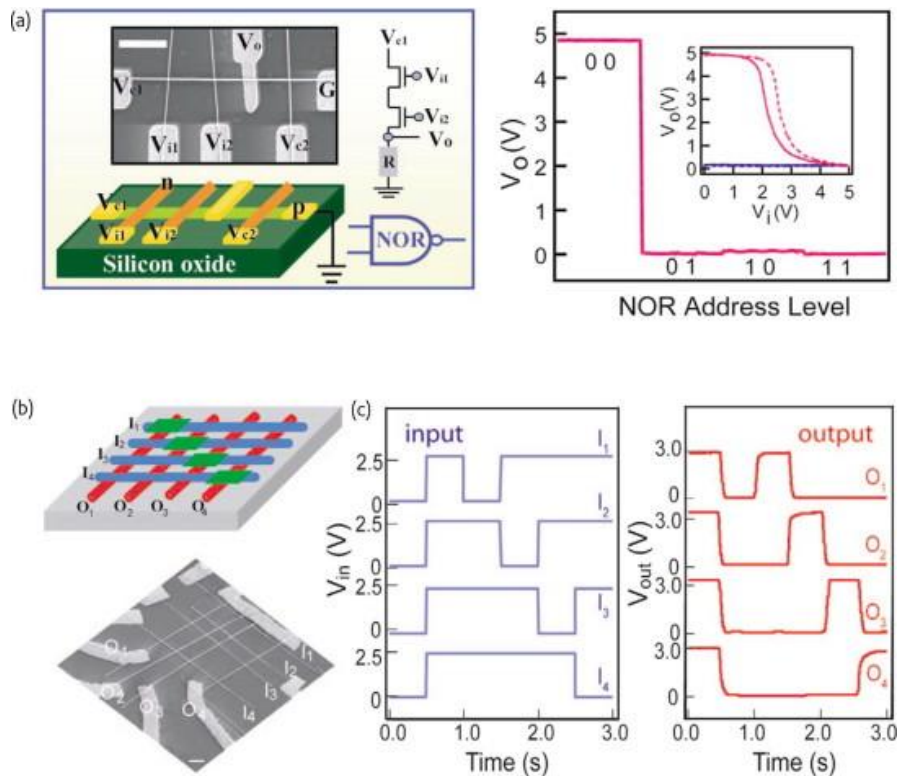
Fig. 1. Crossed nanowire electronic devices.

The crossed nanowire concept has also been used to create nanoscale *p-n* diodes by crossing *p-* and *n*-type nanowires [7]. It is significant that the capability to assemble a wide range of different *n*-type direct band-gap nanowires, including GaN (ultraviolet), CdS (green), and

CdSe (near infrared), with *p*-type Si nanowires can simplify the design of multicolor light-emitting diodes on a single substrate which is not possible with planar technology. Crossed nanowire *p-n* junctions can also be configured as photodetectors critical for integrated photonics.

4. Nanowire heterostructures

The cylindrical symmetry of nanowires permits two types of heterostructure: axial and radial (Fig. 2). Varying the composition and/or doping during axial elongation, we can obtain axial junctions with a controlled nanoscale device function without the need for lithography. A representative example is a GaAs/GaP compositionally modulated axial heterostructures [8]. These nanowire heterostructures can emit light and be used as light-emitting diodes.

Radial composition and doping modulation in nanowire structures represent another approach for enhancing performance through synthesis versus lithography [5]. Radial heterostructure nanowires are also known as core−shell nanowires. The radial nanowire concept also offers substantial opportunities for nanowire optoelectronics since the required *n*- and *p*-type active materials can be incorporated as a core and a shell, which enables carrier injection or collection over a much larger area than in crossed nanowire devices.
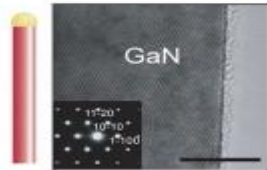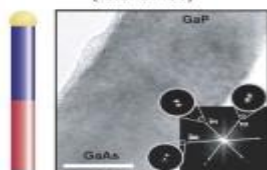
	Group IV	Group III/V	Group II/VI
Homogeneous Structure (refs. 18, 21-36)	Si Si:B (p-type) Si:P (n-type) Ge Ge:B (p-type) Ge:P (n-type) Si_xGe_{1-x}	GaN GaN:Mg (p-type) GaN:Si (n-type) GaN:Mn GaP InP InP:Zn (p-type) InP:Te (n-type) GaAs InAs $GaAs_yP_{1-y}$ $InAs_yP_{1-y}$	ZnS ZnS:Mn CdS CdS:Mn ZnSe CdSe
Axial Heterostructure (refs. 37-39)	n-Si/p-Si n-Si/i-Si/p-Si $(n-Si/n^+-Si)_n$ Si/NiSi	$(GaAs/GaP)_n$ n-InP/p-InP	
Radial Heterostructure (refs. 40-46)	i-Si/p-Si Si/Ge Ge/Si Si/SiO_2 Si/Ge/Si $i-Si/SiO_x/p-Si$ $p-Si/i-Ge/SiO_x/p-Ge$	n-GaN/InGaN/p-GaN n-GaN/InGaN/p-AlGaN/p-GaN n-GaN/(InGaN MQW)/p-AlGaN/p-GaN GaN/AlN/AlGaN	CdS/CdSe Si/CdS

Fig. 2. Semiconductor nanowires and nanowire heterostructures.

5. Nanowire lasers

About 15 years ago, the authors of [9] first introduced the idea of semiconductor nanowire nanolasers. Using ZnO nanowires as a model system, it has been shown that lasing is possible for nanostructures with subwavelength cross sections. Later, the idea was applied to various semiconductors with different emission wavelengths covering from ultraviolet all the way to infrared. The development of a nanoscopic coherent light source with an extremely small footprint has many important implications. It can be used in integrated photonic circuits, in miniaturized sensor platforms with low-power consumption, and as imaging probes with high spatial resolution. These lasing studies on one-dimensional nanoscale cavities have led to recent efforts on plasmonic assisted nanowires where optical modes can be further compressed at the metal-semiconductor interface, and nanoscopic lasers with all three dimensions less than one wavelength are well on the horizon.

6. Conclusions

It has been shown that semiconductor nanowires offer many opportunities for the assembly of nanoscale electronic and optoelectronic devices. Central point for progress in the field is control of key nanowire parameters during growth, including chemical composition, structure, size, morphology, and doping, since it is these parameters that determine the predictable device function. The examples described here illustrate advantages of nanowires in electronics and optoelectronics compared with conventional technologies. Continued advances in capability of controlling the structural/compositional complexity of nanowires during growth, which accordingly determines the functional complexity of the building blocks, together with advances in organizing them into larger integrated arrays, will lead to increasingly unique nanoelectronic and optoelectronic circuits and systems that will create the technologies of the future.

References

[1] Y. Li et al., Mater. Today, 9 (10), 18, (2006).
[2] L. Samuelson, Mater. Today, 6 (10), 22, (2003).
[3] X. Wang *et al.,* Nature, 437, 121, (2005).
[4] Z. Yao *et al.,* Carbon Nanotubes: Synthesis, Structure, Properties and Applications, Springer, New York (2000).
[5] H. J. Joyce et al., Prog. Quantum Electron. 35, 23, (2011).
[6] F. Patolsky and C.M. Lieber, Mater. Today, 8 (4), 20, (2005).
[7] Y. Huang et al., Science 294, 1313, (2001).
[8] M. Gudiksen et al., Nature 415, 617, (2002).
[9] P. Yang, R. Yan, and M. Fardy, Nano Lett. 10, 1529, (2010).

TWO-DIMENSIONAL CAVITY POLARITONS UNDER THE INFLUENCE OF STRONG PERPENDICULAR MAGNETIC AND ELECTRIC FIELDS

S. A. Moskalenko[1], I. V. Podlesny[1], E. V. Dumanov[1,2], L. Shutova[1], and I. Leleacov[1]

[1]*Institute of Applied Physics, Academy of Sciences of Moldova, Academiei str.5, Chisinau, MD-2028 Republic of Moldova*
[2]*Technical University of Moldova, bd. Stefan cel Mare 168, Chisinau, MD-2004 Republic of Moldova*

Abstract

The properties of two-dimensional (2D) cavity polaritons subjected to the action of strong perpendicular magnetic and electric fields giving rise to the Landau quantization (LQ) of the 2D electrons and holes accompanied by the Rashba spin-orbit coupling (RSOC) and by the Zeeman splitting (ZS) have been investigated. A strong magnetic field, where the electron and the hole cyclotron energy frequencies are greater than the binding energy of the 2D Wannier-Mott excitons, completely reconstructs it transforming into a magnetoexciton, the structure of which is determined by the Lorentz force rather than by the Coulomb electron−hole (e−h) interaction.

We predict drastic changes in the optical properties of the cavity polaritons including those in the state of Bose-Einstein condensation. The main of them is the existence of a multitude of the polariton energy levels closely adjacent on the energy scale, their origin being related with the LQ of the electrons and holes. Most of these levels exhibit nonmonotonous dependences on magnetic field strength B with overlapping and intersections. More so, the selection rules for the band-to-band optical quantum transitions, as well as the quantum transitions from the ground state of the crystal to the magnetoexciton states, essentially depend on numbers n_e and n_h of the LQ levels of the e−h pair forming the magnetoexciton. By slowly changing the external magnetic and electric fields, it is possible to change the lowest polariton energy level, its oscillator strength, the probability of the quantum transition, and the Rabi frequency of the polariton dispersion law. They depend on the relation between numbers n_e and n_h and can lead to dipole-active, quadrupole-active, or forbidden optical transitions. Our results are based on the exact solutions for the eigenfunctions and the eigenvalues of the Pauli-type Hamilonian with third order chirality terms and a nonparabolic dispersion law for heavy-holes and with first order chirality terms for electrons. They were obtained using the method proposed by Rashba [1].

We expect that these results will also determine the collective behavior of the cavity polaritons, for example, in the GaAs-type quantum wells embedded into a microcavity, which have recently revealed the phenomenon of the Bose-Einstein condensation in the state of the thermodynamic quasi-equilibrium but in the absence of a strong perpendicular magnetic field.

1. Introduction

The aim of this study is to determine the properties of the two-dimensional (2D) polaritons arising in the frame of a quantum well (QW) embedded into a microcavity and

subjected to the action of a strong perpendicular magnetic field, giving rise to the Landau quantization (LQ) of the 2D electrons and holes accompanied by the Rashba spin−orbit coupling (RSOC) and Zeeman splitting (ZS) effect. In the case of free electron−hole (e−h) pairs and a band-to-band quantum transition, the magnetic and electric fields with arbitrary intensities were considered; these aspects are discussed in the second section of this paper. The properties of 2D magnetoexcitons are investigated under the condition of a strong magnetic field when cyclotron energies frequencies ω_{ci} with $i = e, h$ are greater than the binding energy of the 2D Wannier−Mott excitons and magnetic length l_0 is smaller than the exciton Bohr radius. The binding energy of the 2D magnetoexcitons is obtainer taking into account the ionization potential determined by the Coulomb interaction in the frame of the e−h pair.

      In section two of our paper, the wave functions and the energy levels of the 2D electrons and heavy-holes are discussed. The calculations of the electron−electron Coulomb interaction are conducted in the third section using the spinor-type conduction and valence electron wave functions describing the LQ accompanied by the RSOC and by the ZS effects. The magnetoexciton energy levels arising from different combinations of the electron and hole states are investigated.

      The fourth section is focused on the electron−radiation interaction in the frame of the e−h system confined on the 2D layer and the electromagnetic field arbitrarily propagating in the three-dimensional (3D) space as regards the 2D layer. The corresponding Hamiltonian describing the magnetoexciton-photon interaction is deduced. The formation of magnetoexciton-polaritons in a microcavity is discussed. It is the main goal of our paper. The conclusions are made in the fifth section.

2. 2D electrons and holes under the influence of the perpendicular magnetic and electric fields.

      The Hamiltonians describing the LQ, RSOC, and ZS effect involving 2D electrons and holes were deduced in [1−6]. They have the form

$$H_e = \hbar \omega_{ce} \left\{ \left(a^+ a + \frac{1}{2} \right) \hat{I} + i\sqrt{2}\,\alpha \begin{vmatrix} 0 & a \\ -a^+ & 0 \end{vmatrix} + Z_e \hat{\sigma}_z \right\}$$

$$H_h = \hbar \omega_{ch} \left\{ \left[\left(a^+ a + \frac{1}{2} \right) + \delta \left(a^+ a + \frac{1}{2} \right)^2 \right] \hat{I} + i2\sqrt{2}\,\beta \begin{vmatrix} 0 & (a^+)^3 \\ -(a)^3 & 0 \end{vmatrix} - Z_n \hat{\sigma}_z \right\}$$

$$\tag{1}$$

      Here, Bose-type operators a^+, a generating Fock states $|m\rangle$ were introduced and the following notation was used:

$$Z_i = \frac{g_i \mu_B B}{2 \hbar \omega_{ci}} = \frac{g_i m_i}{4 m_0}, \quad \omega_{ci} = \frac{eB}{m_i c}, \quad i = e, h.$$

$$\hat{I} = \begin{Vmatrix} 1 & 0 \\ 0 & 1 \end{Vmatrix}, \quad \hat{\sigma}_z = \begin{Vmatrix} 1 & 0 \\ 0 & -1 \end{Vmatrix}, \quad \mu_B = \frac{e\hbar}{2 m_0 c}, \quad e = |e| > 0.$$

$$\alpha = \frac{8 \cdot 10^{-3} x}{\sqrt{y}}, \quad \beta = 1.062 \cdot 10^{-2} x \sqrt{y},$$

$$\delta = 10^{-4} C x y, \quad B = y \, \mathrm{T}, \quad E_z = x \frac{\mathrm{kV}}{\mathrm{cm}}$$

(2)

where ω_{ci} are the cyclotron frequencies, z_i are the Zeeman parameters proportional to g-factors g_i and to effective masses m_i of the electrons and holes, whereas m_0 is the bare electron mass; δ is the nonparabolicity (NP) of the heavy-hole dispersion law, α and β are the parameters of the chirality terms, which are of the first order in the case of electrons [1] and of the third order in the case of heavy holes [7−8].

The solutions of these equations were chosen in the dimensionless forms. For the electron case, we have

$$\mathscr{H}_e = \frac{H_e}{\hbar \omega_{ce}}; \quad \mathscr{H}_e |\psi_e\rangle = \varepsilon |\psi_e\rangle; \quad |\psi_e\rangle = \begin{Vmatrix} |f_1\rangle \\ |f_2\rangle \end{Vmatrix}$$

(3)

$$|f_1\rangle = \sum_n a_n |n\rangle; \quad |f_2\rangle = \sum_n b_n |n\rangle; \quad \sum_n |a_n|^2 + \sum_n |b_n|^2 = 1$$

In the coordinate representation, the wave functions are as follows:

$$\left| \psi_m^{\pm}(\vec{r}) \right\rangle = \frac{e^{ipx}}{\sqrt{L_x}} \begin{Vmatrix} a_m^{\pm} \varphi_m(\eta) \\ b_{m+1}^{\pm} \varphi_{m+1}(\eta) \end{Vmatrix}; \quad \eta = \frac{y}{l} - pl$$

(4)

where L_x is the length of the layer. These states were obtained firstly by Rashba [1] and are repeated here including Zeeman coefficient z_e.

Along with the solutions $|\psi_m^{\pm}\rangle$ with $m \geq 0$, there exists another solution with $b_0 = 1$ of the type

$$\varepsilon_0 = \frac{1}{2} - Z_e; \quad |\psi_0\rangle = \begin{Vmatrix} 0 \\ 0 \end{Vmatrix}; \quad |\psi_0(\vec{r})\rangle = \frac{e^{ipx}}{\sqrt{L_x}} \begin{Vmatrix} 0 \\ \varphi_0(\eta) \end{Vmatrix}$$

(5)

which is orthogonal to any solutions (4).
In energy units, the energy spectrum is as follows:

$$E_m^{\pm} = \hbar \omega_{ce} \varepsilon_m^{\pm}, \quad m \geq 0,$$

$$E_0 = \hbar \omega_{ce} \varepsilon_0$$

(6)

Below, we will consider only two lowest Landau levels (LLs) for conduction electrons, namely state $|\psi_0^-\rangle$ (4) and $|\psi_0\rangle$ (5).

The heavy-hole Hamiltonian in a dimensionless form has the form

$$\mathcal{H} = \frac{H_h}{\hbar \omega_{ch}} = \left\{ \left[\left(a^+ a + \frac{1}{2} \right) + \delta \left(a^+ a + \frac{1}{2} \right)^2 \right] \hat{I} + i 2\sqrt{2}\beta + \begin{vmatrix} 0 & (a^+)^3 \\ -(a)^3 & 0 \end{vmatrix} - Z_h \hat{\sigma}_z \right\};$$

$$\mathcal{H} \left| \psi \right\rangle = \varepsilon \left| \psi \right\rangle$$

$$\left| \psi \right\rangle = \begin{Vmatrix} f_1 \\ f_2 \end{Vmatrix}; \quad \left| f_1 \right\rangle = \sum_{n \geq 0} c_n \left| n \right\rangle; \quad \left| f_2 \right\rangle = \sum_{n \geq 0} d_n \left| n \right\rangle$$

(7)

The respective wave functions have the form

$$\left| \psi_m^{\pm} \right\rangle = \begin{vmatrix} c_m^{\pm} \left| m \right\rangle \\ d_{m-3}^{\pm} \left| m-3 \right\rangle \end{vmatrix}, \quad \left| \psi_m^{\pm}(\vec{r}) \right\rangle = \frac{e^{iqx}}{\sqrt{L_x}} \begin{vmatrix} c_m^{\pm} \varphi_m(\eta) \\ d_{m-3}^{\pm} \varphi_{m-3}(\eta) \end{vmatrix},$$

(8)

$$\eta = \frac{y}{l} + q l, \quad m \geq 3.$$

They obey the normalization and orthogonality   conditions

$$\left\langle \psi_m^{\pm} \middle| \psi_m^{\pm} \right\rangle = \left| c_m^{\pm} \right|^2 + \left| d_{m-3}^{\pm} \right|^2 = 1, \quad \left\langle \psi_m^{+} \middle| \psi_m^{-} \right\rangle = c_m^{+*} c_m^{-} + d_{m-3}^{+*} d_{m-3}^{-} = 0$$

(9)

Along with solutions (8), there exist three other solutions with $m = 0, 1, 2$. They are:

$$c_0 = 1, \quad \left| \psi_0 \right\rangle = \begin{vmatrix} 0 \\ 0 \end{vmatrix}, \quad \left| \psi_0(\vec{r}) \right\rangle = \frac{e^{iqx}}{\sqrt{L_x}} \begin{vmatrix} \varphi_0(\eta) \\ 0 \end{vmatrix},$$

$$\varepsilon_0 = \frac{1}{2} + \frac{\delta}{4} - Z_h,$$

$$c_1 = 1, \quad \left| \psi_1 \right\rangle = \begin{vmatrix} 1 \\ 0 \end{vmatrix}, \quad \left| \psi_1(\vec{r}) \right\rangle = \frac{e^{iqx}}{\sqrt{L_x}} \begin{vmatrix} \varphi_1(\eta) \\ 0 \end{vmatrix},$$

(10)

$$\varepsilon_1 = \frac{3}{2} + \frac{9}{4}\delta - Z_h,$$

$$c_2 = 1, \quad \left| \psi_2 \right\rangle = \begin{vmatrix} 2 \\ 0 \end{vmatrix}, \quad \psi_2(\vec{r}) = \frac{e^{iqx}}{\sqrt{L_x}} \begin{vmatrix} \varphi_2(\eta) \\ 0 \end{vmatrix},$$

$$\varepsilon_2 = \frac{5}{2} + \frac{25}{4}\delta - Z_h$$

All of them are orthogonal to previous solutions (8).

3. The Coulomb electron−electron interaction and magnetoexcitons

The three LLLs for 2D heavy-holes (h, R_j) with $j = 1, 2, 3$ were combined with two LLLs for 2D conduction electrons (e, R_i) with $i = 1, 2$ giving rise to six 2D magnetoexciton states F_n with $n = 1, 2 \ldots 6$ [3, 4]. To calculate their ionization potentials, the Hamiltonian of the Coulomb electron−electron interaction under the conditions of LQ, RRSOC, and ZS is required. It was deduced in [3, 4] taking into account only the first two conditions, namely LQ and RSOC. Below, we will generalize those results adding the third condition, namely the ZS effects. The more so, it can be done because the Pauli Hamiltonians containing the Zeeman effects are represented by

operators $\pm g_i \dfrac{\mu_B B}{2} \hat{\sigma}_z$, where $\hat{\sigma}_z$ have only diagonal matrix elements. For the electron–hole (e–h) pair in the concrete combination (R_i, ε_m^-) the Hamiltonian of the Coulomb interaction has the form

$$
\begin{aligned}
H_{coul}\left(R_i, \varepsilon_m^-\right) &= \frac{1}{2} \sum_a \left\{ W_{e-e}\left(\vec{R}_i; \vec{Q}\right)\left[\hat{\rho}_e\left(R_i; \vec{Q}\right)\hat{\rho}_e\left(R_i, -\vec{Q}\right) - \hat{N}_e\left(R_i\right)\right] \right. \\
&+ W_{h-h}\left(\varepsilon_m^-; \vec{Q}\right)\left[\hat{\rho}_h\left(M_h, \varepsilon_m^-; \vec{Q}\right)\hat{\rho}_h\left(M_h, \varepsilon_m^-; \vec{Q}\right) - \hat{N}_h\left(M_h, \varepsilon_m^-\right)\right] \\
&\left. - 2W_{e-h}\left(R_i, \varepsilon_m^-; \vec{Q}\right)\hat{\rho}_e\left(R_i; \vec{Q}\right)\hat{\rho}_h\left(M_h, \varepsilon_m^-; -\vec{Q}\right)\right\}
\end{aligned}
$$

(11)

Here, the electron and hole density operators are:

$$
\hat{\rho}_e\left(R_i; \vec{Q}\right) = \sum_t e^{iQ_y t l_0^2} a^+_{R_i, t + \frac{Q_x}{2}} a_{R_i, t - \frac{Q_x}{2}}
$$

$$
\hat{\rho}_h\left(M_h, \varepsilon_m^-; \vec{Q}\right) = \sum_t e^{-iQ_y t l_0^2} b^+_{M_h, \varepsilon_m^-, t + \frac{Q_x}{2}} b_{M_h, \varepsilon_m^-, t - \frac{Q_x}{2}}
$$

(12)

$$
\hat{N}_e\left(R_i\right) = \hat{\rho}_e\left(R_i, 0\right); \quad \hat{N}_h\left(M_h, \varepsilon_m^-\right) = \hat{\rho}_h\left(M_h, \varepsilon_m^-; 0\right)
$$

Coefficients $W_{i-j}(Q)$ in the case of the electron state R_1 described by formula (4) with coefficients a_0^- and b_1^- and the hole states (M_h, ε_m^-) were deduced in [4]:

$$
W_{e-e}\left(\vec{R}_1; Q\right) = W(Q)\left(\left|a_0^-\right|^2 A_{0,0}\left(\vec{Q}\right) + \left|b_1^-\right|^2 A_{1,1}\left(\vec{Q}\right)\right)^2
$$

$$
W_{h-h}\left(\varepsilon_m^-; \vec{Q}\right) = W\left(\vec{Q}\right)\left(\left|d_{m-3}^-\right|^2 A_{m-3,m-3}\left(Q\right) + \left|c_m^-\right|^2 A_{m,m}\left(Q\right)\right)^2, \quad m \geq 3
$$

$$
W_{e-h}\left(R1, \varepsilon_m^-; \vec{Q}\right) = W\left(\vec{Q}\right)\left(\left|a_0^-\right|^2 A_{0,0}\left(\vec{Q}\right) + \left|b_1^-\right|^2 A_{1,1}\left(\vec{Q}\right)\right) \times
$$

$$
\times \left(\left|d_{m-3}^-\right|^2 A_{m-3,m-3}\left(\vec{Q}\right) + \left|c_m^-\right|^2 A_{m,m}\left(\vec{Q}\right)\right), \quad m \geq 3
$$

(13)

with the normalization conditions

$$
\left|a_0^-\right|^2 + \left|b_1^-\right|^2 = 1 \quad \left|d_{m-3}^-\right|^2 + \left|c_m^-\right|^2 = 1 \quad m \geq 3
$$

(14)

The first five functions $A_{m,m}\left(\vec{Q}\right)$ with $m \leq 4$ are:

$$
A_{0,0}\left(\vec{Q}\right) = 1; \quad A_{1,1}\left(\vec{Q}\right) = 1 - \frac{Q^2 l_0^2}{2},
$$

$$
A_{2,2}\left(\vec{Q}\right) = 1 - Q^2 l_0^2 + \frac{Q^4 l_0^4}{8},
$$

$$
A_{3,3}\left(\vec{Q}\right) = 1 - \frac{3}{2}Q^2 l_0^2 + \frac{3}{8}Q^4 l_0^4 - \frac{1}{48}Q^6 l_0^6,
$$

$$
A_{4,4}\left(\vec{Q}\right) = 1 - 2Q^2 l_0^2 + \frac{3}{4}Q^4 l_0^4 - \frac{Q^6 l_0^6}{12} + \frac{Q^8 l_0^8}{384}
$$

(15)

Along with the electron state R_1, we will consider state R_2 described by formulas (5).

The combination of electron state R_2 with hole states ε_m^- gives rise to the e−h states $(eR_2, h, \varepsilon_m^-)$. Coefficients $W_{i-j}(R_2, \varepsilon_m^-; \vec{Q})$ can be obtained from coefficients $W_{i-j}(R_1, \varepsilon_m^-; \vec{Q})$ putting $b_1^- = 0$ in them as follows:

$$W_{i-j}\left(R_2, \varepsilon_m^-; \vec{Q}\right) = W_{i-j}\left(R_1, \varepsilon_m^-; \vec{Q}\right)\Big|_{b_1^- = 0}, \tag{16}$$

$$i, j = e, h$$

The terms proportional to $\hat{N}_e(R_1)$ and $\hat{N}_h(M_h, \varepsilon_m^-)$ in (11) have coefficients $I_e(R_1)$ and $I_h(\varepsilon_m^-)$ describing the Coulomb self-actions of the electrons and holes. They are as follows:

$$I_e(R_1) = \frac{1}{2}\sum_Q W_{e-e}\left(R_1, \vec{Q}\right); \quad I_h\left(\varepsilon_m^-\right) = \frac{1}{2}\sum_Q W_{h-h}\left(\varepsilon_m^-; \vec{Q}\right) \tag{17}$$

$$I_s\left(R_1, \varepsilon_m^-\right) = I_e(R_1) + I_h\left(\varepsilon_m^-\right)$$

To determine the binding energy of the magnetoexciton, its wave functions $\left|\psi_{ex}\left(F_i, \vec{K}\right)\right\rangle$ were obtained acting on vacuum state $|0\rangle$ by magnetoexciton creation operator $\psi_{ex}^\dagger(k_{||}, M_h, R_i, \varepsilon)$ constructed from electron and hole creation operators $a_{R_i,t}^\dagger$ and $b_{M_h, \varepsilon, t}^\dagger$, respectively, as follows:

$$\psi_{ex}^\dagger\left(\vec{k}_{//}, R_i, M_h, \varepsilon\right) = \frac{1}{\sqrt{N}}\sum_t e^{ik_y t l_0^2} a_{R_i, t + \frac{k_x}{2}}^\dagger b_{M_h, \varepsilon; -t + \frac{k_x}{2}}^\dagger, \tag{18}$$

$$\left|\psi_{ex}\left(R_i; M_h, \varepsilon; \vec{k}_{//}\right)\right\rangle = \psi_{ex}^\dagger\left(\vec{k}_{//}, R_i, M_h, \varepsilon\right)|0\rangle$$

The vacuum state is determined by the equalities

$$a_{\xi, t}|0\rangle = b_{\xi, t}|0\rangle = 0. \tag{19}$$

Below, a concrete composition $F_i = \left(R_1, M_h, \varepsilon_m^-\right)$ with $m \geq 3$ of the electron and hole states will be considered.

The binding energy of the magnetoexciton is determined by the diagonal matrix element of Hamiltonian (11) calculated with wave function $\left|\psi_{ex}\left(F_i, \vec{k}\right)\right\rangle$:

$$\left\langle\psi_{ex}\left(F_i, \vec{k}\right)\left|H_{coul}\right|\psi_{ex}\left(F_i, \vec{k}\right)\right\rangle = -I_{ex}(F_i) + E\left(F_i, \vec{k}\right)$$

$$I_{ex}(F_i) = I_{ex}\left(R_1, \varepsilon_m^-\right) = \sum_Q W_{e-h}\left(R_1; \varepsilon_m^-; \vec{Q}\right)$$

$$E\left(F_i, \vec{k}\right) = E\left(R_1; \varepsilon_m^-; \vec{k}\right) = 2\sum_Q W_{e-h}\left(R_1; \varepsilon_m^-; \vec{Q}\right)\sin^2\left(\frac{\left[\vec{k}\times\vec{Q}\right]_z l_0^2}{2}\right) \tag{20}$$

$$\lim_{k\to\infty} E\left(R_1; \varepsilon_m^-; \vec{k}\right) = I_{ex}\left(R_1; \varepsilon_m^-\right)$$

The binding energy of the magnetoexciton and its ionization potential, which has the opposite sign as compared with the binding energy, tend to zero if the wave vector k tends to infinity and the magnetoexciton is transformed into a free e−h pair.

4. Interaction of magnetoexcitons with the electromagnetic radiation and the formation of cavity polaritons

In [9−12], the Hamiltonians describing, using different approximations, the electron-radiation interaction in the system of two-dimensional coplanar electrons and holes accumulated in the semiconductor QW and subjected to the action of a strong perpendicular magnetic field giving rise to the LQ of their energy levels were deduced. Only the case of the interband optical quantum transitions with the creation or annihilation of one electron−hole pair in [9-12] was considered. The intraband quantum transitions were discussed in [13]. In [9], the exciton-cyclotron resonance and the optical orientation phenomena [14] arising under the influence of the circularly polarized laser radiation were studied without taking into account the RSOC. The Hamiltonian deduced in [9] in the e−h representation was transcribed in [10] so as to describe the magnetoexciton-photon interaction for the light arbitrarily propagating in the three-dimensional (3D) space as well as being confined in the microcavity. The dispersion law of the magnetoexciton-polariton in a microcavity was deduced. The dependence of the Rabi frequency on the magnetic field strength and the selection rule concerning the numbers of the LQ levels of the e−h pair engaged in the dipole-active and quadrupole-active transitions were determined [10]. The influence on the optical properties of the magnetoexcitons on the band-to-band quantum transitions of the RSOC arising due to the action of a supplementary electric field perpendicular to the plane of the QW was investigated in [3, 4, 11, 12]. The third order chirality terms in Hamiltonian (1) of the heavy hole induced by the electric field obliged one to introduce an additional NP term of the same origin in the heavy-hole dispersion law. The NP term, together with the chirality terms, essentially changes the dependence of the energy levels on the magnetic field strength. The role of the NP term is to prevent the unlimited deep penetration of the energy levels of the 2D heavy-hole, as well as of the e−h pair and the magnetoexciton, inside the energy band gap and contribute to the stability of the semiconductor band structure. In [3, 4, 11, 12], the effects related with the ZS were not discussed. This shortage is pieced out below. We will discuss the properties of magnetoexcitons and magnetoexciton polaritons taking into account the influence of a full set of four factors, such as LQ, RSOC, ZS, and NP. The Hamiltonian describing the magnetoexciton−photon interaction including the ZS effects has exactly the same form as in [11] with only one difference that coefficients a_0^-, b_1^-, c_m^-, and d_{m-3}^- with $m \geq 3$ must be determined in [13] by the expressions containing nonzero Zeeman coefficients z_e and z_h. In previous papers [3, 4, 11, 12], these coefficients were absent.

Following formula (41) of [11], the Hamiltonian of the magnetoexciton−photon interaction has the form

$$
\hat{H}_{e-rad} = \left(-\frac{e}{m_0 l_0}\right)_- \sum_{k(k_\parallel,k_z)} \sum_{M_h=\pm1} \sum_{i=1,2} \sum_{\varepsilon=\varepsilon_m,\varepsilon_m^-} \sqrt{\frac{\hbar}{L_z \omega_k^-}} \times
$$

$$
\times \{ P_{cv}(0) T\left(R_i, \varepsilon, \vec{k}_\parallel\right) [C_{k,-}^- (\vec{\sigma}_k^+ \cdot \vec{\sigma}_{M_h}^*) + C_{k,+}^- (\vec{\sigma}_k^- \cdot \vec{\sigma}_{M_h}^*)] \hat{\Psi}_{ex}^\dagger (\vec{k}_\parallel, M_h, R_i, \varepsilon) +
$$

$$
+ P_{cv}^*(0) T^*\left(R_i, \varepsilon, \vec{k}_\parallel\right) [\left(C_{k,-}^-\right)^\dagger (\vec{\sigma}_k^- \cdot \vec{\sigma}_{M_h}) + \left(C_{k,+}^-\right)^\dagger (\vec{\sigma}_k^+ \cdot \vec{\sigma}_{M_h})] \hat{\Psi}_{ex} (\vec{k}_\parallel, M_h, R_i, \varepsilon) + \tag{21}
$$

$$
+ P_{cv}(0) T\left(R_i, \varepsilon, -\vec{k}_\parallel\right) [\left(C_{k,-}^-\right)^\dagger (\vec{\sigma}_k^- \cdot \vec{\sigma}_{M_h}^*) + \left(C_{k,+}^-\right)^\dagger (\vec{\sigma}_k^+ \cdot \vec{\sigma}_{M_h}^*)] \hat{\Psi}_{ex}^\dagger (-\vec{k}_\parallel, M_h, R_i, \varepsilon) +
$$

$$
+ P_{cv}^*(0) T^*\left(R_i, \varepsilon, -\vec{k}_\parallel\right) [C_{k,-}^- (\vec{\sigma}_k^+ \cdot \vec{\sigma}_{M_h}) + C_{k,+}^- (\vec{\sigma}_k^- \cdot \vec{\sigma}_{M_h})] \hat{\Psi}_{ex} (-\vec{k}_\parallel, M_h, R_i, \varepsilon) \}
$$

It differs from Hamiltonian (9) of [10] by the more complicate coefficients $T\left(R_i, \varepsilon, \vec{k}_{\parallel}\right)$, which in turn now contain generalized coefficients a_0^-, b_1^-, c_m^-, and d_{m-3}^- given by the expressions determined in [13].

Hamiltonian (21) contains the creation and annihilation operators of magnetoexcitons $\hat{\Psi}_{ex}^{\dagger}(k_{\parallel}, M_h, R_i, \varepsilon)$, $\hat{\Psi}_{ex}(k_{\parallel}, M_h, R_i, \varepsilon)$ and photons $C_{k,\xi}^{\dagger}$, $C_{k,\xi}$. The former were determined by formula (18) and are characterized by in-plane wave vectors $k_{\parallel}$ by orbital projection M_h of the hole state in the frame of the p-type valence band and by quantum states R_i and ε of the electron and hole under the conditions of the LQ accompanied by the RSOC, ZS, and NP. Instead of quantum number M_h, circular polarization vector $\vec{\sigma}_{M_h}$ will be introduced. The photon operators depend on wave vectors $\vec{k} = \vec{a}_3 k_z + k_{\parallel}$ arbitrary oriented in the 3D space, where $\vec{a}_3$ is an unit vector perpendicular to the layer, and on polarization label ξ, which takes two values—1 and 2—in the case of the light with linear polarizations $\vec{e}_{k,i}$ or the signs $\pm$ in the case of circular polarizations $\vec{\sigma}_k^{\pm}$. The required denotations are:

$$C_{k,\pm} = \frac{1}{\sqrt{2}}\left(C_{k,1} \pm iC_{k,2}\right), \quad \left(C_{k,\pm}\right)^{\dagger} = \frac{1}{\sqrt{2}}\left(C_{k,1}^{\dagger} \mp iC_{k,2}^{\dagger}\right),$$

$$\vec{\sigma}_k^{\pm} = \frac{1}{\sqrt{2}}\left(\vec{e}_{k,1} \pm i\vec{e}_{k,2}\right), \quad \left(\vec{e}_{k,1} \cdot \vec{k}\right) = 0, \quad i = 1, 2,$$

$$\sum_{i=1}^{2} C_{k,i} \vec{e}_{k,i} = C_{k,-} \vec{\sigma}_k^{+} + C_{k,+} \vec{\sigma}_k^{-},$$

$$\sum_{i=1}^{2} \left(C_{k,\pm}\right)^{\dagger} \vec{e}_{k,i} = \left(C_{k,-}\right)^{\dagger} \vec{\sigma}_k^{-} + \left(C_{k,+}\right)^{\dagger} \vec{\sigma}_k^{+}, \tag{22}$$

$$\vec{\sigma}_{M_h} = \frac{1}{\sqrt{2}}\left(\vec{a}_1 \pm i\vec{a}_2\right), \quad \vec{k}_{\parallel} = k_x \vec{a}_1 + k_y \vec{a}_2,$$

$$\left(\vec{\sigma}_{M_h} \cdot \vec{a}_3\right) = 0, \quad M_h = \pm 1,$$

Here $\vec{a}_1$ and $\vec{a}_2$ are the in-plane orthogonal unit vectors. The scalar products $(\vec{\sigma}_k^{\pm} \cdot \vec{\sigma}_{M_h}^{*})$ appearing in Hamiltonian (22) determine the ability of photon circular polarization $\vec{\sigma}_k^{\pm}$ to create circular polarization $\vec{\sigma}_{M_h}$ with probability $\left|(\vec{\sigma}_k^{\pm} \cdot \vec{\sigma}_{M_h}^{*})\right|^2$. It can be denoted as a geometrical selection rule. This probability is the same for any in-plane wave vector $k = k_{\parallel}$ and equals to 1/4. If incident wave vector k is perpendicular to layer $\vec{k} = \vec{a}_3 k_z$, the light with circular polarization $\vec{\sigma}_k^{\pm}$ excites the magnetoexciton with the same circular polarization $\vec{\sigma}_{M_h} = \vec{\sigma}_k^{\pm}$ with the probability equal to unity. Another spin–orbital selection rule is determined by coefficients $T\left(R_i, \varepsilon, \vec{k}_{\parallel}\right)$, which are expressed by formulas (36) of [11] as follows:

$$T\left(R_1, \varepsilon_m^-; \vec{k}_\parallel\right) = a_0^{-*} d_{m-3}^{-*} \tilde{\phi}\left(0, m-3; \vec{k}_\parallel\right) - b_1^{-*} c_m^{-*} \tilde{\phi}\left(1, m; \vec{k}_\parallel\right), \quad m \geq 3,$$

$$T\left(R_1, \varepsilon_m; \vec{k}_\parallel\right) = -b_1^{-*} \tilde{\phi}\left(1, m; \vec{k}_\parallel\right), \quad m = 0, 1, 2,$$

$$T\left(R_2, \varepsilon_m^-; \vec{k}_\parallel\right) = -c_m^{-*} \tilde{\phi}\left(0, m; \vec{k}_\parallel\right), \quad m \geq 3, \tag{23}$$

$$T\left(R_2, \varepsilon_m; \vec{k}_\parallel\right) = -\tilde{\phi}\left(0, m; \vec{k}_\parallel\right), \quad m = 0, 1, 2$$

Integrals $\tilde{\phi}\left(n_e, n_h; \vec{k}_\parallel\right)$ were introduces by formulas (32) of [11]. They have a general form and some particular values given below

$$\tilde{\phi}\left(n_e, n_h; \vec{k}_\parallel\right) = \int_{-\infty}^{\infty} dy\, \varphi_{n_e}\left(y - \frac{k_x l_0^2}{2}\right) \varphi_{n_h}\left(y + \frac{k_x l_0^2}{2}\right) e^{ik_y y},$$

$$\tilde{\phi}\left(0, 0; \vec{k}_\parallel\right) = 1 - \left(\frac{k_x^2}{2} + k_y^2\right) \frac{l_0^2}{4}, \tag{24}$$

$$\tilde{\phi}\left(0, 1; \vec{k}_\parallel\right) = \frac{\left(k_x + ik_y\right) l_0}{\sqrt{2}}$$

At point $k_\parallel = 0$, they coincide with the normalization and the orthogonality conditions for wave functions $\varphi_n(y)$, which have real values.

Integrals (24) play the role of the orbital selection rules for the quantum transitions from the ground state of the crystal to the magnetoexciton states as well as for the band-to-band optical transitions. Following them in the case of the dipole-active transitions with $k_\parallel = 0$, the selection rule is $n_e = n_h$.

The zeroth order Hamiltonian describing the free 2D magnetoexcitons, the cavity photons, and their interaction has a quadratic form and consists of three parts

$$H_2 = H_{mex}^0 + H_{ph}^0 + H_{mex-ph} \tag{25}$$

For simplicity, denotation (18) of the magnetoexciton creation operators will be shortened as follows:

$$\psi_{ex}^+\left(F_1, \vec{k}_\parallel\right) = \psi_{ex}^+\left(\vec{k}_\parallel, R_1, -1, \varepsilon_3^-\right)$$

$$\psi_{ex}^+\left(F_2, \vec{k}_\parallel\right) = \psi_{ex}^+\left(\vec{k}_\parallel, R_2, -1, \varepsilon_3^-\right)$$

$$\psi_{ex}^+\left(F_3, \vec{k}_\parallel\right) = \psi_{ex}^+\left(\vec{k}_\parallel, R_1, 1, \varepsilon_0\right)$$

$$\psi_{ex}^+\left(F_4, \vec{k}_\parallel\right) = \psi_{ex}^+\left(\vec{k}_\parallel, R_2, 1, \varepsilon_0\right) \tag{26}$$

$$\psi_{ex}^+\left(F_5, \vec{k}_\parallel\right) = \psi_{ex}^+\left(\vec{k}_\parallel, R_1, -1, \varepsilon_4^-\right)$$

$$\psi_{ex}^+\left(F_6, \vec{k}_\parallel\right) = \psi_{ex}^+\left(\vec{k}_\parallel, R_2, -1, \varepsilon_4^-\right)$$

In Hamiltonian H_2, only dipole-active magnetoexciton states F_1 and F_4 and quadrupole-active states F_3 and F_5 were included:

$$H_{mex}^{0} = \sum_{n=1,3,4,5} E_{ex}\left(F_n,\vec{k}_{\parallel}\right)\psi_{ex}^{+}\left(F_n,\vec{k}_{\parallel}\right)\psi_{ex}\left(F_n,\vec{k}_{\parallel}\right) \tag{27}$$

The remaining two states F_2 and F_6 were excluded because they are forbidden in both approximations.

The cavity photons have wave vectors $\vec{k} = \vec{a}_3 k_z + k_{\parallel}$ consisting of two parts. The longitudinal component is oriented along the axis of the resonator determined by unit vector $\vec{a}_3$ perpendicular to the surface of the QW embedded inside a microcavity. It has a well-defined value of $k_z = \pm\dfrac{\pi}{L_c}$, where L_c is the cavity length. Transverse component $\vec{k}_{\parallel} = \vec{a}_1 k_x + \vec{a}_2 k_y$ is a 2D vector oriented in-plane with respect to the QW and determined by two in-plane unit vectors $\vec{a}_1$ and $\vec{a}_2$. Vectors $\vec{\sigma}_k^{\pm}$ of the light circular polarizations can be constructed introducing two unit vectors s and t perpendicular to light wave vector k and to each other as follows:

$$\vec{\sigma}_k^{\pm} = \frac{1}{\sqrt{2}}\left(\vec{s}\pm i\vec{t}\right); \quad \vec{k} = \vec{a}_3 k_z + \vec{k}_{\parallel}; \quad k_z = \pm\frac{\pi}{L_c}$$

$$\vec{s} = \vec{a}_3 \frac{\left|\vec{k}_{\parallel}\right|}{\left|\vec{k}\right|} - \frac{\vec{k}_{\parallel}\cdot k_z}{\left|\vec{k}\right|\left|\vec{k}_{\parallel}\right|}; \quad \vec{t} = \frac{a_1 k_y - a_2 k_x}{\left|\vec{k}_{\parallel}\right|} \tag{28}$$

They obey the orthogonality and normalization conditions

$$\left(\vec{k}\cdot\vec{t}\right) = \left(\vec{s}\cdot\vec{k}\right) = \left(\vec{t}\cdot\vec{s}\right) = 0; \quad \left|\vec{s}\right| = \left|\vec{t}\right| = 1$$

$$\left(\vec{\sigma}_k^{\pm}\right)^{*} = \vec{\sigma}_k^{\mp}; \quad \left|\vec{\sigma}_k^{\pm}\right| = 1 \tag{29}$$

$$\left(\vec{\sigma}_k^{\pm}\cdot\vec{\sigma}_k^{\mp*}\right) = 0; \quad \left(\vec{\sigma}_k^{\pm}\cdot\vec{\sigma}_k^{\pm*}\right) = 1$$

and have the form

$$\vec{\sigma}_k^{\pm} = \frac{1}{\sqrt{2}\left|\vec{k}\right|\left|\vec{k}_{\parallel}\right|}\left\{\vec{a}_3\left|\vec{k}_{\parallel}\right|^2 + \vec{a}_1\left(-k_x k_z \pm i k_y\left|\vec{k}\right|\right) + \vec{a}_2\left(-k_y k_z \mp i k_x\left|\vec{k}\right|\right)\right\};$$

$$\vec{\sigma}_{\pm 1} = \frac{1}{\sqrt{2}}\left(\vec{a}_1 \pm i\vec{a}_2\right) \tag{30}$$

Here, magnetoexciton circular polarization vectors $\vec{\sigma}_{\pm 1}$ determined by formula (22) are mentioned. The required scalar products of the photon and magnetoexciton circular polarization vectors are listed below:

$$\left|\left(\vec{\sigma}_k^{\pm}\cdot\vec{\sigma}_1^{*}\right)\right|^2 = \frac{1}{2}\left(1\pm\frac{k_z}{\left|k_z\right|}\right)\left(1 - \frac{x^2}{2} + \frac{x^4}{2}\right) \mp \frac{x^4}{16}\cdot\frac{k_z}{\left|k_z\right|},$$

$$\left|\left(\vec{\sigma}_k^{\pm}\cdot\vec{\sigma}_{-1}^{*}\right)\right|^2 = \frac{1}{2}\left(1\mp\frac{k_z}{\left|k_z\right|}\right)\left(1 - \frac{x^2}{2} + \frac{x^4}{2}\right) \pm \frac{x^4}{16}\cdot\frac{k_z}{\left|k_z\right|}, \tag{31}$$

$$x^2 = \frac{\left|\vec{k}_{\parallel}\right|^2 L_c^2}{\pi^2} < 1.$$

In the case $k_z = \dfrac{\pi}{L_c} > 0$, we obtain the expression

$$\left| \left(\vec{\sigma}_k^{\pm} \cdot \vec{\sigma}_1^* \right) \right|^2 = \left| \left(\vec{\sigma}_k^{\mp} \cdot \vec{\sigma}_{-1}^* \right) \right|^2 \approx \left(1 - \frac{x^2}{2} + \frac{7}{16} x^4 \right),$$

$$\left| \left(\vec{\sigma}_k^{\pm} \cdot \vec{\sigma}_{-1}^* \right) \right|^2 = \left\| \vec{\sigma}_k^{\mp} \cdot \vec{\sigma}_1^* \right\rangle \right|^2 = \frac{x^4}{16},$$

(32)

whereas in the opposite case $k_z = -\dfrac{\pi}{L_c} < 0$ they are

$$\left| \left(\vec{\sigma}_k^{\pm} \cdot \vec{\sigma}_1^* \right) \right|^2 = \left| \left(\vec{\sigma}_k^{\mp} \cdot \vec{\sigma}_{-1}^* \right) \right|^2 = \frac{x^4}{16}$$

$$\left| \left(\vec{\sigma}_k^{\pm} \cdot \vec{\sigma}_{-1}^* \right) \right|^2 = \left| \left(\vec{\sigma}_k^{\mp} \cdot \vec{\sigma}_1^* \right) \right|^2 \approx \left(1 - \frac{x^2}{2} + \frac{7}{16} x^4 \right)$$

The zeroth order Hamiltonian of the cavity photons with wave vectors k and circular polarizations $\vec{\sigma}_k^{\pm}$ described in (28) has the form

$$H_{ph}^0 = \sum_{\vec{k}_\parallel, k_z = \pm \frac{\pi}{L_c}} \hbar \omega_k \left[\left(C_{k,+}^- \right)^+ C_{k,+}^- + \left(C_{k,-}^- \right)^+ C_{k,-}^- \right]$$

(33)

The creation and annihilation operators of the photons with circular polarizations $\vec{\sigma}_k^{\pm}$ and with linear polarizations s and t are related as follows:

$$C_{k,\pm}^- = \frac{1}{\sqrt{2}} \left(C_{k,s}^- \pm i C_{k,t}^- \right)$$

$$\left(C_{k,\pm}^- \right)^+ = \frac{1}{\sqrt{2}} \left(C_{k,s}^+ \mp i C_{k,t}^+ \right)$$

$$s C_{k,s}^- + t C_{k,t}^- = C_{k,-}^- \vec{\sigma}_k^+ + C_{k,+}^- \vec{\sigma}_k^-$$

$$s C_{k,s}^+ + t C_{k,t}^+ = \left(C_{k,-}^- \right)^+ \vec{\sigma}_k^- + \left(C_{k,+}^- \right)^+ \vec{\sigma}_k^+$$

(34)

The Hamiltonian describing the magnetoexciton–photon interaction including only the resonance terms and taking into account the two photon circular polarizations has the form

$$\begin{aligned}
H_{mex-ph} = \sum_{\vec{k}_\parallel, k_z = \pm \frac{\pi}{L_c}} & \left\{ \varphi \left(F_1, \vec{k}_\parallel \right) \left[C_{k,-}^- \left(\vec{\sigma}_k^+ \cdot \vec{\sigma}_{-1}^* \right) + C_{k,+}^- \left(\vec{\sigma}_k^- \cdot \vec{\sigma}_{-1}^* \right) \right] \psi_{ex}^+ \left(F_1, F_\parallel \right) + \right. \\
& + \varphi \left(F_4, \vec{k}_\parallel \right) \left[C_{k,-}^- \left(\vec{\sigma}_k^+ \cdot \vec{\sigma}_1^* \right) + C_{k,+}^- \left(\vec{\sigma}_k^- \cdot \vec{\sigma}_1 \right) \right] \psi_{ex}^+ \left(F_4, \vec{k}_\parallel \right) + \\
& + \varphi \left(F_3, \vec{k}_\parallel \right) \left[C_{k,-}^- \left(\vec{\sigma}_k^+ \cdot \vec{\sigma}_1^* \right) + C_{k,+}^- \left(\vec{\sigma}_k^- \cdot \vec{\sigma}_1 \right) \right] \psi_{ex}^+ \left(F_3, \vec{k}_\parallel \right) + \\
& \left. + \varphi \left(F_5, \vec{k}_\parallel \right) \left[C_{k,-}^- \left(\vec{\sigma}_k^+ \cdot \vec{\sigma}_{-1}^* \right) + C_{k,+}^- \left(\vec{\sigma}_k^- \cdot \vec{\sigma}_{-1}^* \right) \right] \psi_{ex}^+ \left(F_5, \vec{k}_\parallel \right) + H.C. \right\}
\end{aligned}$$

(35)

Coefficients $\varphi \left(F_n, k_\parallel \right)$ and their square moduli are:

$$\varphi\left(F_{1},\vec{k}_{\parallel}\right) = -\phi_{cv}a_{0}^{-*}d_{0}^{-*}; \quad \left|\varphi\left(F_{1},\vec{k}_{\parallel}\right)\right|^{2} = \left|\phi_{cv}\right|^{2}\left|a_{0}^{-}\right|^{2}\left|d_{0}^{-}\right|^{2}$$

$$\varphi\left(F_{4},\vec{k}_{\parallel}\right) = \phi_{cv}; \quad \left|\varphi\left(F_{4},\vec{k}_{\parallel}\right)\right|^{2} = \left|\phi_{cv}\right|^{2}$$

$$\varphi\left(F_{3},\vec{k}_{\parallel}\right) = \phi_{cv}b_{1}^{-*}\left(-\frac{k_{x}+ik_{y}}{\sqrt{2}}\right)l_{0}; \quad \left|\varphi\left(F_{3},\vec{k}_{\parallel}\right)\right|^{2} = \left|\phi_{cv}\right|^{2}\left|b_{1}^{-}\right|^{2}\frac{\left|\vec{k}_{\parallel}\right|^{2}l_{0}^{2}}{2} \tag{36}$$

$$\varphi\left(F_{5},\vec{k}_{\parallel}\right) = -\phi_{cv}a_{0}^{-*}d_{0}^{-*}\left(\frac{k_{x}+ik_{y}}{\sqrt{2}}\right)l_{0}; \quad \left|\varphi\left(F_{5},\vec{k}_{\parallel}\right)\right|^{2} = \left|\phi_{cv}\right|^{2}\left|a_{0}^{-}\right|^{2}\left|d_{0}^{-}\right|^{2}\cdot\frac{\left|\vec{k}_{\parallel}\right|^{2}l_{0}^{2}}{2}$$

$$\phi_{cv} = \frac{e}{m_{0}l_{0}}\sqrt{\frac{\hbar n_{c}}{\pi c}}P_{cv}(0); \quad \left|\phi_{cv}\right|^{2} = \left(\frac{\hbar n_{c}}{\pi c}\right)\left|\frac{eP_{cv}(0)}{m_{0}l_{0}}\right|^{2}; \quad f_{osc} = \left|\frac{\phi_{cv}}{\hbar\omega_{c}}\right|^{2} = \frac{\hbar n_{c}}{\pi c}\cdot\left|\frac{eP_{cv}(0)}{m_{0}l_{0}\hbar\omega_{c}}\right|^{2}$$

Below, the dimensionless value of $f_{osc} = \left|\dfrac{\phi_{cv}}{\hbar\omega_{c}}\right|^{2}$ playing the role of the oscillator strength

will be used. Looking at those expressions, one can observe that the probabilities of the dipole-active quantum transitions in magnetoexciton states F_{1} and F_{4} determined by expressions $\left|\varphi\left(F_{1},\vec{k}_{\parallel}\right)\right|^{2}$ and $\left|\varphi\left(F_{4},\vec{k}_{\parallel}\right)\right|^{2}$ are proportional to $\left|\phi_{cv}\right|^{2} \approx l_{0}^{-2} \approx B$ and exhibit an increasing linear dependence on magnetic field strength B. In contrast, the probabilities of the quadrupole-active quantum transitions in magnetoexciton states F_{3} and F_{5} are proportional to expression $\left|\phi_{cv}\right|^{2}\cdot l_{0}^{2}$, which does not depend on magnetic field strength B at all.

The equations of motion for four magnetoexciton annihilation operators $\psi_{ex}\left(F_{n},\vec{k}_{\parallel}\right)$ with $n = 1,3,4,5$ as well as for the similar photon operators $C_{\vec{k},\pm}^{-}$ under the stationary conditions have the form

$$i\hbar\frac{d}{dt}\psi_{ex}\left(F_{n},\vec{k}_{\parallel}\right) = \left[\psi_{ex}\left(F_{n},\vec{k}_{\parallel}\right),\hat{H}_{2}\right] = \hbar\omega\psi_{ex}\left(F_{n},\vec{k}_{\parallel}\right)$$

$$i\hbar\frac{d}{dt}C_{\vec{k},\pm}^{-} = \left[C_{\vec{k},\pm}^{-},\hat{H}_{2}\right] = \hbar\omega C_{\vec{k},\pm}^{-} \tag{37}$$

Their particular expressions are:

$$\left(\hbar\omega - E_{ex}\left(F_{i},\vec{k}_{\parallel}\right)\right)\psi_{ex}\left(F_{i},\vec{k}_{\parallel}\right) = \left[C_{\vec{k},-}^{-}\left(\vec{\sigma}_{k}^{\pm}\cdot\vec{\sigma}_{-1}^{*}\right) + C_{\vec{k},+}^{-}\left(\vec{\sigma}_{k}^{\mp}\cdot\vec{\sigma}_{-1}^{*}\right)\right]\varphi\left(F_{i},\vec{k}_{\parallel}\right)$$

$$i = 1,5$$

$$\left(\hbar\omega - E_{ex}\left(F_{j},\vec{k}_{\parallel}\right)\right)\psi_{ex}\left(F_{j},\vec{k}_{\parallel}\right) = \left[C_{\vec{k},-}^{-}\left(\vec{\sigma}_{k}^{\pm}\cdot\vec{\sigma}_{1}^{*}\right) + C_{\vec{k},+}^{-}\left(\vec{\sigma}_{k}^{\mp}\cdot\vec{\sigma}_{1}^{*}\right)\right]\varphi\left(F_{j},\vec{k}_{\parallel}\right)$$

$$j = 3,4 \tag{38}$$

$$\left(\hbar\omega - \hbar\omega_{k}^{-}\right)C_{\vec{k},\pm}^{-} = \left(\vec{\sigma}_{k}^{\pm}\cdot\vec{\sigma}_{-1}\right)\varphi^{*}\left(F_{1},\vec{k}_{\parallel}\right)\psi_{ex}\left(F_{1},\vec{k}_{\parallel}\right) +$$

$$+ \left(\vec{\sigma}_{k}^{\pm}\cdot\vec{\sigma}_{1}\right)\varphi^{*}\left(F_{4},\vec{k}_{\parallel}\right)\psi\left(F_{4},\vec{k}_{\parallel}\right) + \left(\vec{\sigma}_{k}^{\pm}\cdot\vec{\sigma}_{1}\right)\varphi^{*}\left(F_{3},\vec{k}_{\parallel}\right)\psi_{ex}\left(F_{3},\vec{k}_{\parallel}\right) +$$

$$+ \left(\vec{\sigma}_{k}^{\pm}\cdot\vec{\sigma}_{-1}\right)\varphi^{*}\left(F_{5},\vec{k}_{\parallel}\right)\psi_{ex}\left(F_{5},\vec{k}_{\parallel}\right)$$

Dipole-active state F_1 and quadrupole-active state F_5 can be preferentially excited by the light with circular polarization $\vec{\sigma}_k^{\,-}$ propagating with $k_z = \dfrac{\pi}{L_c} > 0$, whereas dipole-active state F_4 and the quadrupole-active state F_3 mainly react to the light with circular polarization $\vec{\sigma}_k^{\,+}$ propagating in the same direction with $k_z = \dfrac{\pi}{L_c} > 0$. In the case where Hamiltonians (33) and (35) contain photons only with one circular polarization—either $\vec{\sigma}_k^{\,+}$ or $\vec{\sigma}_k^{\,-}$ — equations (38) give rise to the relations

$$\psi\left(F_i, \vec{k}_\parallel\right) = C_{k,\pm}^{-} \frac{\left(\vec{\sigma}_k^{\,\mp} \cdot \vec{\sigma}_{-1}^{\,*}\right)\varphi\left(F_i, \vec{k}_\parallel\right)}{\hbar\omega - E_{ex}\left(F_i, \vec{k}_\parallel\right)}$$

$$i = 1, 5$$

$$\psi\left(F_j, \vec{k}_\parallel\right) = C_{k,\pm}^{-} \frac{\left(\vec{\sigma}_k^{\,\mp} \cdot \vec{\sigma}_1^{\,*}\right)\varphi\left(F_j, \vec{k}_\parallel\right)}{\hbar\omega - E_{ex}\left(F_j, \vec{k}_\parallel\right)}$$

(39)

$$j = 3, 4$$

Substituting these relations into equations of motion (38) for photon operators $C_{k,\pm}^{-}$, we will find two dispersion equations describing five branches of the energy spectrum of two different systems. One of them concerns the photons with circular polarization $\vec{\sigma}_k^{\,-}$ propagating with $k_z = \dfrac{\pi}{L_c} > 0$ and exciting mainly magnetoexciton state F_1 as well as other states F_3, F_4, F_5 with smaller oscillator strengths. The second system consists of magnetoexcitons in the same four states F_1, F_3, F_4, F_5 existing in the frame of a microcavity filled by the photons with circular polarization $\vec{\sigma}_k^{\,+}$ propagating with $k_z = \dfrac{\pi}{L_c} > 0$. These fifth order algebraic dispersion equations are

$$\left(\hbar\omega - \hbar\omega_k^{-}\right) = \frac{\left|\left(\vec{\sigma}_k^{\,\mp} \cdot \vec{\sigma}_{-1}^{\,*}\right)\right|^2 \left|\varphi\left(F_1\vec{k}_\parallel\right)\right|^2}{\hbar\omega - E_{ex}\left(F_1, \vec{k}_\parallel\right)} + \frac{\left|\left(\vec{\sigma}_k^{\,\mp} \cdot \vec{\sigma}_1^{\,*}\right)\right|^2 \left|\varphi\left(F_4, \vec{k}_\parallel\right)\right|^2}{\hbar\omega - E_{ex}\left(F_4, \vec{k}_\parallel\right)} +$$

$$+ \frac{\left|\left(\vec{\sigma}_k^{\,\mp} \cdot \vec{\sigma}_1^{\,*}\right)\right|^2 \left|\varphi\left(F_3\vec{k}_\parallel\right)\right|^2}{\hbar\omega - E_{ex}\left(F_3, \vec{k}_\parallel\right)} + \frac{\left|\left(\vec{\sigma}_k^{\,\mp} \cdot \vec{\sigma}_{-1}^{\,*}\right)\right|^2 \left|\varphi\left(F_5, \vec{k}_\parallel\right)\right|^2}{\hbar\omega - E_{ex}\left(F_5, \vec{k}_\parallel\right)}$$

(40)

They describe four magnetoexciton branches and one photon branch with a given circular polarization—either $\vec{\sigma}_k^{\,-}$ or $\vec{\sigma}_k^{\,+}$ —where the photons propagate with $k_z = \dfrac{\pi}{L_c} > 0$.

Now we will consider a particular case of cavity photons with circular polarization $\vec{\sigma}_k^{\,-}$ propagating in the direction with $\vec{k} = \dfrac{\pi}{L_c} > 0$ in the frame of a microcavity with cavity mode $\hbar\omega_c$

tuned so as to coincide with the magnetoexciton level in state F_1 with wave vector $k_{\parallel} = 0$ at a given values of magnetic field B, of the electric field E_z, with the parameter of the NP C and with g – factors g_e and g_h. In this case, we can put $\hbar \omega_c = E_{ex}(F_1, B, 0)$. To simplify the dispersion equation, we will use the dimensionless values introduced as follows:

$$\hbar \omega = \hbar \omega_c + E \atop \hbar \omega_c = E_{ex}(F_1, B, 0) ; \quad \frac{\hbar \omega}{\hbar \omega_c} = 1 + \varepsilon ; \quad \varepsilon = \frac{E}{\hbar \omega_c} = \frac{E}{E_{ex}(F_1, B, 0)} \tag{41}$$

The fifth order dispersion equation has the form

$$\left(\varepsilon - \frac{x^2}{2} \right) = \left(\frac{\hbar n_c}{\pi c} \right) \left| \frac{e P_{cv}}{m_0 l_0 E_{ex}(F_1, B, 0)} \right|^2 \times$$

$$\times \left\{ \frac{\left| a_0^- \right|^2 \left| d_0^- \right|^2 \left(1 - \frac{x^2}{2} \right)}{\left(\varepsilon - \frac{n_c^2 E_{ex}(F_1, B, 0)}{M(F_1, B) c^2} \cdot \frac{x^2}{2} \right)} + \frac{\frac{x^4}{16}}{\left(\varepsilon + 1 - \frac{E_{ex}(F_4, B, 0)}{E_{ex}(F_1, B, 0)} - \frac{n_c^2 E_{ex}(F_1, B, 0)}{M(F_4, B) c^2} \cdot \frac{x^2}{2} \right)} + \right. \tag{42}$$

$$\left. + \frac{\left| b_1^- \right|^2 \left(\frac{\pi l_0}{L_c} \right)^2 \frac{x^6}{32}}{\left(\varepsilon + 1 - \frac{E_{ex}(F_3, B, 0)}{E_{ex}(F_1, B, 0)} - \frac{n_c^2 E_{ex}(F_1, B, 0)}{M(F_3, B) c^2} \cdot \frac{x^2}{2} \right)} + \frac{\left| a_0^- \right|^2 \left| d_0^- \right|^2 \left(\frac{\pi l_0}{L_c} \right)^2 \frac{x^2}{2} \left(1 - \frac{x^2}{2} \right)}{\left(\varepsilon + 1 - \frac{E_{ex}(F_5, B, 0)}{E_{ex}(F_1, B, 0)} \right) - \frac{n_c^2 E_{ex}(F_1, B, 0)}{M(F_5, B) c^2} \cdot \frac{x^2}{2}} \right\}$$

In another special case, the cavity photons have circular polarization $\vec{\sigma}_k^+$ and propagate in the direction with $\vec{k}_z = \frac{\pi}{L_c} > 0$. Cavity mode energy $\hbar \omega_c$ is tuned to magnetoexciton energy $E_{ex}(F_4, B, 0)$. In this case, the energy is accounted from energy level $E_{ex}(F_4, B, 0)$ as follows:

$$\hbar \omega = E_{ex}(F_4, B, 0) + E ; \quad \frac{\hbar \omega}{E_{ex}(F_4, B, 0)} = 1 + \varepsilon$$

$$\varepsilon = \frac{E}{E_{ex}(F_4, B, 0)} \tag{43}$$

The dispersion equation in the dimensionless variables has the form

$$
\left(\varepsilon - \frac{x^2}{2} \right) = \left(\frac{\hbar n_c}{\pi c} \right) \left| \frac{e P_{cv}}{m_0 l_0 E_{ex}(F_4, B, 0)} \right|^2 \times
$$

$$
\left\{ \frac{\left(1 - \dfrac{x^2}{2} \right)}{\left(\varepsilon - \dfrac{n_c^2 E_{ex}(F_4, B, 0)}{M(F_4, B) c^2} \cdot \dfrac{x^2}{2} \right)} + \frac{\dfrac{x^4}{16} \left| a_0^- \right|^2 \left| d_0^- \right|^2}{\left(\varepsilon + 1 - \dfrac{E_{ex}(F_1, B, 0)}{E_{ex}(F_4, B, 0)} - \dfrac{n_c^2 E_{ex}(F_4, B, 0)}{M(F_1, B) c^2} \cdot \dfrac{x^2}{2} \right)} + \right.
$$

(44)

$$
+ \frac{\left| b_1^- \right|^2 \left(\dfrac{\pi l_0}{L_c} \right)^2 \dfrac{x^2}{2} \left(1 - \dfrac{x^2}{2} \right)}{\left(\varepsilon + 1 - \dfrac{E_{ex}(F_3, B, 0)}{E_{ex}(F_4, B, 0)} - \dfrac{n_c^2 E_{ex}(F_4, B, 0)}{M(F_3, B) c^2} \cdot \dfrac{x^2}{2} \right)} + \frac{\left| a_0^- \right|^2 \left| d_0^- \right|^2 \left(\dfrac{\pi l_0}{L_c} \right)^2 \dfrac{2 x^6}{32}}{\left(\varepsilon + 1 - \dfrac{E_{ex}(F_5, B, 0)}{E_{ex}(F_4, B, 0)} - \dfrac{n_c^2 E_{ex}(F_4, B, 0)}{M(F_5, B) c^2} \cdot \dfrac{x^2}{2} \right)} \right\}
$$

Figure 1 shows five dimensionless polariton energy branches as a function of dimensionless wave vector x in the absence of RSOC. They correspond to two different values of magnetic field strength $B = 20$ and 40 T as well as to two different values of heavy-hole g-factor $g_h = \pm 5$. The electron g-factor is assumed to be $g_e = 1$. Figures 1a and 1b suggest that a change in magnetic field strength B does not have a considerable effect on the resulting pattern. Nevertheless, it should be borne in mind that the dimensionless values of $E_p(x) / \hbar \omega_c$ were calculated with different values of cavity mode $\hbar \omega_c = E_{ex}(F_4, B, 0)$ depending on B. Figures 2 and 3 show the influence of the RSOC with third order chirality terms and NP parameter *C*. The main effect consists in the transposition of the magnetoexciton energy levels on the energy scale in comparison with their position in the absence of RSOC.
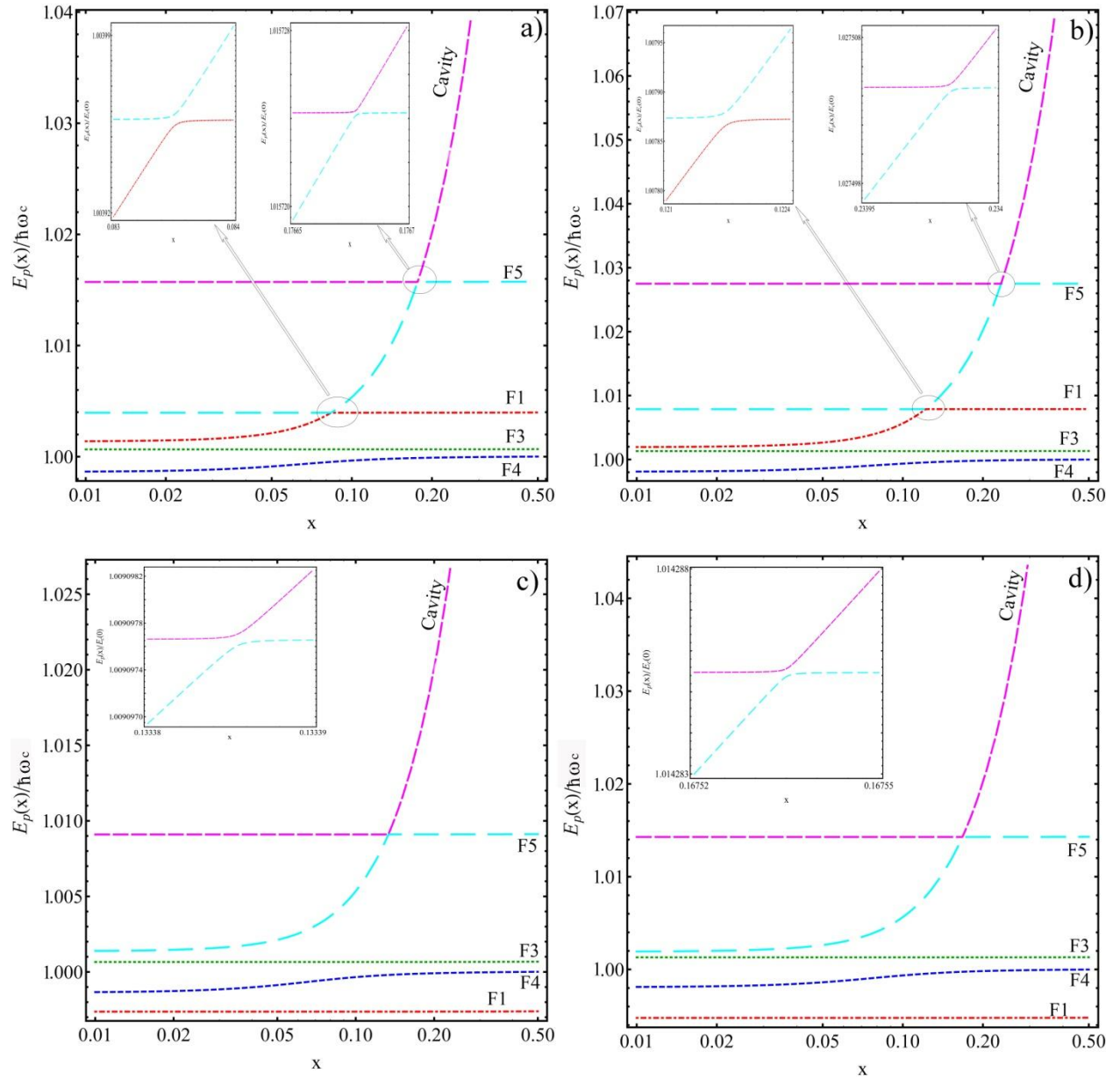
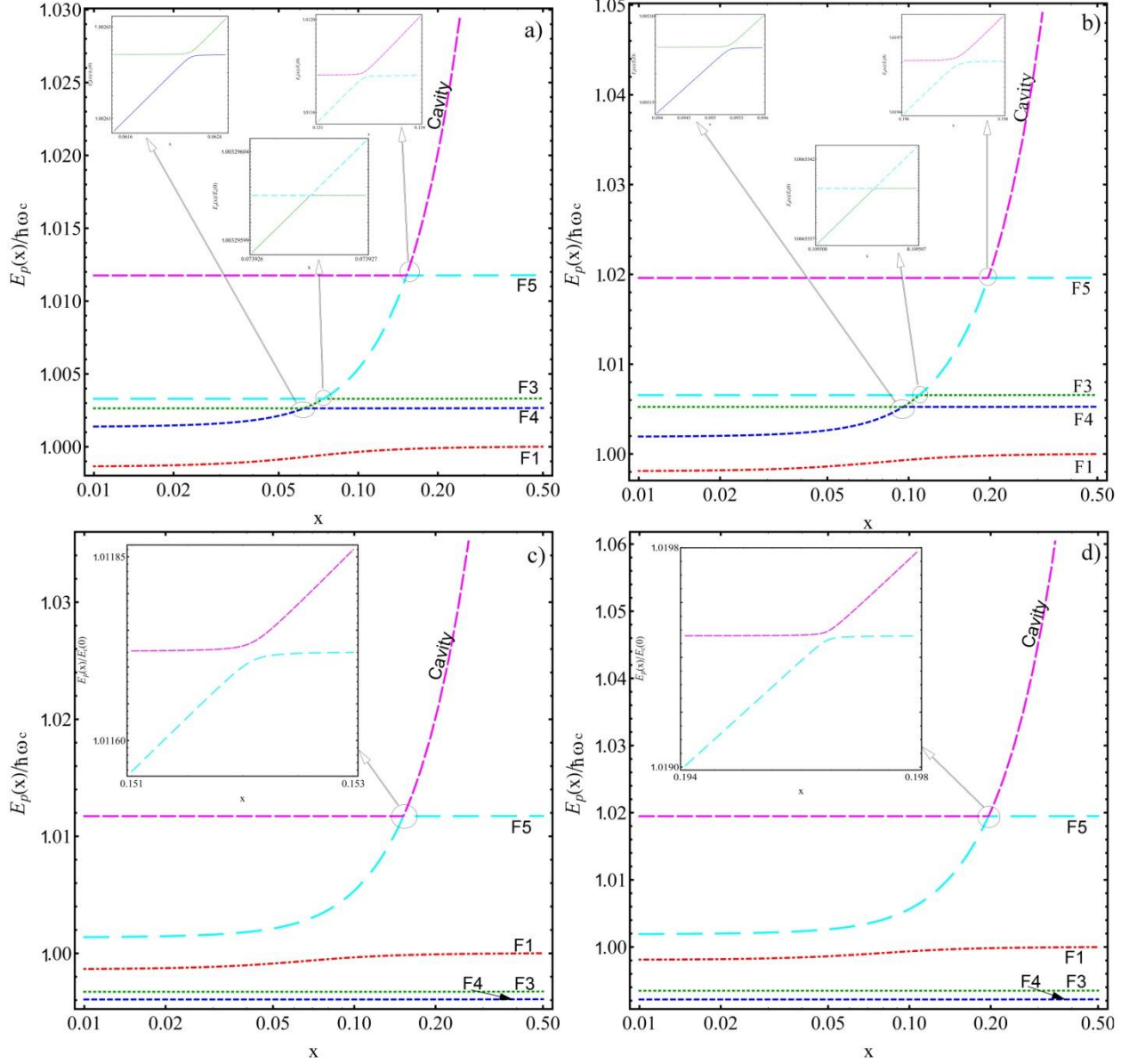**Fig. 1.** Dimensionless polariton energy branches as a function of dimensionless wave vector x in the absence of RSOC ($E_z = 0$; $C = 0$) at different values of magnetic field strength B, two values of the heavy-hole $g - factor\ g_h = \pm 5$ and at a given value of the electron g - factor $g_e = 1$, as follows: $a) B = 20$ T, $g_h = 5$; $b) B = 40$ T, $g_h = 5$; $c) B = 20$ T, $g_h = -5$; $d) B = 40$ T, $g_h = -5$. The magnetoexciton energy levels are denoted by F_1, F_3, F_4, F_5, whereas the cavity mode by Cavity $\hbar\omega_c = E_{ex}(F_4, B, 0)$.
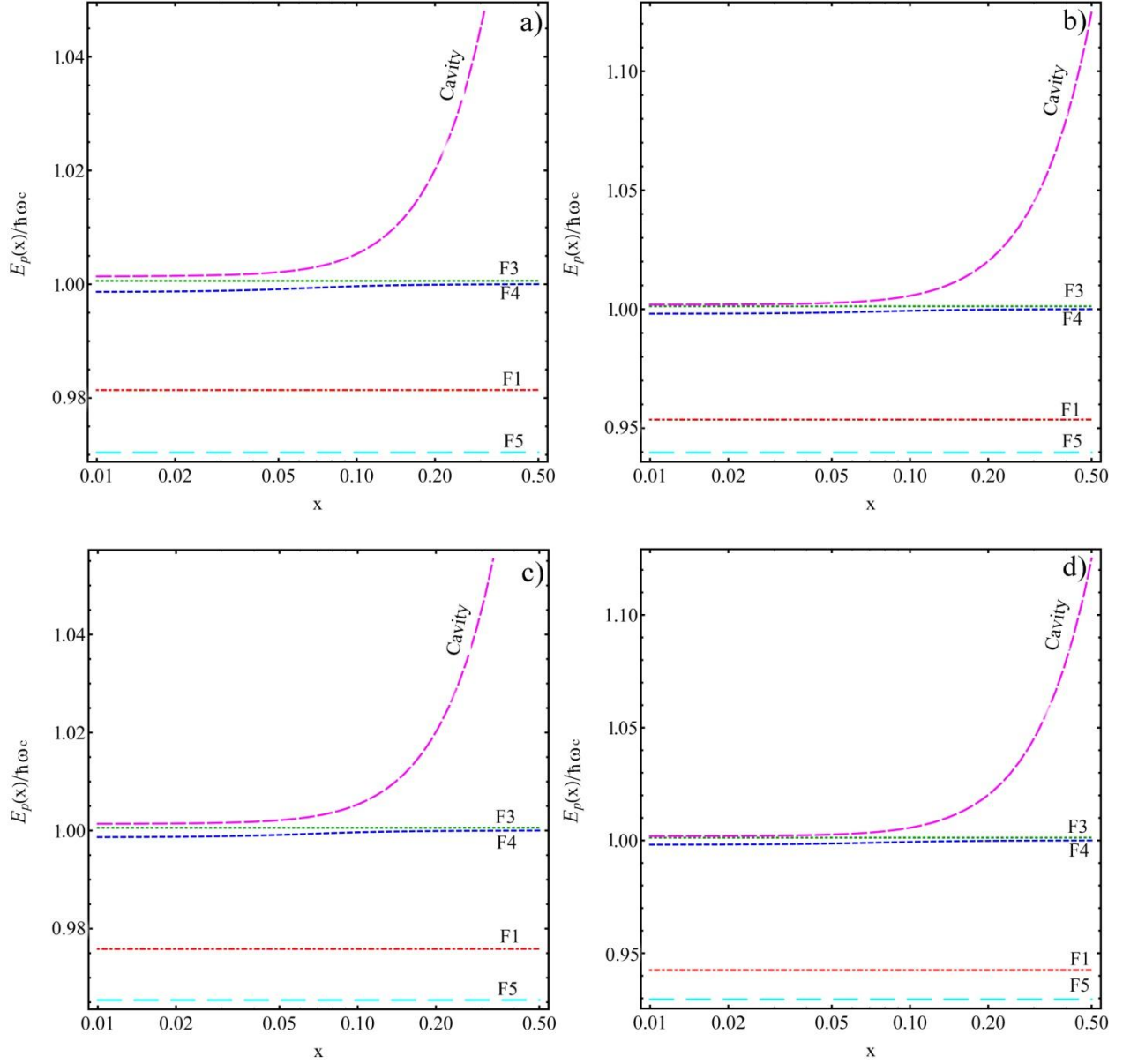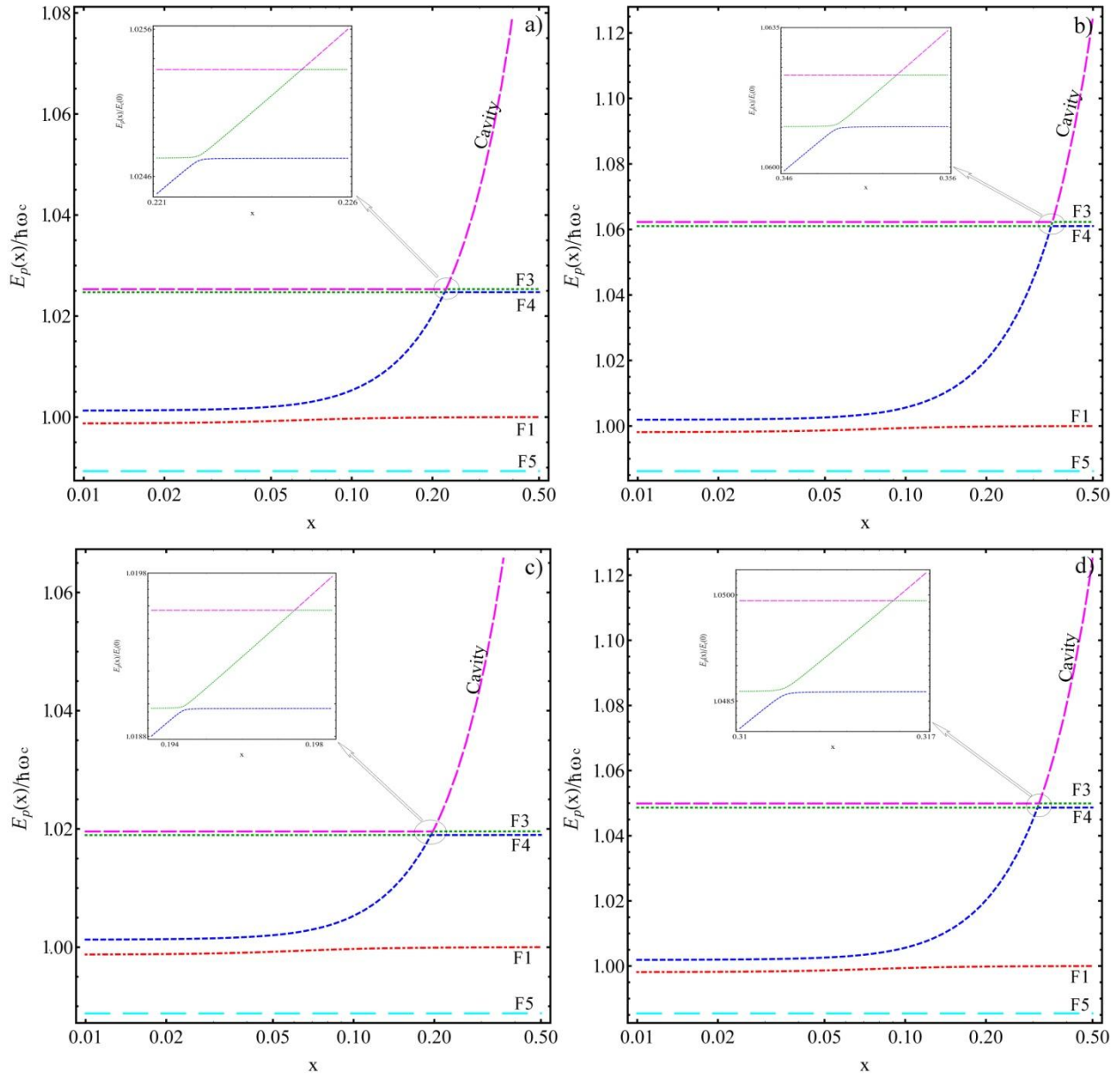
Fig. 2. Dimensionless polariton energy branches as a function of dimensionless wave vector x in the presence of the *RSOC* with electric field strength $E_z = 30 \frac{kV}{cm}$ and the parameter of the NP $C = 20$ at different values of magnetic field strength B, two values of the heavy-hole $g - factor\ g_h = \pm 5$ and electron $g - factor\ g_e = 1$, as follows: $a)\ B = 20\ T,\ g_h = 5;$ $b)\ B = 40\ T,\ g_h = 5;$ $c)\ B = 20\ T,\ g_h = -5;$ $d)\ B = 40\ T,\ and\ g_h = -5$. The magnetoexciton energy levels are denoted by F_1, F_3, F_4, F_5, whereas the cavity mode by Cavity. $^{\hbar}\omega_c = E_{ex}(F_4, B, 0)$.
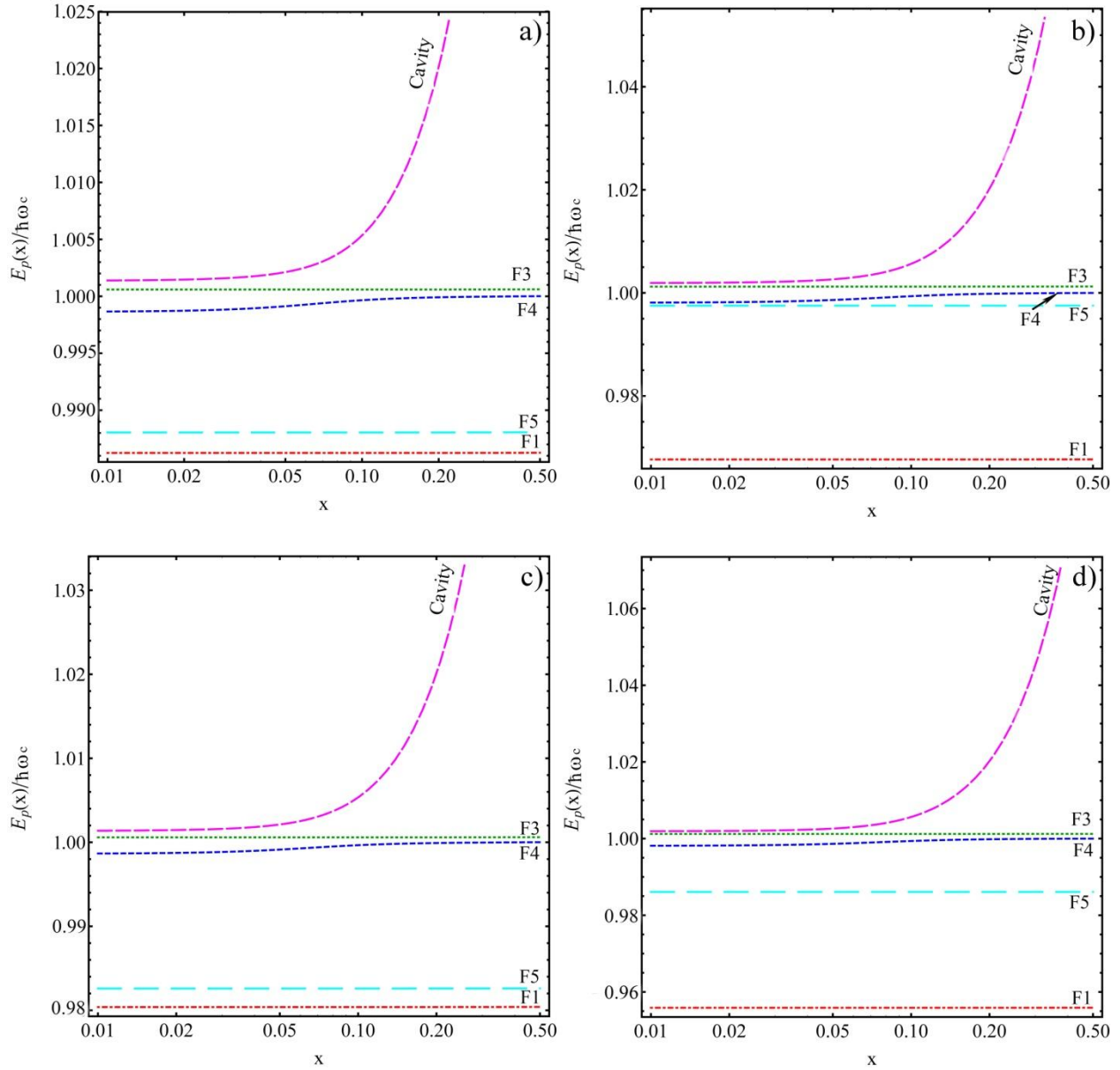
Fig. 3. Dimensionless polariton energy branches as a function of dimensionless wave vector x in the presence of the *RSOC* with electric field strength $E_z = 30 \dfrac{kV}{cm}$ and the parameter of the NP $C = 30$ at different values of magnetic field strength B, two values of the heavy-hole $g-factor\ g_h = \pm 5$ and electron $g-factor\ g_e = 1$, as follows: $a)\ B = 20\ T,\ g_h = 5;$ $b)\ B = 40\ T,\ g_h = 5;$ $c)\ B = 20\ T,\ g_h = -5;$ $d)\ B = 40\ T,\ and\ g_h = -5$. The magnetoexciton energy levels are denoted by F_1, F_3, F_4, F_5, whereas the cavity mode by Cavity. $\hbar \omega_c = E_{ex}(F_4, B, 0)$

The following three figures show the case where the cavity mode is tuned to magnetoexciton energy level $E_{ex}(F_1,B,0)$ rather than to level $E_{ex}(F_4,B,0)$ as was supposed in the previous three ones. The three variants at a given energy level $E_{ex}(F_1,B,0)$ are related with the absence (Fig. 4) and presence (Figs. 5, 6) of the RSOC with two different values of NP constant $C = 20$ and 30.

Fig. 4. Dimensionless polariton energy branches in circular polarization $\vec{\sigma}^{-}$ as a function of dimensionless wave vector x in the absence of the RSOC ($E_z = 0$, $C = 0$) at the two different values of the magnetic field strength, at two values of the heavy-hole g-factor $g_h = \pm 5$ and at a given value of the electron g-factor $g_e = 1$ as follows: (a) $B = 20$ T, $g_h = 5$; (b) $B = 40$ T, $g_h = 5$; (c) $B = 20$ T, $g_h = -5$; (d) $B = 40$ T, $g_h = -5$. The magnetoexciton energy levels are denoted by F_1, F_3, F_4, F_5, whereas the cavity mode by Cavity. $\hbar\omega_c = E_{ex}(F_1,B,0)$.

Fig. 5. Dimensionless polariton energy in circular polarization $\vec{\sigma}^{-}$ as a function of dimensionless wave vector x in the presence of the RSOC with electric field strength $E_z = 30\,kV/cm$ and the parameter of NP $C = 20$ at different values of magnetic field strength B, at two values of the heavy-hole g-factor $g_h = \pm 5$ and at the electron g-actor $g_e = 1$ as follows: (a) $B = 20$ T, $g_h = 5$; (b) $B = 40$ T, $g_h = 5$; (c) $B = 20$ T, $g_h = -5$; (d) $B = 40$ T, $g_h = -5$. The magnetoexciton energy levels are denoted by F_1, F_3, F_4, F_5, whereas the cavity mode by Cavity. $\hbar\omega_c = E_{ex}(F_1, B, 0)$.
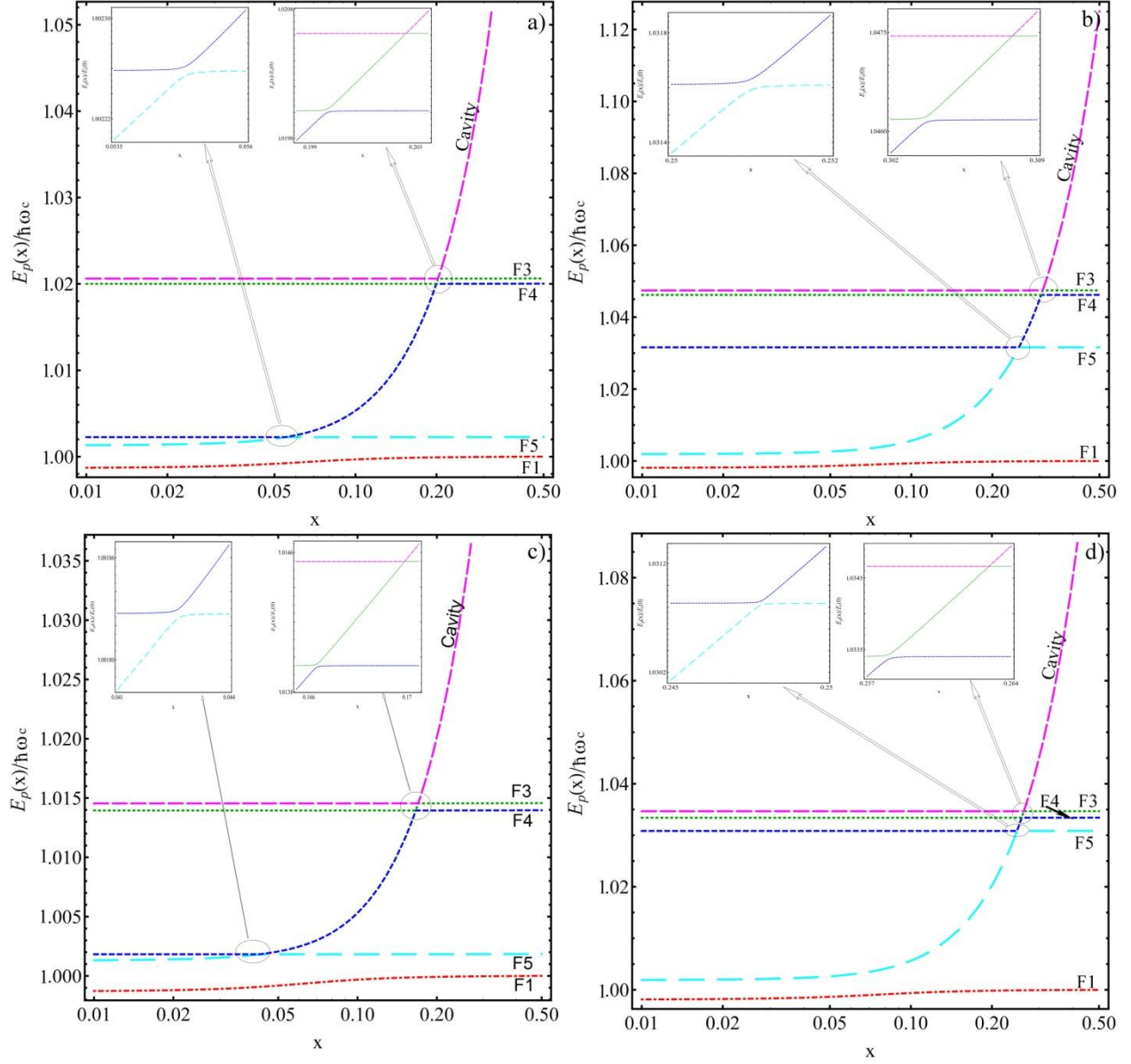
Fig. 6. Dimensionless polariton energy in circular polarization $\vec{\sigma}^{-}$ as a function of dimensionless wave vector x in the presence of the RSOC with electric field strength $E_z = 30\,kV/cm$ and the parameter of NP $C = 30$ at different values of magnetic field strength B, at two values of the heavy-hole g-factor $g_h = \pm 5$ and at the electron g-actor $g_e = 1$ as follows: (a) $B = 20$ T, $g_h = 5$; (b) $B = 40$ T, $g_h = 5$; (c) $B = 20$ T, $g_h = -5$; (d) $B = 40$ T, $g_h = -5$. The magnetoexciton energy levels are denoted by F_1, F_3, F_4, F_5, whereas the cavity mode by Cavity. $\hbar\omega_c = E_{ex}(F_1, B, 0)$.

5. Conclusions

The properties of the 2D cavity polaritons subjected to the action of strong perpendicular magnetic and electric fields have been studied. To this end, the exact solutions of the LQ of the 2D heavy-holes accompanied by the RSOC with third order chirality terms, by the ZS effects as

well as by the nonparabolicity of their dispersion law have been obtained following the method proposed by Rashba [1]. His results concerning the conduction electrons have been supplemented taking into account the ZS effects. Using the mentioned wave functions for the 2D electrons and holes, the Hamiltonians describing the Coulomb electron-electron and the electron-radiation interactions in the second quantization representation have been deduced. In turn, the electron-radiation interaction Hamiltonian has made it possible to construct another Hamiltonian describing the magnetoexciton–photon interaction and begin the development of the theory of magnetoexciton-polaritons. To do this, the wave functions of the 2D magnetoexcitons are required. The six magnetoexciton states arising due to the composition of two LLLs for conduction electrons with three LLLs for heavy-holes have been taken into consideration. Between them, two states— F_1 and F_4 —are dipole-active, other two— F_3 and F_5 —are quadrupole-active, and the last two— F_2 and F_6 —are forbidden in the inter-band optical quantum transitions as well as from the ground state of the crystal to the magnetoexciton states in the GaAs-type QWs. The dispersion equation describing the magnetoexciton-polariton energy spectrum includes the first four states F_1, F_3, F_4 and F_5 interacting with the cavity photons in two selections of the cavity mode. These four magnetoexciton degrees of freedom together with the branch of the cavity photons give rise to five order dispersion equation with five polariton-type renormalized energy branches. They are represented in six figures. Three of them show the case of cavity mode energy $\hbar\omega_c$ tuned exactly to the magnetoexciton dipole-active level energy $E_{ex}(F_4,B,0)$, whereas the other three figure show the polariton pictures where the cavity mode energy is tuned exactly to the other dipole-active magnetoexciton level energy $E_{ex}(F_1,B,0)$. In both cases, a multitude of the polariton energy branches has been obtained.

References:

[1] E. I. Rashba, Sov. Phys. Solid. State, 2, 1109, (1960)
[2] S. A. Moskalenko, I. V. Podlesny, P. I. Khadzhi, B. V. Novikov, and A. A. Kiselyov, Solid State Commun., 151, 1690, (2011)
[3] T. Hakioglu, M. A. Liberman, S. A. Moskalenko, and I. V. Podlesny, J. Phys.: Cond. Matt., 23, 345405, (2011)
[4] I. V. Podlesny, S. A. Moskalenko, T. Hakioglu, A. A. Kiselyov, and L. E. Gherciu, Physica E, 49, 44, (2013)
[5] S. A. Moskalenko, I. V. Podlesny, E. V. Dumanov, and A. A. Kiselyov, J. Nanoelectron. Optoelectron., 9, 219, (2014)
[6] S. A. Moskalenko, I. V. Podlesny, E. V. Dumanov, M. A. Liberman, and B. V. Novikov, Physica Status Solidi B (in press)
[7] R. Winkler, Spin-Orbit Coupling Effects in Two-Dimensional Electron and Hole Systems, Berlin, Springer Tracts in Modern Physics, vol. 191, (2003)
[8] T. Hakioglu and M. S. Sahin, Phys. Rev. Lett., 98, 166405 (2007)

[9] S. A. Moskalenko, M. A. Liberman, and I. V. Podlesny, Phys. Rev. B, 79(12), 125425, (2009)

[10] S. A. Moskalenko, I. V. Podlesny, M. A. Liberman, and B. V. Novikov, J. Nanophoton. 6, 061806, (2012)

[11] S. A. Moskalenko, I. V. Podlesny, E. V. Dumanov, and A. A. Kiselyov, J. Nanoelectron. Optoelectron. 9(2), 219, (2014)

[12] S. A. Moskalenko, E. V. Dumanov, I. V. Podlesny, M. A. Liberman, B. V. Novikov, S. S. Rusu, and V. M. Bajireanu, Mold. J. Phys. Sc. 13(1-2), (2014)

[13] S. A. Moskalenko, I. V. Podlesny, E. V. Dumanov, and A. A. Kiselyov, J. Nanoelectron. Optoelectron. (in press)

3D MODELING OF THE PEIERLS TRANSITION IN TTF-TCNQ ORGANIC CRYSTALS

Silvia Andronic

Technical University of Moldova, Stefan cel Mare Avenue 168, Chisinau,
MD-2004 Republic of Moldova
E-mail: andronic_silvia@yahoo.com

(Received June 29, 2015)

Abstract

The Peierls structural transition in quasi-one-dimensional (Q1D) TTF-TCNQ organic crystals of is studied in the 3D approximation. Two the most important electron–phonon interactions are considered. The analytic expression for the phonon polarization operator is obtained in the random phase approximation. The polarization operator as a function of temperature is determined for different values of dimensionless Fermi momentum k_F. Different cases are analyzed: $k_F = 0.59\pi/2$ and where the carrier concentration varies and $k_F = 0.59\pi/2 \pm \delta$, where δ represents the variation of Fermi momentum k_F. In all cases, Peierls critical temperature T_p is determined.

Introduction

Organic materials represent an important research direction, because it is assumed that they may have much better properties than inorganic materials known so far. The most extensively studied Q1D organic crystals include those of the tetrathiofulvalinium tetracyanoquinodimethane (TTF-TCNQ) type. For a complete description of the crystal model, it is necessary to determine the parameters of these crystals. In this paper, we propose to use the Peierls structural transition for this aim. According to this phenomenon, which has been theoretically predicted by Rudolf Peierls, at some lowered temperatures, the one-dimensional metallic crystal has to pass in a dielectric state. This temperature is referred to as Peierls critical temperature T_p. The Peierls transition has been studied by many authors (see [1−3] and references therein).

In previous papers [4, 5], the 1D physical model of the TTF-TCNQ crystals has been investigated. The renormalized phonon spectrum has been calculated for different temperatures in two cases: where the conduction band is half filled and the Fermi dimensionless quasi momentum $k_F = \pi/2$ and where the concentration of conduction electrons is reduced and the band is filled up to a quarter of the Brillouin zone, $k_F = \pi/4$, [5]. The Peierls critical temperature was established in the both cases.

The 2D physical model for the same crystals has been investigated in [6−8]. The polarization operator as a function of temperature was numerically calculated for different values of parameters d and δ, where d is the ratio of the electron transfer energy in the transversal direction to conductive chains to the transfer energy along the conductive chains and δ represents the increase in Fermi momentum k_F determined by an increase in the carrier concentration. In all cases, the transition temperature has been determined.

In [9], a 3D physical model of the crystal has been studied. The structural transition has

been investigated in the case where the conduction band is filled up to a quarter of the Brillouin zone and the dimensionless Fermi momentum $k_F = \pi/4$ and in the case where the carrier concentration varies and $k_F = \pi/4 \pm \delta$, where δ represents the variation in Fermi momentum k_F. The critical temperature transition has been determined.

In this paper, we also investigate the 3D physical model of the crystal, but in a more realistic aspect. Computer modeling is performed and the Peierls transition is investigated for the case where the dimensionless Fermi momentum is $k_F = 0.59\pi/2$ for different values of parameters d_1 and d_2 which represents the ratio of the transfer energy in the transversal y and z directions to the transfer energy along the x direction of conductive chains. Note that this value of k_F is estimated for real crystals of TTF-TCNQ. The polarization operator as a function of temperature is also calculated for different values of increase or decrease δ in Fermi momentum k_F determined by an increase or decrease in the carrier concentration. For a complete description, two electron-phonon interactions are considered. The first is of deformation potential type and the second one is similar to that of the polaron. The analytic expression for the phonon polarization operator is obtained in the random phase approximation. Peierls critical temperature T_p is determined for different values of dimensionless Fermi momentum $k_F \pm \delta$. The results obtained in the 3D physical model are analyzed and commented in detail.

1. Three-dimensional crystal model

The compound of TTF-TCNQ forms quasi-one-dimensional organic crystals composed of TCNQ and TTF linear segregated chains. The TCNQ molecules are strong acceptors, and the TTF molecules are donors. The conductivity of TTF chains is much lower than that of TCNQ chains, and can be neglected in the first approximation. Thus, in this approximation, the crystal is composed of strictly one-dimensional chains of TCNQ that are packed in a three-dimensional crystal structure. The crystal lattice constants are $a = 12.30$ Å, $b = 3.82$ Å, $c = 18.47$ Å, b is in the chains directions.

The Hamiltonian of the crystal was described in [6, 8] for the 2D physical model. Now it has the form:

$$H = \sum_{k} \varepsilon(k) a_k^+ a_k + \sum_{q} {}^h \omega_q b_q^+ b_q + \sum_{k,q} A(k,q) a_k^+ a_{k+q} (b_q + b_{-q}^+), \tag{1}$$

In expression (1), $\varepsilon(k)$ represents the energy of a conduction electron with 3D quasi-wave vector k and projections (k_x, k_y, k_z).

$$\varepsilon(k) = 2w_1 \cos(k_x b) + 2w_2 \cos(k_y a) + 2w_3 \cos(k_z c), \tag{2}$$

where w_1, w_2 and w_3 are the transfer energies of a carrier from one molecule to another along the chain (with lattice constant b, x direction) and in a perpendicular direction (with lattice constant a in y direction and c in z direction). In (1) a_k^+, a_k are the creation and annihilation operators of a conduction electron.

The second term in Eq. (1) is the energy of longitudinal acoustic phonons with three-dimensional wave vector q and projections (q_x, q_y, q_z) and with frequency ω_q:

$$\omega_q^2 = \omega_1^2 \sin^2(q_x b/2) + \omega_2^2 \sin^2(q_y a/2) + \omega_3^2 \sin^2(q_z c/2), \tag{3}$$

where ω_1, ω_2 and ω_3 are the limit frequencies in the x, y and z directions. In (1) b_q^+, b_q are the

creation and annihilation operators of an acoustic phonon.

The third term in Eq. (1) describes the electron-phonon interaction. It contains two important mechanisms. The first one is of the deformation potential type; it is determined by the fluctuations of energy transfer w_1, w_2 and w_3, due to the intermolecular vibrations (acoustic phonons). The coupling constants are proportional to derivatives w_1', w_2', and w_3' of w_1, w_2, and w_3 with respect to intermolecular distances, $w_1' > 0$, $w_2' > 0$, $w_3' > 0$. The second mechanism is similar to that of polaron.

The square module of matrix element of electron–phonon interaction is represented in the following form:

$$|A(k,q)|^2 = 2^{\hbar}/(NM\omega_q) \times \{ w_1'^2 [\sin(k_x b) - \sin(k_x - q_x, b) + \gamma_1 \sin(q_x b)]^2 + \tag{4}$$
$$+ w_2'^2 [\sin(k_y a) - \sin(k_y - q_y, a) + \gamma_2 \sin(q_y a)]^2 + w_3'^2 [\sin(k_z c) - \sin(k_z - q_z, c) + \gamma_3 \sin(q_z c)]^2 \},$$

In Eq. (4), M is the mass of the molecule, N is the number of molecules in the basic region of the crystal; parameters γ_1, γ_2, and γ_3 describe the ratio of amplitudes of polaron-type interaction to the deformation potential one in the *x*, *y* and *z* directions:

$$\gamma_1 = 2e^2\alpha_0 / b^5 w_1'; \gamma_2 = 2e^2\alpha_0 / a^5 w_2'; \gamma_3 = 2e^2\alpha_0 / c^5 w_3', \tag{5}$$

The analytic expression for the phonon polarization operator is obtained in the random phase approximation. The real part of the polarization operator is presented in the form:

$$\mathrm{Re}\,\overline{\Pi}(q,\Omega) = -\frac{\overline{N}}{2\pi^3 \hbar \omega_q} \int_{-\pi}^{\pi} dk_x \int_{-\pi}^{\pi} dk_y \int_{-\pi}^{\pi} dk_z \left|A(k,-q)\right|^2 \times \frac{n_k - n_{k+q}}{\varepsilon(k) - \varepsilon(k+q) + \hbar\Omega}, \tag{6}$$

Here, $\overline{N}$ is the number of elementary cells in the basic region of the crystal, $N = r\overline{N}$, where *r* is the number of molecules in the elementary cell, $r = 2$. In (6) $A(k,-q)$ is the matrix element of electron–phonon interaction presented in Eq. (2), $\varepsilon(k)$ is the carrier energy, $\hbar$ is the Planck constant, n_k is the Fermi distribution function, and $\Omega(q)$ is the renormalized phonon frequency.

The critical temperature of Peierls transition is determined from the condition that the renormalized phonon frequency $\Omega(q)$ is diminished to zero at this temperature, i.e. $\Omega(q) = 0$. It means that

$$1 - \mathrm{Re}\,\overline{\Pi}(q,\Omega) = 0. \tag{7}$$

where $\mathrm{Re}\,\overline{\Pi}(q,\Omega)$ was represented in Eq. (6).

2. Results and discussion

Expression (7) shows that the critical temperature of Peierls transition is determined when $\Omega = 0$, and $q_x = 2k_F$, $q_y = 2k_F$, $q_z = 2k_F$. The polarization operator as a function of temperature was calculated for different values of parameters d_1 and d_2, where $d_1 = w_2/w_1 = w_2'/w_1'$, and $d_2 = w_3/w_1 = w_3'/w_1'$. The polarization operator as a function of temperature was determined for different values of k_F. Different cases when

$k_F = 0.59\pi/2$ and when $k_F = 0.59\pi/2 \pm \delta$ were analyzed.

Numerical modeling was performed for the following parameters: $M = 3.74 \cdot 10^5 m_e$ (m_e is the electron rest mass), $w_1 = 0.125$ eV, $w_1' = 0.22$ eVÅ^{-1}, $a = 12.30$ Å, $b = 3.82$ Å, $c = 18.47$ Å. The sound velocity at low temperatures is $v_{s1} = 3.4 \cdot 10^5$ cm/s along chains, $v_{s2} = 5.25 \cdot 10^5$ cm/s in a direction and $v_{s3} = 5.25 \cdot 10^5$ cm/s in c direction [10]. $\gamma_1 = 1.6$, γ_2 and γ_3 are determined from the relations: $\gamma_2 = 32\gamma_1 b^5/(a^5 d_1)$ and $\gamma_3 = 32\gamma_1 b^5/(c^5 d_2)$.

Figures 1–4 show the calculation results (the polarization operator is denoted by Polar). From all figures, one can determine the transition temperatures from the intersections of the calculated curves with the horizontal line at 1.0.

Figures 1 and 2 shows the calculations for $d_1 = 0.015$ and $d_2 = 0.01$ and different values of the dimensionless Fermi momentum k_F. The solid, dashed, dotted, and dash-dotted lines correspond to $\delta = 0$ ($k_F = 0.59\pi/2$), $\delta = 0.031$ (~ 3.35 % variation of k_F), $\delta = 0.063$ (~ 6.8% variation of k_F), and $\delta = 0.094$ (~10.15% variation of k_F), respectively. Figure 1 shows the case where the Fermi momentum increase with δ, so $k_F = 0.59\pi/2 + \delta$. It is evident that T_p decreases with an increase in parameter δ. For $\delta = 0$, $T_p \sim 59$ K; for $\delta = 0.031$, $T_p \sim 43$ K; for $\delta = 0.063$, $T_p \sim 26$ K and for $\delta = 0.094$ Peierls transition does not take place.

Figure 2 shows the case where the Fermi momentum decrease with δ and $k_F = 0.59\pi/2 - \delta$. In this case, for $\delta = 0$, $T_p \sim 59$K; for $\delta = 0.031$, $T_p \sim 75$ K; for $\delta = 0.063$, $T_p \sim 93$ K and for $\delta = 0.094$, $T_p \sim 114$ K. It is observed that the Peierls critical temperature considerably increases with decreasing carrier concentration.

Figure 3 shows the case where $k_F = 0.59\pi/2$, $d_2 = 0.01$ and d_1 takes different values. The solid, dashed, dotted, and dash-dotted lines correspond to $d_1 = 0.015, 0.025,$

Fig. 1. Polarization operator as a function of temperature for different values of δ and $d_1 = 0.015$; $d_2 = 0.01$; $k_F = 0.59\pi/2 + \delta$.
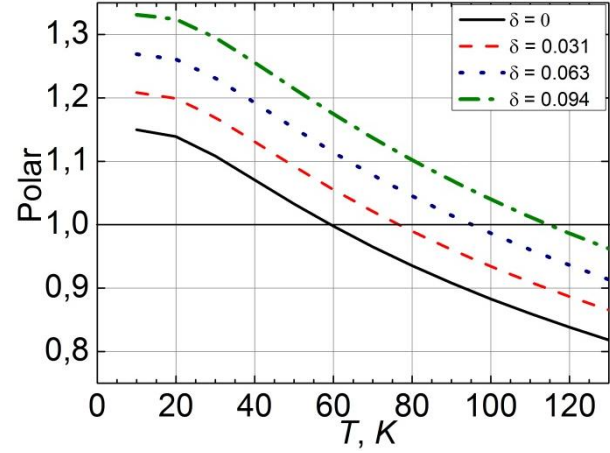

Fig. 2. Polarization operator as a function of temperature for different values of δ and $d_1 = 0.015$; $d_2 = 0.01$; $k_F = 0.59\pi/2 - \delta$.
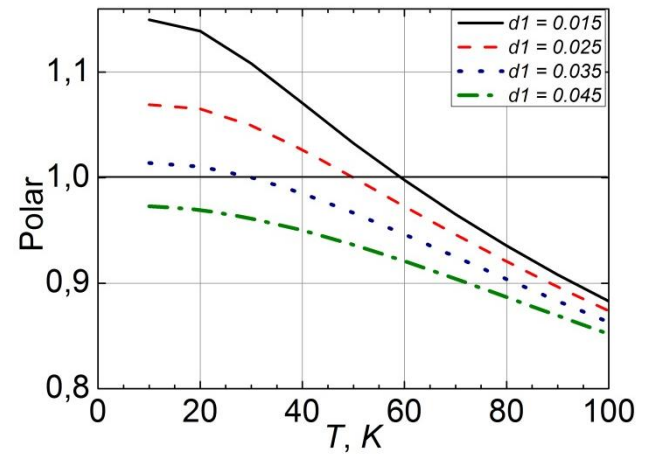

Fig. 3. Polarization operator as a function of temperature for different values of d_1 and $d_2 = 0.01$ and $k_F = 0.59\pi/2$.

0.035, and 0.045, respectively. The value $d_1 = 0.015$ is estimated for real crystals of TTF-TCNQ.

This graph shows that Tp strongly decreases with increasing parameter d_1,. For $d_1 = 0.015$, $T_p \sim 59$ K, as it was obtained experimentally. For $d_1 = 0.025$, $T_p \sim 50$ K; for $d_1 = 0.035$, $T_p \sim 30$ K; and for $d_1 = 0.045$, the Peierls transition disappears.

Figure 4 corresponds to the case where $k_F = 0.59\pi/2$ and parameters d_1 and d_2 vary. In this graph the solid, dashed, dotted, and dash-dotted lines correspond to $d_1 = 0.015$, 0.025, 0.035, and 0.045 and $d_2 = 0.01$, 0.013, 0.015, and 0.017, respectively. In this case, Tp decreases faster. For $d_1 = 0.015$ and $d_2 = 0.01$, $T_p \sim 59$ K; for $d_1 = 0.025$ and $d_2 = 0.013$, $T_p \sim 46$ K. In the other two cases, i.e., for $d_1 = 0.035$, $d_2 = 0.015$ and $d_1 = 0.045$, $d_2 = 0.017$, the Peierls transition will not take place.

Fig. 4. Polarization operator as a function of temperature for different values of d_1 and d_2 and $k_F = 0.59\pi/2$.

From Figs. 3 and 4, one can observe that even a small increase in three-dimensionality leads to a considerable decrease in the transition temperature. This feature is attributed to the fact that the Peierls structural transition is characteristic of crystals with pronounced quasi-one-dimensional properties.

4. Conclusions

The Peierls transition has been studied in quasi-one-dimensional organic crystals of the TTF-TCNQ type in the 3D approximation. The polarization operator as a function of temperature has been calculated in the random phase approximation for different values of parameters d_1 and d_2, where d_1 and d_2 are the ratio of the transfer energy in the transversal y and z directions to the transfer energy along the x direction of conductive chains. For a more complete description of the crystal model, two the most important electron–phonon interactions were considered. The first is of the deformation potential type and the second one is similar to that of a polaron. The amplitude ratios between the second and first interactions are characterized by parameters γ_1, γ_2, and γ_3, respectively. Peierls transition temperature T_p has been determined. In this paper, the behavior of Peierls structural transition where the carrier concentration varies has been studied. We have investigated the cases where the dimensionless Fermi momentum $k_F = 0.59\pi/2$ and $k_F = 0.59\pi/2 \pm \delta$, where δ represents the variation in the Fermi momentum determined by a variation in carrier concentration n. It has been established that, with an increase in carrier concentration, the T_p value decreases and vice versa.

In addition, it has been shown that, with an increase in three-dimensionality, the transition temperature considerably decreases, and for some values of parameters d_1 and d_2 the Peierls structural transition will not occur. This feature is attributed to the fact that the Peierls structural transition is characteristic only of crystals with pronounced quasi-one-dimensional properties.

References

[1] L. N. Bulaevskii, Usp. Fiz. Nauk 115, 263, (1975).

[2] M. Hohenadler, H. Fehske, and F.F. Assaad, Phys. Rev. B, 83, 115105, (2011).

[3] V. Solovyeva et al., J. Phys. D: Appl. Phys. 44, 385301, (2011).

[4] A. Casian and S. Andronic, Proc. 4th Int. Conf. on Telecommun., Electron. Inf., ICTEI 2012, vol. 1, pp. 258–261, (2012).

[5] S. Andronic and A. Casian, Mold. J. Phys. Sci. 12, 3–4, 192, (2013).

[6] S. Andronic, Mold. J. Phys. Sci. 13, 3–4, (2014).

[7] S. Andronic, A. Casian, and V. Dusciac, Abstr. 10th Int. Conf. on Phys. Adv. Mater., ICPAM-10, pp.95, (2014).

[8] S. Andronic, I. Balmus, and A. Casian, 8th Int. Conf. on Microelectron. Comp. Sci., pp. 16–19, (2014).

[9] S. Andronic, I. Balmus, and A. Casian, Proc. 5th Int. Conf. on Telecommun., Electron. Inf., ICTEI 2015, pp. 201–203, (2015).

[10] T. Tiedje and R. R. Haering, Solid State Commun., 23, 713, (1977).

LANCED MULTI-PORT ELECTRIC NETWORK AND ITS PROJECTIVE COORDINATES

A. Penin and A. Sidorenko

Gitsu Institute of Electronic Engineering and Nanotechnologies,
Academy of Sciences of Moldova
E-mails: aapenin@mail.ru; anatoli.sidorenko@kit.edu

Abstract

For an active multi-port network of direct current, as a model of distributed power supply system, the problem of recalculation of the changeable load currents is considered. Conditions of utilization of projective coordinates for the interpretation of changes or "kinematics" of regime parameters of the network are determined. Therefore, changes in regime parameters are introduced by the cross ratio of four points. Easy-to-use formulas of the recalculation of the currents, which possess the group properties at a change in the conductivity of the loads, are obtained to express the final values of currents through the intermediate changes in the load currents and conductivities. The obtained results contribute to the development of the basics of the electric circuit theory.

1. Introduction

In the electric circuit theory, attention is given to the networks with variable parameters of elements. In particular, a new method, which can determine the functional dependence of any circuit variable with respect to any set of design variables, is presented in [1].

At present, special consideration is given to distributed renewable power supply systems with a lot of loads and voltage sources [2–5]. In turn, a particular problem of convenient recalculation of changeable load currents is raised. The conventional approach uses the changes in load conductivities in the form of increments. Recalculation of currents leads to the solution of a system of algebraic equations of a corresponding order. Therefore, for a number or group of changes in these conductivities, these increments should be counted concerning an initial circuit and the solution of the equations system is repeated. So, this nonfulfilment of group properties (when the final result should be obtained through intermediate results) complicates recalculation and limits the capabilities of this approach.

An approach for the interpretation of changes or "kinematics" of the circuit regimes on the basis of projective geometry is represented in [6]. The changes in regime parameters are introduced otherwise. Therefore, as if obvious changes in the form of increments are formal and do not reflect the substantial aspect of the mutual influences: conductivities $\rightarrow$ currents. The offered approach allows obtaining the convenient formulas of recalculation of load currents. In particular, a network with a common node for a lot of loads is also shown [7, 8]. In this context, it is important to consider the general structure of the network.

2. Projective coordinates of an active two-port network

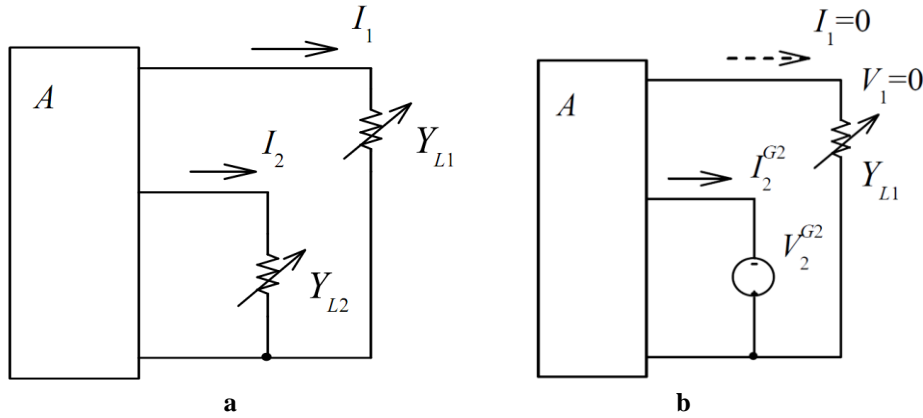Consider an active two-port with changeable load conductivities Y_{L1}, Y_{L2} in Fig. 1a.

<center>a   b</center>

Fig. 1. Active two-port (**a**) and active two-port regime with the second load base parameters (**b**).

Let us give the necessary relationships for this circuit [7]. The circuit is described by the following system of the Y - parameters equations

$$\begin{pmatrix} I_1 \\ I_2 \end{pmatrix} = \begin{pmatrix} -Y_{11} & Y_{12} \\ Y_{12} & -Y_{22} \end{pmatrix} \cdot \begin{pmatrix} V_1 \\ V_2 \end{pmatrix} + \begin{pmatrix} I_1^{SC} \\ I_2^{SC} \end{pmatrix}, \tag{1}$$

where I_1^{SC}, I_2^{SC} are the short circuit SC currents.

Taking into account the voltages $V_1 = I_1 / Y_{L1}$, $V_2 = I_2 / Y_{L2}$, two bunches of load straight lines with parameters Y_{L1}, Y_{L2} are shown in Fig. 2.

The bunch center, point G_2, corresponds to the bunch with parameter Y_{L1}. The bunch center corresponds to such a regime of the load Y_{L1} that does not depend on its values. It is carried out for $I_1 = 0, V_1 = 0$ at the expense of the characteristic regime parameter of the second load in Fig. 1b:

$$I_2 = I_2^{G2}, \quad V_2 = V_2^{G2}, \quad Y_{L2} = \frac{I_2}{V_2} = Y_{L2}^{G2}. \tag{2}$$

The parameters of the center G_1 of bunch Y_{L2} have the similar form. Another form of the characteristic regime is the short circuit regime of both loads ($Y_{L1} = \infty, Y_{L2} = \infty$) that is presented by point SC. The open circuit regime of both loads is also characteristic and corresponds to the origin of coordinates, point 0.

Let the initial or running regime correspond to point M^1, which is set by the values of conductivities Y_{L1}^1, Y_{L2}^1 or currents I_1^1, I_2^1 of the loads. Also, this point is defined by the projective non-uniform m_1^1, m_2^1 and homogeneous $\xi_1^1, \xi_2^1, \xi_3^1$ coordinates which are set by a reference triangle $G_1\,0\,G_2$ and a unit point SC [7, 9]. Point 0 is the origin of coordinates and straight line $G_1 G_2$ is the line of infinity ∞.
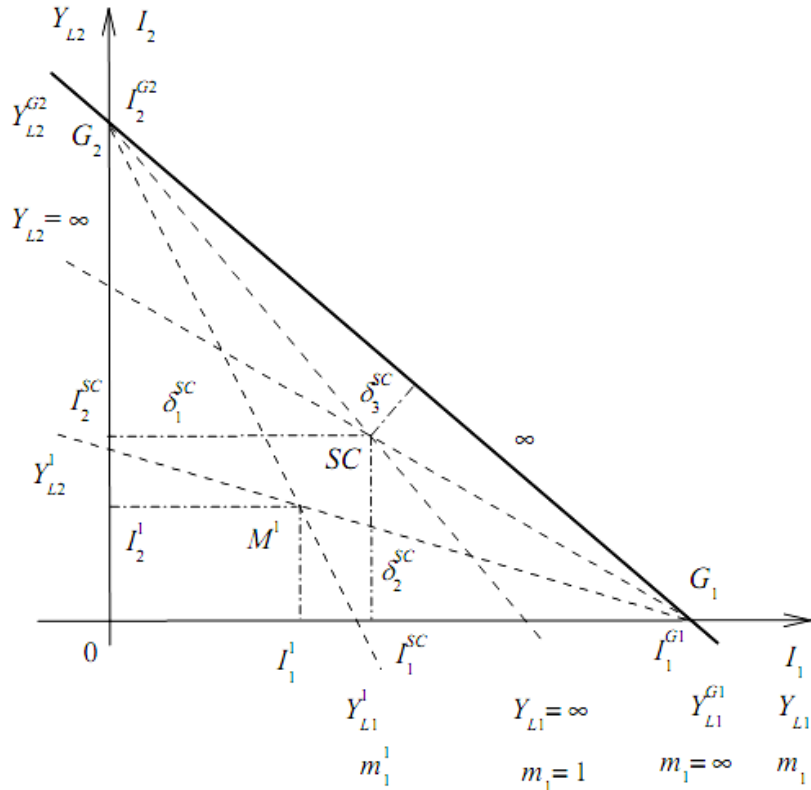
<center>103</center>

Fig. 2. Two bunches of load straight lines with the parameters Y_{L1}, Y_{L2}.

The non-uniform projective coordinate m_1^1 is set by a cross ratio of four points, three of them correspond to the points of the characteristic regimes, and the fourth corresponds to the point of the running regime

$$m_1^1 = (0 \; Y_{L1}^1 \; \infty \; Y_{L1}^{G1}) = \frac{Y_{L1}^1}{Y_{L1}^1 - Y_{L1}^{G1}} \div \frac{\infty - 0}{\infty - Y_{L1}^{G1}} = \frac{Y_{L1}^1}{Y_{L1}^1 - Y_{L1}^{G1}}. \tag{3}$$

Here, the points $Y_{L1} = 0$, $Y_{L1} = Y_{L1}^{G1}$ correspond to the extreme or base values. The point of $Y_{L1} = \infty$ is a unit point. These values of m_1 are also shown in Fig. 2. For the point $Y_{L1}^1 = Y_{L1}^{G1}$, the projective coordinate $m_1 = \infty$ defines the sense of line of infinity $G_1 G_2$. The cross ratio for the projective coordinate m_2^1 is expressed similarly. The homogeneous projective coordinates ξ_1, ξ_2, ξ_3 set the non-uniform coordinates as follows:

$$m_1 = \frac{\xi_1}{\xi_3} = \frac{\rho \xi_1}{\rho \xi_3}, \quad m_2 = \frac{\xi_2}{\xi_3} = \frac{\rho \xi_2}{\rho \xi_3}, \tag{4}$$

where ρ is a coefficient of proportionality.

The homogeneous coordinates are defined by the ratio of the distances of the points M^1, SC to the sides of the reference triangle:

$$\rho \, \xi_1^1 = \frac{\delta_1^1}{\delta_1^{SC}} = \frac{I_1^1}{I_1^{SC}}, \quad \rho \, \xi_2^1 = \frac{I_2^1}{I_2^{SC}}, \quad \rho \, \xi_3^1 = \frac{\delta_3^1}{\delta_3^{SC}}.$$

For finding distances $\delta_3^1, \delta_3^{SC}$ to straight line $G_1 G_2$, the equation of this straight line is

used. Then

$$\left(\frac{I_1^1}{I_1^{G1}} + \frac{I_2^1}{I_2^{G2}} - 1 \right) = \mu_3 \delta_3^1 \,, \qquad \left(\frac{I_1^{SC}}{I_1^{G1}} + \frac{I_2^{SC}}{I_2^{G2}} - 1 \right) = \mu_3 \delta_3^{SC} \,,$$

where μ_3 is a normalizing factor.

The homogeneous coordinates have a matrix form

$$\rho [\xi^1] = [\mathbf{C}] \cdot [\mathbf{I}^1] \,, \tag{5}$$

where matrix and vectors

$$[\mathbf{C}] = \begin{pmatrix} \dfrac{1}{I_1^{SC}} & 0 & 0 \\[2mm] 0 & \dfrac{1}{I_2^{SC}} & 0 \\[2mm] \dfrac{1}{I_1^{G1} \mu_3 \delta_3^{SC}} & \dfrac{1}{I_2^{G2} \mu_3 \delta_3^{SC}} & -\dfrac{1}{\mu_3 \delta_3^{SC}} \end{pmatrix} \,, \quad [\mathbf{I}^1] = \begin{pmatrix} I_1^1 \\ I_2^1 \\ 1 \end{pmatrix}, \quad [\xi^1] = \begin{pmatrix} \xi_1^1 \\ \xi_2^1 \\ \xi_3^1 \end{pmatrix}.$$

From here, we may pass to the non-uniform coordinates

$$m_1^1 = \frac{\rho \xi_1^1}{\rho \xi_3^1} = \frac{I_1^1 / I_1^{SC}}{\dfrac{I_1^1}{I_1^{G1}} + \dfrac{I_2^1}{I_2^{G2}} - 1} \mu_3 \delta_3^{SC} \,, \quad m_2^1 = \frac{\rho \xi_2^1}{\rho \xi_3^1} = \frac{I_2^1 / I_2^{SC}}{\dfrac{I_1^1}{I_1^{G1}} + \dfrac{I_2^1}{I_2^{G2}} - 1} \mu_3 \delta_3^{SC} \,. \tag{6}$$

The inverse transformation of (5)

$$\rho[\mathbf{I}^1] = [\mathbf{C}]^{-1} \cdot [\xi^1] \,, \quad [\mathbf{C}]^{-1} = \begin{pmatrix} I_1^{SC} & 0 & 0 \\[2mm] 0 & I_2^{SC} & 0 \\[2mm] \dfrac{I_1^{SC}}{I_1^{G1}} & \dfrac{I_2^{SC}}{I_2^{G2}} & -\mu_3 \delta_3^{SC} \end{pmatrix} \,. \tag{7}$$

From here, we pass to the currents

$$I_1^1 = \frac{\rho I_1^1}{\rho 1} = \frac{I_1^{SC} m_1^1}{\dfrac{I_1^{SC}}{I_1^{G1}} m_1^1 + \dfrac{I_2^{SC}}{I_2^{G2}} m_2^1 - \mu_3 \delta_3^{SC}} = \frac{I_1^{SC} m_1^1}{\dfrac{I_1^{SC}}{I_1^{G1}} (m_1^1 - 1) + \dfrac{I_2^{SC}}{I_2^{G2}} (m_2^1 - 1) + 1} \,,$$

$$\tag{8}$$

$$I_2^1 = \frac{\rho I_2^1}{\rho 1} = \frac{I_1^{SC} m_2^1}{\dfrac{I_1^{SC}}{I_1^{G1}} (m_1^1 - 1) + \dfrac{I_2^{SC}}{I_2^{G2}} (m_2^1 - 1) + 1} \,.$$

Obtained transformation allows finding currents I_1, I_2 for the preset values of conductivities Y_{L1}, Y_{L2} by using coordinates m_1, m_2. Furthermore, we note these expressions (6) and (8) have the common form, which is convenient for practice.

We consider now the recalculation of the load currents. Let a subsequent regime correspond to point M^2 with load parameters $Y_{L1}^2, Y_{L2}^2, I_1^2, I_2^2$.

The non-uniform m_1^2, m_2^2 coordinates are defined similarly to (3). Therefore, the regime changes m_1^{21}, m_2^{21} are naturally expressed through the cross ratio

$$m_1^{21} = (0 \; Y_{L1}^2 \; Y_{L1}^1 \; Y_{L1}^{G1}) = m_1^2 \div m_1^1, \quad m_2^{21} = m_2^2 \div m_2^1.$$

We also define the homogeneous coordinates of the point M^2 and represent nonuniform coordinates m_1^2 and m_2^2 in the form

$$m_1^2 = m_1^{21} \frac{\xi_1^1}{\xi_3^1}, \quad m_2^2 = m_2^{21} \frac{\xi_2^1}{\xi_3^1}.$$

Using (7) and (8), we immediately obtain the required currents

$$I_1^2 = \frac{I_1^1 m_1^{21}}{\dfrac{I_1^1}{I_1^{G1}}(m_1^{21} - 1) + \dfrac{I_2^1}{I_2^{G2}}(m_2^{21} - 1) + 1}, \quad I_2^2 = \frac{I_2^1 m_2^{21}}{\dfrac{I_1^1}{I_1^{G1}}(m_1^{21} - 1) + \dfrac{I_2^1}{I_2^{G2}}(m_2^{21} - 1) + 1}. \tag{9}$$

The obtained relationships carry out the recalculation of currents at a respective change in load conductivities. These relations are the projective transformations and possess group properties.

3. Active multi-port network with a common node for loads

Consider the active multi-port network in Fig. 3 with given elements and a common node N for load conductivities Y_{L1}, Y_{L2}, Y_{L3}. In particular, internal conductance y_{0N} of voltage source V_0 defines the mutual influence of the loads.

A circuit is described by the following system of the Y-parameters equation

$$\begin{pmatrix} I_1 \\ I_2 \\ I_3 \end{pmatrix} = \begin{pmatrix} -Y_{11} & Y_{12} & Y_{13} \\ Y_{12} & -Y_{22} & Y_{23} \\ Y_{13} & Y_{23} & -Y_{33} \end{pmatrix} \cdot \begin{pmatrix} V_1 \\ V_2 \\ V_3 \end{pmatrix} + \begin{pmatrix} I_1^{SC} \\ I_2^{SC} \\ I_3^{SC} \end{pmatrix}, \tag{10}$$

where I_1^{SC}, I_2^{SC}, and I_3^{SC} are the short circuit SC currents of all the loads.

Similarly to the above, let us give the necessary relationships and geometrical interpretation for this active multi-port. We accept that coordinate axes I_1, I_2, I_3 determine the three-dimensional Cartesian coordinate system (I_1, I_2, I_3) in Fig. 4.

Taking into account voltages $V_1 = I_1 / Y_{L1}, V_2 = I_2 / Y_{L2}$, and $V_3 = I_2 / Y_{L3}$, the equations of three bunches of planes are obtained in the form

$$(I_1, I_2, I_3, Y_{L1}) = 0, \quad (I_1, I_2, I_3, Y_{L2}) = 0, \quad (I_1, I_2, I_3, Y_{L3}) = 0.$$

Crossing of the planes of one bunch among themselves defines a bunch axis. The equation of the axis of bunch Y_{L1} corresponds to the condition $I_1 = 0, V_1 = 0$ and to equation $(I_2, I_3) = 0$. Therefore, this axis is located in the plane of I_2, I_3 in Fig. 4 and determines the points of

intersection or the base values of I_2^{G2}, I_3^{G3}. Similarly, we get the base value of I_1^{G1}.

Thus, we accept the $G_1 G_2 G_3$ plane, which passes through these three points I_1^{G1}, I_2^{G2}, and I_3^{G3}, as the plane of infinity ∞. So, we get the coordinate tetrahedron $0 G_1 G_2 G_3$.
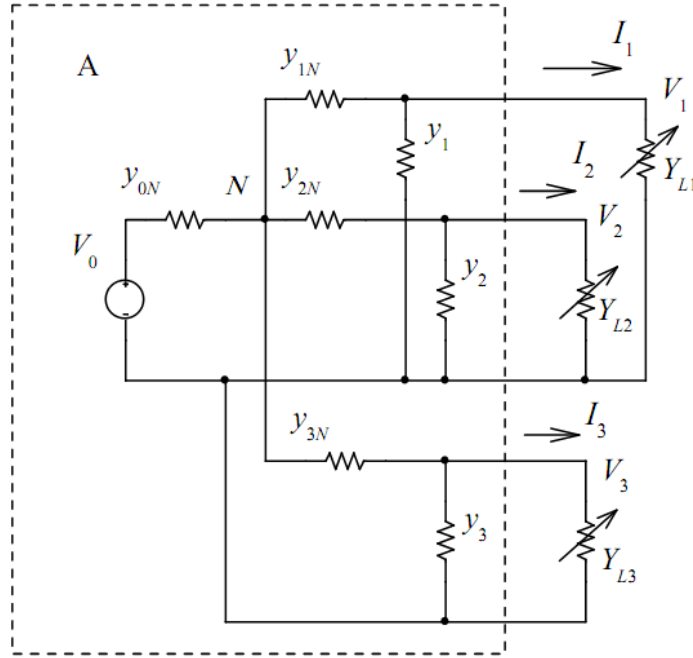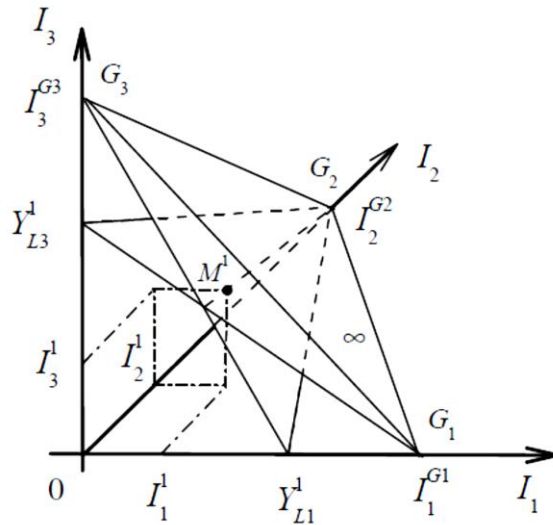

Fig. 3. Active multi-port with a common node N.

Fig. 4. Cartesian coordinate system (I_1, I_2, I_3) and projective coordinate $0 G_1 G_2 G_3$.

Let the initial or running regime correspond to point M^1, which is set by load conductivities $Y_{L1}^1, Y_{L2}^1, Y_{L3}^1$ and currents I_1^1, I_2^1, I_3^1. Then, the running value Y_{L3}^1 corresponds to the plane which passes through point M^1 and straight line $G_1 G_2$. This line corresponds to the

intersection of the $G_1 G_2 G_3$, $0 G_1 G_2$ planes.

Similarly, the Y_{L2}^1 value agrees with the plane that passes through point M^1 and straight line $G_1 G_3$.

In addition, the Y_{L1}^1 value matches point M^1 and straight line $G_2 G_3$. We recall that this line is the axis of bunch plane Y_{L1}. In turn, the values of $Y_{L1} = 0$, $Y_{L1} = \infty$, and Y_{L1}^{G1} are the characteristic values of Y_{L1}. Therefore, the running value Y_{L1}^1 corresponds to the non-uniform coordinate m_1^1 in the form of cross ratio of four points:

$$m_1^1 = (0 \; Y_{L1}^1 \; \infty \; Y_{L1}^{G1}) = \frac{Y_{L1}^1}{Y_{L1}^1 - Y_{L1}^{G1}} \div \frac{\infty - 0}{\infty - Y_{L1}^{G1}} = \frac{Y_{L1}^1}{Y_{L1}^1 - Y_{L1}^{G1}}.$$

There, points $Y_{L1} = 0$, $Y_{L1} = Y_{L1}^{G1}$ are the base points and $Y_{L1} = \infty$ is a unit point.

The cross ratio for m_2^1, m_3^1 is expressed similarly:

$$m_2^1 = (0 \; Y_{L2}^1 \; \infty \; Y_{L2}^{G2}) = \frac{Y_{L2}^1}{Y_{L2}^1 - Y_{L2}^{G2}}, \quad m_3^1 = (0 \; Y_{L3}^1 \; \infty \; Y_{L3}^{G3}) = \frac{Y_{L3}^1}{Y_{L3}^1 - Y_{L3}^{G3}}.$$

For points Y_{L1}^{G1}, Y_{L2}^{G2}, and Y_{L3}^{G3}, the coordinates $m_1 = m_2 = m_3 = \infty$ define the sense of the plane of infinity $G_1 G_2 G_3$.

In addition to nonuniform coordinates m_1^1, m_2^1, m_3^1 of a point M^1, there are homogeneous projective coordinates $\xi_1^1, \xi_2^1, \xi_3^1, \xi_4^1$, which are set by a coordinate tetrahedron and a unit point SC. These homogeneous coordinates are defined as the ratio of the distances $\delta_1^1, \delta_2^1, \delta_3^1, \delta_4^1$ for the point M^1 and distances $\delta_1^{SC}, \delta_2^{SC}, \delta_3^{SC}, \delta_4^{SC}$ for a unit point SC to the planes of the coordinate tetrahedron $0 G_1 G_2 G_3$.

Then, the distances δ_1^1, δ_1^{SC} correspond to the $0 G_2 G_3$ plane; therefore, $\delta_1^1 = I_1^1$, $\delta_1^{SC} = I_1^{SC}$. Similarly, δ_2^1, δ_2^{SC} match the plane $0 G_1 G_3$ and $\delta_2^1 = I_2^1$, $\delta_2^{SC} = I_2^{SC}$. Also, δ_3^1, δ_3^{SC} correspond to $0 G_1 G_2$ and $\delta_3^1 = I_3^1$, $\delta_3^{SC} = I_3^{SC}$; δ_4^1, δ_4^{SC} agree with the plane $G_1 G_2 G_3$.

Therefore, we obtain

$$\rho \, \xi_1^1 = \frac{\delta_1^1}{\delta_1^{SC}} = \frac{I_1^1}{I_1^{SC}}, \quad \rho \, \xi_2^1 = \frac{\delta_2^1}{\delta_2^{SC}} = \frac{I_2^1}{I_2^{SC}}, \quad \rho \, \xi_3^1 = \frac{\delta_3^1}{\delta_3^{SC}} = \frac{I_3^1}{I_3^{SC}}, \quad \rho \, \xi_4^1 = \frac{\delta_4^1}{\delta_4^{SC}},$$

where ρ is a coefficient of proportionality.

For finding the distances δ_4^1, δ_4^{SC}, the equation of $G_1 G_2 G_3$ is used

$$\frac{I_1^\infty}{I_1^{G1}} + \frac{I_2^\infty}{I_2^{G2}} + \frac{I_3^\infty}{I_3^{G3}} - 1 = 0.$$

Then,

$$\mu_4 \delta_4^1 = \frac{I_1^1}{I_1^{G1}} + \frac{I_2^1}{I_2^{G2}} + \frac{I_3^1}{I_3^{G3}} - 1, \quad \mu_4 \delta_4^{SC} = \frac{I_1^{SC}}{I_1^{G1}} + \frac{I_2^{SC}}{I_2^{G2}} + \frac{I_3^{SC}}{I_3^{G3}} - 1,$$

where μ_4 is a normalizing factor.

Similarly to (5), (7), and (8), we immediately obtain

$$I_1^1 = \frac{I_1^{SC} m_1^1}{\dfrac{I_1^{SC}}{I_1^{G1}}(m_1^1 - 1) + \dfrac{I_2^{SC}}{I_2^{G2}}(m_2^1 - 1) + \dfrac{I_3^{SC}}{I_3^{G3}}(m_3^1 - 1) + 1},$$

$$I_2^1 = \frac{I_2^{SC} m_2^1}{\dfrac{I_1^{SC}}{I_1^{G1}}(m_1^1 - 1) + \dfrac{I_2^{SC}}{I_2^{G2}}(m_2^1 - 1) + \dfrac{I_3^{SC}}{I_3^{G3}}(m_3^1 - 1) + 1},$$

$$I_3^1 = \frac{I_3^{SC} m_3^1}{\dfrac{I_1^{SC}}{I_1^{G1}}(m_1^1 - 1) + \dfrac{I_2^{SC}}{I_2^{G2}}(m_2^1 - 1) + \dfrac{I_3^{SC}}{I_3^{G3}}(m_3^1 - 1) + 1}.$$

Let the subsequent regime correspond to point M^2 with loads $Y_{L1}^2, Y_{L2}^2, Y_{L3}^2$. The non-uniform coordinates

$$m_1^2 = \frac{Y_{L1}^2}{Y_{L1}^2 - Y_{L1}^{G1}} \ , \quad m_2^2 = \frac{Y_{L2}^2}{Y_{L2}^2 - Y_{L2}^{G2}}, \quad m_3^2 = \frac{Y_{L3}^2}{Y_{L3}^2 - Y_{L3}^{G3}}.$$

The regime change has the form

$$m_1^{21} = m_1^2 \div m_1^1, \qquad m_2^{21} = m_2^2 \div m_2^1 \ , \qquad m_3^{21} = m_3^2 \div m_3^1 .$$

Similarly to (9) we get the subsequent currents

$$I_1^2 = \frac{\rho\, I_1^2}{\rho\, 1} = \frac{I_1^1 \cdot m_1^{21}}{\dfrac{I_1^1}{I_1^{G1}} \cdot (m_1^{21} - 1) + \dfrac{I_2^1}{I_2^{G2}} \cdot (m_2^{21} - 1) + \dfrac{I_3^1}{I_3^{G3}} \cdot (m_3^{21} - 1) + 1},$$

$$I_2^2 = \frac{\rho\, I_2^2}{\rho\, 1} = \frac{I_2^1 \cdot m_2^{21}}{\dfrac{I_1^1}{I_1^{G1}} \cdot (m_1^{21} - 1) + \dfrac{I_2^1}{I_2^{G2}} \cdot (m_2^{21} - 1) + \dfrac{I_3^1}{I_3^{G3}} \cdot (m_3^{21} - 1) + 1},$$

$$I_3^2 = \frac{\rho\, I_3^2}{\rho\, 1} = \frac{I_3^1 \cdot m_3^{21}}{\dfrac{I_1^1}{I_1^{G1}} \cdot (m_1^{21} - 1) + \dfrac{I_2^1}{I_2^{G2}} \cdot (m_2^{21} - 1) + \dfrac{I_3^1}{I_3^{G3}} \cdot (m_3^{21} - 1) + 1}.$$

The obtained relationships are directly generalized to any number of loads and possess a group property.

4. General case of an active multi-port

Let us consider the general case of an active multi-port in Fig. 5. The circuit is also described by system of equations (10).   Similarly to the above, we get the equations of three bunches of planes. Crossing of the planes of one bunch among themselves defines a bunch axis.
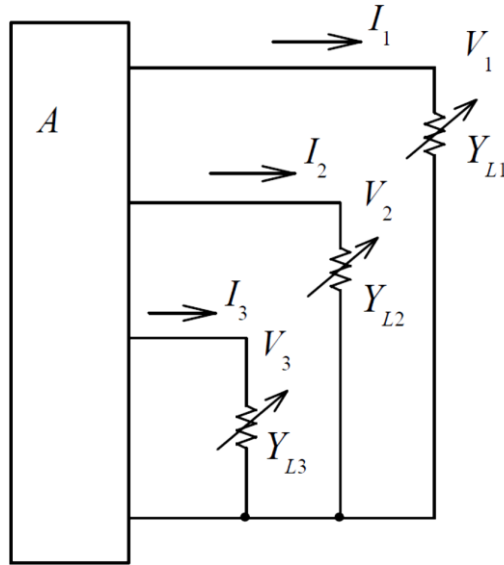
Fig. 5. General case of an active multi-port.

The equation of the axis of bunch Y_{L1} corresponds to the condition of $I_1 = 0$, $V_1 = 0$ and to equation $(I_2, I_3) = 0$. Therefore, this axis is located in the I_2, I_3 plane in Fig. 6a.
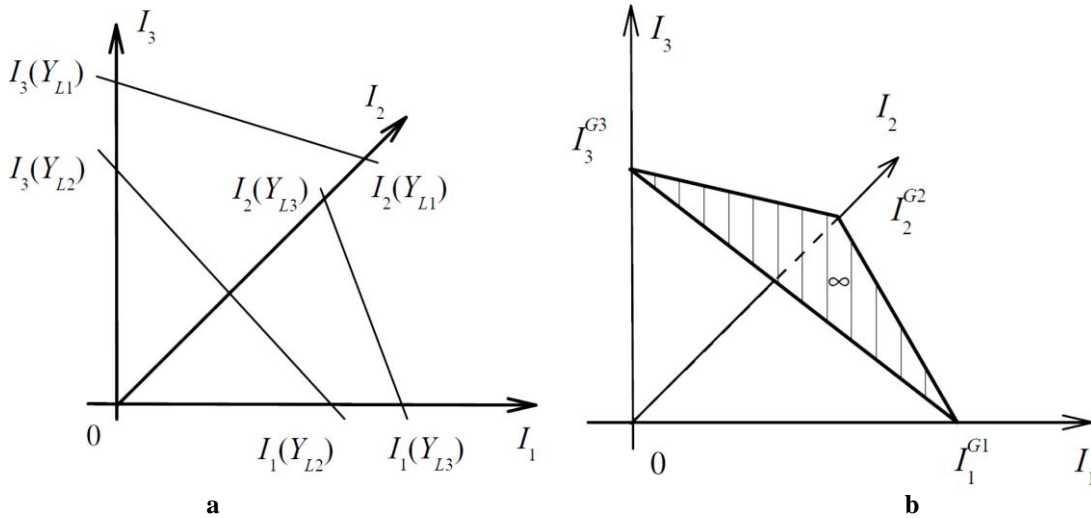

Fig. 6. Points of intersection do not coincide (**a**).
Points of intersection coincide and form the plane of infinity ∞ (**b**).

Points $I_2(Y_{L1})$, $I_3(Y_{L1})$ are the points of intersection with the respective axis. Similarly, we obtain points $I_1(Y_{L2})$, $I_3(Y_{L2})$ of intersection of bunch axis Y_{L2} and points $I_1(Y_{L3})$, $I_2(Y_{L3})$ of intersection of bunch axis Y_{L3}.

On the other hand, the projective system of coordinates must represent a tetrahedron $0, I_1^{G1}, I_2^{G2}, I_3^{G3}$ in Fig. 6b. Therefore, the following conditions must be satisfied:

$$I_1(Y_{L2}) = I_1(Y_{L3}) = I_1^{G1}, \quad I_2(Y_{L1}) = I_2(Y_{L3}) = I_2^{G2}, \quad I_3(Y_{L1}) = I_3(Y_{L2}) = I_3^{G3}.$$

We should determine requirements for Y -parameters. To this end, let us consider the base point or base values, $I_1 = I_1^{G1}$, $V_1 = V_1^{G1}$. Then, $I_2 = 0, V_2 = 0$, $I_3 = 0, V_3 = 0$.

Using (10), we get

$$
\begin{cases}
I_1^{G1} = -Y_{11} V_1^{G1} + I_1^{SC} \\
0 = Y_{12} V_1^{G1} + I_2^{SC} \\
0 = Y_{13} V_1^{G1} + I_3^{SC} .
\end{cases}
$$

From here, the requirements have the form

$$
- V_1^{G1} = \frac{I_2^{SC}}{Y_{12}} = \frac{I_3^{SC}}{Y_{13}} .
$$

Similarly, we consider that $I_2 = I_2^{G2}$, $V_2 = V_2^{G2}$.
Then

$$
\begin{cases}
0 = Y_{12} V_2^{G2} + I_1^{SC} \\
I_2^{G2} = -Y_{22} V_2^{G2} + I_2^{SC} \\
0 = Y_{23} V_2^{G2} + I_3^{SC} ,
\end{cases}
\qquad
- V_2^{G2} = \frac{I_1^{SC}}{Y_{12}} = \frac{I_3^{SC}}{Y_{23}} ;
$$

We consider that $I_3 = I_3^{G3}$, $V_3 = V_3^{G3}$ and obtain

$$
\begin{cases}
0 = Y_{13} V_3^{G3} + I_1^{SC} \\
0 = Y_{23} V_3^{G3} + I_2^{SC} \\
I_3^{G3} = -Y_{33} V_3^{G3} + I_3^{SC} ,
\end{cases}
\qquad
- V_3^{G3} = \frac{I_1^{SC}}{Y_{13}} = \frac{I_2^{SC}}{Y_{23}} .
$$

The obtained requirements or base points (2)−(5) are formally generalized to any number of loads.

We will identify this distributed network as a balanced network for output terminals.

The obtained conductivity values do not limit especially the functional possibility of these circuits, but allow essentially simplifying the calculation and recalculation of currents, as shown above.

Using the network in Fig. 3, we obtain an example of the general case of multi- port in Fig. 7.

If we choose the values of conductivities y_{12}, y_{13}, y_{23} by the required conditions, the balanced network is obtained.
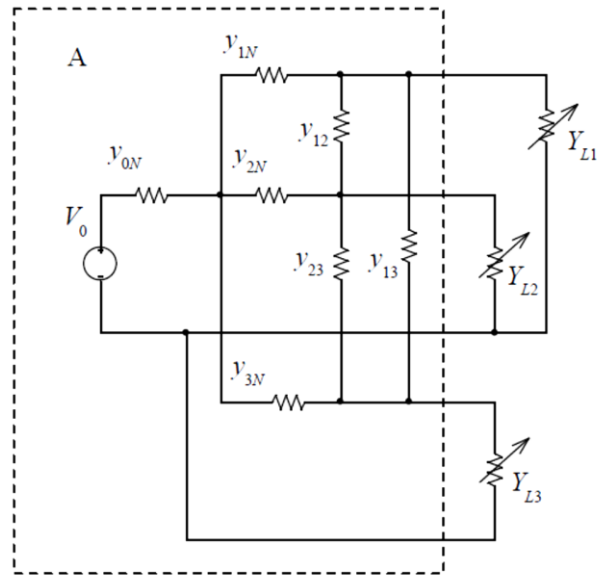
Fig. 7. Example of the general case of multi-port.

5. Conclusions

1. Active two-ports are always the balanced networks.
2. Active multi-ports with any number of loads can be balanced.
3. Application of projective coordinates allows obtaining convenience formulas for the recalculation of load currents.

References

[1] S. P. Bhattacharyya, L. H. Keel, and D. N. Mohsenizadeh, Linear Systems: A measurement based approach. Springer India, 89 p., 2014.

[2] A. St. Leger and C. O. Nwankpa, Analog and Hybrid Computation Approaches for Static Power Flow. In: System Sciences, 2007. HICSS 2007. 40th Annual Hawaii International Conference on, IEEE (2007).

[3] X. Zhao, K. Li, and M. Zheng, J. Power Energy Eng., 2(04), 564-572, (2014).

[4] S. Kim and P. H. Chou, Energies, *7*(11), 7519-7534, (2014).

[5] Y. Levron and D. Shmilovitz, Circuits and Syst., I: Reg. Papers, IEEE Trans., 57(8), 2232-2241, (2010).

[6] A. Penin, Analysis of Electrical Circuits with Variable Load Regime Parameters: Projective Geometry Method, Springer International Publishing AG, 343 p., 2015.

[7] A. Penin, J. Circ. Syst. Comput. 22(05), 1350031 (13 pages) (2013). DOI: 10.1142/S021812661350031X

[8] A. Penin, Mold. J. Phys. Sci., 10(3), 350-357, (2011).

[9] J. A. Frank, Schaum's Outline of Theory and Problems of Projective Geometry, Schaum Publishing Company, 243 p., 1967.

COMMUNICATION WITH CHAOS USING SEMICONDUCTOR LASERS WITH AN AIR GAP

T. Oloinic[1], S. S. Rusu[1], and V. Z. Tronciu[1,2]

[1]*Department of Physics, Technical University of Moldova, Chisinau, Republic of Moldova*
[2]*Ferdinand-Braun-Institut Leibniz-Institut für Höchstfrequenztechnik*
Gustav-Kirchhoff-Straße 4, 12489 Berlin, Germany

This paper reports the numerical results of the dynamical behavior of an integrated semiconductor laser subject to multiple optical feedback loops. The laser setup consists of a distributed feedback active section coupled to multi section cavities. It has been found that, due to the multiple feedback loops and under certain operating conditions, the laser displays chaotic behaviors appropriate for chaos-based communications. The optimal conditions and suitable parameters for chaos generation have been identified. The synchronization of two unidirectional-coupled (master–slave) systems has been studied. Finally, examples of high bit rate message encoding and decoding have been described and discussed.

1. Introduction

During the last years, the dynamics of semiconductor lasers has become the subject of various investigations due to the interest in the prediction of the evolution of laser setups. Distributed feedback (DFB) lasers with multi sections are the key element for various devices used in the optical communication system. It is well known that, in semiconductor laser applications, the presence of an optical feedback is inevitable. The external mirrors of the laser setup or the connection to other optical components of the system can create this feedback. A small amount of the optical feedback created by a plane mirror can cause the system destabilization and the appearance of instabilities. Thus, optical feedback can have a significant effect on the dynamic behavior of the semiconductor laser (for details see [1]). Even simple reflections from the exterior mirrors might cause different phenomena, such as coherent collapse, frequency fluctuations, self-pulsations, chaos, etc. The presence of periodical or chaotic oscillations is a well-known fact in semiconductor lasers with optical feedback. The chaotic behavior can be both useful, for example, in the case of chaos-based communication systems and undesired, and should rather be avoided or fixed in other applications.

In this paper, we analyze the way for the laser to be destabilized by external cavities. Using the chaotic oscillations produced by multi-sections laser setup in a chaos-based communicational system is the main aim of present paper. Chaos-based communication becomes more attractive because it allows a further security improvement of the optical data transmission. Interest in this domain has considerably increased after the practical prove of the optical communication based on chaos in the network of optical fibers in Athens [2]. Different optical feedbacks are usually used in chaos-based communication optical systems: complete optical [3, 4] or electro-optical [5, 6]. Typically, to generate chaos, delay time must be longer than a few hundred picoseconds. The purpose of this paper is to present results related to chaos-based

communication using semiconductor lasers with optical feedback from multi cavities, one being air. Appropriate conditions for the chaotic evolution of the system due to the influence of this feedback have been obtained. We have studied the phenomenon of synchronization of two such systems and determined the regions of synchronization for two identical lasers. Finally, examples of message encoding and decoding have been presented in the chaotic modulation method.

2. Laser Model and Equations

We consider a device shown in Fig. 1; it consists of a semiconductor laser operating under the influence of a multiple optical feedback from an external cavity similar to that described in [7]. For modeling the scheme shown in Fig. 1, we use a single mode model of a laser operating in a continuous wave mode. Phases φ and ϕ can be easily controlled by a low injected current applied to the phase sections.

We apply the approximation of a single loop and neglect the multi-reflections within cavities. Note that, this approximation is used just for simplifying our numerical calculations. Thus, the system dynamics is analyzed in the

Fig. 1. Scheme of a semiconductor laser with optical feedback from multi section cavities.

framework of the extended Lang-Kobayashi model [8] for the complex amplitude of electric field E and carrier density N

$$\frac{dE_{t,r}}{dt} = (1 + i\alpha)\left[\frac{g(N_{t,r} - N_0)}{1 + \varepsilon|E_{t,r}|^2} - \frac{1}{\tau_{ph}}\right]\frac{E_{t,r}}{2} + \gamma_{t1,r1}e^{-i\varphi}E_{t,r}(t - \tau_1)$$

$$+ \gamma_{t2,r2}e^{-i(\varphi+\psi)}E_{t,r}(t - \tau_2) + \gamma_{t3,r3}e^{-i(\varphi+\psi+\phi)}E_{t,r}(t - \tau_3) + k_rE_t, \tag{1}$$

$$\frac{dN_{t,r}}{dt} = \frac{I_{t,r}}{e} - \frac{1}{\tau_e}N_{t,r} - \frac{g(N_{t,r} - N_0)}{1 + \varepsilon|E_{t,r}|^2}|E_{t,r}|^2. \tag{2}$$

Subscripts *t* and *r* refer to transmitting and receiving lasers, respectively. The last term in (1) is present only in the receiving laser and describes the unidirectional coupling between the transmitter and the receiver. Parameter k_r is the laser field intensity injected into the secondary laser. τ_1, τ_2, and τ_3 are the delays of the external cavities. $\gamma_{t1,r1}$, $\gamma_{t2,r2}$ and $\gamma_{t3,r3}$ are the feedback strengths governed by reflectivity R_1, R_2 and R_3, respectively. Other parameters have values: Henry factor $\alpha = 5$, differential gain coefficient $g = 1,5 \cdot 10^{-8} \text{ ps}^{-1}$, and saturation of the gain coefficient is $\varepsilon = 5 \cdot 10^{-7}$. The lifetimes of photons and charge carriers are $\tau_{ph} = 3 \text{ ps}$ and $\tau_e = 2 \text{ ns}$. The parameter values are used for the calculated results that are shown in all figures of the paper.

3. Numerical Results

For a relatively low optical feedback signal intensity, the laser emits in a continuous wave mode or a periodic oscillation mode. Figure 2 shows the pulse traces for (a) output power and (b) carrier density for the periodic behavior. The phase portrait shown in Fig. 2c represents a limit
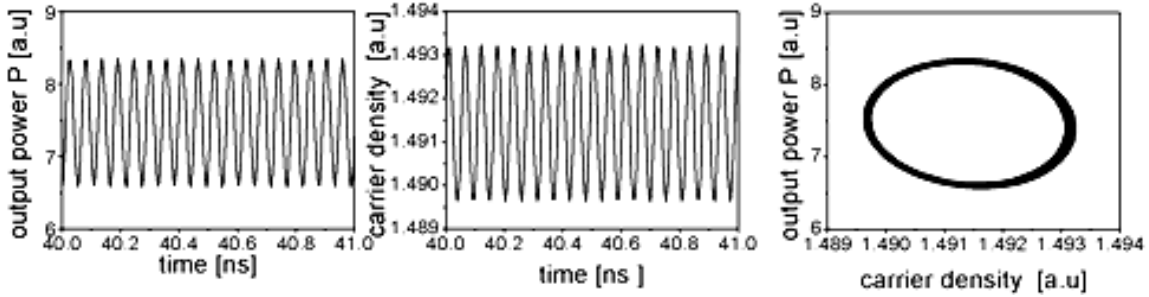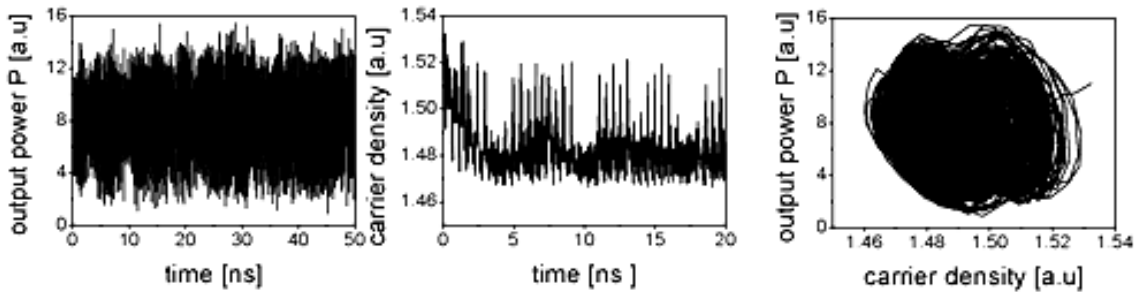

Fig. 2. Periodic behavior. Pulse trace of (a) output power and (b) carrier density. The phase portrait of semiconductor laser under the influence of multiple cavity optical feedback in the plane of two parameters ($P - N$). The other parameters are $\alpha = 5$, $\gamma_1 = 5$, $\gamma_2 = 5$, $\gamma_3 = 5$, $\varphi = \pi/2$, $\psi = 0$.

cycle. The chaotic regime appears only when the returned signal intensity is high enough. Figure 3 shows the time evolution of (a) output power and (b) carrier density of a semiconductor laser under the influence of optical feedback from multi cavity in the chaotic regime. Figure 3c shows

Fig. 3. Chaotic behavior. Pulse trace of (a) output power and (b) carrier density. The phase portrait of semiconductor laser under the influence of multiple cavity optical feedback in the plane of two parameters ($P - N$). The other parameters are $\alpha = 5$, $\gamma_1 = 5$, $\gamma_2 = 10$, $\gamma_3 = 15$, $\varphi = \pi/2$, $\psi = 0.11$

the appearance of a strange attractor in the plane of two parameters. Thus, due to the influence of the multiple feedbacks, the laser behavior has been found to be chaotic for a large range of parameters and laser bias currents. Even both experiments and theoretical calculations for these lasers demonstrate the presence of chaotic behaviors in the laser dynamics [7]. By acting on the bias of the phase sections, the chaos amplitude and bandwidth could also be tuned.

Figure 4 displays typical bifurcation diagrams of a semiconductor laser under the influence of multi section optical feedback, where feedback strengths γ_1 and γ_2 act as bifurcation

parameters. For each value of the feedback strength, the figure displays the values of the maxima (black) and minima (red) of the time traces of the emitted power. Figure 4 shows that
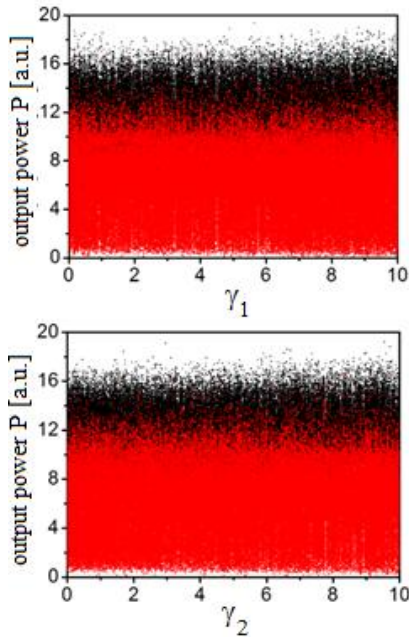

Fig. 4. Bifurcation diagram for γ_1 (top) and γ_2 (bottom) as bifurcation parameters. Other parameters are: $\varphi = \pi/2$, $\psi = 0$, $\phi = 3\pi/2$.
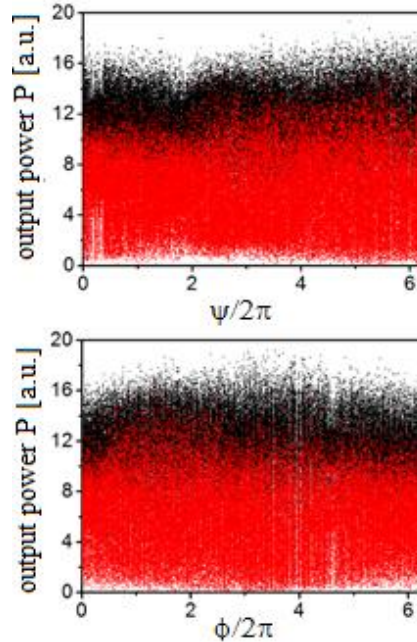
Fig. 5. Bifurcation diagram for $\psi/2\pi$ (top) and $\phi/2\pi$ (bottom) as bifurcation parameters. Other parameters are: $\varphi = \pi/2$.

even for low values of feedback strength γ_1, the dynamics of the laser is already chaotic due to the influence of the feedback of other sections. It is evident from the figure that the amplitude of the chaotic oscillations slightly increases with increasing feedback strengths γ_1 and γ_2. When both feedback strengths are fixed to $\gamma_1 = 20$ ns^{-1} and $\gamma_2 = 15$ ns^{-1}, as shown in Fig. 5, fully developed chaotic dynamics is found for any value of phases ψ and ϕ.

We have clarified different aspects of the dynamics of a semiconductor laser with integrated multi-section feedback for obtaining chaotic behaviors. In what follows, we are interested in the transmitter–receiver configuration (see Fig. 6) and in the evaluation of its synchronization properties. Figure 7 shows

Fig. 6. Transmitter–receiver configuration.

the synchronization diagram in the place of different parameters. One can see the wide region of perfect synchronization (grey region) with the cross correlation coefficient higher than 0.99.

The level of the coupling parameter is $k = 100$ ns^{-1}. Thus, for this set of parameters and coupling
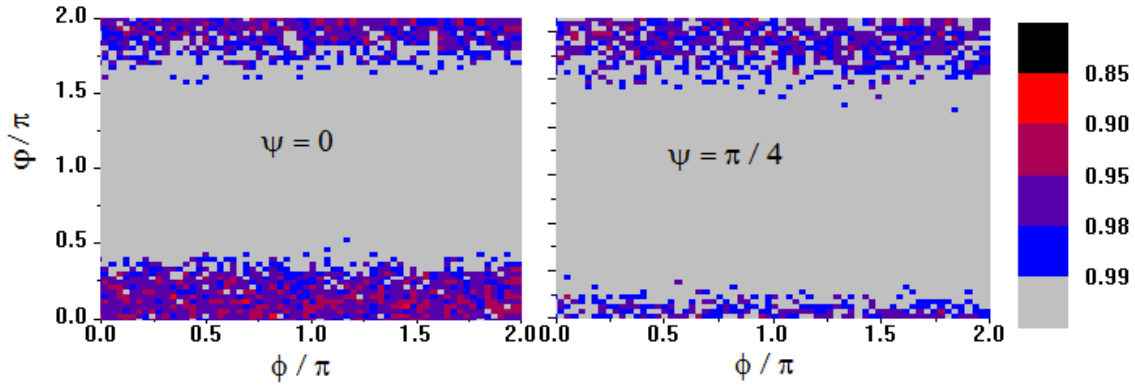

Fig. 7. Synchronization diagram in the $\varphi - \phi$ plane for the level of the coupling parameter of $k = 100$ ns^{-1} and different values of parameter ψ.

coefficient, the synchronization map shows a clear synchronization process.

Further on, we study the transmission–reception configuration and evaluate the synchronization properties of the two lasers. We examine the encrypting and decrypting of a digital message in the optical communication systems based on chaos. In the specialized literature, various methods of chaotic encryption have been proposed, such as modulation chaos [3], chaotic switch of the key [9], chaotic masking [10], etc. We analyze in detail only the case where the informational message is included as a chaotic modulation amplitude, i.e., the so-called chaotic modulation.

Figure 8 illustrates the transmission of a digital signal. Panel (a) shows the shape of an

Fig. 8. Numerical results of a 5-Gbit/s digital message encryption obtained with chaotic lasers.

incident 5Gb/s signal, i.e., the signal that should be sent. Panels (b) and (c) show the output power of the master laser without and with a message, respectively. Panel (d) is the decoded and recovered message after filtering the information signal (solid line) and the incident signal (dotted line). This figure shows that, for an ideal case where the parameters of both lasers coincide, the message is fully recovered. Thus, we have shown theoretically that the chaotic modulation

method can be easily implemented in optical communication systems based on chaos.

4. Conclusions

In the limits of Lang–Kobayashi equations, the dynamics of a single mode semiconductor laser with optical feedback that comes from multi cavities has been studied. The presence of several sections results in a complication of system oscillations. An advantage of the proposed system compared with that of conventional optical feedback is that the chaotic behavior occurs for short lengths of cavities, which makes a more compact device. On the other hand, under certain conditions, two such laser systems could be synchronized when they operate under chaotic emitter–receiver configuration. For the parameter values, the perfect synchronization has been obtained, the possibility of encryption and decryption of the message by chaotic modulation method has been demonstrated. The message can be adequately restored by the receiver even at high speed information transmission.

References

[1] Fundamental Issues of Nonlinear Laser Dynamics, B. Krauskopf and D. Lenstra (Eds.), AIP Conference Proceedings, pp. 548, (2000)
[2] A. Argyris, D. Syvridis, L. Larger, et al., Nature 438, 343 (2005)
[3] C. R Mirasso, P. Colet, and P. Garcia-Fernandez, IEEE Photon. Technol. Lett. 8, 299 (1996)
[4] S. Sivaprakasam and K. A. Shore, Opt. Lett. 24, 466 (1999)
[5] S.Tang and J. M. Liu, Opt. Lett. 26, 596 (2001)
[6] N. Gastaud, S. Poinsot, and L. Larger, Electron. Lett. 40, 898 (2004)
[7] V. Z. Tronciu et al., IEEE J. Quantum Electron. 46, 1840 (2010)
[8] R. Lang and K. Kobayashi, IEEE J. Quantum Electron. 16, 347 (1980)
[9] C. R. Mirasso, Int. Spring School on Fundamental Issues of Nonlinear Laser Dynamics 548, 112 (2000)
[10] T. Heil, J. Mulet, I. Fischer, et al., IEEE J. Quantum Electron. 38, 1162 (2002)

PLASMA FORMATION IN THE AIR MEDIUM UNDER ORDINARY PRESSURE AND ITS INTERACTION WITH SOLID METAL SURFACES

Arefa Hirbu

Alecu Russo Balti State University, Pushkin str. 38, Balti, MD3100, Republic of Moldova
E-mail: arefahirbu@yahoo.com

Abstract

The conditions for obtaining an electrical discharge plasma in a gaseous media, as well as its application in different fields of nanotechnology, are analyzed in this paper. Plasma production under the investigated conditions avoids the use of auxiliary equipment for the preventive ionization of the active media, which does not require synchronization between the base discharge and the moment at which the ionization in the gap is maximal. As a result of the interaction of the produced plasma with different material surfaces, structures of nanometer order were obtained, and the plasma itself can be applied at the construction of quantum generators in non-aggressive gaseous media as well as at the sterilization of objects in medicine.

Keywords: plasma, ionization, biomedicine, nanostructures

Introduction

Plasma of gaseous media is a completely or partially ionized gas consisting of neutral atoms or molecules and charged particles (ions and electrons). A basic characteristic of the plasma is quasi-neutrality, which means that the density of positively and negatively charged particles that form the plasma in a unit volume is approximately the same. The gas is transformed into the plasma state when some of its components, atoms or molecules, in any case have lost or added one or several electrons and thus have been transformed into positive ions; in some cases, as a result of the electrons' "add" by neutral atoms, negative ions can appear too. If there are no neutral particles and free electrons in the gas, then the plasma consists of positive and negative ions. If neutral particles are not presented in the gas, then the plasma is referred to as the completely ionized plasma. Free electrons and ions can be responsible for the appearance of an electric current; therefore, the plasma is a conductor of electricity.

1. Theoretical premises on plasma production in gaseous media

One of the methods of plasma production is the substance heating. To provide the complete plasma ionization thermally, it is necessary to heat the gaseous media to tens or hundreds of thousands of degrees. In a gas at high temperatures, the number of particles whose energy exceeds the ionization limit provides the possibility of the plasma production in partially ionized media. For this reason, to obtain the plasma under laboratory conditions, electrical discharges in gases are used. In order to obtain an electric discharge in a gas, it is necessary to apply a potential difference in the gap between two electrodes in which the studied gaseous medium is included. The charged particles that move in the electric field are formed in this gap; as a result, an electric current appears. In order to sustain the current in the plasma, the negative

electrode (cathode) must emit electrons. The electron emission from the cathode may be provided by various methods, such as the heating of the cathode to a high temperature (thermo-emission) or exposure of the cathode to X-ray or γ radiation, which is capable of tearing out the electrons from the cathode surface. This type of discharge generated by an external source is referred to as the induced discharge [1, 2].

Induced discharges can be spark, arc, and glow discharges. They differ fundamentally one from another in the mechanism of formation of electrons from the cathode or in the interelectrode gap.

A glow discharge is formed in tubes with a low-pressure gaseous active medium at the ends of which the electrodes are placed to which a high voltage is applied. In this case, the cathode emits electrons (through the electronic autoemission mechanism) that are torn out from the metal surface (cathode) under the action of the electric field. The electrical discharge plasma is comprised between the cathode and the anode to form dark zones (near the cathode and the anode) and a glow zone, which is referred to as the "positive" zone, for which the electric field intensity is approximately constant value. A glow discharge in a molecular gas plasma is widely applied as an active medium for the construction of lasers at the oscillator-rotational transitions of the molecules. The ionization process in the electrical discharge plasma is accompanied by the current passing through the active gaseous medium and has the nature of an avalanche with the ionizing effect. It follows that the occurrence of free electrons in the gap is caused by the fact that, at free pass of electrons accelerated by the electric field, they accumulate a sufficient energy to ionize neutral gas particles, which produce the avalanche multiplication of electrons and ions capable of maintaining a steady current in the gap [1, 2].

Quasi-neutrality is the one of the most important features of plasma and lies in the fact that the negative charge of the electrons neutralizes the positive charge of the ions. In any type of action on the gaseous medium placed between the electrodes, the plasma tends to keep its quasi-neutrality. If there is a movement of a group of electrons in some place of the medium between the electrodes (e.g., owing to density fluctuation), where an excess of electrons is identified (and an electron deficiency (in terms of concentration) in another place), a strong electric field arises in the plasma and annihilates the electric charge concentration and immediately restores its quasi-neutrality.

If in a plasma layer of thickness Δx, a volume of charge of the same density q is formed, then, in accordance with the laws of electrostatics, an electric field of $E = 4\pi q \Delta x$ arises on this length. If Δn_e electrons are in a volume of 1 cm^3, more in number than those that neutralize the ions charge, then the volumetric density of the charge will be: $q = e\Delta n_e$, where $e = 1.6 \cdot 10^{-19}$ C is the electron charge.

The electric field that arises as a result of the charge separation is $E = 1.8 \cdot 10^{-6}\Delta x$ V/cm. For air, $n = 2.7 \cdot 10^{19}$ molecules/cm^3 are contained at the Earth's surface. If we suppose that, as a result of ionization, all the molecules become ionized, then the concentration of electrons in the plasma will be $n_e = 2.7 \cdot 10^{19}$ electrons/cm^3. If we assume that the electron concentration has varied by 1% at the gap length of 1 cm, then the charge density will be $\Delta n_e = 2.7 \cdot 10^{19}$ electrons/cm^3, and it will generate an electric field of intensity of $E \approx 10^{12}$ V/cm [1].

In order to generate this strong electric field, it would require a very high energy; therefore, we can affirm that the formation of a high-density plasma takes place at very short distances.

The space dimensions of the charge separation can be appreciated by a work that must be done for the charge separation at distance d that is performed by the forces occurring on the distance x out of the electric field intensity $E = 4\pi n_e e x$. Taking into account the fact that $F = eE$,

this work can be calculated by the relationship [1]:

$$A = \int_0^d eE\,dx = 2\pi n_e e^2 d^2 .$$

This work cannot exceed the kinetic energy of the thermal movement of the particles in the plasma and, for the one-dimensional case of the particle movement, it will be as follows:

$$\overline{W_c} = \frac{1}{2}kT$$

where k is the Boltzmann constant and T is the absolute temperature, then

$$A \le \frac{1}{2}kT .$$

Using this relationship, the maximal dimension of the charge separation can be estimated [1, 2]:

$$d = \left(\frac{\varepsilon_0 kT}{n_e e^2}\right)^{1/2}$$

This measure is referred to as the Debye length. For air plasma under ordinary condition $n_e = 2.7 \cdot 10^{19}$ cm^{-3}, $T = 273$ K, $k = 1.38 \cdot 10^{-23}$ J/K,

$$\varepsilon_0 = 8.85 \cdot \frac{10^{-12}C^2}{N} \cdot m^2$$

$$d = 2.2 \cdot 10^{-12} cm .$$

Length d (or Debye radius $r_0 = \frac{d}{\sqrt{2}}$) represents a basic characteristic of the plasma; in particular, the electric field generated by each of the charged particles from the plasma is screened by the field generated by the particle charge of the opposite sign. On the other hand, measure d determines the depth of penetration of the external electric field in the plasma. Under ordinary conditions, any volume of the gas comprises a certain number of electrons and ions. On the average ~1000 of positive and negative ions are contained in the air under ordinary condition that results from the interaction of the medium with ultraviolet and other types of radiation, including cosmic. Due to these conditions, a certain number of electrons are torn from the electrode surface. The rate of gas ionization and electron emission from the electrode can be increased under laboratory conditions by the application of additional radiation sources. If a potential difference is applied to the gap, the current (whose density j is proportional to applied electric field intensity E) will pass through the gaseous medium. For the electric field values of about 10–20 V/cm, the current intensity will be $j \approx 10^{-9}$ A/cm^2 [3]. For these conditions, the gaseous medium is in balance; therefore, the recombination and formation of charged particles occur (electron and ion mobilities are almost equal). With an increase in electric field intensity E and current density j, the balance is violated, which increases the recombination coefficient and decreases the number of charged particles, and, as a result, leads to an increase in the gap resistance and a decrease in the current. In this case, the current density on the electrode surface will be [3, 4]:

$$j = S \cdot e \cdot \frac{dn}{dt},$$

where S is the gap size; e is the electron charge; $\frac{dn}{dt}$ is the overall speed of generation of charged particles in a unit of volume.

Therefore, the current density does not depend either on electric field intensity or on the

mobility of charged particles; in this case, the situation leads to the current density saturation.

If the potential difference between the electrodes increases further after the achievement of current density saturation, then it will be a moment when the current will increase again. The pattern of the current growth will depend on the gas pressure. With an increase in electric field intensity *E,* the electrons near the cathode are accelerated stronger and the energy that they acquire exceeds the ionization energy, which leads to the formation of a greater number of electrons; accordingly, the current will rise again. To explain the current increase, Townsend introduced measure α, which is referred to as the first ionization coefficient, which determines the number of collisions with ionizing effect per centimeter of the path in the direction of the electric field force lines.

The number of electrons that cross the surface located in the immediate vicinity of the cathode surface at distance *dx* in the direction of the electric field force lines will be [3, 4]:

$$dn = \alpha \cdot n \cdot dx.$$

Taking into account the distance between the cathode to the elementary surface which is located at distance *dx*, by integrating this relationship over *x,* we obtain [3, 4]

$$\int_{n_0}^{n} \frac{dn}{n} = \int_{0}^{x} \alpha \cdot dx .$$

Considering that *α* does not depend on *x,* in accordance with the authors of [3, 4], we obtain

$$n = n_0 \exp(\alpha \cdot x) ,$$

where n_0 is the number of electrons that leave the cathode per second.

Taking into account the fact that the distance between the electrodes (the gap size) is *S,* for the current intensity, the following relationships are derived [3, 4]:

$$i = n_0 \cdot e \cdot \exp(\alpha \cdot S) = i_0 \cdot \exp(\alpha \cdot S) ,$$

where $i_0 = n_0 \cdot e$ is the photoelectric current near the cathode caused by the external radiation.

Difference $i - i_0$ represents the current caused by the positive ions in the immediate vicinity of the cathode surface.

The increase in *dn* caused by the ionization of collision with electrons in interval *dx* (*n* per second), as well as those of photoionization along the same interval *dx,* will be [3, 4]:

$$dn = \alpha \cdot n \cdot dx + n_i \cdot dx.$$

Using the method of separation of variables, from the above relationship for the electron concentration, we obtain

$$\int_0^n \frac{dn}{\alpha \cdot n + n_i} = \int_0^x dx;$$

$$\alpha \cdot n + n_i = n_i \exp(\alpha \cdot x);$$

$$n = \frac{n_i}{\alpha}[\exp(\alpha \cdot x) - 1].$$

or for the current [3, 4]:

$$i = \frac{n_i \cdot e}{\alpha}[\exp(\alpha \cdot S) - 1];$$

$$i_0 = \frac{n_i \cdot e}{\alpha};$$

$$i = i_0[\exp(\alpha \cdot S) - 1].$$

The last relationship suggests that the total current in the gap depends on values of α and S. If the free path length until the collision is λ, then the average energy that the electrons accumulate between two consecutive collisions will be [3, 4]:

$$W = e \cdot E \cdot \lambda.$$

However, the length of free path is inversely proportional to the pressure of the active medium [3, 4]:

$$\lambda \sim \frac{1}{p},$$

Townsend coefficient α is proportional to electric field intensity E and gas pressure p and can be expressed by the function:

$$\alpha = p \cdot f(e \cdot E \cdot \lambda),$$

or

$$\alpha = p \cdot F\left(\frac{e \cdot E}{p}\right),$$

where F is the function of the same type as f. Because e is a constant, according to the authors of [3, 4], we obtain

$$\frac{\alpha}{p} = \varphi\left(\frac{E}{p}\right).$$

2. Experimental

The circuit of the experimental setup shown in Fig. 1 consists of the following elements [5, 6]: a DC power supply operating at voltage $U = 25$ kV, discharger (Ecl), condenser battery (C), ballast resistor R, special electrode *1*, and counter-electrode *2*. The special electrode consisting of multiple wires with the clearly defined active resistance causes the division of the discharge current through all the formed channels. This facilitates the deployment of pulsed discharge in several channels simultaneously leading to the formation of high current densities and thereby to an increase in the efficiency of the energy used for discharge and plasma homogenization in the gap.

The gap size is $S = 7$ mm. The area of the cross-section of the special electrode is 17×7 mm, where about 600 copper wires of 0.35-mm diameter isolated one from another are located. The measurement and observation of current pulses (duration, shape, and amplitude) [5, 6] are conducted through an oscilloscope with memory Osc (C8-13) shunted by resistance $R_s = 0.003$ Ω. The circuit is grounded to protect the setup and the oscilloscope and eliminate the effects of reactive elements on the discharge process.

The shape and duration of current pulses of the discharges obtained in the investigations are shown in Fig. 2. It is evident that the pulse shape directly depends on the value of the ballast resistance and capacity, which, with a special electrode, form an RLC-type generator. In Fig. 2 the AB curve corresponds to auto-ionization (in this case, the special electrode functions as an electron gun); the BC curve corresponds to the base discharge (plasma production); the CD curve corresponds to the relaxation process (the gaseous media properties return to the original state); after that, the process repeats from one discharge to another with the frequency required by the control electrical circuit.
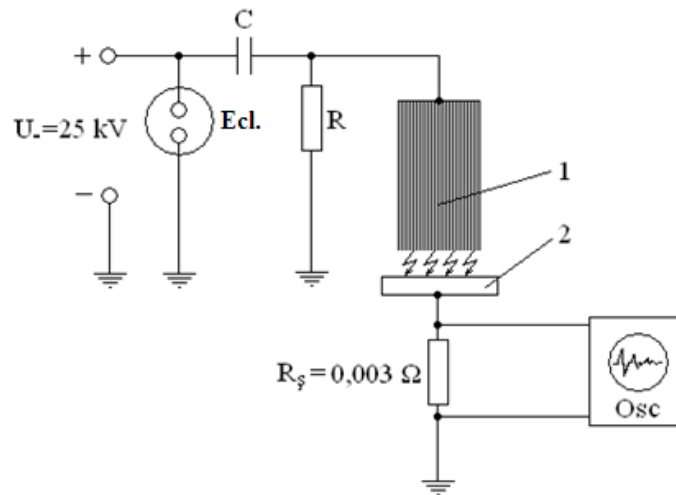
Fig. 1. Circuit schematic of the experimental setup and measurement of discharge impulse parameters [5, 6]: Ecl, discharger; Osc, oscilloscope with memory; R_S, shunt resistance; *1*, special electrode; and *2*, counter-electrode.
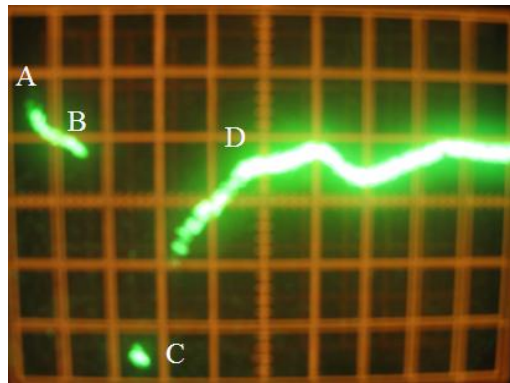

Fig. 2. General view of the current pulses for capacity $C = 1/12$ µF and ballast resistance $R = 8.2$ MΩ [5–7]; the size of time divisions is 0.2µs/div; the size of voltage divisions is 100 V/div.

The characteristics of electrical discharge pulses of the used experimental setup are as follows: the capacity of the condenser battery, $C = 1/12$ µF; the energy accumulated on the condenser battery, $W_C = 26$ J; the pulse duration, $\tau_{imp}=0.15$ µs; the pulse amplitude on the oscilloscope, $U_{osc}= 350$ V; the current pulse amplitude, $I_s= 100$ kA; and the current intensity in the gap, $\int_0^\tau i_s\, dt = 50$ kA·s. The energy accumulated on the condenser battery ($W_c= \dfrac{CU^2}{2}$) is approximately equal to 26 J. Since the used circuit is unipolar and taking into account the losses that occur on the electrical circuit elements, as low as about 8 J is transformed to thermal energy.

3. Experimental results

Owing to the use of a unipolar circuit of the experimental setup (Fig. 1), the stability of plasma formation was reached under laboratory conditions without preventive ionization of the

active media. The AB curve in Fig. 2 represents the intense ionization of the active media.

Fig. 3. Plasma of pulse electrical discharges obtained under laboratory conditions.

Auto-ionization occurs owing to the design of special electrode *1* in Fig. 1 and an increase in the electric field inhomogeneity in the space between the electrodes and consumes about 5−7% of the total energy stored in the condenser battery.
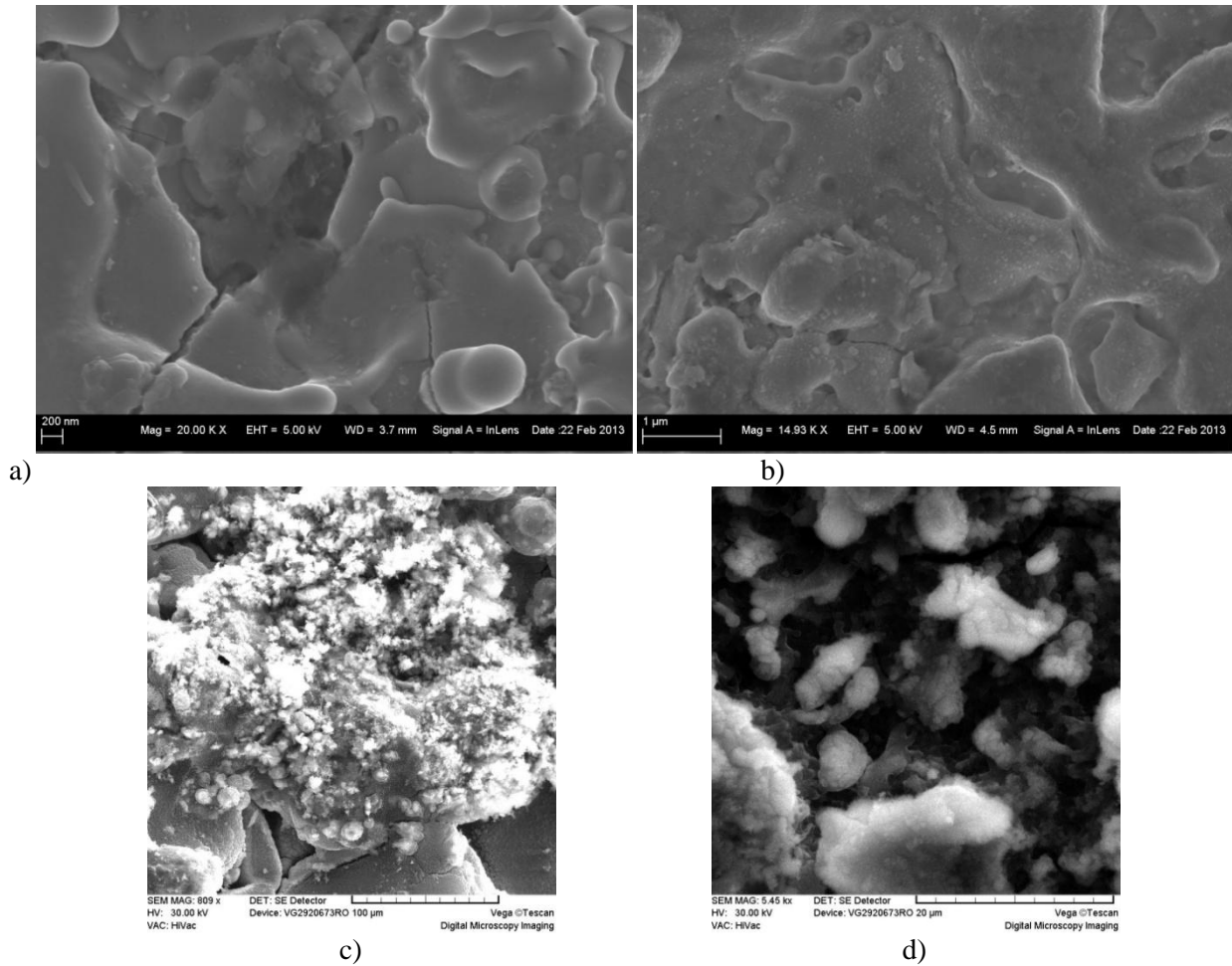

a)
b)
c)
d)

Fig. 4. Morphology of the surface layer of counter-electrode *2* in Fig. 1 formed as a result of plasma interaction:

(a) steel 45, (b) titanium alloy BT8, (c) aluminum alloy D16, and (d) bronze BrA5

The base discharge (the BC sector, Fig. 2) occurs within 0.15 mS with the pulse discharge current amplitude of I_s = 100 kA. A portion of the energy released in the gap is transformed into luminescent radiation of intensity $L = 10^8–10^9$ W/cm^2. These types of discharges can be applied in the construction of quantum generators, which operate in non-aggressive active media. The general view of a pulse of the electric discharge plasma produced on the developed experimental setup is shown in Fig. 3. It is evident that the amount of energy released on the electrode surfaces and in the gap is different.

Counter-electrode *2* in the circuit in Fig. 1 was made of different materials (steel 45, titanium alloy BT8, duralumin D16, and bronze BrA5) of a flat shape. Electron microscope studies of the surfaces showed that the interaction of these electrodes with the obtained plasma resulted in the formation of nanostructures on the surfaces that have different shapes and properties depending on the type of the material. The morphology of the surface layer of the samples processed via applying the obtained plasma using the experimental setup is shown in Fig. 4.

Since the temperature of the plasma obtained on the developed experimental setup reaches values higher than 10^4 K with its duration of existence of hundreds of nanoseconds, it can be applied for the formation of nanostructures on metal surfaces and for the destruction of microorganisms in biomedicine.

4. Conclusions

Based on theoretical and experimental analysis of the plasma formation by electrical discharges under laboratory conditions, we can make the following conclusions:

(i) The electrical discharge plasma was producted under laboratory conditions without the use of special devices for the preventive ionization of the active media and did not require synchronization between the connection of these devices and base discharge.

(ii) The experimental setup provide the energy emission in pulses capable of forming the volumetric plasma in air under ordinary pressure.

(iii) The pulsed electrical discharge plasma obtained with the developed experimental setup provides the formation of nanostructures on metal surfaces, such as clusters, nanotubes, nanowires, etc.

References

[1] S. K. Zhdanov et al., Osnovy fizicheskikh protsessov v plazme i plazmennykh ustanovkakh, MIFI, Moscow, 2000, 184 p.

[2] F. Chen, Vvedenie v fiziku plazmy, Mir, Moscow, 1987, 398 p.

[3] A. M. Khovantson, Vvedenie v teoriyu gazovogo razryada, Atomizdat, Moscow, 1980, 182 p.

[4] E. P. Velikov, A. S. Kovalev, and A. T. Rakhimov, Fizicheskie yavleniya v gazeorazryadnoi plazme, Nauka, Moscow, 1987, 160 p.

[5] P. Topala, A. Hirbu, and A. Ojegov, Nonconv. Technol. Rev. 1, 49, (2011).

[6] P. Topala, A. Hirbu, and A. Ojegov, Fiz. Tehnol. Mod. 10 (1−2), 13, (2012).

IN MEMORIAM NICOLAE POPOVICI

(December 19, 1943 – March 7, 2015)

Nicolae Popovici was born on December 19, 1943 in the Sarateni village, Telenesti district. In 1962–1967, he was a student of the Faculty of Physics and Mathematics of the A. Russo State University. N. Popovich began his academic activity as a physics teacher in a secondary school in the BratuseniiVech village, Edinet district in 1967. In 1970–1974, he was a post-graduate student at the Institute of Applied Physics of the Academy of Sciences of Moldova.

N. Popovich defended his candidate's dissertation in 1976 and his doctoral dissertation in 1986 (both on physics and mathematics); in 1990 he became Professor in physics of semiconductors and dielectrics. After post-graduate courses at the Institute of Applied Physics of the Academy of Sciences of Moldova, N. Popovici worked at the same institute as an inferior researcher (1974–1978), a senior researcher (1978–1986), a leading researcher (1986–1988), head of the Laboratory for physics of anisotropic semiconductors (1988–2006), and a principal researcher (1996–2006). Since 2006, he was principal researcher at the Gitsu Institute of Electronic Engineering and Nanotechnologies of the Academy of Sciences of Moldova.

As a result of scientific activity for more than four decades, Prof. Popovici has laid the foundation of a new scientific direction in condensed matter physics—physics of $A^{III}B^{V}C_2^{VI}$ semiconductors and alloys thereof with $A^{IV}B^{VI}$.

The basic developments that have determined the success of research in this field primarily include the growth technology for $A^{III}B^{V}C_2^{VI}$ semiconductors and alloys thereof, which was developed in strict accordance with respective state diagrams. The high quality of the crystals obtained by Prof. Popovich during these years was repeatedly confirmed at various scientific centers in Russia, Ukraine, Lithuania, Germany, the Czech Republic, and other countries. A particularly convincing evidence of the high quality of $TlSbTe_2$ and $TlBiS_2$ crystals is the Shubnicov-de Haas oscillations, which have been first detected in crystals of this type.

Of particular interest are the results of Prof. Popovich in the study of the optical and photoelectric properties of layered $TlSbTe_2$ and $TlBiS_2$ semiconductors, $(TlSbS_2)_{1-x}$ $(TlSbSe_2)_x$ solid solutions, and electronic devices based on these crystals. In recent years, physics of layered semiconductors has become a separate scientific direction; we believe that an important role in the formation of this research trend rightfully belongs to Prof. Popovici and his disciples.

Another area of research of Nicolae Popovici is related to studying the electrophysical properties of rhombohedral $A^{III}B^VC_2^{VI}$ crystals and $(A^{III}B^VC_2^{VI})_{1-x}$ $(2A^{IV}B^{VI})_x$ solid solutions, in particular under extreme conditions (high hydrostatic pressures of ~300 kbar and low temperatures of ~0.05 K). As a result of these studies, the basic kinetic parameters and the model (shape) of the charge carrier bands for these semiconductors have been first determined.

Of primary concern are the results of Prof. Popovich in the study of the specific features of heat transfer and the thermoelectric efficiency of $(A^{III}B^VC_2^{VI})_{1-x}$ $(2A^{IV}B^{VI})_x$ solid solutions. In studies of the $(TlBiS_2)_{1-x}$ $(2PbS)_x$ system, Prof. Popovici found that the thermal conductivity of the lattice of these alloys achieves extremely low values (K_L ~ 0.26 W/mK), which almost achieves the lower limit of parameter K_L theoretically determined for crystalline semiconductors, and, therefore, leads to a significant increase in thermoelectric efficiency Z in these materials. The new systems of $(A^{III}B^VC_2^{VI})_{1-x}$ $(2A^{IV}B^{VI})_x$ solid solutions discovered by Prof. Popovici open the way to the implementation of a new strategy in the field of engineering of thermoelectric materials.

It should be noted that a large portion of the research of Prof. Popovici were completed with specific developments, which were protected by patents and subsequently implemented in actual practice in various research centers and specialized technical offices. These developments include $TlSbSe_2$ temperature-sensitive resistors; Au-n–$TlSbSe_2$ broadband diodes (0.6–1.4 μm); $TlSbS_2$ photoresistors (τ ~ 10^{-8} s, ρ_d /ρ_f ~ 10^7, I ~ 10^{25} photon/cm^2 s) for the generation of giant ruby laser pulses; a device for measuring the electric conductivity and thermopower of semiconductor materials in a temperature range of 300–1200 K; and a device for measuring the thermal conductivity of thermoelectric materials using the Peltier effect.

The results of Prof. Popovici have been appreciated by experts in the field. This is confirmed by the fact that, in recent years, he was repeatedly invited to the United States (Ferrotec Corporation) as scientific consultant in the field of engineering of thermoelectric materials.

Professor Nicolae Popovici has made a considerable contribution to the training of highly skilled scientific personnel. He was a research supervisor of seven doctors in physics and mathematics.

In 1969–1972, N. Popovich worked as a lecturer at the Department of Physics at the Ion Creanga Pedagogical University and the Department of Physics at the N. Testemitanu University of Medicine and Pharmacy. He delivered lectures on physics and engineering of semiconductor materials and energy-converting electronic devices and master class courses at the Technical University of Moldova (1977–1985), Tiraspol University located in Chisinau (2003–2009), and Al. Russo State University of Balti (2006).

Professor Nicolae Popovici will be remembered by his disciples and colleagues as a recognized expert in condensed matter physics and a highly skilled specialist in semiconductor material technology.

Academician Valeriu Kantser
Dr. Sofia Donu

CONTENTS

Bulk Materials

Nanostructures and Nanomaterials

Condensed Matter Theory

Devices Physics

Miscellaneous and General Physics

Personalia